Excited-State Dynamics in Open-Shell Molecules

Anja Röder

NNT : 2017SACLS099

THESE DE DOCTORAT
DE
L'UNIVERSITE DE WÜRZBURG
ET DE
L'UNIVERSITE PARIS-SACLAY
PREPAREE A L'UNIVERSITE PARIS-SUD

ÉCOLE DOCTORALE N°571
Sciences chimiques : molécules, matériaux, instrumentation et biosystèmes

Spécialité de doctorat : Chimie

Par

Mme Anja M. Röder

Excited-State Dynamics in Open-Shell Molecules

Thèse présentée et soutenue à Versailles, le 17 juillet 2015 :

Composition du Jury :

M Roland Mitrić	Professeur, Université de Würzburg	Président du Jury
M. Volker Engel	Professeur, Université de Würzburg	Rapporteur
Mme Valérie Blanchet	HDR, Université de Bordeaux	Rapporteur
Mme Séverine Boyé-Péronne	Maître de Conférences, Université Paris Sud	Examinatrice
M. Lionel Poisson	HDR, Université Paris Saclay	Directeur de thèse
M. Ingo Fischer	Professeur, Université de Würzburg	Co-Directeur de thèse

Julius-Maximiliams-Universität Würzburg

Université Paris Sud

Anja M. Röder from Schwebheim

Excited-State Dynamics in Open-Shell Molecules

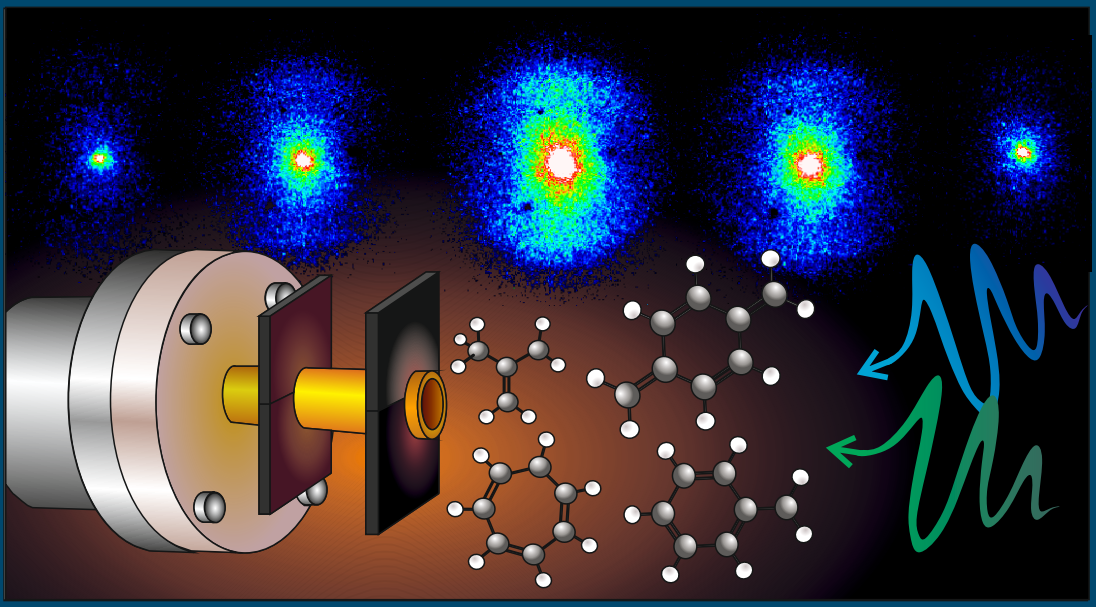

A thesis submitted for the degree of Doctor of Natural Sciences

Dissertation zur Erlangung des naturwissenschaftlichen Doktorgrades der Julius-Maximiliams-Universität Würzburg

Pour obtenir le grade de Docteur en Sciences de l'Université Paris-Sud

Supervisors:
Prof. Dr. I. Fischer (Würzburg/Germany)
Dr. L. Poisson (Saclay/France)

Paris/Würzburg
2017

German Committee:

Eingereicht am: 04.05.2017

bei der Fakultät für Chemie und Pharamzie

1. Gutachter: Ingo Fischer
2. Gutachter: Lionel Poisson

der Dissertation

1. Prüfer: Volker Engel
2. Prüfer: Roland Mitric
3. Prüfer: Valérie Blanchet
4. Prüfer: Severine Boyé-Pérone

Tag des öffentlichen Promotionskolloquiums: 10.07.2017

Doktorurkunde ausgehändigt am: .....

French Committee:

Soutenue: 10.07.2017

devant la comission d'examen:

1. Rapporteur: Valérie Blanchet
2. Rapporteur: Volker Engel

de thèse de doctorat

1. Directeur de thèse: Lionel Poisson

No. d'ordre: 2017SACLS099

ÉCOLE DOCTORALE
Sciences chimiques : molécules, matériaux, instrumentation et biosystèmes

No. d'ordre: 2017SACLS099

These de Doctorat
de
l'Universite Paris-Saclay

École Doctorale N° 571
Sciences Chimiques: Molécules, Matériaux, Instrumentation et Biosystèmes
Spécialité de doctorat: Chimie

Par

Mme Anja Röder

Excited-State Dynamics in Open-Shell Molecules

Thèse présentée et soutenue à Würzburg, le 10 juillet 2017:

Composition du Jury:

Dr. Valérie Blanchet	Rapporteur
Prof. Dr. Volker Engel	Rapporteur
Dr. Séverine Boyé-Péronne	Examinateur
Prof. Dr. Roland Mitrić	Examinateur
Prof. Dr. Ingo Fischer	Directeur de thèse
Dr. Lionel Poisson	Directeur de thèse

"In the beginning there was nothing, which exploded."
-Terry Pratchett, Lords and Ladies

Acknowledgments

Here I would like to thank all those who supported me during my studies and during my years as a PhD-student. First I would like to thank my two PhD-supervisors, Ingo Fischer and Lionel Poisson. Thank you very much for giving me this unique chance to discover both the German and French world of research in physical chemistry and for the numerous scientific discussions. Your uncomplicated nature and good collaboration made this project not only possible, but also enriching and enjoyable, and the things I learned under your supervision are too numerous too count.

Danke hier auch an die ganze fischerische Arbeitsgruppe, es war ein sehr angenehmes Arbeitsklima und eine echt schöne Zeit mit euch! Die wissenschaftlichen Diskussionen, die zahlreichen Kuchen, Weißwurstfrühstücke, Käseplatten und Ausflüge, sowie die Tatsache dass alle immer ein offenes Ohr für die Probleme der anderen haben, war eine große Bereicherung.

Ein herzliches Dank auch an die Arbeitsgruppe Mitrić, insbesondere an Roland Mitrić, Jens Petersen, Alexander Humeniuk und Kevin Issler für die theoretische Untermauerung unserer Ergebnisse - ohne euch würden wir noch bei einigen Ergebnissen mit der Interpretation kämpfen.

Engelbert Reusch, ich möchte mich bei dir für die zwei Wochen in Saclay für die Synthese des Propargylens bedanken, auch wenn das Projekt leider nicht so erfolgreich war. Deine Erfahrung in der Landwirtschaft und mit Bienen haben immer für interessante Diskussion gesorgt. Vielen Dank auch an Hans-Christian Schmitt und Florian Hirsch, die auch mit in Saclay waren und mir bei den Experimenten geholfen haben. Jens Giegerich und Florian Hirsch, meine Bürokollegen, die meine An- und Abwesentheit stoisch ertragen haben, möchte ich für die bereichernden wissenschaftlichen und nicht-wissenschaftlichen Diskussionen sowie für das eine oder ander Schachspiel bzw. Gospiel bedanken.

Ein herzliches Dank auch an die Studenten Hubert Gerwe and Pascal Kunkel, es war eine große Freude euch beide zu betreuen.

Un grand merci aussi à mon collègue de bureau français, Marc-André Gaveau, qui a enrechi mon vocabulaire et ma connaissance générale avec ses calembours et avec ses explications de ceux-ci quand je les comprendrais pas. Je voudrais également remercier Jean-Michel Mestdagh, Benoit Soep, Marc Briant, Patrick De-Pujo et Barbara Miranda pour les discussions scientifiques et non-scientifiques le midi. Vous étiez toujours à l'écoute de mes questions et prêt à m'aider si j'en avais besoin. Je tiens également à remercier Ephriem Mengesha, Sana Habka, Thibaut Very et Tiia-Maaria Ketola pour les nombreuses discussions et sorties entre jeunes et pour une fête de Noël mémorable.

I also want to thank all the technicians, namely Reiner Eck, Wolfgang Lieber, Ralf Kohrmann, Katharina Schreckling and Peter Lang from the workshop of the Institute for Physical and Theoretical Chemistry in Würzburg, as well as Christophe Pothier, Olivier Gobert, Michel Perdrix, Pascal D'Oliveira, Fabien Lepetit and Delphine Guillaumet from the Laboratire Interactions, Dynamiques et Lasers (LIDyL). Without your support this scientific work would not have been possible, thank you very much!

Vielen Dank auch an meine Familie, für die Unterstützung während meines Studiums und meiner Doktorarbeit. Es war sicherlich nicht immer leicht mit meiner ständigen Hin-und Herreiserei, besonders möchte ich mich hier bei meiner Mutter bedanken, die sich während meiner Abwesentheit um meine Wohnung gekümmert hat. Ein herzliches Dank an euch, ohne euch wäre ich nicht der Mensch, der ich heute bin!

I also would like to thank all my kayaking friends, too numerous to list here, who showed me the non-scientific way of enjoying dynamics (whitewater), pyrolysis (evenings around a bonfire) and how fast a concial intersection flips two states (pushing me during playing kayak polo). Un merci spécial ici à Damien Le Guidec, pour m'avoir montré tant des films français et me les avoir expliqueés dans le cadre de la culture française.

Another very important contributor is all the funding I received, I want to thank you for financing the travel and extra living expenses due to the joint thesis. Specifically I want to thank the Procope programme of the deutscher akademischer Austauschdienst (DAAD), the Bourse Eiffel and the MOLIM grant, from which I beneficated during my different stays in Saclay. I also want to acknowledge the GRK 2112 'Molecular biradicals: structure, properties and reactivity', who financed my work in Würzburg. Lastly I would also like to thank the Deutsch-französische Hochschule/l'université franco-allemande (DFH/UFA) for the financial support during the thesis and for the defense of the thesis.

Summary

In this thesis the excited-state dynamics of radicals and biradicals were characterized with femtosecond pump-probe spectroscopy.

These open-shell molecules play important roles as combustion intermediates, in the formation of soot and polycyclic aromatic hydrocarbons, in atmospheric chemistry and in the formation of complex molecules in the interstellar medium and galactic clouds. In these processes molecules frequently occur in some excited state, excited either by thermal energy or radiation. Knowledge of the reactivity and dynamics of these excited states completes our understanding of these complex processes.

These highly reactive molecules were produced via pyrolysis from suitable precursors and examined in a molecular beam under collision-free conditions. A first laser now excites the molecule, and a second laser ionizes it. Time-of-flight mass spectrometry allowed a first identification of the molecule, photoelectron spectroscopy a complete characterization of the molecule - under the condition that the mass spectrum was dominated by only one mass. The photoelectron spectrum was obtained via velocity-map imaging, providing an insight in the electronic states involved. Ion velocity map imaging allowed separation of signal from direct ionization of the radical in the molecular beam and dissociative photoionization of the precursor. During this thesis a modified pBasex algorithm was developed and implemented in *python*, providing an image inversion tool without interpolation of data points. Especially for noisy photoelectron images this new algorithm delivers better results.

Some highlighted results:

- **The 2-methylallyl radical** was excited in the ππ*-state with different internal energies using three different pump wavelengths (240.6 , 238.0 and 236.0 nm). Ionized with 800 nm multi-photon probe, the photoelectron spectra shows a s-Rydberg fingerprint spectrum, a highly positive photoelectron anisotropy of 1.5 and a bi-exponential decay ($\tau_1 = 141 \pm 43$ fs, $\tau_2 = 4.0 \pm 0.2$ ps for 240.6 nm pump), where the second time-constant shortens for lower wavelengths. Field-induced surface hopping dynamics calculations confirm that the initially excited ππ*-state relaxes very fast to an s-Rydberg state (first experimentally observed time-constant), and then more slowly to the first excited state/ground state (second time-constant). With higher excitation energies the conical intersection between the s-Rydberg-state and the first excited state is reached faster, resulting in shorter lifetimes.
- **The benzyl radical** was excited with 265 nm and probed with two wavelengths, 798 nm and 398 nm. Probed with 798 nm it shows a bi-exponential decay ($\tau_1 = 84 \pm 5$ fs, $\tau_2 = 1.55 \pm 0.12$ ps), whereas with 398 nm probe only the first time-constant is observed ($\tau_1 = 89 \pm 5$ fs). The photoelectron spectra with 798 nm probe is comparable to the spectrum with 398 nm probe during the first 60 fs, at longer times an additional band appears. This band is due to a [1+3']-process, whereas with 398 nm only signal from a [1+1']-process can be observed. Non-adiabatic dynamic on the fly calculations show that the initially excited, nearly degenerate ππ/p-Rydberg-states relax very fast (first time-constant) to an s-Rydberg state. This s-Rydberg state can no longer be ionized with 398 nm, but with 798 nm ionization via intermediate resonances is still possible. The s-Rydberg state then decays to the first excited state (second time-constant), which is long-lived.
- ***Para*-xylylene**, excited with 266 nm into the S_2-state and probed with 800 nm, shows a bi-exponential decay ($\tau_1 = 38 \pm 7$ fs, $\tau_2 = 407 \pm 9$ fs). The initially excited S_2-state decays quickly to S_1-state, which shows dissociative photoionization. The population of the S_1-state

is directly visible in the masses of the dissociative photoionization products, benzene and the *para*-xylylene -H.

- ***Ortho*-benzyne**, produced via pyrolysis from benzocyclobutendione, was excited with 266 nm in the S_2 state and probed with 800 nm. In its time-resolved mass spectra the dynamic of the ortho-benzyne signal was superposed with the dynamics from dissociative photoionization of the precursor and of the *ortho*-benzyne-dimer. With time-resolved ion imaging gated on the *ortho*-benzyne these processes could be seperated, showing that the S_2-state of *ortho*-benzyne relaxes within 50 fs to the S_1-state.

Zusammenfassung

In der vorliegenden Dissertation wurde die Dynamik angeregter Zustände von Radikalen und Biradikalen mittels femtosekunden-zeitaufgelöster Anrege-Abfragespektroskopie untersucht.

Radikale und Biradikale sind nicht nur wichtige Zwischenprodukte in Verbrennungsprozessen, sondern auch bei der Bildung von Ruß und polyzyklischen aromatischen Kohlenwasserstoffen beteiligt. Des Weiteren spielen sie eine wichtige Rolle in der Atmosphärenchemie und bei der Bildung komplexer Moleküle im interstellaren Medium. Von entscheidender Bedeutung ist in den genannten Prozessen die Anregung der Radikalen und Biradikale in energetisch höhere Zustände, dies geschieht entweder durch thermische Energie oder mittels Strahlung. Für das Verständnis der ablaufenden Vorgänge ist es zwingend erforderlich die Dynamik der angeregten Zustände zu verstehen.

Die Radikale und Biradikale wurden dafür mittels Pyrolyse eines geeigneten Vorläufers erzeugt, und anschließend unter kollisionsfreien Bedingungen im Molekularstrahl spektroskopisch untersucht. Hierbei regt ein erster Laser das Molekül an, ein zweiter Laser ionisiert es. Mittels Flugzeitmassenspektrometrie wurden die Moleküle identifiziert, und mittels Photoelektronenspektroskopie weiter charackterisiert - unter der Bedingung, dass im Massenspektrum eine Masse dominiert. Das Photoelektronenspektrum wurde mittels Velocity-Map Imaging aufgenommen und gibt einen Einblick in den elektronischen Zustand im Augenblick der Ionisations. Die Velocity-Map Imaging-Technik von Ionen erlaubt außerdem die Unterscheidung von Ionen aus direkter Ionisation und dissoziativer Photoionisation. In diesem Rahmen wurde auch ein modifizierter pBasex-Algorithmus entwickelt und in *Python* implementiert. Dieser kommt im Gegensatz zum herkömmlichen pBasex-Algorithmus komplett ohne Interpolation der Datenpunkte aus. Besonders bei verrauschten Photoelektronenspektren liefert dieser Algorithmus bessere Ergebnisse.

Einige Resultate sollten besonders hervorgehoben werden:

- **Das 2-Methylallylradikal** wurde in einen ππ*-Zustand mit drei verschiedenen Anregungswellenängen (240.6, 238.0 und 236.0 nm) angeregt, um eine Variation der inneren Energie innerhalb dieses Zustandes zu ermöglichen. Es wurde mit bis zu drei 800-nm-Photonen ionisiert. Das Photoelektronenspektrum zeigt ein s-Rydberg-photoelektronenspektrum, eine positive Photoelektronenanisotropie von 1.5 sowie einen biexponentiellen Zerfall (τ_1= 141±43 fs, τ_2= 4.0±0.2 ps für 240.6 nm als Anregelaser). Die zweite Zeitkonstante verkürzt sich mit kürzeren Wellenlängen. *Field-induced surface hopping* Dynamikrechungen bestätigen, dass der ursprünglich angeregte ππ*-Zustand schnell in einen s-Rydbergzustand relaxiert (erste Zeitkonstante), um dann anschließend langsamer in den ersten angeregten Zustand zu relaxieren (zweite Zeitkonstante). Mit einer höheren inneren Energie wird die konische Durchschneidung zwischen dem s-Rydbergzustand und dem ersten angeregten Zustand schneller erreicht, somit verkürzt sich die zweite Zeitkonstante bei kürzeren Wellenlängen.

- **Das Benzylradikal** zeigt in einem 265 nm Anrege-/798 nm Abfrage-experiment einen biexponentiellen Zerfall ($\tau_1 = 84 \pm 5$ fs, $\tau_2 = 1.55 \pm 0.12$ ps), wohingegen mit 398 nm lediglich ein monoexponentieller Zerfall sichtbar ist ($\tau_1 = 89 \pm 5$ fs). Das 798 nm Abfrage-Photoelektronenspektrum ist in den ersten 60 fs ähnlich dem 398 nm Abfrage-Photoelektronenspektrum, bei späteren Zeiten erscheint eine weitere Bande bei höheren kinetischen Energien der Elektronen. Diese Bande stammt aus einem [1+3']-Prozess, während bei 398 nm nur Signal aus einem [1+1']-Prozess beobachtbar ist. Laut nichtadiabatische Dynamikrechungen relaxiert der ursprünglich angeregte ππ-Zustand bzw. der fast energiegleiche p-Rydbergzustand sehr schnell in einen s-Rydbergzustand (erste Zeitkonstante), welcher mit 798 nm über intermediäre Resonanzen noch ionisiert werden kann, aber nicht mehr mit 398 nm. Anschließend relaxiert der s-Rydbergzustand in den ersten angeregten, langlebigen Zustand (zweite Zeitkonstante).

- ***Para*-Xylylen** wurde mit 266 nm in den S_2-Zustand angeregt und mit 800 nm in einem Multiphotonenprozess ionisiert. Es zeigt einen biexponentialen Zerfall ($\tau_1 = 38 \pm 7$ fs, $\tau_2 = 407 \pm 9$ fs). Der ursprünglich angeregte S_2-Zustand relaxiert schnell in den S_1-Zustand, welcher im Ion dissoziert. Somit lässt sich die Besetzung des S_1-Zustands direkt an den Signalen der Dissoziationsprodukte Benzol und dem Wasserstoffabstraktionsprodukt von *para*-Xylylen verfolgen.
- ***Ortho*-Benzin** wurde via Pyrolyse des Vorläufers Benzocyclobuten-1,2,-dion hergestellt, mit 266 nm in den S_2-Zustand angeregt und mit 800 nm ionisiert. In den zeitaufgelösten Massenspektren wird die Dynamik des *ortho*-Benzinsignals durch die dissoziative Photoionisationdynamik des Vorläufers und des *ortho*-Benzindimers überlagert. Mittels zeitaufgelöste Ionenspektren vom *ortho*-Benzin konnten diese Prozesse voneinander getrennt werden, und es konnte gezeigt werden, dass der S_2-Zustand von *ortho*-Benzin innerhalb von 50 fs in den S_1-Zustand relaxiert.

Résumé

Dans cette thèse, la dynamique des états excités des radicaux et biradicaux a été examinée en utilisant la spectroscopie pompe-sonde résolue en temps à l'échelle femto-seconde. Les molécules à couche ouverte jouent un rôle primordial comme intermédiaires dans les processus de combustion, dans la formation de la suie et des hydrocarbures aromatiques polycycliques, dans la chimie atmosphérique ou dans la formation des molécules organiques complexes du milieu interstellaire et des nuages galactiques. Dans tous ces processus les molécules sont souvent excitées, soit par échauffement thermique, soit par irradiation. En conséquence la réactivité et la dynamique de ces états excités sont particulièrement intéressantes afin d'obtenir une compréhension globale de ces processus.

Dans ce travail les radicaux et biradicaux ont été produits par pyrolyse à partir de molécules précurseur adaptées et ont été examinés dans un jet moléculaire en absence de collisions. Les radicaux sont ensuite portés dans un état excité bien défini, et ionisés avec un deuxième laser. La spectrométrie de masse à temps de vol permet une première identification de la molécule. Via des spectres de photoélectrons la molécule est characterisée, pourvu que le spectre de masse ne montre majoritairement qu'une seule masse. Les spectres de photoélectrons ont été obtenus par l'imagerie de vitesse, permettant d'obtenir des informations sur l'état électronique du radical au moment de l'ionisation. L'imaginerie de vitesse des ions permet de distinguer les ions issus d'une ionisation directe et ceux issus d'une ionisation dissociative. Pendant cette thèse un algorithme modifié de pBasex a été développé et implémenté en langage *python*: cet algorithme inverse des images sans interpolation des points expérimentaux, il montre une meilleure performance pour le traitement des images bruités. Pour des images bruitées cet algorithme montre une meilleure performance.

Quelques résultats sélectionnés:

- **Le radical de 2-méthylallyle** a été excité dans l'état $\pi\pi^*$ avec différentes énergies internes en utilisant trois différentes longueurs d'onde de pompe (240.6, 238.0 et 236.0 nm). Après ionisation par un laser 800 nm selon un processus multi-photonique, le spectre de photoélectrons montre le charactéristiques d'un état de Rydberg, une anisotropie des photoélectrons proche de 2 et un déclin biexponentiel ($\tau_1 = 141 \pm 43$ fs, $\tau_2 = 4.0 \pm 0.2$ ps avec 240.6 nm comme pompe). La deuxième constante de temps se réduit si la longueur d'onde de la pompe diminue. Des calculs de dynamique de saut de surface induite par champ confirment que l'état $\pi\pi^*$ initialement excité relaxe très vite dans un état de Rydberg s (première constante de temps expérimentale), qui se relaxe ensuite plus lentement vers le premier état excité (deuxième constante de temps). Avec une excitation plus énergétique, cette intersection conique est atteinte plus vite, de sorte que la seconde constante de temps diminue.

- **Le radical de benzyle** montre un déclin biexponentiel lorsqu'il est excité avec 265 nm et sondé avec 798 nm ($\tau_1 = 84 \pm 5$ fs, $\tau_2 = 1.55 \pm 0.12$ ps); si on sonde avec 398 nm un seul déclin est mesuré ($\tau_1 = 89 \pm 5$ fs). Le spectre de photoélectrons obtenu avec 798 nm comme sonde est comparable à celui avec 398 nm sonde pendant les premières 60 fs. À des temps plus longs une autre bande apparaît, issue d'un processus [1+3'], tandis qu'avec 398 nm seul le processus [1+1'] est visible. Des simulations non-adiabatique de la dynamique montrent que l'état $\pi\pi$ initialement excité relaxe vers un état de Rydberg s (première constante de temps). L'état de Rydberg s ne peut plus être ionisé avec un photon de 398 nm; mais 798 nm l'ionise avec 3 photons en passant par des états intermédiaires. Cet état de Rydberg s se relaxe vers le premier état excité (deuxième constante de temps).

- **Le *para*-xylylène** a été excité avec 266 nm dans l'état S_2. Sondé avec 800 nm, il montre un déclin biexponentiel ($\tau_1 = 38 \pm 7$ fs, $\tau_2 = 407 \pm 9$ fs). L'état S_2 initialement excité se relaxe très vite dans

l'état S_1, qui se dissocie une fois ionisé. La population de l'état S_1 peut donc être directement suivie par l'évolution de ses produits de dissociation, le benzène et le produit d'abstraction d'un hydrogène.

- ***Ortho*-benzyne**, produit via pyrolyse de benzocyclobutendione, a été excité dans l'état S_2 avec 266 nm et ionisé avec 800 nm. Dans les spectres de masse résolus en temps, la dynamique de l'*ortho*-benzyne a été altérée par la dynamique de photoionisation dissociative du precurseur et du dimère de l'*ortho*-benzyne. Ces deux processus ont pu néanmoins être différienciés par l'imagerie d'ion d'*ortho*-benzyne, montrant que l'état S_2 d'*ortho*-benzyne se relaxe vers l'état S_1 en 50 fs.

Contents

List of Abbreviations

ADC(2)	Algebraic Diagrammatic Construction through second order
amu	Atomic Molecular Units
ATR	Attenuated Total Reflectance
Basex	BAsis Set EXpansion
CASSCF	Complete Active Space Self Consistent Field
CASPT2	Complete Active Space Perturbation Theory 2^{nd} order
CC2	Second-Order approximate Coupled-Cluster
CCD	Charge-Coupled Device
CCSD	Coupled Cluster with Singles and Doubles
CI	Conical Intersection
eKe	Electron Kinetic Energy
EOM-CCSD	Equation Of Motion Coupled Cluster with Single and Double excitation
EPR	Electron Paramagnetic Resonance
ESR	Electron Spin Resonance
CFCs	ChloroFluoroCarbons
DFT	Density Functional Theory
DPI	Dissociative PhotoIonisation
FISH	Field-Induced Surface Hopping
FWHM	Full Width Half Maximum
HOMO	Highest Occupied Molecular Orbital
IE	Ionization Energy
IR	InfraRed
IRF	Instrument Response Function
ISC	InterSystem Crossing
JT	Jahn-Teller
LUMO	Lowest Unoccupied Molecular Orbital
MA	MethylAllyl
MCP	Micro-Channel Plate
MO	Molecular Orbital
MRCI	MultiReference Configuration Interaction
NMR	Nuclear Magnetic Resonance
NOPA	Noncollinear Optical Parametric Amplifier

PAD	Photoelectron Angular Distribution
PAH	Polycyclic Aromatic Hydrocarbons
PEPICO	PhotoElectron PhotoIon COincidence
pBasex	Polar BAsis Set EXpansion
PES	Potential Energy Surface
REMPI	Resonant Enhanced MultiPhoton Ionization
RRKM	Rice-Ramsperger-Kassel-Marcus
SA-CASSCF	State-Averaged Complete Active Space SCF
SCF	Self-Consistent Field
SiC	Silicium Carbid
S/N	Signal to Noise ratio
SOMO	Single Occupied Molecular Orbital
SPES	Slow PhotoElectron Spectrum
SVD	Singular Value Decomposition
TDDFT	Time-Dependent Density Functional Theory
TOF	Time-Of-Flight
TRPES	Time-Resolved-PhotoElectron Spectra
UV-Vis	UltraViolet-VISible
VMI	Velocity Map Imaging
VOC	Volatile Organic Compound

Part I

Introduction

Chapter 1 Motivation

Hydrocarbon radicals and biradicals are fascinating species: they possess at least one unpaired electron and are, for the most part, very reactive.

During the last three years of my graduate work I examined several hydrocarbon radicals and biradicals using time-resolved mass and photoelectron spectrometry. In the following a presentation of three areas of research will demonstrate possible applications of the obtained fundamental research data.

PAH and soot formation

Combustion processes have shaped human history for millennia. While in preindustrial times combustion was mainly used as a heat source, this changed during the industrial revolution. Nowadays the energy provided by the combustion process is stored or converted into mechanical energy e.g. for transportation, or into electricity for efficient energy transfer, making it the basis of our modern society.

Most people understand combustion as a complete reaction between fuel and atmospheric oxygen, to form only carbon dioxide CO_2 and water H_2O. This simplified picture doesn't hold up to reality, however. The ongoing discussions about global warming, pollution, particulate matter and last but probably not least the Volkswagen scandal has established in the public mind that combustion results in a multitude of other side-products. These side-products - consisting of soot, particulate matter, polyaromatic hydrocarbons (PAH) and other organic molecules - are often harmful or even

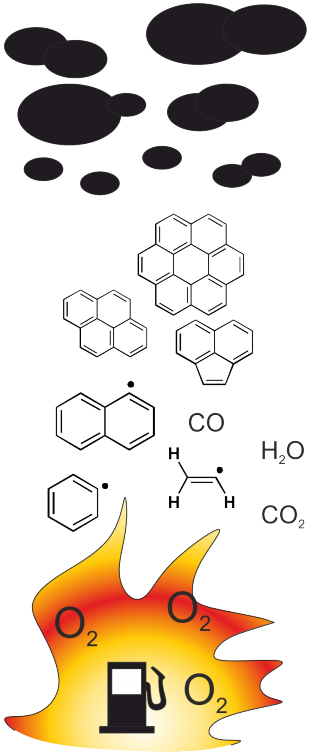

Figure 1.1: *Schematic picture of the formation of soot in flames*

outright toxic to humans [1,2]. PAH and particulate air pollution are mutagens [3–5], and have been associated with lung cancer and cardiopulmonary disease [6].

The molecular mechanism for the formation from the fuel to soot particles with PAH as the intermediary is still not fully understood in all its complexity. It depends for example on the fuel composition: the sooting tendencies increase in the following order: parafins< monoolefins <diolefins<benzenes<naphthalenes [7]. The mixture ratio of C/O, meaning fuel to oxygen, is also critical: soot formation normally begins when this ratio is smaller than one; but again, it depends strongly on the type of fuel used [8].

A simplified picture of soot particle formation is shown in fig. 1.1: The fuel reacts with oxygen, forming CO, CO_2 and H_2O, but also numerous radicals. The exact nature of the first radical formed depends of the type of fuel. These radicals then react with other molecules in addition and elimination reactions to form more and more complex ring systems. These addition and elimination reactions are illustrated in fig. 1.2 for the formation of the first and second aromatic ring from acetylene [9]. Acetylene reacts with an hydrogen atom - which are ubiquitous in combustion processes- to form a vinyl radical, which can then react with another acetylene molecule to form the butadienyl radical. This hydrogen-abstraction-C_2H_2-addition (HACA) process continues until larger, heavier PAH (500-1000 amu) are formed, fig. 1.2 stops with the naphthyl radical. These start to conglomerate to form particles, which in turn grow via reactive particle-particle collisions. Carbonization of the particle material, hydrogen abstraction and chemical modification continues throughout this process [10].

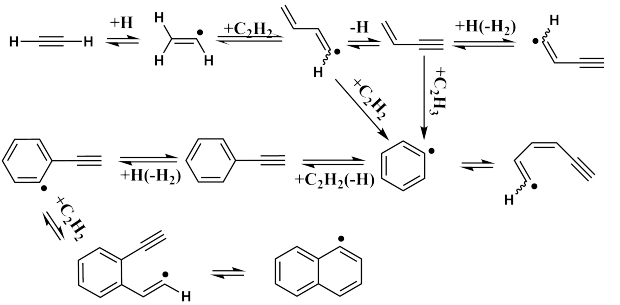

Figure 1.2: *Formation of the first and second aromatic ring from acetylene* [9]

The HACA mechanism alone, however, is too slow to explain the formation of soot [11], other mechanisms need to be involved as well to explain these reaction networks.

These reaction networks are very complex. They require lots of physicochemical data for a realistic simulation [12, 13], since in addition to the great number of species different flow regimes of the combustion processes [14, 15] (linear flame, explosion etc.) have to be taken into consideration. Time-resolved pump-probe mass and photoelectron spectroscopy allow to obtain data on the deactivation processes of excited states in hydrocarbon radicals and biradicals. These data might contribute to perfect existing combustion models as to one day be able to understand and successfully model combustion inside an engine and to minimize emissions of harmful and toxic side-products of combustion.

Moreover, many spectroscopic photodissociations experiments assume that the initally excited molecules dissociates on the ground state potential surface. Fs-time-resolved spectroscopy is one approach to verify whether this hypothesis is valid.

Atmospheric chemistry

The concentration of PAH, toxic combustion side-products and pollutants in the atmosphere is directly correlated to the ingoing flow: the amount released into the atmosphere and the outgoing one that leaves the atmosphere. The amount of organic compounds released into the atmosphere can be divided into two categories: human-induced via e.g. combustion of fuel and natural processes, e.g. terpenes from plants, so-called volatile organic compounds (VOCs) [16] or volcanic eruptions.

Species can leave the atmosphere via two paths: either via wet deposition (e.g. dissolved in rain or snow) or via dry deposition (direct transfer to earth's surface) [17]. Whereas particle PAHs are most commonly photolyzed and/or deposited via dry or wet deposition [18], photolysis of gaseous PAH with light that reaches the lower atmosphere (λ>290 nm in the troposphere) has not yet been observed [19].

Moreover, PAHs are unpolar molecules, wet and or dry deposition is also not directly possible. They can persist for a long time in the atmosphere unless they undergo chemical modifications. Typically they react with two highly abundant radicals in the atmosphere: OH or NO_3 [17], to ultimately form aldehydes and nitrites, more polar and water soluble [19]. These products are washed out into the sea, where they damage and accumulate in aqueous organisms [20, 21]. The lifetime of gaseous PAHs depends on the concentration of OH and NO_3 radicals in air, naphthalene, for example has a lifetime of 14 years in clean air, whereas in polluted air this is reduced to three days [19].

Long lifetimes allow molecules to reach the upper atmosphere (stratosphere), whose chemistry substantially differs from those in the lower atmosphere.

One well-known example of a stratospheric reaction due to a human pollutant is the depletion of the ozone layer due to chlorofluorocarbons (CFCs), a discovery for which the Nobel prize in chemistry was awarded in 1995 [22].

HCFCs in the atmosphere are completely of human origin, they were mainly used as refrigerants and aerosol sprays [23]. Their use has been severely restricted and/or forbidden depending on the concrete molecule and use [24]. CFCs were commercially attractive also because of their low reactivity - which in the atmosphere gives them ample time to diffuse into the stratosphere. They are dissociated by UV radiation, resulting in halogen radicals. Chlorine and bromine radicals act as catalysts, transforming ozone into molecular oxygen and robbing thus the earth's atmosphere of its protective ozone layer. One chlorine atom can remove about 100 000 ozone molecules from the atmosphere- before it is finally washed out [22, 25].

These two examples demonstrate effectively that atmospheric science is a complex field, whose reactions are dominated by radical-radical reactions and photodissociations. Fs-pump-probe spectroscopy is one method to examine especially photodissociations and the processes in a molecule once it is excited by UV radiation.

Galactic clouds/interstellar medium

The physical conditions in combustion and in the atmosphere are very different compared to those in galactic clouds or in the interstellar medium. Combustion in a motorized engine happens at least at normal pressure or under increased pressure at temperatures higher than 273 K, this corresponds to a density of $3{\cdot}10^{19}$molecules/cm^3(for a standard pres-

sure of 1 bar and 273 K). Even in the stratosphere the density is only about a 1000^{th} lower. This is in stark contrast to dense galactic clouds with densities of 10^4-10^8 hydrogen atoms/cm^3 [26], which corresponds to a pressure of $1{\cdot}10^{-10}$-$1{\cdot}10^{-14}$ bar. The adjective 'dense' has to be seen in the context of the interstellar medium with densities as low as 100 hydrogen atoms/cm^3 [26].

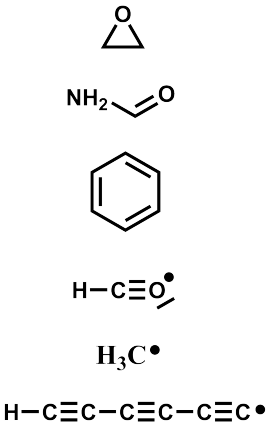

Figure 1.3: *Examples of molecules identified in the interstellar medium [28]*

Molecular clouds are mainly composed of hydrogen gas, with about 10% helium and only 0.1% of other atoms such as C, N, and O. The distribution varies greatly depending on the specific molecular cloud and even on the location in the molecular cloud [27]. Almost 200 organic molecules were identified due to their characteristic absorption or emission bands; including nitriles, aldehydes, acids, ethers, ketones, amines, amides, long-chain hydrocarbons [26,28,29] and even PAHs [30]. Small radicals such as the formyl radical or the methyl radical, and even a comparatively big radical, the hexatrienyl radical [28] were identified as well (see fig. 1.3). Elucidation of the formation mechanisms of these molecules is necessary to use the molecules themselves as tracers for the physical conditions of the molecular cloud. Formaldehyde for example is used to determine the temperature and spatial density within molecular clouds [31].

A lot of the chemistry is surface chemistry on grains, meaning that molecules or atoms adsorb on the surface of a grain, wander and meet to form bigger molecules. Molecular hydrogen is formed in this way [32]. In gas phase the density is low compared to the earth's atmosphere: 10^4-10^8 hydrogen atoms/cm^3 means that less than one collision with another molecule happens per year, and even on cosmic time-scales reactions need to have a very low

activation barrier and a high collision cross sections to form complex molecules. Ion-neutral, dissociation and radical-neutral reactions are the mechanisms of the rich chemistry in molecular clouds [26, 32]. An example is the formation of methane by the ion-radical reaction of CH_3 and $H_3{}^+$ [33]. The low density in the gas phase also allows radicals to persist that would react immediately in earth's denser atmosphere.

The only information from galactic clouds available is the light which reaches us. Via radio frequencies celestial features can be characterized, and the absorption spectrum, spanning from the infrared to the ultraviolet, gives information on molecules present in these celestial features. In these absorption spectra up to 500 bands were distinguished, they are called diffuse interstellar bands [34]. The carrier of many of these bands are still unidentified, but it is clear that the carriers need low-lying electronic states to show absorbtion in that region. Possible candidates - composed of only carbon and hydrogen atoms leading to uncharacteristic absorption spectra - are radicals, biradicals, carbenes and ions.

To correctly simulate and understand the available astrochemical data, more information on a wide variety of radical and cation species is required. This includes information about their excited states and about their deactivation pathways, since molecules are easily excited via cosmic radiation [35]. Fs-pump-probe mass and photoelectron spectroscopy is a convenient tool to obtain useful information of these processes.

Chapter 2 Interactions of molecules with light

Light interacts with a single isolated molecule in numerous ways. Some of these interactions are depicted schematically in fig. 2.1 and will be presented briefly in the following.

A molecule has different electronic states. The lowest electronic state is referred to as the electronic

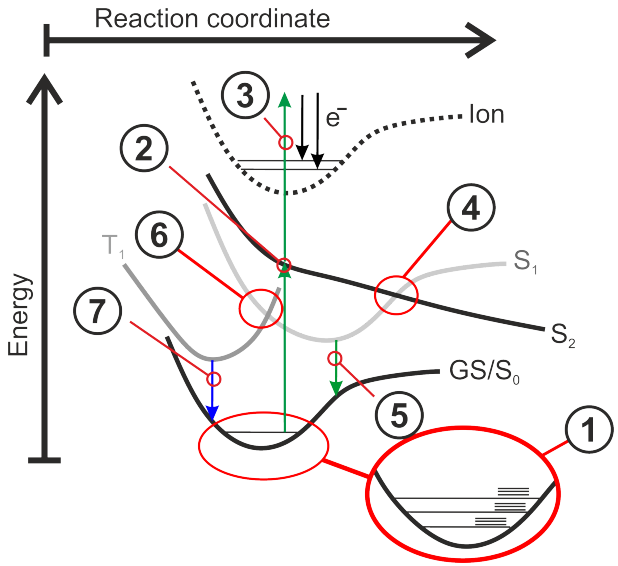

Figure 2.1: *Selected possible interactions of light with a single molecule. ①: Vibrational and rotational levels of the ground state; ②: Excitation of the molecule into the singlet excited state S_2; ③: Ionization of the molecule; ④: Conical intersection between the singlet states S_2 and S_1; ⑤: Fluorescence; ⑥: Intersystem crossing from the singlet S_1 to the triplet T_1 state; ⑦: Phosphorescence*

ground state (GS in fig. 2.1, here a singlet ground state S_0), higher excited states are numbered with increasing energy. On each electronic state vibrational levels are superimposed, depicted schematically with the long, straight lines for the ground state in ① . Vibrations are excited with light in the infrared range (IR, typically from 500 to 3600 cm^{-1}), and the transitions are approximately described by the model of the harmonic oscillator. The range of excitation of a vibration is characteristic for each functional group, it is therefore used to identify the molecule [36].

On each vibrational state in turn, rotational levels are superimposed. These are - for the vibrational ground state - excited via light in the microwave region (0.3-30 GHz). Rotationally resolved spectra allow characterization of bond length and angles; the geometry of a molecule is characterized [37, 38]. This description of electronic states with superimposed vibronic and rotational states is only valid in the framework of the Born-Oppenheimer approximation, which assumes that the motion of nuclei and electrons can be separated [39].

A molecule can be excited into an electronic excited state via light in the UV-visible range (200 - 800 nm). This transition is represented in fig. 2.1 by the green arrow (②). Such a transition can be one-photon allowed or not depending on the symmetry of both the excited and ground state.

Via another photon ③ the molecule is ionized resonantly - this type of spectroscopy is called *Resonant Enhanced MultiPhoton Ionization* (REMPI). A molecule can be, of course, also ionized by just one photon of suitable energy, normally in the XUV range (60-200 nm). If the energy of the ionization photon(s) exceed the ion ground state energy, as

depicted in fig. 2.1, the electron recuperates this excess energy as kinetic energy and leaves an ion in the ground or excited vibrational/electronic state, should the molecule in the ground state geometry distort to reach the ionic most stable geometry. This is detailed in chapter 4. Contrary to excitation of a molecule, ionization is an always-allowed process.

The depicted excited singlet state S_2 is dissociative and crosses the excited singlet state S_1, this crossing is called a *conical intersection* (CI) ④ (see fig. 2.2 for a more artistic representation). A molecule in the S_2 at position two can deactivate via the conical intersection towards the S_1-state. Because of the larger energy difference between S_0 and the S_1-state than between S_1 and higher excited states, ultrafast relaxation through a conical intersection to the ground state do not occur, depending on the molecule. This opens the door to other relaxation channels such as fluorescence ⑤, meaning deexcitation into the ground state while emitting light. The molecule in the S_1 state can also pass into the triplet state T_1 via *intersystem crossing* (ISC) ⑥. Whether such a transition is allowed depends on the electronic character of both states, as described by the El Sayed Rules [40, 41]. Emission of light from a triplet state is called phosphorescence ⑦ [39, 42].

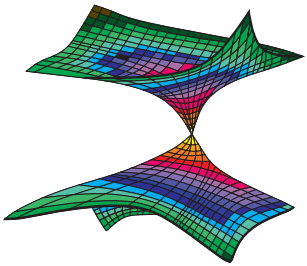

Figure 2.2: *An artistic view or a conical intersection*

Part II

Experimental Setup and Background

General setup

The general setup of an experiment examining reactive molecules is depicted in fig. 2.3. The precursor molecule is seeded directly into a rare gas (①) - before the radical is produced from the precursor via pyrolysis ④. The radical/rare gas mixture is then adiabatically expanded via a pulsed valve ③ into the vacuum of the source chamber ② , forming a supersonic molecular beam [43] ⑤. It then passes a skimmer ⑦, which lets only the coldest, inner part of the molecular beam (molecules depicted in blue) enter the main chamber/detection chamber (⑧). Here the spectroscopic experiments take place. The molecules are ionized using lasers (⑨) and the resulting charged particles are detected.

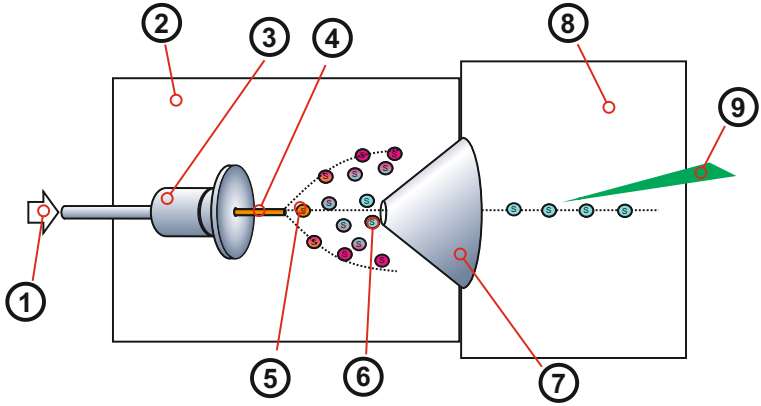

Figure 2.3: *General setup of a supersonic beam experiment: ①: Gas inlet flow; ②: Source chamber; ③: Pulsed valve; ④: Pyrolysis; ⑤: Supersonic molecular beam, warm molecules shown in red; ⑥: Supersonic molecular beam, cold molecules shown in blue; ⑦: Skimmer; ⑧: Main chamber; ⑨: Spectrometer*

Different methods are combined in this general setup to examine reactive species, these are detailed in chapter 3. First the radicals have to be produced. The pyrolysis method - used for this effect - is detailed in section 3.1. The radicals need to be examined under collision-free conditions, since otherwise they would react which each other. For this the seeded molecular beam technique is employed, detailed in section 3.2. The different spectroscopic methods used to examine the radicals are explained in section 3.3.

The next chapter 4 describes the principles behind the detection method velocity map imaging (VMI), its application in photoion (section 4.1) and photoelectron imaging (section 4.2). In section 4.3 reconstruction methods and a new sampling method for the pBasex algorithm are explained, followed by calibration methods for photoelectron and chlorine photoion imaging (section 4.4).

Chapter 5 then treats the technical details of the setups in Würzburg and Saclay used during this work.

Chapter 3 Experimental Principles

3.1 Production of radicals

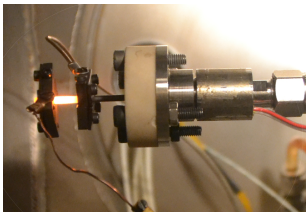

Figure 3.1: *Picture of the pyrolysis setup*

Reactive species can be produced from suitable precursors by different methods, for example via pyrolysis [44], photolysis [45], microwave [46], electrical discharge [47] and chemical methods [48, 49]. In this thesis pyrolysis was used to produce reactive species, and will be detailed in the following.

Different designs [44, 50, 51] for a pyrolysis nozzle are possible, the one used in this work is a variation of the pyrolysis nozzle proposed by Kohn et al. [44], depicted in fig. 3.2 and fig. 5.13 .

The functionality of such a pyrolysis setup is deceptively simple: A suitable precursor molecule is seeded into a rare gas, passes the pulsed valve ① and then the heated pyrolysis tube ⑨. The heated SiC tube serves as miniature flow reactor [52], the applied high temperatures during the brief residence time lead to the rupture of only the weakest chemical bond(s). Typically those are either halogen bonds; or the precursor molecules eject stable small molecules such as CO (ex: benzocyclobutendion, precursor of *ortho*-benzyne, see chapter 10), N_2 (e.g. diazopropargylene) or formaldehyde and NO (nitrites, e.g. phenylethylnitrite, precursor of the benzyl radical, see chapter 7.1). Other typical precursors include dimers of the desired radical, e.g. bitropyl for the production of the tropyl radical. An overview of different reaction energies for radical precursor molecules is given in table 3.1.

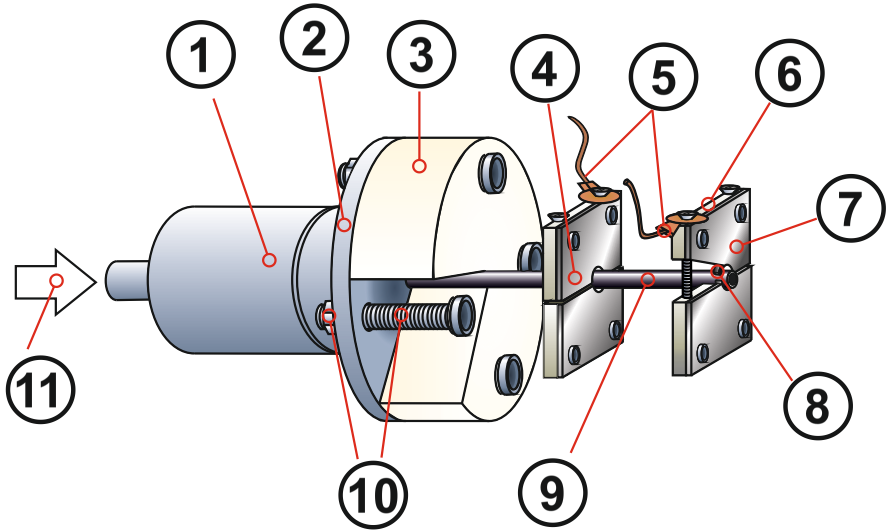

Figure 3.2: *Scheme of the pyrolysis setup: ①: Pulsed valve; ②: Faceplate of the pulsed valve; ③: Pyrolysis mount made out of MACOR®; ④: Stainless steel electrode block consisting of an upper and lower block; ⑤: Copper contacts to the DC power supply; ⑥: Back plate of the electrode block; ⑦: Front plate of the electrode block; ⑧: SiC splits wedged between the front and back plates of the electrode block; ⑨: SiC-tube; ⑩: 4 screws and corresponding nuts which fixate the pyrolysis mount on the pulsed valve faceplate; ⑪: Gas inlet flow*

reaction	$\Delta E(kJ/mol)$[1]
$R\text{-}CH_2\text{-}H \longrightarrow R\text{-}CH_2^{\bullet} + {}^{\bullet}H$	440 - 370
$R\text{-}CH_2\text{-}CH_2\text{-}R \longrightarrow 2\ R\text{-}CH_2^{\bullet}$	380 - 260
$R\text{-}CH_2\text{-}Cl \longrightarrow R\text{-}CH_2^{\bullet} + {}^{\bullet}Cl$	350
$R\text{-}CH_2\text{-}Br \longrightarrow R\text{-}CH_2^{\bullet} + {}^{\bullet}Br$	310 - 300
$R\text{-}CH_2\text{-}I \longrightarrow R\text{-}CH_2^{\bullet} + {}^{\bullet}I$	243 - 234
$H_2C{=}N_2 \longrightarrow H_2C{:} + N_2$	171 [53,54]
$R\text{-}CH_2\text{-}ONO \longrightarrow R^{\bullet} + CH_2O + NO$	228 [54]

Table 3.1: *Overview of different reaction energies for radical precursor molecules*

3.2 Molecular beam

Radicals and biradicals are often very reactive (see chapter 1), collision-free methods are therefore necessary to examine these species. The molecular beam technique [39] used in this thesis is one method to ensure collision-free conditions [43], other methods are for example matrix-isolation techniques [56] and isolation in helium droplets [57].

The principle of a molecular beam is illustrated in fig. 3.3. In container ① with a hole at one end, molecules are at room temperature, their velocity distribution follows a Boltzmann distribution as indicated by the green curve.

[1] The bond-dissociation energies of the reactions except for the last two were calculated/taken using values from Ellison et al. [55], with R ranging from methyl to allyl.

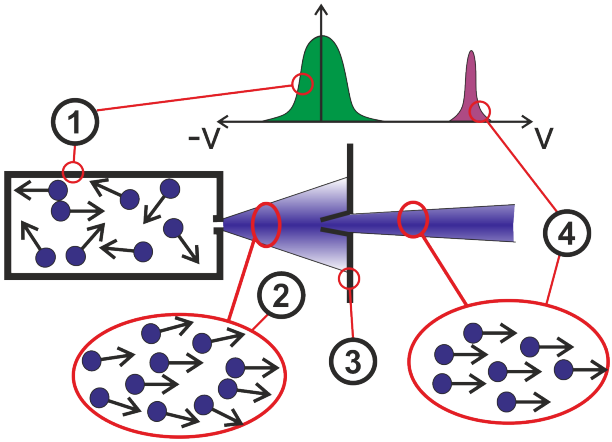

Figure 3.3: *Scheme of a molecular beam. ①: Container with molecules at room temperatures; ②: Adiabatic expansion; ③: Skimmer; ④: Skimmed molecular beam*

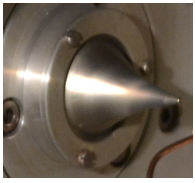

Figure 3.4: *Skimmer*

Assuming that outside of the container is under vacuum, two cases are possible [39]:

- The pressure inside the container is low enough to avoid any collisions between particles when they are leaving the container through the hole, and the flow leaving the hole does not reach supersonic speed. Such beams are called subsonic or effusive beams. Individual particles have a long mean free path and their velocity is determined by the boundary conditions. A slit in a distance of the origin of the molecular beam collimates the molecular beam, which reduces the Doppler broadening (sub-doppler-spectroscopy) [39].
- If the pressure inside the container is high enough to induce a large amount of collision between particles within the hole, the flow leaving the hole will reach supersonic velocities. The atoms collide until the spread of their relative velocities are

so small that no more collisions occur. The central part of this beam will only have a velocity component in direction of the molecular beam, letting only this part pass the skimmer ③ leads to a velocity distribution as displayed with the purple curve. The special form of the skimmer (see fig. 3.4) reduces turbulences in the chamber due to reflection of the molecules from the chamber wall.

Spectroscopic methods are applied to this part of the beam. This does not only lead to sharper absorption lines due to a reduced Doppler effect, but also to a narrower thermal distribution. This means that less rotational and vibrational levels of the molecule are occupied, and is therefore the basis for most gaseous pump-probe spectroscopic techniques. Cooling in a supersonic beam composed of the pure molecule will lead to the formation of clusters (or multimeres in the case of reactive molecules). A convenient solution are seeded molecular beams, where the molecule of interest is seeded into a rare gas (for example helium or argon), which allows to control easily the back pressure of the supersonic expansion and also increases strongly the collision number and the cooling efficiency. The low concentration of the molecule of interest in the molecular beam diminishes the probability of collisions between two molecules of interest. If a light gas is used as a carrier gas (for example helium or argon), the velocity of the beam in ③ is often supersonic, these beams are called supersonic molecular beams. Cooling in such beams is more efficient than in subsonic beams [58].

The principle described here is for a continuous molecular beam. If the employed lasers are pulsed, the molecular beam is generally pulsed as

well. A pulsed valve, opening only shortly, allows to use lower pressure in the expansion chamber and after the skimmer ③, consequently the cooling of the molecules is more efficient while using smaller (and also cheaper) vacuum pumps. More details on molecular beams can be found in [58]. As explained already, the translational temperature of the molecular beam components is low due to the collisions. In this process, energy exchanges lead to vibrational and rotational cooling of the molecules, meaning that only the lowest rovibrational levels are occupied. This greatly simplifies spectra. Direct supersonic expansion of stable molecules can achieve temperatures of 20 K or lower [39]; for reactive intermediates produced with the pyrolysis technique the temperatures reached are in the range of 100-150 K [59, 60].

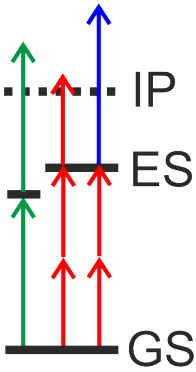

Figure 3.5: *Three schematic REMPI processes, [1+1], [2+1] and [2+1'] from left to right.*

3.3 Pump-Probe spectroscopy

Once the radicals are seeded in the molecular beam, they can be examined with different spectroscopic methods, depending on the subject of interest.

For the measurement of the molecular excited states, the already mentioned REMPI-spectroscopy is very sensitive compared to absorption spectroscopy, and also allows an easy identification of the molecule via its molecular mass [39]. In fig. 3.5 three such REMPI-processes are depicted schematically. The common nomenclature is to write it as [n+m'], where n photons excite the molecule from the ground state GS to some excited state ES, and m photons ionize the molecule. If both n and m photons have the same wavelength, the prime is omitted. On the left of fig. 3.5 we have therefore a [1+1]-REMPI, in the middle a [2+1]-REMPI pro-

cess, and on the right a [2+1']-REMPI.

Interesting is, however, not only the question where these excited states are located energetically, but what happens once the molecule is excited. This is of fundamental importance in many processes - from excitation of a molecule via light (e.g. in photosynthesis or in solar cells) to excitation of a molecule via thermal energy (combustion processes). These processes are examined in the field of reaction dynamics. Action spectroscopy allows to obtain information about the final products, this method consists in varying the excitation energy and detecting the final products using for example mass spectrometry or photoion imaging.

Time-resolved pump-probe spectroscopy gives information about the time-scales and the internal dynamics of photoreactions. Let's discuss this exemplary with fig. 3.6 for a model molecule possessing two excited states (ES_1 and ES_2). A first laser with a defined temporal and spectral width excites the molecule into ES_2, this laser is called the pump laser (here depicted as the green arrow). This state can now evolve, it can decay for example into ES_1. So we are interested in the temporal evolution after a molecule is excited. A second laser (= probe laser) with a defined temporal and spectral width probes the system, meaning the system returns a signal. The time delay between both laser pulses is known and can be changed, therefore the evolution of the system over time can be obtained.

The temporal width of both lasers defines the temporal resolution of the experiment, since measuring signals shorter than the temporal length of both lasers with those same lasers is not feasible. The observed signal is based on the interactions of a molecule with light as shown in chapter 2:

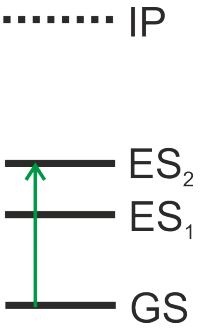

Figure 3.6: *Schematic model for the discussion of pump-probe spectroscopy of a molecule with GS=ground state, ES_1/ES_2=excited state 1/2 and IE=ionization energy*

- The **fluorescence** of the molecule can be measured directly without a second probe pulse using either Time-Correlated Single Photon Counting [61] or a streak-camera [39]. Alternatively a second laser pulse probes the fluorescence via fluorescence upconversion [62] or fluorescence Kerr-gating [63].
- The **absorption** of the probe can be measured (transient absorption). ES_1 and ES_2 will have different absorption spectra compared to the ground state, meaning that the decay to ES_1 can be followed easily. This technique is mostly applied in liquid phase, since high concentrations of the molecule are needed for a sufficient absorption. The molecule is therefore not isolated, but interacts with the molecules around it-which are also interesting processes [64].
- The probe can **ionize** the molecule (pump-probe mass/photoelectron spectroscopy). This has major advantages:
  - ▷ Ionization is an always allowed process, provided that the photon energy is high enough.
  - ▷ The detection of charged particles is very efficient. This method works in the gas phase, normally in combination with the molecular beam technique [39, 65], and consequently examines isolated molecules in their rotational and vibrational ground states.
  - ▷ In combination with mass spectrometry the information of the molecular mass allows identification of the molecule and of its fragmentation channels.
  - ▷ The kinetic energy of the electron and the kinetic energy of the ion as well as their angular distributions contain information on the electronic states populated at the ionization time.

Pump-probe mass time-of-flight/photoelectron spec-

troscopy was used during this thesis to examine the dynamics of several radicals. Both methods rely on the detection of charged particles.

The principle of time-of-flight (TOF) mass spectrometry is rather straigthforward:
Theoretically all molecules are ionized at the same time in the same localized point. By applying an external electric field the cations are accelerated by the same amount, all single-charged molecules obtain the same kinetic energy. Molecules of different masses possess consequently a different end velocity. After flying through a field-free tube they arrive on the detector at different times, which are measured. The resolution of a TOF-mass spectrometer is mostly limited by the size of the ionization region, an electrical field without defects and the distance of the flight tube [66].

In reality the size of the ionization region is always finite, as is illustrated in fig. 3.7 with two molecules approximated as green circles: The molecule closer to the repeller (R) will leave the whole electrostatic optics later, but will also undergo greater acceleration. It will therefore start to catch up to the other molecule in front of him, until they are at the same position (indicated as the gray slab in the background). This corresponds to the best resolution, where the peaks are the narrowest. The distance of the best resolution relative to the ground electrode depends on the electrical fields applied.

The mass is proportional to the square of the flight-time:

$$m \sim t^2 \tag{3.1}$$

The velocity-map imaging (VMI) technique was used for photoelectron spectroscopy and is explained in the next chapter.

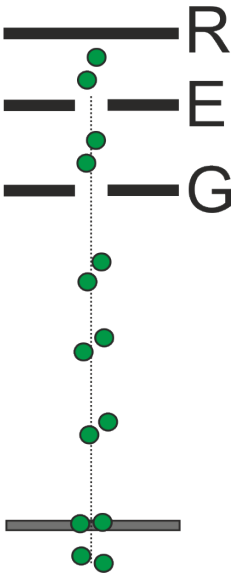

Figure 3.7: *Focalisation of the mass spectrum signal depends on the flight time*

In the experiments during this thesis both the pump and the probe laser were linearly polarized. The orientation of both lasers respectively to each other can vary between the extreme cases of both parallel to each other or orthogonal to each other. Both the excitation and the ionization process happen according to the orientation of the corresponding transition momenta, where the extreme cases are parallel and orthogonal orientation of both transition moments.

In a complete isotropic sample (random orientation of the molecules), the first linearly polarized laser will only excite molecules whose excitation transition dipole moment is in the direction of the electric field. This will create an oriented population of excited molecules. If the reorientation of the molecules is slow compared to the time resolution of the pump-probe experiment, a rotational anisotropy may be observed when comparing the effect of a probe with a different direction [67].

The rotational anisotropy is defined as

$$\beta = \frac{S_{\parallel} - S_{\perp}}{S_{\parallel} + 2S_{\perp}} \tag{3.2}$$

where $S_{\parallel}$ and $S_{\perp}$ correspond to the obtained signal of parallel and orthogonal laser polarization between the pump and the probe. No rotational anisotropy will be observed if the state excited in the pump step is isotropic (e.g. s-orbital character) or if the molecule rotates faster than the time-resolution of the experiment and dephases.

To exclude rotational anisotropy and thus only address relaxation decays, the rotational mean of the signal is analyzed:

$$S_{\mathrm{mean}} = (S_{\parallel} + 2S_{\perp})/3 \tag{3.3}$$

Chapter 4 Velocity map imaging

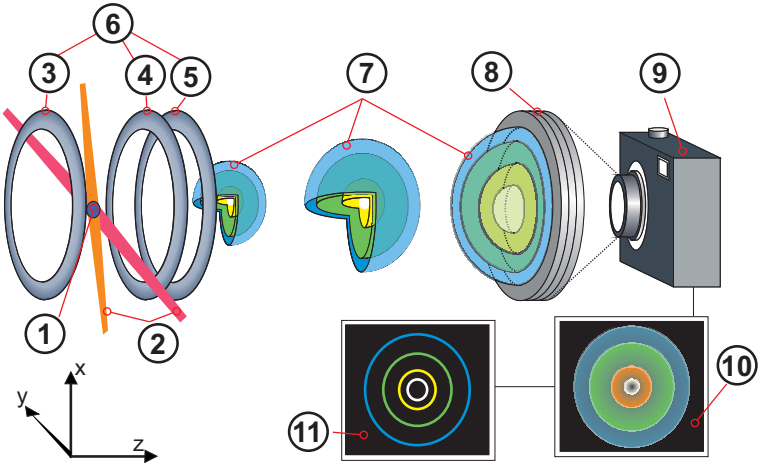

Figure 4.1: *General scheme of velocity map imaging. ①: Ionization volume; ②: Two laser beams; ③: Repeller electrode; ④: Extractor electrode; ⑤: Ground electrode; ⑥: Electrostatic optics; ⑦: Newton spheres; ⑧: Detector consisting of two MCPs and a phosphor screen (see fig. 4.4); ⑨: CCD camera; ⑩: Picture taken by the camera; ⑪: Picture after inversion*

Figure 4.1 illustrates the principle of velocity map imaging as developed by Eppink and Parker [68], and as implemented in Würzburg and with minor modifications in Saclay. Charged particles are created in the spherical volume ① either by crossing two lasers ② (as shown here) or by ionizing with a single laser. The created charged particles will have a total recoil kinetic energy (eq. 4.1), which depends on the energy introduced in the system as

well as on the state of the final particles. If one of the lasers induces dissociation, the energy needed for that will also be reflected in the kinetic energy of the particles.

$$E_{kin} = E_{lasers} - E_{ionization} - E_{vib} - E_{rot}\,(-E_{diss}) \qquad (4.1)$$

In conclusion particles with the same mass but with different kinetic energies correspond to different creation processes, so-called 'channels'. During ionization, for example, different vibrational levels of the cation can be occupied, as illustrated in fig. 4.2. Differentiating the electrons according to their kinetic energy allows a direct insight in the electronic states of a molecule.

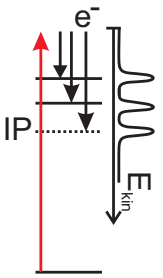

Figure 4.2: *Creation of electrons with different kinetic energies during ionization*

How does the physical chemist now obtain this information out of the spherical volume ①? The ionization takes place in an electric field which projects the expanding spheres ⑦ on the detector ⑧. Particles with the same kinetic energy will expand of the same surface of the sphere ⑦, these spheres are called newton spheres. This is depicted schematically here for four particles with different kinetic energy (order from low to high kinetic energy: white < yellow < green < blue).

For this an electrostatic optics ⑥ is used. The field lines of those electrodes resemble an optical lens (see fig. 4.3), and just as the name implies, by applying the correct voltages on this electrostatic optics the newton spheres ⑦ are focused on the detector; they arrive on the detector as depicted in fig. 4.1. The electrostatic optics consists in its most basic design of three electrodes, repeller ③, extractor ④ and ground ⑤ electrodes. Onto repeller and extractor a voltage is applied, with $|V_{repeller}| > |V_{extractor}|$, the last electrode is grounded or adjusted to the voltage of the time-of-

flight tube. Grounding the last electrode ⑤ together with the first micro-channel plate of the detector ⑧ ensures field-free (unperturbed) flight conditions of the newton spheres ⑦ (for a detailed discussion of the detector see later in the text and fig. 4.4). The voltage ratio between repeller and extractor is decisive for a proper focus of the particles with the same velocity vector on the radius. In the analogy of a lens changing the voltage ratio corresponds to changing the focal length of the lens. This focal length should be equal to the distance of ionization point to the detector ⑧, otherwise the image will be blurred and distorted.

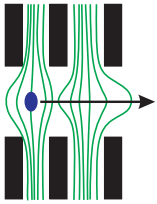

Figure 4.3: *Schematic view of an electrostatic optics's field lines*

The most commonly used detector consists of two *micro-channel plates* (MCPs) and a phosphor screen, allowing position-sensitive detection. This detector is shown schematically in fig. 4.4.

A MCP (② and ③) is a circular slab with a regular array of micro-channels made from a highly resistive material such as lead glass [69]. They are signal amplifiers (gain: 10^4-10^7) [69], commonly used in night vision goggles [70]. They work as follows: the first MCP ② is grounded, on the second MCP ③ a positive voltage is applied. A charged particle ① arriving in such micro-channel of the first MCP, hits the wall and provokes a cascade of electrons (10^4-10^7electrons per charged particle). This electrode cascade is then accelerated by the electrical field of the second MCP ③, hits the wall again, leading to further cascades. The electrons created in the second MCP ③ are accelerated in direction of the phosphor screen ④, kept at a higher positive voltage. The signal is thus amplified again. Both MCPs are most commonly orientated in the chevron setup, meaning that the angles of the channels are orientated in a chevron shape (90°, see MCPs schematic in the blue rectangle in fig. 4.4).

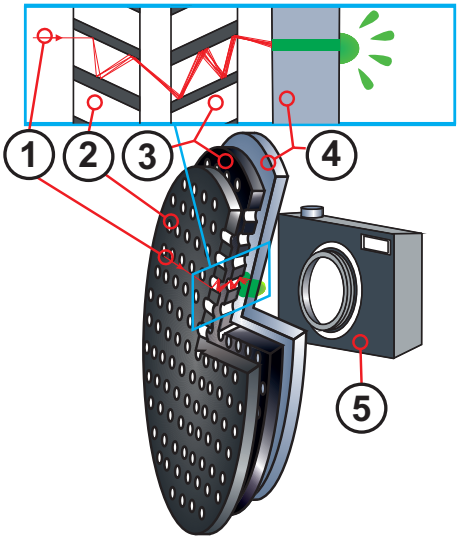

Figure 4.4: *General scheme of the mode of operation of a VMI detector. ①: Charged particle; ②/③: MCP plates in chevron setup; ④: Phosphor screen; ⑤: CCD camera*

This setup ensures that particles which pass the first MCP without touching the wall of a micro-channel, will certainly hit the wall of the second MCP. [71]

The electron cloud then arrives on the phosphor screen ④, where they stimulate luminosity. This luminosity is photographed by a *Charged-Coupled Device* (CCD) camera ⑤. The different phosphor screens are named after the phosphor type used (for example: P20=(Zn,Cd)S:Ag, P43=Gd_2O_2S:Tb), they differ in the emitted spectrum and the decay time of the fluorescence [72, 73]. Phosphor screens have decay times of 1-100 ms [74], longer than the flight time of the charged particles (which is around

several µs). To obtain mass resolution, the second MCP needs to be gated. It is kept at a base voltage where electrons do not have a high enough kinetic energy to cause luminescence on the phosphor screen, and only when the particle of interest arrives (meaning for a given mass) the voltage of the second MCP is ramped up so that the phosphor screen emits light.

Returning to fig. 4.1, the CCD camera ⑨ takes a picture of the luminosity of the phosphor screen which corresponds to the spatial distribution of the charged particles. The x and y direction is immediately apparent out of the image. This is not the case for the z-direction, since we have a 2D detector to image a 3D distribution.

Recovering the z-component can be either done experimentally via for example slicing, or mathematically using so-called inversion methods. Only the mathematical methods are presented in the following in detail, for the experimental methods the reader is referred to several detailed reviews [75–77].

The charged particles arrive in a filled circle, corresponding to the flattened Newton spheres (⑩). Physical information is in the cut through the newton spheres (⑪), the mathematical process from ⑩ to ⑪ is called inversion. After successful inversion the image has to be calibrated from pixels to energy/velocity.

The following chapter is organized as follows: First ion imaging (section 4.1) and then photoelectron imaging (section 4.2) will be treated, with the focus on what information can be obtained from those two methods. Then the inversion process will be elucidated (section 4.3), and the results of a new algorithm for the pBasex inversion method (subsection 4.3.2) will be presented. Finally, two calibra-

tion protocols for photoelectron imaging (subsection 4.4.1) and chlorine imaging (subsection 4.4.2) are given.

4.1 Ion imaging

Ion imaging is used to examine photodissociations or dissociative photoionization. The principle is displayed in fig. 4.5 with a molecule consisting of a red and a blue atom.

The molecule is excited by a first laser (blue), leading to photodissociation, the bond breaks. A second laser (red) now ionizes one of the photofragments (here the red one). The kinetic distribution of the ion is imaged, using velocity map imaging as described above. Two different information can be extracted out of such an image:

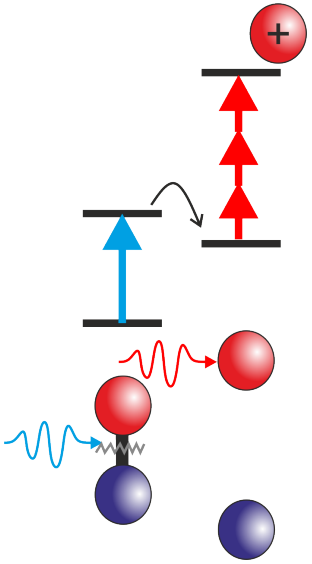

Figure 4.5: *Principle of photofragment imaging*

a) The kinetic energy of the fragment: Assuming the molecule breaks into only two parts, the kinetic energy of the fragment is directly correlated to the kinetic energy of both fragments via conservation of momentum:

$$\frac{m_1}{m_2} = \frac{v_2}{v_1} \tag{4.2}$$

Consequently it is advantageous to image the lighter fragment: the lighter fragment has the higher velocity, imaging it allows a more precise determination of v_1 and v_2. With knowledge of these two parameters one can determine in first approximation the total kinetic energy release, which combined with e. g. *Rice-Ramsperger-Kassel-Marcus* (RRKM) theory simulations [78] give insight in the dissociation mechanism. These relationships are well explained in the thesis of J. Giegerich [59]. The same bond can break via different processes, for example out

of different excited states, and in molecule consisting of more than two atoms different bonds can break as well. These different channels lead to different kinetic energies of the fragments, and they can therefore be distinguished, as was the case for e.g. cyclopropanylidene [79].

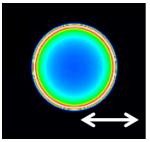

Figure 4.6: *Isotropic image*

b) Angular distribution of the ions: Ion images from photodissociation (by a polarized laser) can be isotropic (see fig. 4.6), but anisotropic images are also observed (see fig. 4.7 and fig. 4.8). The white arrow in all three images corresponds to the laser polarization of the linearly polarized dissociation laser. Where does this anisotropy come from?

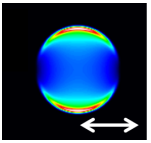

Figure 4.7: *Anisotropic image with* β*=-1*

Molecules absorb the laser light more or less as the function of the overlap between the laser polarization and its transition dipole momentum. As depicted in fig. 4.9, the transition dipole moment can be aligned differently in respect to the dissociation axis -either perpendicular (left) or parallel (right) in extreme cases. If the dissociation of the molecule is faster than the rotation of the molecule itself, the fragmentation will occur without reorientation of the initially populated excited molecules. For molecules where the transition dipole moment is perpendicular to the dissociation axis, we obtain an image such as displayed in fig. 4.7; are both parallel, an image like in fig. 4.8 is seen. Slow photodissociation leads to an isotropic distribution, since the molecule can rotate, the obtained distribution will be more isotropic.

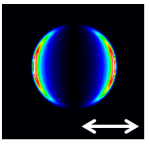

Figure 4.8: *Anisotropic image with* β*=+2*

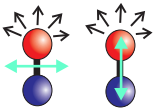

Figure 4.9: *Transition dipole axis aligned perpendicular or parrallel in respect to the dissociation axis*

To describe this phenomenon, first the intensity relationship between the 3D newton sphere and its projection (upper image in fig. 4.10) and its cut in the middle (lower image in fig. 4.10) need to be established. The anisotropic newton sphere (displayed schematically in fig. 4.10) has cylindrical

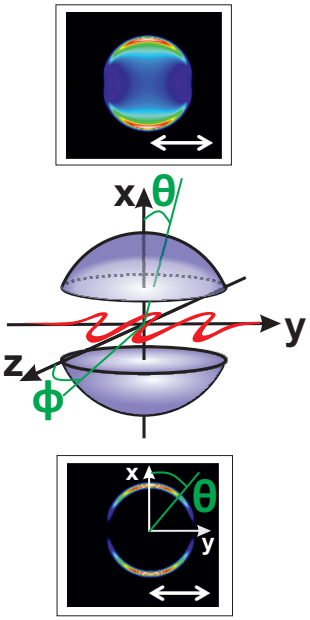

Figure 4.10: *Intensity relationship between the 3D newton sphere, its projection and its cut through the newton sphere*

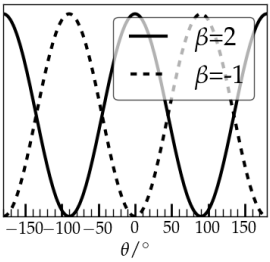

Figure 4.11: *Intensity distribution for the extreme cases with β=2 and β=-1*

symmetry, and is described in polar coordinates by the angles θ, ϕ and the radius r. For the cut through the middle of the newton sphere (the x-y plane) and the angular distribution, only the angle θ and the radius r are conserved as variables.

Considering the intensity distribution, for points with θ=0/180° it is condensed to some points, but for points with $\theta \neq$0/180° it is distributed around the circumference described by the angle ϕ. To incorporate the correct intensity distribution in the cut through the newton sphere, it needs to be multiplied with the Jacobien, sinθ.

The anisotropy of the cut through the newton sphere is quantified by the value β. This is defined as follows (for linearly polarized lasers and one-photon transitions):

$$I(\theta) = \frac{1}{4\pi}(1 + \beta P_2(\cos\theta)) \tag{4.3}$$

where the intensity I is a function of the angle θ, defined as the angle with respect to the polarization of the laser and the electrical field.

$P_2(\cos\theta)$ is the second-order Legendre Polynomial:

$$P_2(\cos\theta) = \frac{1}{2}(3\cos^2\theta - 1) \tag{4.4}$$

For isotropic images β=0, as the intensity does not depend on the angle. For a parallel transition dipole moment to the dissociation axis we have β=+2, and for a perpendicular transition dipole moment to the dissociation axis β=-1 [80–83].

The intensity distributions as a function of the angle for both extreme cases are depicted in fig. 4.11. The beta parameter does not only give insight into the orientation of the transition dipole

moment (information that is difficult to obtain otherwise experimentally), but also allows insight into the timescales of the dissociation - since a real angular distribution rarely shows the two extreme case values with β=+2/-1 [84].

4.2 Photoelectron imaging

Analogous to ion imaging, photoelectron imaging allows to obtain the angular and energetic information of the electron produced by ionization.

The maximal energy of an electron correlates directly to the number of photons of the ionization process, provided that the ionization energy IE and the internal energy E_{int} (and of course the photon energy) is known:

$$E_{max,\,electron} = E_{photon/photons} - IE - E_{int} \quad (4.5)$$

This is a very useful information in pump-probe experiments, where varying the laser power of one laser is not a suitable way of finding the order of the ionization process (e.g. if it is [1+3'] or [1+4']).

Another useful information is the *Photoelectron Angular Distribution* (PAD). In the case of autoionization the anisotropy reflects a timescale: the lifetime of the final state may be long before it ejects the electron (greater than 10^{-13} s), the molecule can rotate and an isotropic photoelectron angular distribution will be obtained [85].

If no autoionization is involved, however, the photoelectron anisotropy does not reflect the timescales on which the dissociation occurs or the relative position of the dissociation axis to the transition dipole moment as in ion imaging, the photoelectron anisotropy stems from a different mecha-

nism. In the following only fast ionization processes (where the ionization energy is exceeded by the energy of the photon or photons) are considered.

Ionization is always allowed, but the conservation laws of energy and of total angular momentum still hold. Since the initial and the final ionic state have both a given total angular momentum, the ejected photoelectron has to obey the momentum conservation rule. In other words: the angular momentum of the ejected photoelectron is the difference between the angular momenta of the initial state + photon(s) and the final state.

While the initial state is well defined, this is not the case for the final state. For an ionization out of an atomic p-orbital (l=1), for example, the final state can either be an s-type orbital (l=0) or a d-type orbital (l=2), both are allowed. Both outgoing channels are part of the electron wavefunction and interfere, giving rise to the photoelectron angular distribution [85, 86].

Consequently the angular distribution of photoelectrons gives us a valuable insight in the orbitals/electronic states of the molecule, though far less intuitive than in the case of the angular distribution of photofragments. In the following part of this section the general expression for n-photon ionization will be presented before discussing the photoelectron angular distributions in the case of atoms, to allow the reader to develop an appreciation for this experimental (yet tricky) observable.

4.2.1 General description

The general form of the PAD is [86]:

$$I(\theta,\phi) \propto \sum_{L=0}^{L_{max}} \sum_{M=-L}^{L} \beta_{LM} Y_{LM}(\theta,\phi) \qquad (4.6)$$

where $Y_{LM}(\theta,\phi)$ are spherical harmonic functions, which are interchangeable with Legendre polynomials in the case of cylindrically symmetric problems [87] (see section 4.3).

All the physics of the photoionization is in the anisotropy parameters β_{LM} which depend on the process itself, e.g. on the orbital from which the electron is ejected, on the photoionization energy, whether the sample is aligned, how many photons are involved in ionization and on the polarization of the laser.

For a one-photon ionization with a linearly polarized (or unpolarized) laser, Cooper and Zare showed that the PAD simplifies to [88]:

$$I(\theta) \propto 1 + \beta_2 P_2(\cos\theta) \qquad (4.7)$$

which is of the same form as equation 4.3 for photoion anisotropy. $P_n(\cos\theta)$ corresponds to the n^{th}-order Legendre polynomial and β_n to corresponding order of the photoelectron anisotropy.

Assuming the same, linearly polarized laser causes multi-photon ionization, equation 4.7 has to be extended to [89,90]:

$$I(\theta) \propto 1 + \beta_2 P_2(\cos\theta) + \beta_4 P_4(\cos\theta) + ... + \beta_{2n} P_{2n}(\cos\theta) \qquad (4.8)$$

where n corresponds to the maximum number of photons. For circularly polarized light odd Legendre polynomials have to be considered as well.

While the equations 4.7 and 4.8 allow a description of the experimentally observed PAD (=extraction of the anisotropy values), they do not give any straightforward insight into the orbital from with the electron is ejected.

4.2.2 Cooper-Zare formula, classic formula

In the following the simplest case for PAD will be treated, meaning PAD in the case of atoms ionized via one linearly-polarized photon. As mentioned in the introduction of this section, when ionizing from an orbital other than an s-orbital, different channels interfere. For example a p-orbital (l=1) can either ionize in a s-continuum (l=0) or in a d-continuum (l=2). Each angular momentum of the ejected electron will lead to a specific anisotropy [85].
The l+1 channel leads to the following anisotropy:

$$\beta_2 = \frac{l+2}{2l+1} \tag{4.9}$$

where l is the initial angular momentum, this corresponds in our example to the p→d transition and gives a β-value of 1.
For the l-1 channel following anisotropy is obtained:

$$\beta_2 = \frac{l(l-1)}{2l+1} \tag{4.10}$$

which corresponds in our example to the p→s transition gives a β-value of 0. Only for ionization out of an s-orbital we have only one channel (case l+1) and the β-value is 2 [85]. The different channels interfere, which leads to the rather complicated formula developed 1968 by Cooper and Zare [88, 91] for atoms:

$$\beta_2 = \frac{l(l-1)\sigma_{l-1}^2 + (l+1)(l+2)\sigma^2{}_{l+1} - 6l(l+1)\sigma_{l+1}\sigma_{l-1}\cos(\delta_{l+1} - \delta_{l-1})}{(2l+1)[l\sigma_{l-1}^2 + (l+1)\sigma_{l+1}^2]} \quad (4.11)$$

with l as the orbital quantum number of the electronic state from which ionization occurs, δ_l is the phase shift of the l^{th} partial wave and $\sigma_{l\pm1}$ corresponds to the dipole radial matrix element:

$$\sigma_{l\pm1} = \int_0^\infty R_{nl} r R_{kl\pm1} dr \quad (4.12)$$

$\cos(\delta_{l+1} - \delta_{l-1})$ is the difference in the phase angle between the two channels. $\sigma_{l\pm1}$ depends on the energy of the photoelectron, and consequently also on the energy of the initial photon used for ionization.

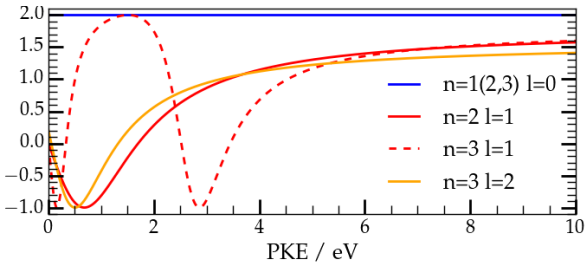

Figure 4.12: *Anisotropy parameters β_2 for ionization from the 1s, 2s, 3s (blue line), 2p (red solid line), 3p (red dotted line) and 3d (orange line), calculated for atomic hydrogen with the Cooper-Zare formula. Many thanks to Alexander Humeniuk for providing the python code to calculate this graph.*

In fig. 4.12 with the Cooper-Zare formula the anisotropy parameters are calculated for the hydrogen atom

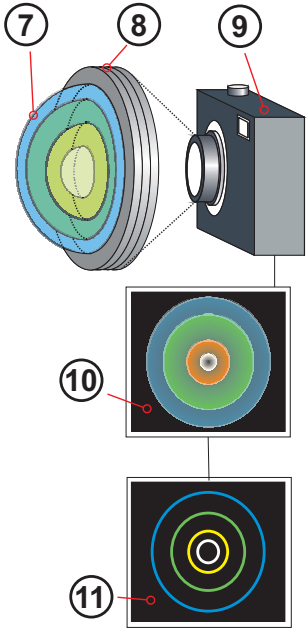

Figure 4.13: *Excerpt of fig. 4.1. See fig. 4.1 for a detailed explanation.*

ionized out of different atomic orbitals while varying the photon energy, which results in different kinetic energies of the photoelectrons (x-axis).

We see that for s-orbitals (l=0) β_2 is always 2, since we have no interference between different channels.

For p-type orbitals (l=1) this is not the case, the different channels (p→s and p→d) interfere. The specific value of β_2 not only depends on the type of the orbital, but also on its quantum number n. The 2p orbital (red straight line) and the 3p orbital (red dotted line) show at 0.5 eV nearly opposite anisotropies: β_2(2p)=-0.8 and β_2(3p)=2.0.

This example alone shows that the PAD is a very sensitive tool of the electronic structure. Fig. 4.12 also demonstrates effectively that just knowing the anisotropy value alone - without knowledge of the molecular structure or the energy used for ionization/kinetic energy of the electrons - allows no identification of the initial state. Moreover, unlike atomic ions, molecular ions possess vibrational levels, and therefore the the kinetic energy of a photoelectron can be varied within certain limits. A measured anisotropy β_2=2.0 at 1.5 eV, for example, could stem from either an s-orbital or from a 3p orbital. A clear identification is only possible if the energy of the photon used for ionization is varied- which experimentally is not a simple task, especially in the case of the fs-pump-probe photoelectron spectroscopy setup (see section 5.4).

The example discussed here was for the hydrogen atom ionized with one linearly-polarized photon. What about the anisotropy for molecules or the anisotropy in multi-photon processes? In the case of Rydberg orbitals the situation is analogous to those in atoms. When bound states of molecules

are ionized, the situation is more complex [92], especially if autoionization [93] and/or multiphoton ionization [94–96] comes into play. Even though a quantitative simple calculation and/or interpretation of the photoelectron anisotropy is often difficult, it remains a very sensitive observable, via which a change in electronic character can be detected [86, 90, 97]. The free electron in radicals and carbenes has often p-character, and shows therefore a photoelectron anisotropy. Theoretical methods exists to calculate the anisotropy based on *ab inito* or TDDFT calculations [98], but this is not further developped here.

4.3 Reconstruction methods

As already explained in the introduction of this chapter, for interpretation of the image we do not need the measured flattened newton spheres (⑩ in fig. 4.13, which is an excerpt of fig. 4.1), but the cut through the xy-plane of the newton spheres (⑪ in fig. 4.13). Therefore we need to reconstruct the 3D newton spheres from the flattened 2D projection. But due to the cylindrical symmetry - symmetry issued from the fact that the ionization laser is polarized - this projection depends only on 2 parameters. Therefore it is a priori possible to recover the complete information from a 2D projection, under the condition that the symmetry axis given by the polarized laser is in the projection plane. This is depicted schematically in fig. 4.14.

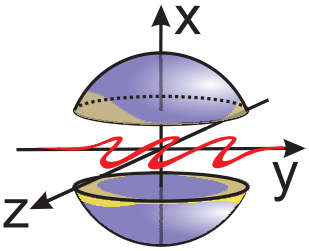

Figure 4.14: *Symmetry of the newton sphere in respect to the linearly polarized laser(in red)*

First let's tackle the problem from the inverse manner. If we had the cut through the middle of the newton sphere, how can we reconstruct the whole, flattened newton sphere assuming cylindrical symmetry?

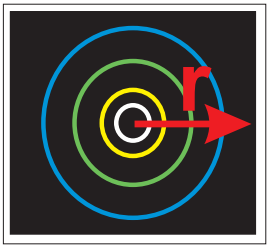

Figure 4.15: *Radius r of the cut throught the newton sphere)*

The reconstruction of the whole, flattened newton sphere (or the projection of the cut through the newton sphere) is achieved using the forward Abel transform:

$$g(R) = 2\int_R^\infty \frac{f(r)r}{\sqrt{(r^2 - R^2)}}dr \tag{4.13}$$

where r is the distance to the symmetry axis (see fig. 4.15), f(r) the axially symmetric function of interest (the cut through the newton sphere orthogonal to the symmetry axis) dependent on the radius r and g(R) corresponds to the projection of the newton sphere dependent on the radius R (z-axis in fig. 4.14). This equation, found 1823 by the mathematician Niels Henrik Abel, has many other applications for example in combustion diagnostics [99], holography and interferometry [100].

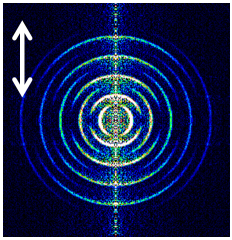

Figure 4.16: *Inversion with the Fourier-Hankel inversion leads to noise along the centerline.*

Formally it would suffice to take the reverse of function 4.13:

$$f(r) = -\frac{1}{\pi}\int_r^\infty \frac{g'(R)}{\sqrt{(R^2 - r^2)}}dR \tag{4.14}$$

Calculation of the forward Abel transform (equation 4.13) is relatively straightforward. That is not the case for the inverse Abel transform (equation 4.14) where the derivative in the integrand tends to amplify noise [101]. Therefore several other algorithms to circumvent the inverse Abel transform were engineered.

Among them are the Fourier-Hankel Abel inversion [102], which consists of taking the Hankel transform of the Fourier-transformed raw data, for which computationally efficient algorithms exist [103, 104]. Even though this method is less sensitive to noise

than the direct Abel inversion, it magnifies the noise along the centerline of the reconstructed velocity distribution, as shown in fig. 4.16.

Recursive methods to calculate both the forward Abel transform and the inverse Abel transform were developed by Hansen and Law, but as expected, their inverse Abel transform deals not very well with noisy data [105].

Another algorithm is the onion-peeling algorithm. This is an iterative procedure, starting at the outermost circle of the image, calculating the contribution of these particles to the whole image and subtracting those from it. The algorithm then continues with the inner circles, until the whole image is inverted. It proceeds in layers going from the outmost layer inward, hence the name onion-peeling algorithm [106, 107].

The Basex method, yet another inversion algorithm, is explained in detail in the next chapter. These four methods were compared in 2005 by Eppink et al., concluding that that the Basex method and the onion-peeling algorithm perform best [101].

Newer methods are the pBasex algorithm, based on the Basex algorithm but using basis functions in the polar coordinate system, [108] and the maxEntropy method by B. Dick [109]. The maxEntropy method has already been compared to the pBasex algorithm in the thesis of J. Giegerich for ion images, [59] and its performance of time-resolved photoelectron spectra for the 2-methylallyl radical is discussed in section 6. In the following chapter the Basex and the pBasex method will be explained in detail, before the presentation of an improved sampling procedure which improves the performance of pBasex.

4.3.1 The Basex and pBasex method

The principle of the *basis set expansion* (Basex) method is depicted in fig. 4.17. As previously stated, efficient algorithms exists for the forward Abel transform (going from ① to ②), but not for the inverse case.

The principle of the Basex method is to take a set of analytical basis functions (e.g. Gaussian-shaped radial distributions ③/④ with different radii) and project them using the forward Abel transform, resulting in a set of projected basis functions (⑤/⑥). The set of projected basis functions is used to adjust the experimental raw image ②, providing fitting coefficients ⑦. Applying these same coefficients on the original analytic basis functions reconstructs the inverted image ①.
Mathematically this procedure can be described in the following:

The image to be reconstructed is described as a function I(r,z) depending on two coordinates: the radius r to the symmetry axis z, which corresponds to the laser symmetry axis. The forward Abel projection of this function on the (x,z) plane is simply the application of equation 4.13:

$$P(x,z) = 2\int_x^\infty \frac{rI(r,z)}{\sqrt{r^2-x^2}}dr \qquad (4.15)$$

The data for the projection (x,z) out of a real experiment, however, is no smooth function, but binned by the CCD detector. The CCD detector has the size of N_x*N_z pixels, which lead to the digitized projection function P_{ij}:

$$P_{ij} = 2\int h(x-x_i, z-z_i)dxdz \int_x^\infty \frac{rI(r,z)}{\sqrt{r^2-x^2}}dr \qquad (4.16)$$

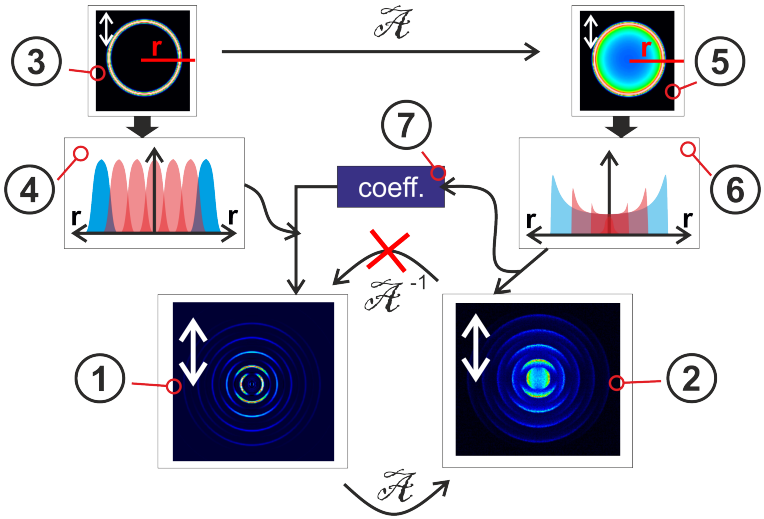

Figure 4.17: *Principle of the basis set expansion (BASEX) method. ①: Inverted image; ②: Raw image; ③: Inverted basis function; ④ : Radial cut through the inverted basis function, depicted as blue. The red functions correspond to basis functions at different radii; ⑤: Projected basis function; ⑥: Radial cut through the projected basis function, in blue. The red functions correspond to projected basis functions at different radii; ⑦: Coefficients used to adjust the projected basis functions to the raw image. The white double arrow in the images represents the symmetry axis.*

where h(x,z) describes an instrumental function. In fig. 4.17 equation 4.16 corresponds to the transformation of ① into ②. Let's introduce a set of basis functions $f_k(r,z)$ (with k=0,1,... K-1).

Applying eq. 4.16 on the basis set functions $f_k(r,z)$ results in the projected basis set functions:

$$G_{kij} = \int h(x-x_i, z-z_i)dxdz \int_x^{\infty} \frac{rf_k(r,z)}{\sqrt{r^2-x^2}}dr \qquad (4.17)$$

We can now write the whole problem into a matrix form:

$$P = [G] * c \tag{4.18}$$

where P is the projected image ⑤ as a 1D vector, G corresponds to the projected basis functions matrix ($G=(G_0,G_1,...G_{K-1})^T$) and c are the coefficients as a 1D vector. With the coefficients the inverted image can be calculated with a simple matrix multiplication:

$$I = [F] * c \tag{4.19}$$

where I is the image and F the basis function set ($F=(f_1,f_2,...f_{K-1})^T$). The coefficients can be obtained by the inversion of G.

$$c = [G]^{-1} * P \tag{4.20}$$

Since [G] is not a square matrix, methods like the *singular value decomposition* (SVD) [110] or the Tikhonov regularization [111] method can be used for the inversion.

How big should now such a basis function array G be - or otherwise put - how many basis functions should be chosen? Ideally the amount of basis functions K should be chosen equal to the number of data points, meaning in the order of 10^5-10^6, the typical size of a CCD array.

Luckily the problem is separable into two independent variables, which leaves a product basis set of the size K_x *K_y. Since G is independent of the projected matrix P, they are calculate only once and then stored for future calculations. The basis-set functions chosen for the Basex method are able to account for sharp features in the order of one

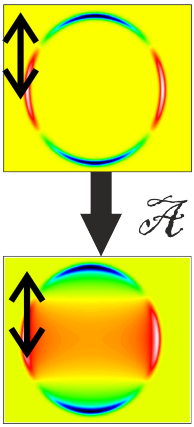

Figure 4.18: *2D second-order Legendre polynomial(top) and its projection(bottom), red corresponds to negative intensities, blue/green to positive intensities. The black arrow indicates the laser polarization axis.*

pixel and are smooth on a small scale:

$$f_k(r) = \left(\frac{e}{k^2}\right)^{k^2} \left(\frac{r}{\sigma}\right)^{2k^2} e^{-(r/\sigma)^2} \qquad (4.21)$$

where σ is in the order of the distance between two pixels. These functions are for big k virtually indistinguishable from Gaussian functions. Once the image is inverted in this manner, speed and angular distributions can be extracted [101, 112]. The basis functions are only 1D and are calculated fast, but when the size of the image or the center of the image changes, they need to be recalculated.

This is not the case in the *polar basis set expansion* (pBasex) method, developed by G. Garcia, L. Nahon and I. Powis. Here the basis functions can be reused if the center of the image changes. In the Basex method, the basis functions are chosen in the Cartesian coordinate system (more like ④/⑥ than ③/⑤ in fig. 4.17), whereas in pBasex the inversion happens in polar coordinates and includes some physical assumptions issued from the physics of the system observed.

Since the angular distribution follows equation 4.8, it can be expressed as an expansion in Legendre polynomials, and the basis set functions are also 2D Legendre polynomials. A zero-order 2D Legendre polynomial (P_0) basis function and the corresponding projection are shown in fig. 4.17 (③ and ⑤ respectively), a second-order Legendre polynomial (P_2) with its corresponding projection is displayed in fig. 4.18, a fourth-order Legendre polynomial (P_4) in fig. 4.19. Since with linearly polarized light odd terms in equation 4.6 disappear, the number of basis functions is even further reduced.

The raw image is, however, measured in Carte-

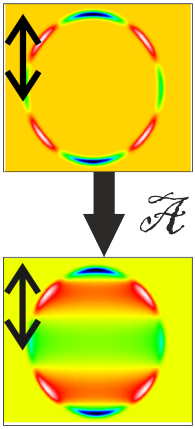

Figure 4.19: *2D fourth-order Legendre polynomial(top) and its projection(bottom), red corresponds to negative intensities, blue/green to positive intensities. The black arrow indicates the laser polarization axis.*

sian coordinates (x,z), the pixels of the CCD detector. For inversion the image coordinates need to be converted into polar coordinates (r,θ), which - in principle - is easily possible. But mathematically the basis set should be a rectangular matrices, so it can be easily inverted (see equations 4.18 and 4.19), so the image has to be transformed into a 1D vector of constant size.

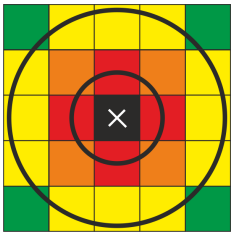

Figure 4.20: *Sampling problem when converting the measured image from Cartesian coordinates into polar coordinates.*

In the current pBasex alghorithm this is done via interpolation between the pixels - since otherwise one would have less points near the center and more further away from the center. This is indicated in fig. 4.20, where the inner circumference covers only 8 pixels (4 red and 4 orange pixels), whereas the outer circumference covers 16 pixels (12 yellow and 4 green pixels). In practice the size of the circumference is chosen - e.g. 256 - and the polynomial and cubic spline interpolation method are used to obtain the interpolated pixels. This also means that below a circumference of 256 pixels the points are oversampled, and above a circumference of 256 pixels undersampled.

Having done that, equation 4.18 can be applied, and the coefficients c are determined using SVD [110]. The number of basis-functions is smaller than the number of radii, so that the system is over-determined, which allows for a more efficient and stable SVD. Just as for the Basex method, the calculation of the basis function set and the SVD procedure on the projected basis function set have only to be done once and can then be stored on a hardrive, making this method very time-efficient. Garcia et al. also compared the pBasex method to Basex and Abel, showing that for odd Legendre polynomials it performs better, for even Legendre polynomials it gives the same results. In either case it is less

time-consuming [108].
To obtain the inverse of [G], necessary for obtaining the coefficients c:

$$c = [G]^{-1} * P \tag{4.20}$$

the SVD procedure is used, which is implemented in many programming languages, e.g. in the python module *numpy*. For more information about the SVD procedure the reader is referred to [113,114].

The coefficients obtained from this method directly reflect the contribution of the different Legendre polynomials. The contribution of the first-order Legendre polynomial P_0 corresponds to the total intensity of the signal. P_2, if only one linearly polarized laser was used for either photofragmentation (ions, see section 4.1) or ionization (ions, electrons, see section 4.2), represents the amount of anisotropy. β_2 can be simply calculated with P_2/P_0.

With multi-photon processes the basis set functions have to be enlarged accordingly, for linearly polarized N-photon processes it has to incorporate $P_0 P_2 ... P_{2N}$.

4.3.2 pBasex**- a new pBasex algorithm-principle

As mentioned in the previous chapter and as illustrated in fig. 4.20, the pBasex algorithm interpolates each radius to a specific number of points, large radii are thus undersampled and small radii oversampled.

The idea for the pBasex** algorithm is to consider the whole information of the image and to reduce efficiently the number of points used for the image description. This is illustrated in fig. 4.21-

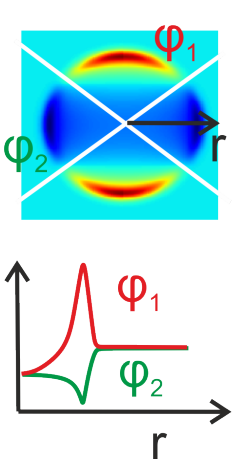

Figure 4.21: *Principle of pBasex**: a) A projected P^2 b) The sorted angles*

a) for a projected P_2 basis function: The image is divided here into 4 areas by the white lines, these correspond to the angles where a not-projected P_2-basis function is zero. This identifies regions of strong contrast for an efficient P_2 measurement. In each area the data points are then sorted corresponding to the radius (distance to the center) and divided by the number of pixels having that radius, as shown in fig. 4.21 b). Since the image is still a Cartesian data grid, we define a distance *dr* between the radial data points into which each data point is sorted. This way all experimental points are incorporated and no interpolation is necessary.

The number of areas depends on the type of basis function included: P_0 is always positive (no angles with zero intensity), P_2 has four angles where the intensity is zero, P_4 eight (see also fig 4.18 and 4.19). The positions of the angles are added up, so for the basis function $P_0P_2P_4$ the data points are sorted in 12 areas.

This angle-radius sorting is done on each basis function (2D Gaussian Legendre polynomials with different radii) and on the image to be inverted. We now apply the same procedure as we did previously on equation 4.18:

$$P = [G] * c \tag{4.18}$$

with the difference that P are the concatenated sorted angles of the image, and G the concatenated sorted angles of the Legendre polynomial basis set. Using the SVD procedure the matrix G is inverted and by multiplication of the inverse matrix with P we obtain the coefficients c, which reflect the contribution of the different Legendre polynomials.

4.3.3 pBasex**-results and comparison to pBasex

4.3.3.1 Ideal test image

The test image in fig. 4.22 consists of 9 photoelectron bands with alternating anisotropies β_2 of +2 and -1, the β_4-part of this image is zero. Since the image is symmetric, ϕ_0/ϕ_2 and ϕ_1/ϕ_3 are identical.

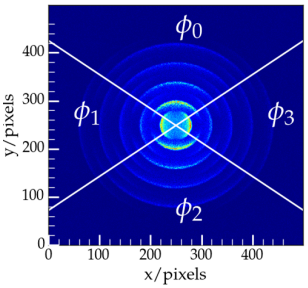

Figure 4.22: *Test image having 9 bands with the same total photoelectron counts*

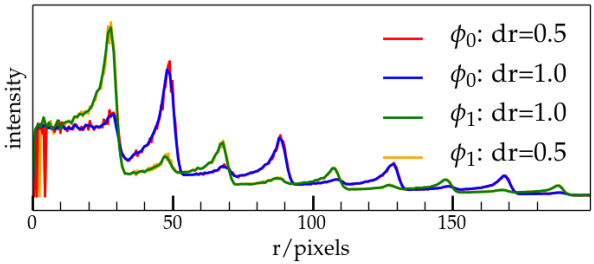

Figure 4.24: *Comparison of the sorted angles ϕ_0 and ϕ_1 for two different dr.*

Sorting the data points corresponding to the four angles and the radii r with a defined dr (distance between two radii points r) works fine. The smaller the chosen dr, the higher will be the final resolution in the inverted image. However, choosing dr to be smaller than one pixel is problematic (see fig. 4.24): this leads to the sorted points close to the center where no data point corresponds to that particular radius and angle. Therefore the chosen dr should be at least one pixel.

Once a dr has been decided, the basis set needs to be calculated. This involves deciding up to which Legendre polynomial the image should be inverted, here for this test image P_0P_2 is sufficient. A basis function is calculated on every second sorted radial

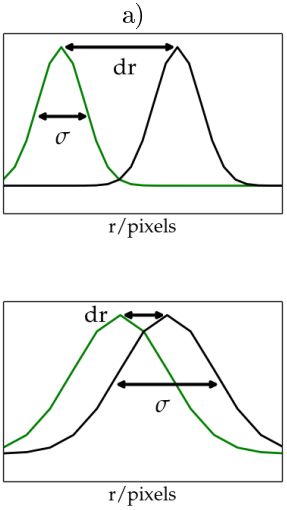

Figure 4.23: *Bad examples of basis functions. a) width chosen too small b) width chosen too large*

point r (N=0.5 for the method *invert_image*). The maximum radius of the basis function rmax, which should be bigger than the radius of the image, and a suitable standard deviation σ of the Gaussian basis function needs to be chosen as well. Following formula for the Gaussian basis function was used:

$$g_k(r) = e^{-(\frac{r-k}{\sqrt{2}\sigma})^2} \tag{4.22}$$

with k the center position of the curve, σ the standard deviation and r the radius variable.

The Gaussian basis function should be wide enough so that all points are covered (see fig. 4.23-a for the bad example), but not so wide that they overlap too extensively (see fig. 4.23-b for the bad example). σ should be $\frac{2}{3} \cdot dr$.

The Gaussian basis functions are also plotted as a 2D-image, projected (forward Abel transformed) using the algorithm by Hansen and Law [105] and then sorted. Here another problem arises for small dr: the 2D-image is no longer smooth since the width σ of the basis function is in the order of one to two pixels. This problem is circumvented by 'doubleing' the sampling of the basis functions: instead of calculating the basis function with the parameters (rmax, dr, σ) on rmax points, it is calculated with the parameters on 2·rmax points. The radii of the obtained basis set are divided by two to make them compatible with the sample image.

Calculating a basis set with dr=1 for P_0P_2 this way takes several hours. But since this basis set needs only to be calculated once, this method is still very time-efficient. With the basis set the images can now be inverted in the manner described in section 4.3.2.

In fig. 4.25 the contribution of the Legendre poly-

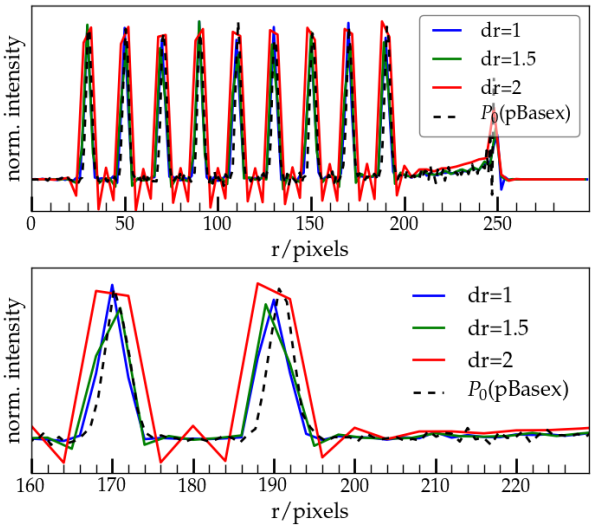

Figure 4.25: *Comparison of the Legendre Polynomial P_0-contribution with different dr to the regular pBasex algorithm as implemented in the Analyse-program. σ is each time $\frac{2}{3} \cdot$ dr.*

nomial P_0 for different dr is compared with the regular pBasex algorithm. The position of the bands obtained with all three different basis sets fit nicely with those by the regular pBasex algorithm (dotted line). But with dr=2 (red line) the peaks are wider and overshoot into negative intensities. This effect is still visible for dr=1.5, but it is a lot less pronounced. The best results are achieved with dr=1. Since the test image has a background, this background is seen as a tenth isotropic electronic band at r=250, corresponding to the maximal radius of the test image.

These results are analogous for the comparison of the contribution of the Legendre polynomial P_2 for different dr with the regular pBasex algorithm

(fig. 4.26). Comparing the P_2 part with the original image in fig. 4.22, the alternating intensities correspond exactly to the different bands observed.

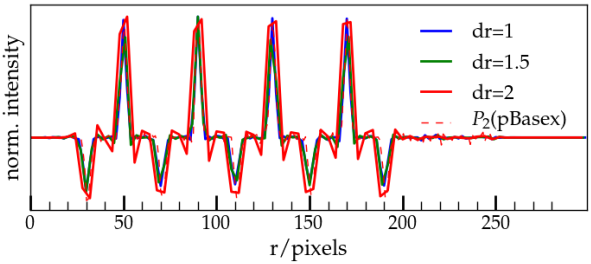

Figure 4.26: *Comparison of the Legendre Polynomial P_2-contribution with different dr to the regular pBasex algorithm as implemented in the Analyse-program. σ is each time $\frac{2}{3} \cdot$ dr.*

Not only can the dr be varied for a basis set, but σ can be varied as well. The effect of varying σ is illustrated in fig. 4.27. With larger basis functions the basis functions start to overshoot, which is best visible for σ=0.83·dr. For σ smaller than $\frac{2}{3} \cdot$ dr the basis function undershoot at the base, the peaks are larger.

The photoelectron anisotropy β_2 for pBasex and pBasex** is compared in fig. 4.28. In either case the anisotropy was calculated with $\beta_2 = P_2/P_0$, points with an intensity below 5 % are not displayed, since for points with low intensity P_2/P_0 starts to diverge. The P_2 legendre contribution is shown in the background. The varying anisotropies of -1/+2 are clearly recovered for both methods, though pBasex** performs better, since less points with an intensity between -1 and 2 are observed. The anisotropy β_2=0 around 250 pixels corresponds to the maximum radius of the image.

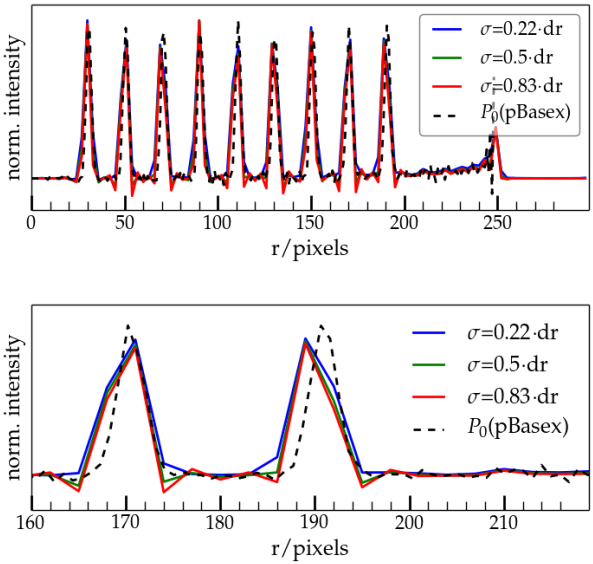

Figure 4.27: *Comparison of the Legendre Polynomial P_0-contribution with different σ to the regular pBasex algorithm as implemented in the Analyse-program. dr is each time 1.5.*

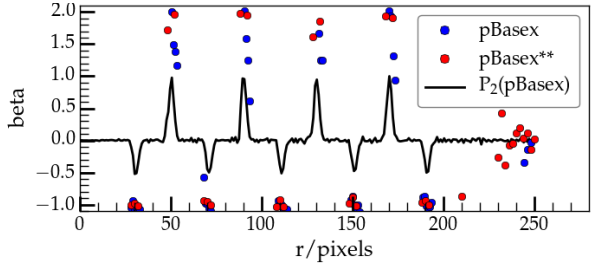

Figure 4.28: *Photoelectron anisotropy β_2 of the sample image displayed in fig. 4.22, calculated with P_2/P_0. The P_2 legendre contribution is shown in the background.*

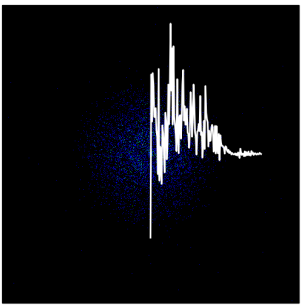

Figure 4.29: *An exemplary noisy image from the* Kr_2 *measurements.*

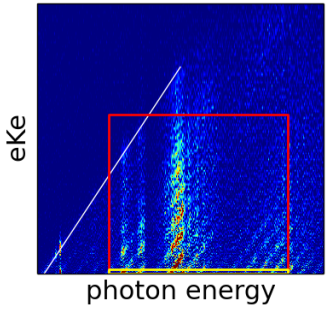

Figure 4.30: *2D map of the photoelectron energy as a function of the photon energy.*

So in conclusion the pBasex** and pBasex algorithm show the same performance for images with a good S/N ratio such as the test image. More interesting is to see how pBasex** performs for noisy images compared to the pBasex algorithm.

4.3.3.2 Treatment of noisy images

The noisy images stem from an experiment measured in 2012 by Lionel Poisson at the DESIR beamline at the SOLEIL synchrotron, an example for one of the less noisier images of the measurment series is shown in fig. 4.29. The Slow PhotoElectron Spectrum (SPES) of the Krypton dimer (Kr_2) was measured analogous to the SPES of the Argon dimer (Ar_2) [115]. The SPES technique is an improvement of the Threshold PhotoElectron PhotoIon COincidence (TPEPICO) technique. In the TPEPICO technique only coincidences between electrons with zero kinetic energies and ions are considered to obtain the dependence of the ionization efficiency with varying photon energy [116], so no inversion is formally necessary. The electrons with zero kinetic energy at a given photon energy will appear for higher-energetic photons as bands around the center. The SPES technique consists in inverting the images and considering electrons with non-zero kinetic energy to enhance the signal.

Fig. 4.30 shows a 2D map of the photoelectron energy as a function of the photon energy. For the TPEPICO spectrum only the signal in the yellow rectangle (photoelectrons with no kinetic energy) is considered, whereas in SPES the signal in the red rectangle is also taken into account. Each electronic state appears as a tilted line (see the white line to guide the eye). The signal is projected along the white line to obtain the SPES spectrum. Further

details to the treatment of SPES is described in [115] and is not important for the further discussion of the pBasex** performance.

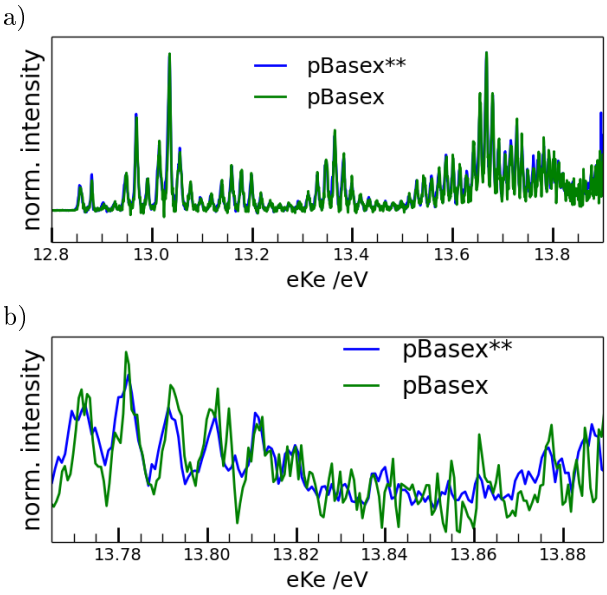

Figure 4.31: *SPES of Kr_2 with pBasex** and pBasex. a) Complete spectrum. b) Zoom.*

For the evaluation of pBasex** SPES of Kr_2 is compared to the SPES obtained with pBasex (see fig. 4.31). The complete SPES look at a first glance very similar (fig. 4.31 a)). Zooming in (fig. 4.31 b)), the pBasex** SPES is less noisy than the pBasex SPES. Similar to Ar_2, the position and width of the different bands can be fitted. While neither this procedure nor its results will be described here in detail, the fit uncertainties of pBasex** were about half than those of pBasex.

In conlusion the new pBasex algorithm performs

better for noisy data and may even be able to invert images that are too noisy to be recovered with the previous pBasex algorithm.

4.4 Calibration of Velocity map imaging

4.4.1 Photoelectron imaging

For the calibration of the photoelectron energies of VMI molecular oxygen is ionized with 266 nm in the $X^2\Pi_g$ state. The vibrational bands of the molecular oxygen cation in the photoelectron image (see fig. 4.33) are used for calibration.

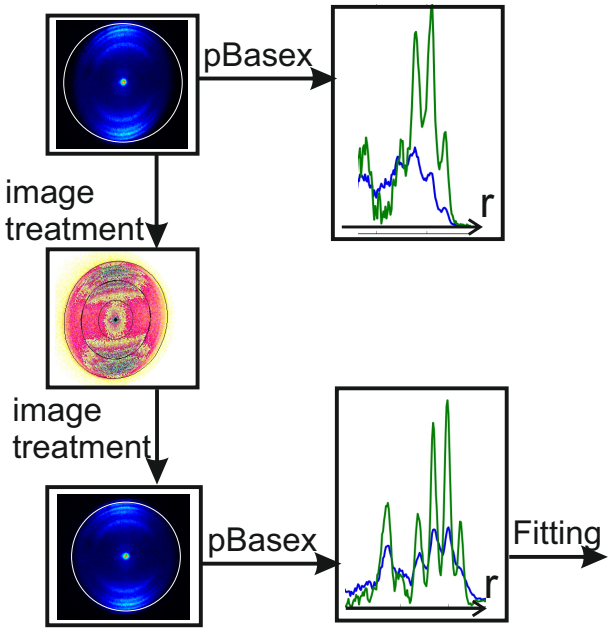

Figure 4.32: *Image treatment for calibration*

a)

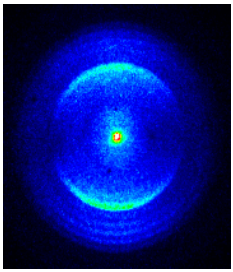

b)

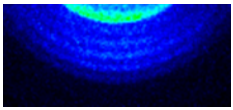

Figure 4.33: *a) Photoelectron image of oxygen with 266 nm. b) The vibrational bands at the outer parts of the image are better visible in the zoom.*

Experimental

The experimental setup in Saclay is described in section 5.4, 40% oxygen in helium was expanded via a pulsed valve into the source chamber. The obtained images should be perfectly round. Due to parasitic magnetic fields, however, this may not always be the case. Using image treatment algorithms, the image can be corrected and the best corrective parameters determined (see fig. 4.32). The images are inverted with the pBasex algorithm as implemented in the *Analyse*-program.

Results

$\omega_e(cm^{-1})$	1904.7
$\omega_e\chi_e(cm^{-1})$	16.25

Vibrational level	$E_v\,(cm^{-1})$	$E_v\,(eV)$	E_{pos}
v=0	948.29	0.117	1.910
v=1	2820.49	0.350	1.678
v=2	4660.19	0.578	1.450
v=3	6467.39	0.802	1.226
v=4	8242.09	1.022	1.006

Table 4.1: *Positions of the bands of molecular oxygen used for calibration* [117]

The first five vibrational levels of the $X^2\Pi_g$ are calculated with equation 4.23, the results are summarized in table 4.1. Then the energetic position of these vibrational bands can be calculated, since the ionization energy of oxygen (12.0697 eV) and the ionization wavelength (determined via a spectrometer, around 4.66 eV) are known.

$$E_v\,(cm^{-1}) = \omega_e(v+\frac{1}{2}) - \omega_e\chi_e(v+\frac{1}{2})^2 \qquad (4.23)$$

$$E_{pos} = 3E_{266nm-photon} - IP - E_v\,(eV) \qquad (4.24)$$

With these energetic position the calibration factor a is determined:

$$E_{pos\,in\,pixels} = \sqrt{\frac{E_{pos\,in\,eV}}{a}} \qquad (4.25)$$

The positions of all five vibrational levels are adjusted simultaneously in a python macro, leading to a precise calibration factor (see fig. 4.34). The most intense, not fitted experimental band corresponds to intermediary resonances in the ionization process.

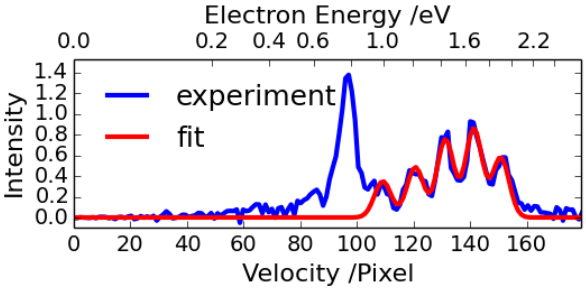

Figure 4.34: *Manual adjustment of the oxygen vibrational level positions*

The calibration factor varies not only with the position of the laser focal point, but also with the resolution of the image. To obtain an equation which is valid for different laser focal points and for different repeller voltages, two series of measurements were combined.

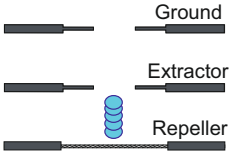

Figure 4.35: *Laser focal points between extracter+repeller plate*

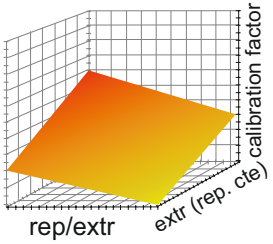

Figure 4.36: *2 D surface assumed for the calibration*

Resolution: To change the resolution of a photoelectron spectrum, the absolute values of the repeller voltages is changed while keeping the repeller/extractor ratio constant. Higher voltages compress the image, thus capturing even higher-energetic electrons; while lower voltages enlarge the image, allowing a better resolution of lower-energetic electrons. The calibration factors have been determined for repeller voltages between 1000 and 4500 V. These are then fitted with a linear equation:

$$y = a \cdot (Rep - b) \tag{4.26}$$

Position of the laser focus: The laser focal point, the intersection between the laser focal point and the molecular beam, can vary vertically; resulting in different ionization origins (see fig 4.35). Different ionization origins mean a different extractor voltage (with constant repeller voltage) is necessary to obtain a round image, or put differently, the repeller/extractor ratio has to be changed. For the calibration curve, the repeller voltage was held constant at 2000 V and the laser focal points varied vertically. The extractor voltage is adjusted until the image is round, then the calibration factors are determined. Plotting the calibration factors versus the repeller/extractor voltage ratio, results in equation 4.27:

$$y = c \cdot \left(\frac{Rep}{Extr} - d\right) \tag{4.27}$$

Both equations can be seen as cuts through a 2-dimensional surface. (see fig 4.36) Assuming a flat surface, both equations 4.26 and 4.27 are combined

to the calibration equation 4.28:

$$y = a \cdot c \cdot (Rep - b)\left(\frac{Rep}{Extr} - d\right) \cdot r^2 \qquad (4.28)$$

If the flight path, the detector and the ions optic remain unchanged, the same calibration is used.

4.4.2 Ion imaging of chlorine

In Würzburg (see chapter 5.3.1 for details of the setup) photofragment imaging of the hydrogen fragment has resulted in numerous publications [59, 118, 119]. Hydrogen atoms are detected via [1+1']-REMPI via the Lyman-α-line with 121.6 nm and 354 nm. Images of pyrrol at different dissociation wavelengths is used for calibration [120].

But the hydrogen atom is not the only interesting photofragment. In the following a calibration method for chlorine will be presented. HCl was used as a calibration substance, with the hope of verifying the chlorine calibration with the hydrogen velocity distribution.

The calibration is based on a publication by Romanescu et al. [121], who examined superexcited states of HCl. As displayed in fig. 4.37, HCl was excited via a 2+1-REMPI scheme. The resonant state $E^1\Sigma^+(0^+)$ has the origin at 83 780.2 cm^{-1} [122]. The final excited state of HCl is dissociative, leading to either hydrogen or chlorine in the electronic ground state and chlorine or hydrogen in an excited state. With a fourth photon excited hydrogen or chlorine can be ionized. Romanescu et al. measured photoelectron images, and ion images of both chlorine and hydrogen, not only of the $E^1\Sigma^+(0^+)$ state, but also of the $g^3\Sigma^-$, $F^1\Delta(2)$ and $V^1\Sigma^+$ state, which allowed them to qualitative characterize the superex-

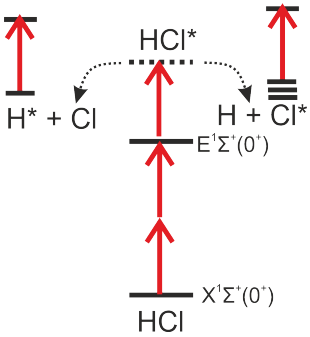

Figure 4.37: *Scheme for chlorine velocity map imaging calibration. The photons represented by red arrows have identical energy.*

cited state. They determined the branching ratios between autoionization and dissociation channels for the different intermediate states, and concluded that a single superexcited state must act as a gateway state for the autoionization/dissociation into H+Cl*(4s). Their measured image of ^{35}Cl with attributed electronic excited states of chlorine is shown in fig. 4.38.

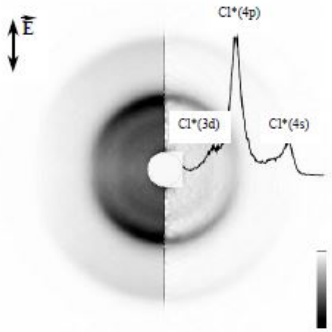

Figure 4.38: *Chlorine photoion image measured by C. Romanescu of the $X^1\Sigma^+ \rightarrow E^1\Sigma^+$transition via the Q(1) line. The left part of the image corresponds to the raw image, the right to the inverted image (onion-peeling algorithm). Reproduced from [123] with the permission of Hans-Peter Loock*

Experimental

HCl was diluted in Argon (final concentration 5%) as described in section 5.1.1, and expanded into vacuum using the setup in Würzburg. First mass spectra for an ionization energy between 41 825-41 950 cm^{-1}were measured. For calibration a photoion image at the Q(1) line of the $E^1\Sigma^+(0^+)$ -state gated

$U_{repeller}$	2000 V
$U_{extractor}$	1730 V
$U_{phosphor}$	4800 V
$U_{detector}$	1780 V
T(C)	0.570620 µs
T(D)	C+300 ns

Table 4.2: *Experimental parameters of the chlorine calibration image.*

on ^{35}Cl was collected. The experimental parameters are summarized in table 4.2.

A background image (pulse valve off) was then subtracted from the calibration image, and the image was treated according to the procedure developped by J. Giegerich specific to this experimental setup. This involves cutting off the detector border and taking only the upper right quadrant, which was symmetrized to recover the whole picture. This procedure was developped since the phosphor screen of this aparatus was damaged. These three steps were carried out as described in the thesis of J. Giegerich using the programs he developed [59]. The image was inverted using the pBasex algorithm as implemented in the *Analyse*-program, the calibration itself was analogous as described in [120].

Results

First the rotationally resolved [2+1] REMPI-spectrum of the $X^1\Sigma^+ \rightarrow E^1\Sigma^+$ was measured (fig. 4.39 for $H^{35}Cl$). HCl is a non-rigid rotor, both electronic states can be characterized by the origin T_e rotational constant B_e and the rotational constant D_e, which represents the influence of the centrifugal force [38]. These constants are shown in table 4.3.

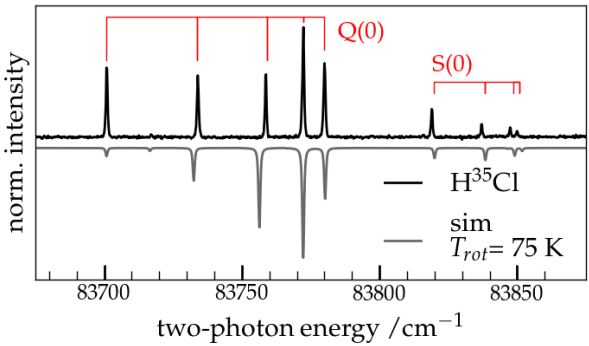

Figure 4.39: *Experimental rotational spectra of $H^{35}Cl$ for the $X^1\Sigma^+ \rightarrow E^1\Sigma^+$ two-photon transition compared to the pgopher [124] simulation using the rotational constants listed in table 4.3. The experimental spectrum is vacuum-corrected but not corrected in intensity, it had to be shifted by 20.4 cm^{-1} (two-photon energy) to lower wavelengths to coincide with the simulated rotational spectrum.*

$H^{35}Cl$	T_e/cm^{-1}	B_e/cm^{-1}	$D_e x10^3/cm^{-1}$	source
$X^1\Sigma^+$		10.59341	0.53194	[125]
$E^1\Sigma^+$	83780.2	6.6257	3.11342	[122]

Table 4.3: *Rotational constants for the $X^1\Sigma^+$ and $E^1\Sigma^+$ state for $H^{35}Cl$. T_e is the minimum electronic energy, B_e the rotational constant at equilibrium and D_e the centrifugal constant.*

The $X^1\Sigma^+ \rightarrow E^1\Sigma^+$transition is a two-photon transition. The selection rule is consequently $\Delta J=\pm 2$, 0; meaning that the Q-, S- and O-branch are allowed. In the measured rotational spectrum in fig. 4.39 both the Q-branch and S-branch with $J_{max}=4$ are visible. Using constants found in the litera-

ture (see table 4.3), the rotational spectrum for this transition was simulated using the program *pgopher* [124].

Comparing only the positions of the simulated and experimental lines, the position of the bands is roughly reproduced. Q(0) and Q(1) coincide very well with the simulated spectrum as does Q(4), but Q(2), Q(3) and the S-branch are experimentally closer to the Q(0) line than in the simulation. This indicates slightly too high rotational constants, but this observation was not further pursued. It should be noted that the experimental spectrum had to be shifted by 20.4 cm^{-1} (two-photon energy) to lower wavelengths to coincide with the simulated, which is due to the vacuum correction and an uncalibrated dye-laser. The intensity of the rotational simulation, corresponding to a rotational temperature of 75 K, does not fit well to the observed intensity distribution for two peaks, otherwise it is in reasonable good agreement.

Chlorine has two isotopes, ^{35}Cl and ^{37}Cl, which due to their different mass have slightly different rotational constants. This is illustrated in fig. 4.40 on the Q(0) and Q(1) lines seen in the hydrogen mass signal. The left, less intense peaks of both the Q(0) and Q(1) line correspond to the signal from $H^{37}Cl$, the right to $H^{35}Cl$ with the typical isotope distribution of 35:37=3:1. The splitting of both signals is 1.9 cm^{-1}, which corresponds reasonably well with previous reported values of 2.1 cm^{-1} in the literature [122].

After having determined the position of the rotational transitions, a ^{35}Cl chlorine image of the Q(1)-transition at 83 772.3 cm^{-1} was used for calibration (see fig. 4.41). The principle of the energy calibration is displayed in fig. 4.42. HCl is

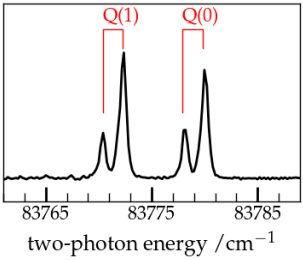

Figure 4.40: *Splitting of the two chlorine isotopes is visible in the hydrogen mass signal.*

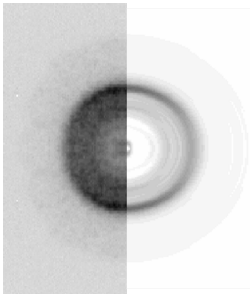

Figure 4.41: *Chlorine image of the Q(1) transition. The left part is the original image, the right part the inverted (pBasex).*

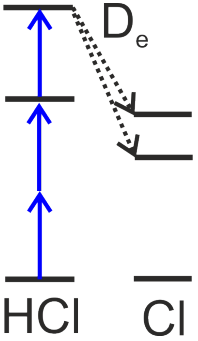

Figure 4.42: *Scheme explaining the different kinetic energies observed for chlorine.*

excited by three photons and dissociates to hydrogen in the electronic ground state and chlorine in a Rydberg state. The dissociation energy D_0 of HCl is 35 748.2±0.8 cm^{-1} [126], the energies of the 4s, 4p and 3d Rydberg states are summarized in table 4.4. The total kinetic energy of the H+Cl system is therefore:

$$TKE = 3h\nu - D_0 - E_{rydberg} \tag{4.29}$$

with $h\nu = 0.5x83\,772.3 = 41\,886.15$ cm^{-1}. The kinetic energy of chlorine is therefore according to conservation of momentum:

$$KE_{^{35}Cl} = \frac{m_H}{m_{H^{35}Cl}} \cdot TKE \tag{4.30}$$

where m_H and m_{HCl} are the mass of hydrogen and HCl respectively. The speed of the chlorine atoms is therefore:

$$v_{^{35}Cl} = \sqrt{\frac{2KE_{^{35}Cl}}{m_{^{35}Cl}}} \tag{4.31}$$

The resulting kinetic energies and velocities for the different Rydberg states of chlorine are summarized in table 4.4.

In fig. 4.43 the cut of the image shown in fig. 4.41 is calibrated on pixel 77 to a speed of 548.3 m/s. Comparing with the measured chlorine image by Romenescu et al. (fig. 4.38), the bands are well reproduced.

State	J	Energy/cm^{-1}	$E_{^{35}Cl}$/meV	$v_{^{35}Cl}$/ m/s
4s ^{2}P	3/2	74 225.846	54.48	548.3
	1/2	74 865.667	52.25	537.0
4p ^{2}D	5/2	84 120.263	20.11	333.1
	3/2	84 121.875	20.10	333.1
4p ^{2}S^0	1/2	85 917.937	13.87	276.6
4p ^{2}P^0	3/2	85 244.330	16.28	299.7
	1/2	85 442.430	15.52	292.6
3d ^{4}D	7/2	87 979.490	6.71	192.4
	5/2	88 080.042	6.36	187.3
	3/2	88 188.55	5.98	181.66
	1/2	88 272.72	5.69	177.2

Table 4.4: *Relevant Rydberg states of chlorine [127] as well as the electron energy corresponding to ionization with 41 886.15 cm^{-1}.*

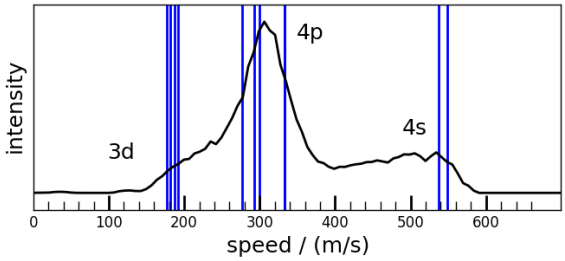

Figure 4.43: *Calibrated chlorine image (35Cl) with the position of the Rydberg states drawn in as blue, vertical lines. For the position of the Rydberg states see table 4.4.*

Conclusion

Even though calibration of chlorine via the Q(1)-line of the $X^1\Sigma^+ \rightarrow E^1\Sigma^+$ transition of HCl is possible, the lines are broad, therefore a precise attribution is not possible. The original goal to verify the chlorine calibration via imaging of the hydro-

gen atoms in the ground state was not successful, no two-color signal could be obtained (238.74 nm for the HCl transition and 121.6 nm for the detection of hydrogen).

For further experiments other calibration methods for chlorine might be preferable, e.g. calibration via Cl_2 photodissociation by 351 nm [84] or photodissociation of ICl [128–130].

Chapter 5 Experimental Setup

Two different experimental setups were used in this thesis, with their main difference being in the laser used to obtain the signals and the kind of signals recorded. In Würzburg nanosecond lasers were used to ionize molecules, with either *time-of-flight* (TOF) spectroscopy or *velocity-map-imaging* (VMI) of the ions as detection methods. In Saclay, however, ionization was achieved using femtosecond lasers, and in addition to TOF and VMI of the ions, *time-resolved photoelectron spectra* (TRPES) were measured.

The common point in both setups is the system of interest and also the way the examined species are brought into gas phase and/or produced on the spot. First the different sources - used to bring the molecules into gas phase - will be described. Then the pyrolysis setup, used to produce the reactive species, will be presented. Lastly the two setups with their corresponding laser setups and detection systems will be shown in detail, as well as the calibration of the mass spectra.

5.1 Sources

All sources are optimized to get a sufficiently high amount of molecules into the gas phase, but still low enough to allow efficient cooling during the supersonic adiabatic expansion and to prevent unwanted reactions during pyrolysis. The deciding factor for each substance is its vapor pressure and its boiling or melting point, determining its physical state at room temperature (gaseous, liquid or solid). The following different sources are described in order of the vapor pressure of these substances, going from substances with low boiling points (gases) to high boiling points (solids).

5.1.1 Gases

A gaseous sample needs to be diluted before introducing it via the pulsed valve into the apparatus, for this a 2 L gas cylinder (fig. 5.1 and fig. 5.2) is used. Via a valve (⑤ in fig. 5.1) the cylinder ④ is first evacuated. It is filled with 0.2 bar of the pure sample gas, then completed with a rare gas like Ar or He to a final pressure of 2.4 bar. This corresponds to a dilution of 8%. Before starting to measure it should be waited for at least half an hour to allow a thorough uniform mixing of the gas. After passing a two-stage pressure regulator ③ the diluted gas mixture was led into the apparatus using metric tubing (②). If the previously used gas was corrosive (like HCl or NO), the gas cylinder should be washed several times with ethanol until it runs clear and dried thoroughly before next use (via pumping it for a long time). One filling lasted up to 6 hours of measurements using a pressure of 1 bar.

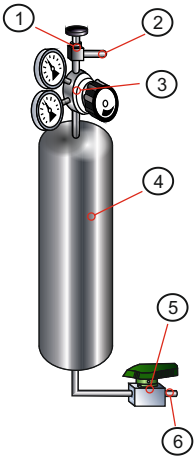

Figure 5.1: *Scheme of the mixing cylinder for gases: ①: Control valve; ②: Connection to the apparatus; ③: Two-stage pressure regulator; ④: Gas cylinder; ⑤: Swagelok ball or control valve; ⑥: Connection to rare gas/sample gas/vacuum*

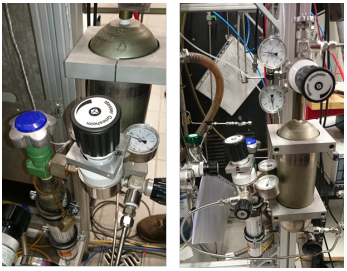

Figure 5.2: *Different views of the 2L gas cylinder used to dilute the molecule in rare gas*

5.1.2 Liquids with low boiling points

i
A shortened syringe cupping is a perfect flexible plastic tube of the right diameter to serve as a 'bubbler'.

If the vapor pressure of a liquid sample is high enough, the setup as detailed in fig. 5.5 may be used. The liquid ⑦ is put into a glass sample container ⑩, and the carrier gas ⑪ is either passes over the liquid (high vapor pressure, no 'bubbler' ⑧ on the gas inlet tube ⑨) or through the liquid (lower vapor pressure, with 'blubberer'). The *swagelok* valves ② at the gas inlet ① and outlet ③ tubes permit isolating the system, as well as eliminating oxygen and other gases out of the liquid by successive applying vacuum and carrier gas pressure.

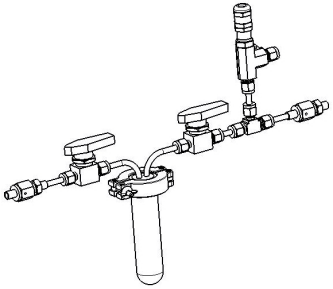

Figure 5.3: *Scheme of the source for liquids in Saclay*

In Würzburg the glass sample container (*Quarzglas Heinrich*) had a diameter of 40 mm (DN40), a height of 120 mm and a wall thickness of 3 mm including a fire polished joint surface. In Saclay a DN25 glass sample container (*Quarzglas Heinrich*) was used. To prevent cracking of the sample containers due to excess pressure , a *SS-RL3S6MM safety valve* was mounted in front of the inlet tube (see fig. 5.3), opening if pressure exceeded 2 bar and evacuating the gases into a fume hood. In both setups a central ring was used to center the joint properly; using a clamp the glass container and the inlet system were fixed tightly together (see fig. 5.4).

Figure 5.4: *Relevant components of the source for liquids*

Generally 4-5 ml sample was enough for 2 days, the sample was usually renewed not because it was empty, but because it had decomposed. Aluminum foil wrapped around the glass sample container was used to prevent light induced decomposition.

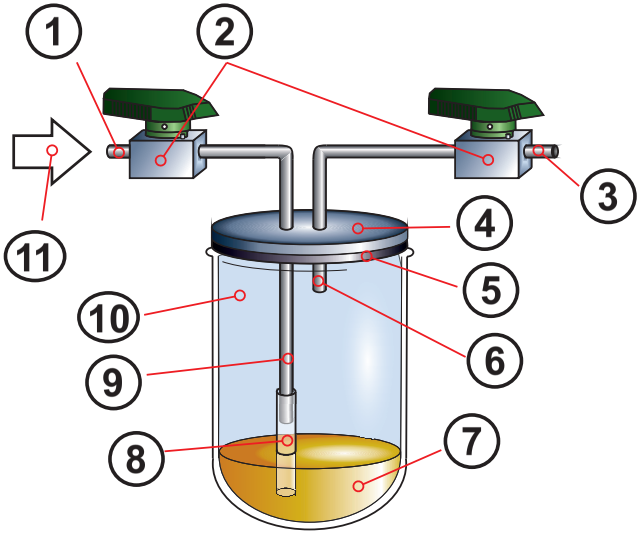

Figure 5.5: *Scheme of the source for liquids, mounted at the exterior of the apparatus: ①: Gas inlet tube; ②: Swagelok ball valves; ③: Gas outlet tube; ④: Steel top lid with welded inlet and outlet tube; ⑤: Rubber joint and distance keeper (see fig 5.4); ⑥: Gas outlet tube; ⑦: Liquid sample ⑧: 'Bubbler'; ⑨: Gas inlet tube; ⑩: Sample container; ⑪: Gas inlet flow*

5.1.3 Solids or liquids with high boiling points

5.1.3.1 T-Filter

Instead of having the sample outside of the apparatus, it is put in a sample container right before the pulsed valve (see fig. 5.6 and 5.7).

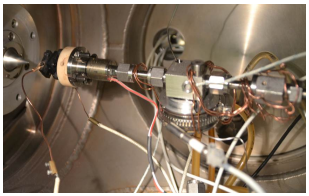

Figure 5.6: *Picture of the T-filter solid source*

The sample container is a steel T-Filter (*swagelok SS-4TF-LE*) ②, with no filter element inside and with the spring removed. Via a *thermocoax* heating element (*1NcAc10/ 100cm/ 2Xcv10*) ⑦ in a home-built heater ⑥, the sample can be heated up to 200°C. The sample can be a liquid with a high boiling point or a solid. The carrier gas ⑧ passes over the heated sample ⑤, incorporates the evaporated molecules, passes the pulsed valve ④, and is then expanded into vacuum. Heating the sample has to be done slowly, with the pulsed valve and pyrolysis (if used) switched on. This allows uniform heating of the tubes connecting the sample container to the pulsed valve, and prevents clogging of the valve as well as overheating of the sample. This procedure leads to constant and stable temperatures during measurements.

The holder for the *thermocoax* heating element was built by the workshop of the Institute of Physical and Theoretical Chemistry of the University of Würzburg. It is fixed with a hose clamp and additionally secured with copper wire. The temperature was measured on top of the filter, using a K-type thermocouple fixed with a screw in one of the two holes of the filter. When this source was used in Saclay, the temperature was measured by inserting a K-thermocouple into the screw hole closest to the pulsed valve.

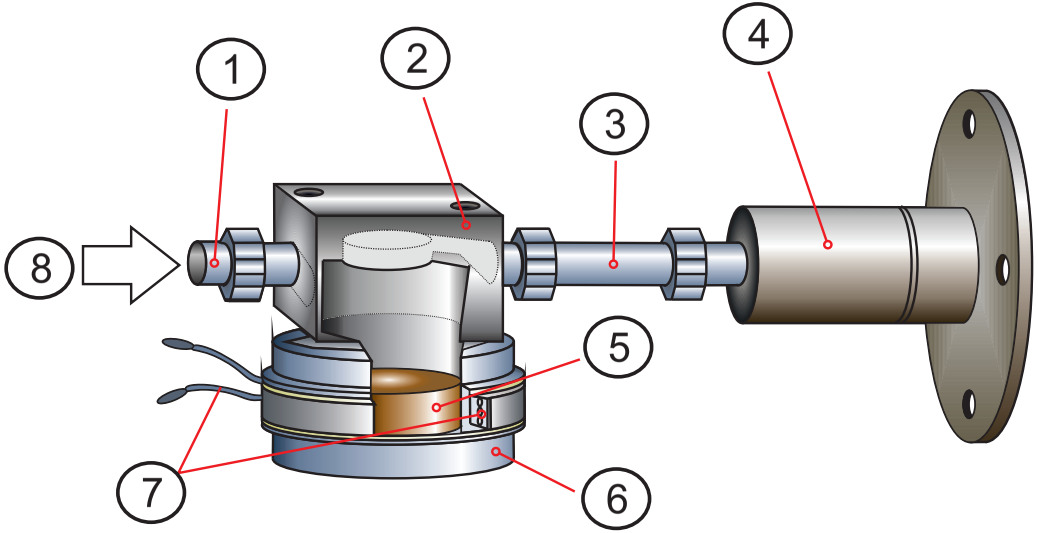

Figure 5.7: *Scheme of the solid source with the sample placed in a T-filter before the pulsed valve: ①: Inlet tube; ②: T-filter (swagelok SS-4TF-LE), temperatures were measured on top of the T-filter; ③: Short connection tube; ④: Pulsed solenoid valve (First Sensor, series 9, 9S1-A1-P1-9B05); ⑤: Solid or liquid sample; ⑥: Home-built heat corpus of heater; ⑦: Thermocoax heating element (1NcAc10/100cm/2Xcv10); ⑧: Gas inlet flow*

5.1.3.2 Solid source with sample under the pulsed valve

Figure 5.8: *Picture of the solid source with sample under the pulsed valve*

For solids with a very high melting point or for molecules with a very low vapor pressure, putting the sample in a T-filter is no longer sufficient. In those cases one possibility is to put it directly under the pulsed valve faceplate [59, 131] (see fig. 5.8 and 5.9) . The distance from sample to pulsed valve is thus very short, the temperature gradient between the oven and the pulsed valve is consequentely small, resulting in a higher signal. The standard pulsed valve faceplate is replaced with a connection piece ⑥, heat block ⑦ and home-built faceplate ⑧. Since the distance of the poppet's point to the faceplate increases, a longer home-built poppet ⑤ had to be used as well. The gas ⑲ passes into the sample via two ways, once directly via ① into the pulsed valve, once it passes over the sample ⑬ before entering the pulsed valve. The sample ⑬ is put in a hollowed screw ⑭, which serves as a sample container. Using a *thermocoax* heating element ⑮ the sample is heated. Seeded into the rare gas, the sample molecules pass the pulsed valve and then either via the here depicted pyrolysis setup (⑨, ⑩ and ⑪ , described in detail in 5.2) or are directly expanded into vacuum.

If the sample is a liquid, glass wool was put as the last layer in the sample container to prevent spilling of the sample into other parts of the source during transport. Once a sample has been mounted, it should only be transported with the sample container being vertical.

One of the main problems with this source is, however, to have it completely air-tight with the pulsed valve off. This often requires several days of trying different poppets and different thicknesses

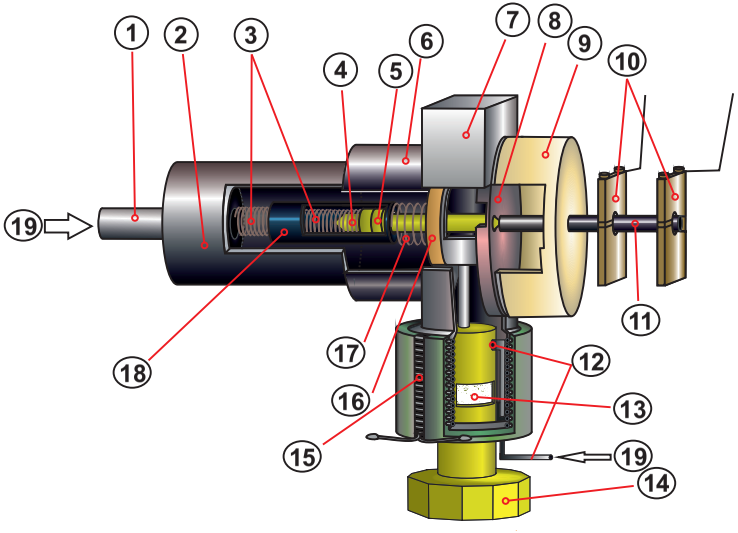

Figure 5.9: *Scheme of the solid source where the sample is directly under the pulsed valve: ①: Tube of the pulsed valve (First Sensor, serie 9, 9S1-A1-P1-9B05); ②: Body of the pulsed valve; ③: Main spring; ④: Small poppet; ⑤: Long poppet; ⑥: Connection piece of the pulsed valve to the heat block; ⑦: Heat block, the temperature was taken on the side; ⑧: Faceplate; ⑨: Pyrolysis mount made out of MACOR®; ⑩: Pyrolysis contacts; ⑪: Pyrolysis tube; ⑫: Tube where a part of the gas enters; ⑬: Liquid or solid sample, if liquid glass wool is put on top; ⑭: Sample container, a hollow screw; ⑮: Thermocoax heating element (1NcAc10/100cm/2Xcv10); ⑯: Guide piece for the buffer spring and long poppet, made out of teflon; ⑰: Buffer spring; ⑱: Guiding piece for the springs and poppets of the pulsed valve; ⑲: Gas inlet flow (2 entries)*

of sealing tape. Once this was achieved, however, only the sample in the hollowed screw needed to be changed, a complete disassembly is often not necessary. It is also noteworthy that if there is only a small leak centered on the faceplate hole, this often becomes more tight when heating or pyrolysis is applied. The heat should be increased slowly as well, since it takes quite some time for the heat to diffuse. The thermocouple was placed on the side of the heat block, fixed with a screw.

5.1.3.3 Sample in front of the pulsed valve

Another possibility is to put the solid sample in an oven ③ mounted on the faceplate ① of the pulsed valve (see fig. 5.10 and 5.12). The sample is mixed thoroughly with fine powdered graphite (CAS: 7782-42-5, 20-50% sample concentration, depending on the sample), and compressed to a pill ④ . Using either a drill after compressing, or by putting in a straight thick wire in the middle during compressing, a continuous hole was made in the pill - necessary as to have a molecular beam. The sample is heated using a *thermocoax* heating element (*1NcAc – 1.5mm*) ⑥ and evaporates into the hole and in the space between the pastille and the front faceplate. When the pulsed valve opens, the rare gas jet is mixed directly in the oven with the gaseous sample, and then expanded into vacuum.

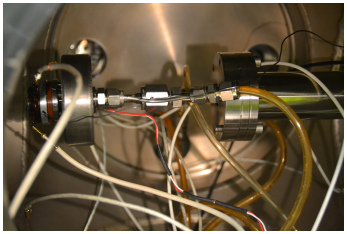

Figure 5.10: *Picture of source with the sample in front of the pulsed valve*

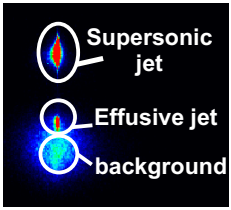

Figure 5.11: *Typical ion image for the oven in front of the pulsed valve*

In the ion image several expansions are visible, an effusive and a supersonic jet (see fig. 5.11). Different positions and sizes of the hole in the front faceplate were tested and simulated [132,133]. The temperature was measured on the side of the oven using a thermocouple ⑦. The *Vespel* connection piece ② is designed to minimize heat transfer between the oven and the pulsed valve, using a cool-

ing element the pulsed valve may be cooled as well. This allows heating to high temperatures (300°C). The *thermocoax* heating element ⑥ is wrapped with copper wire to maximize heat transfer. The round hole in the side of the connection piece allows efficient venting. Using a suitable pyrolysis mount out of *MACOR*® and two longer screws, the pyrolysis setup can be fixed in front of the front faceplate. Since pyrolysis attains very high temperatures, the connection piece was omitted and heat transfer increased using vacuum grease, so that the cooling of the pulsed valve cools the back of the oven as well.

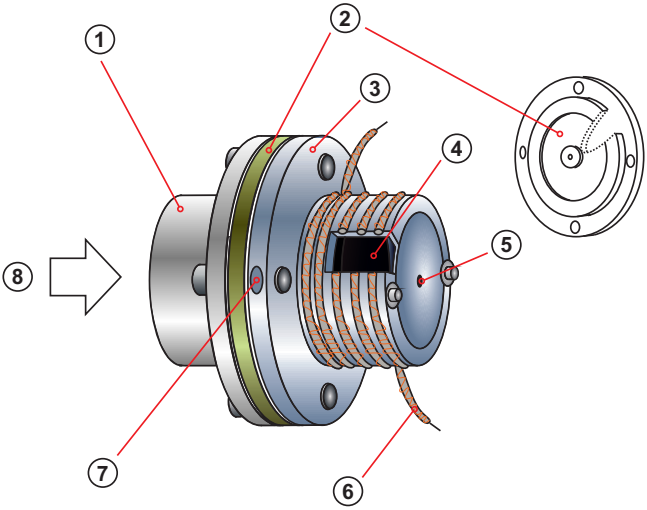

Figure 5.12: *Scheme of the solid source where the sample is mounted after the pulsed valve: ①: Faceplate of the pulsed valve; ②: Vespel isolating piece; ③: Oven; ④: Sample in a graphite pill, which has a hole in the center; ⑤: Front faceplate with a hole in the center; ⑥: Thermocoax heating element; ⑦: Hole in the side of the oven, the temperature was measured here; ⑧: Gas inlet flow*

5.2 Pyrolysis

The variation of the pyrolysis nozzle proposed by Kohn et al. [44] used in this thesis is depicted in fig. 5.14 and fig.5.13 . The functionality of the pyrolysis has already been explained in section 3.1.

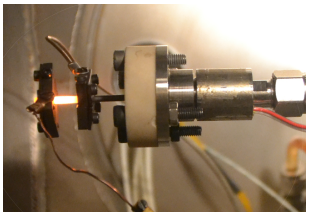

Figure 5.13: *Picture of the pyrolysis setup*

On the faceplate ② of a pulsed valve ① a silicon-carbide (SiC) tube (*Saint Gobain Keramik, Hexololoy SE SiC tube*) ⑨ is fixed using a pyrolysis mount ③. The pyrolysis mount ③ is made out of *MACOR®*, an isolating low-expansion ceramic with a low thermal conductivity and temperature tolerance of over 1000°C [134]. The SiC tube is fixed via a grub screw set in a hole on the side of the pyrolysis mount, which prevents slipping of the SiC tube during the operation of the pulsed valve. The SiC-tube is contacted using two electrode blocks ④.

By applying a constant voltage (typically between 10 and 16 V, powers between 30 and 50 W), this semiconductor heats up to 1800 °C [44] (maximum usable temperature of 1900 °C [135]). SiC has a very low thermal expansion coefficient, a high thermal conductivity and is chemically inert [136], making it an ideal material for a pyrolysis tube. During experiments of our group at the Swiss Light Source, however, where the temperatures of the pyrolysis tube are measured routinely, temperatures of 700 - 1000 °C were measured for powers between 30 to 50 W [137, 138]. Due to its high hardness of 9.6 Mohs it cannot be contacted directly using soft conductive materials such as copper. Instead, a material of equal or higher hardness must be used. SiC splits ⑧, fabricated from a solid tube of SiC (*Berghütten GmbH*), were wedged between the front ⑦ and the back ⑥ plate and are fixed using two screws on top of the front plate. By tightly fix-

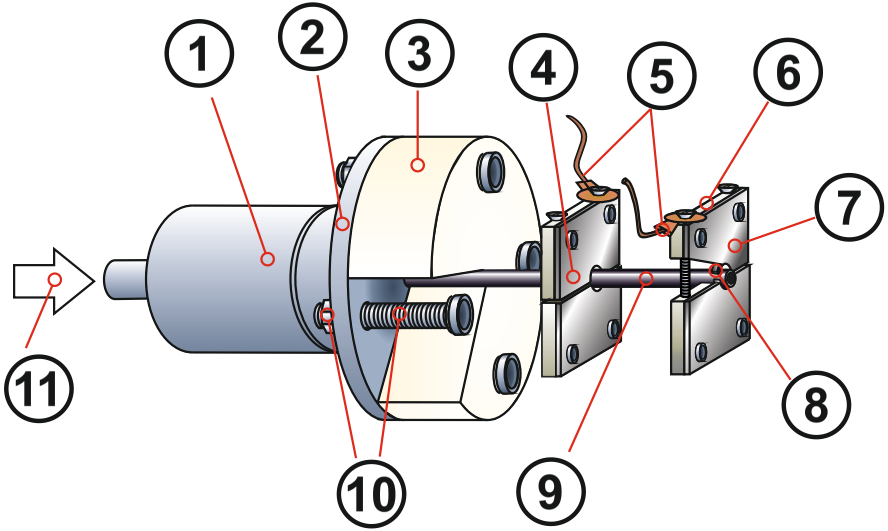

Figure 5.14: *Scheme of the pyrolysis setup: ①: Pulsed valve; ②: Faceplate of the pulsed valve; ③: Pyrolysis mount made out of MACOR®; ④: Stainless steel electrode block consisting of an upper and lower block; ⑤: Copper contacts to the DC power supply; ⑥: Back plate of the electrode block; ⑦: Front plate of the electrode block; ⑧: SiC splits wedged between the front and back plates of the electrode block; ⑨: SiC-tube; ⑩: 4 screws and corresponding nuts which fixate the pyrolysis mount on the pulsed valve faceplate; ⑪: Gas inlet flow*

ing the upper and the lower block of the electrode block with two screws, the SiC tube is efficiently contacted. Both the pyrolysis mount and the stainless steel electrode blocks were fabricated by the workshop of Institute for Physical and Theoretical Chemistry of the University of Würzburg.

Typically the SiC tube was 3.3-3.8 cm long, with an inner diameter of 1 mm. Powers between 30 and 50 W were necessary and sufficient for the production of the radical. The pyrolysis power applied should be just enough to ensure a high conversion of the precursor, but as low as possible to have a cold molecular beam and to prevent secondary reactions. After long use a graphite layer forms on the surface of the SiC tube, leading to lower resistance and to finite lifetimes of the SiC tube. Normally the resistance of a SiC tube was between 20 and 40 Ω, ideally it should be about 100 Ω. The resistance and the lifetime of a tube can be considerably increased using abrasive paper to eliminate the graphite layer [59]. The contacts should be put as close together as possible (typically 0.5-1 cm), ensuring short residence times and minimizing secondary reactions.

5.3 Setup in Würzburg

5.3.1 Apparatus

A schematic overview of the apparatus is shown in fig. 5.15 (top view) and in fig. 5.16 (side view). The apparatus consists of a source chamber and a main chamber. In the source chamber the molecules are brought into the gas phase and expanded in a molecular beam via a pulsed valve in direction of a skimmer. Via the skimmer the molecular beam enters the main chamber, there it crosses the lasers between the first two plates of the electrostatic optics. The detector is - in contrast to the apparatus in Saclay - mounted in line of the molecular beam. Both time-of-flight mass spectra and velocity-map imaging were recorded using this setup.

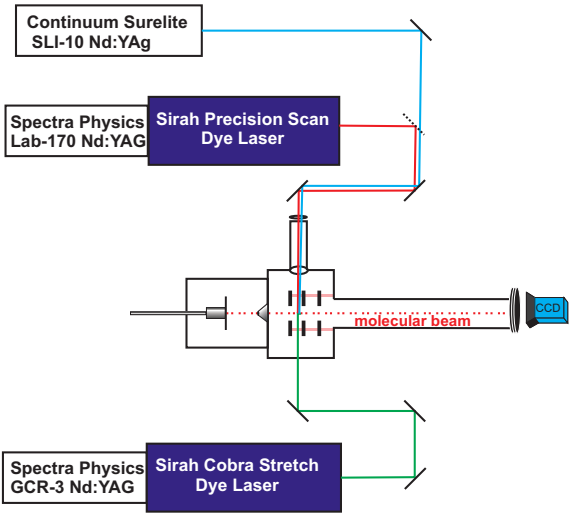

Figure 5.15: *Schematic overview of the apparatus in Würzburg, top view*

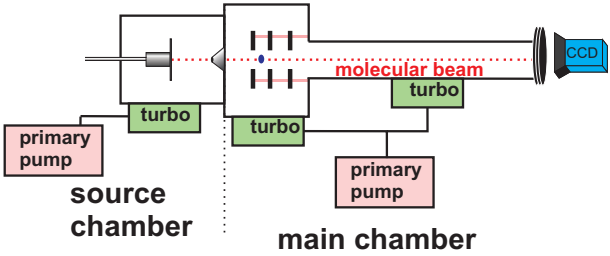

Figure 5.16: *Schematic overview of the setup in Würzburg, side view*

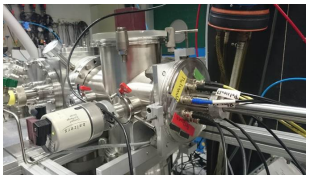

Figure 5.17: *Pictures of the source chamber in Würzburg*

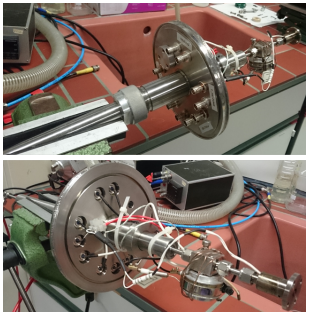

Figure 5.18: *Front and back view of the source flange with a mounted T-filter solid source*

The source chamber consists of a cross with 5 DN160 flanges (see fig. 5.17). On the lowest flange a *TMH 520 pfeiffer* turbopump is mounted, connected to a *Pfeiffer Vacuum Duo 5* primary pump. The central axis flange is pierced by a 40 cm long tube with a diameter of 5 cm fixed via a vacuum-tight screw thread. On both ends of this 5 cm wide tube a 6 mm tube is welded. This 6 mm tube is connected on the outside to the gas inlet via standard *swagelok* connections, on the inside the pulsed valve (and corresponding sources depending on the molecule's characteristics, see section 5.1) is mounted. The tube can slide through the flange, which for reference is called source flange, allowing adjusting of the distance between the different sources to the skimmer.

On the source flange six to eight electrical vacuum connections are mounted, corresponding to 2 BNC connections each for the pulsed valve, the thermosensor and the heater; and 2 SHV connections for the pyrolysis (see fig. 5.18). The pulsed valve was operated via a home-built pulse driver. The side and top flanges are blind flanges; the side flange contains a window to facilitate centering the molecular beam on the skimmer. The molecular

beam is adjusted by four screws holding the front flange (see fig. 5.19). To change the source, the whole front flange with the pulsed valve fixed on the protruding 6 mm tube (with sources and pyrolysis) is dismounted and taken out of the source chamber.

The pressure in the source chamber was measured using a *Balzers PKR 250 pressure gauge*. The source chamber is connected to the main chamber on the opposite side in respect to the source flange. The connecting flange has a central hole, on which the skimmer is mounted. The skimmers were produced using a procedure commonly used in our research group [139]. The main and the source chamber can be separated using a gate valve, designed and constructed by the workshop of the Institute of Physical and Theoretical Chemistry of the university of Würzburg. This allows separate venting of the source chamber (when changing the molecule/or source for example), while keeping the delicate detector under vacuum.

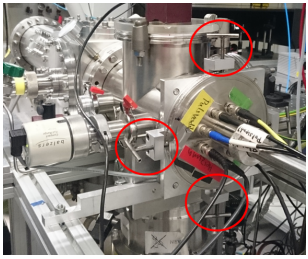

Figure 5.19: *Screws to adjust the molecular beam and the window to verify its position*

i
Typical pressures with the pulsed valve on(off): source chamber: $\approx 10^{-5}$ (3×10^{-7}) mbar main chamber: 1×10^{-6} (7×10^{-7}) mbar

The main chamber consists of a cube but with 6 DN160 flanges (see fig. 5.20). The flange opposite to the source flange is connected to a 500 mm long flight tube with the detector on its end. Two turbopumps are connected to the main chamber: a *TMH 520 C Pfeiffer* turbopump on the bottom flange of the cross, and a *TMU 260U Pfeiffer* turbopump on a flange in the middle of the flight tube. Both are connected to the same *Pfeiffer Vacuum Duo 10-M* primary pump.

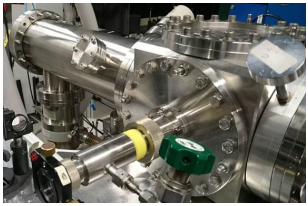

Figure 5.20: *Picture of the main chamber with the flight tube and gas cell*

The side flanges of the cross consists of blind flanges with mounted windows, a dye laser arriving from each side. A VUV gas chamber is mounted on the blind flange in direction of the *precision scan* laser (see fig. 5.15), allowing tripling of the

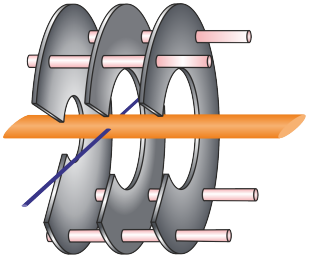

Figure 5.21: *Scheme of the electrostatic optics in Würzburg*

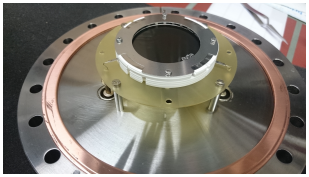

Figure 5.22: *Picture of the dector, a defect on the phosphorous screen is visible. It has since been changed.*

laser beam by appropriate gas fillings [140]. Both lasers cross the molecular beam in the middle of the electrostatic optics, mounted on the inside of the main chamber. The electrostatic optics consists of three circular electrodes with a diameter of 88 mm, called repeller, extractor and ground electrode respectively. The repeller electrode has a central hole with a diameter of 2 mm, for both extractor and ground electrode the diameter of the central hole is 20 mm. The molecular beam (orange in fig. 5.21) passes through all three holes and is ionized by the laser (purple in fig. 5.21) between the repeller and the extractor electrode. How this works in detail is explained in section 4. They are mounted on polyether ether ketone (PEEK) rods, kept at a distance of 15 mm to each other using PEEK spacers. PEEK is a non-conductive polymer suitable for high-vacuum applications [141].

The detector (*MCP-50-D-L-VF-P43, Tectra Physics*) consists of two micro-channel plates in chevron configuration and a P43 phosphorous screen (see fig. 5.22). Behind the phosphorous screen a *ProSilica AVT GC 1380 H* CCD camera is mounted. How the detector works is explained in detail in the beginning of chapter 4.

With this detector two types of measurement were done. Time-of-flight mass spectra were measured by applying a positive voltage of typically between 1.5-1.7 kV on the second MCP plate, and measuring the drop in voltage on arrival of the electron cascade produced by ions arriving on the first MCP. This drop of voltage is measured using a *LeCroy Waverunner LT342* oscilloscope. The other measurement mode is VMI of ions. The second MCP was gated with 1250+550 V, the phosphorous screen was kept typically at 4.4 kV. Imaging of elec-

trons is not possible with this setup, since without protection of parasitic magnetic fields (protection by e.g. an μ-metal tube), the newton spheres of the electrons would be shifted and possibly deformed. On the side of the flight tube a *Balzers PKR 250 pressure gauge* is mounted. When in imaging mode, this gauge was disconnected, otherwise its magnetic field distorts the ions flight path.

More details on the experimental setup can be found in the thesis of J. Giegerich [59] and M. Steinbauer [142].

5.3.2 Laser system

Three lasers could be used with the apparatus (see fig.5.15). Either both nanosecond dye lasers were used, or the *Precision Scan* Dye laser was replaced by a *Continuum Surelite* solid state laser.

The *Continuum Surelite SLi-10* solid state laser has a fundamental wavelength at 1064 nm. Using a birefringent crystal the emitted laserlight is doubled to 532 nm or tripled to 355 nm, or with a second birefringent crystal 532 nm is doubled to 266 nm.

The *Sirah Cobra Stretch* dye laser (see fig. 5.23) is pumped by a *Spectra Physics GCR-3* Nd:YAG solid state laser with either 532 or 355 nm depending on the dye, which corresponds to the doubled or tripled fundamental using a birefringent crystal. The fundamental of this dye laser spans from 400 nm to 870 nm with a pulse length of 8-10 ns and a resolution of 0.08 cm^{-1} at 570 nm [143].

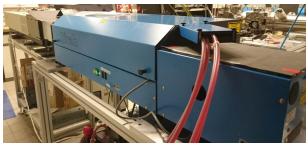

Figure 5.23: *Sirah cobra Stretch dye laser*

The *Sirah Precision Scan* dye laser (see fig. 5.24) is pumped by a *Spectra Physics Lab 170* Nd:YAG solid state laser, whose characteristics are analogous to the pump laser of the *Sirah Cobra Stretch* dye laser. The fundamental of this dye laser has a narrower spectrum (350-740 nm), but its res-

Figure 5.24: *Sirah Precision Scan dye laser*

olution is higher due to a finer grating (0.06 cm^{-1} at 625 nm) with a pulse length of 6-8 ns [144]. This laser was used to produce wavelengths in the VUV (around 118 nm) using a gas cell, described in detail in ref. [59].

5.3.3 Time synchronization

Correct synchronization of laser, pulsed valve and detector is primordial to obtain meaningful (or any) signal. A scheme of the time synchronization with typical times is given in fig. 5.25. The master clock is a *Stanford Research System DG 535*. Its time zero T_0 triggers directly the flash lights of the Cobra dye laser, the Q-switch and the oscilloscope is on channel C. The flash lights of the Precision Scan are triggered by Channel B. Channel D triggers the Q-Switch of the Precision Scan and is relative to Channel B, thus both laser are delayed respectively to each other in time by changing Channel B. Channel A triggers the pulsed valve and CCD-camera.

In VMI-mode it also triggers the *Stanford Research Systems DG645*, where Channel C corresponds to the position of the gate (=which mass is selected) and Channel D to the size of the gate (how long it is open). For the continuum laser T_0 of the master clock serves as trigger for another *Stanford Reserach Systems DG645*, whose channel C and D trigger the flash lights and Q-switch respectively.

5.3.4 Data acquisition

Mass spectra were measured using the program implemented by M. Schneider [145]. For imaging the acquisition program implemented by J. Giegerich [146] was used.

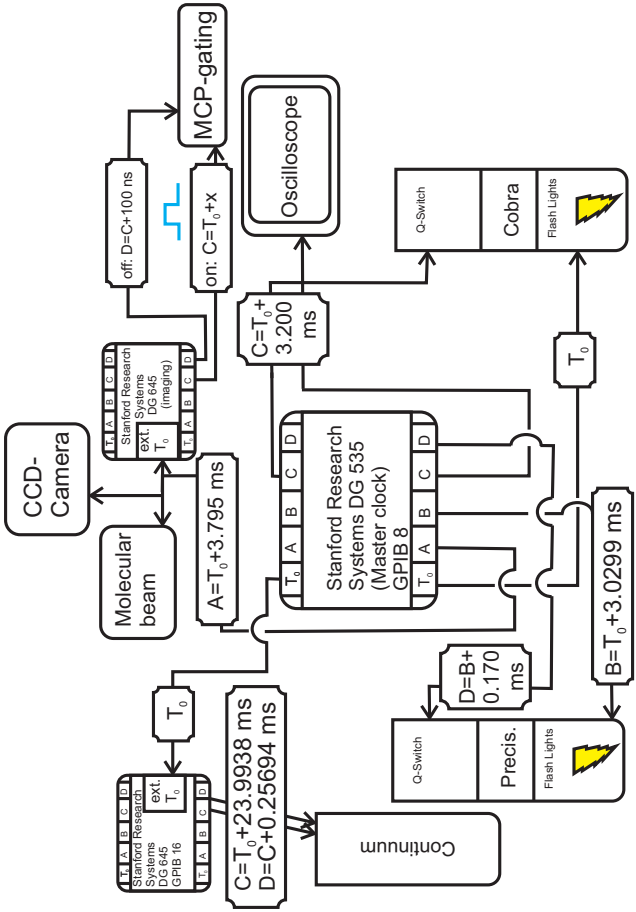

Figure 5.25: *Scheme of the time synchronization of the different elements in Würzburg with typical times for different channels*

5.4 Setup in Saclay

5.4.1 Apparatus

i
Typically pressures were $7*10^{-6}$ mbar and $4*10^{-7}$ mbar in the source and the main chamber respectively, with the pulsed valve on.

A schematic view of the measuring apparatus in Saclay is shown in fig. 5.26, a back and front view of the apparatus in Saclay[1] is shown in fig. 5.27 and fig. 5.28 respectively. Just as for the Würzburg setup (see section 5.3.1), it consists of a source chamber and a main chamber connected via a valve. In the source chamber the molecule is expanded in a molecular beam (see section 3.2). The molecular beam passes the skimmer before entering the main chamber, where it passes the electrostatic optics and the laser. Orthogonal to the laser/molecular beam plane are mounted two detectors. Above a time-of-flight tube connected to a VMI detector, below a time-of-flight tube connected to an MCP detector.

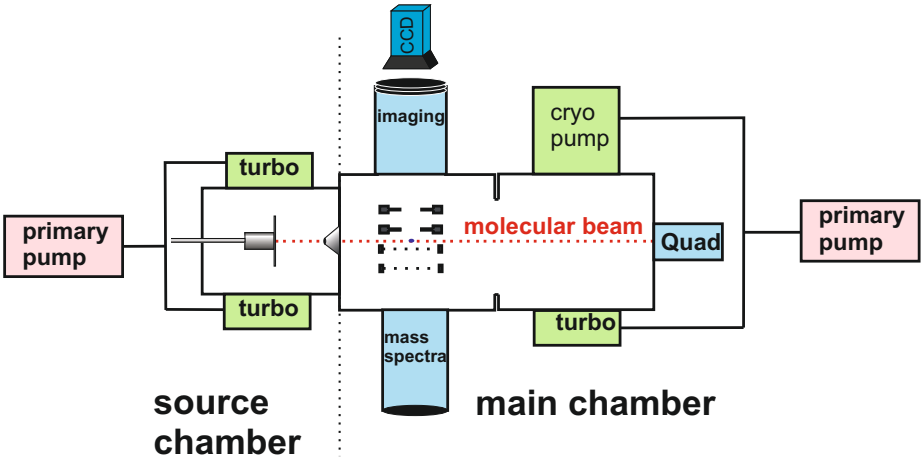

Figure 5.26: *Schematic overview of the setup in Saclay*

[1] Many thanks to Christophe Pothier for the CAD designs

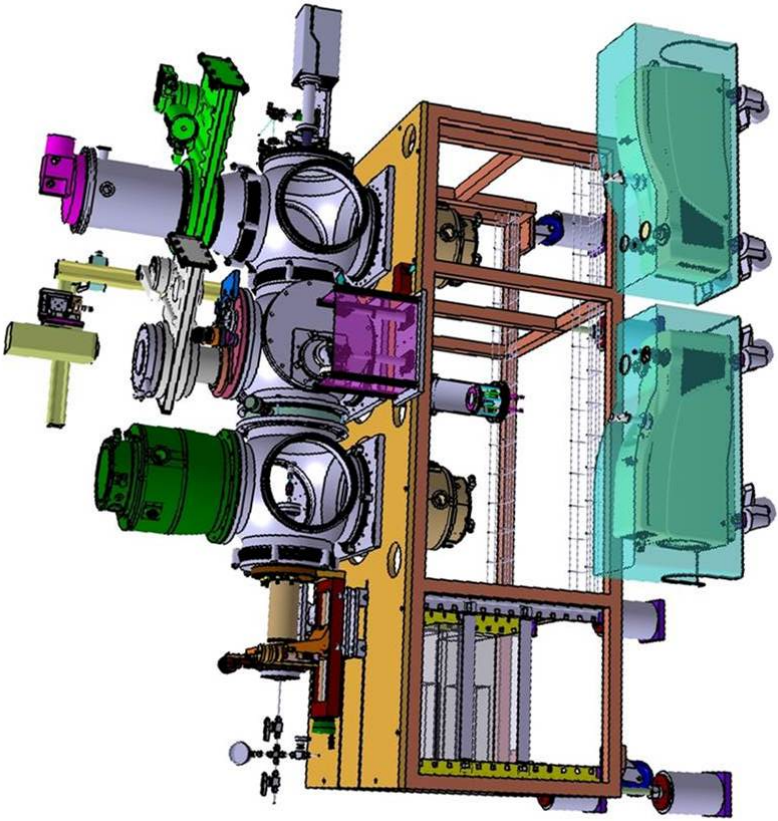

Figure 5.27: *Back view of the measuring apparatus in Saclay* [1]

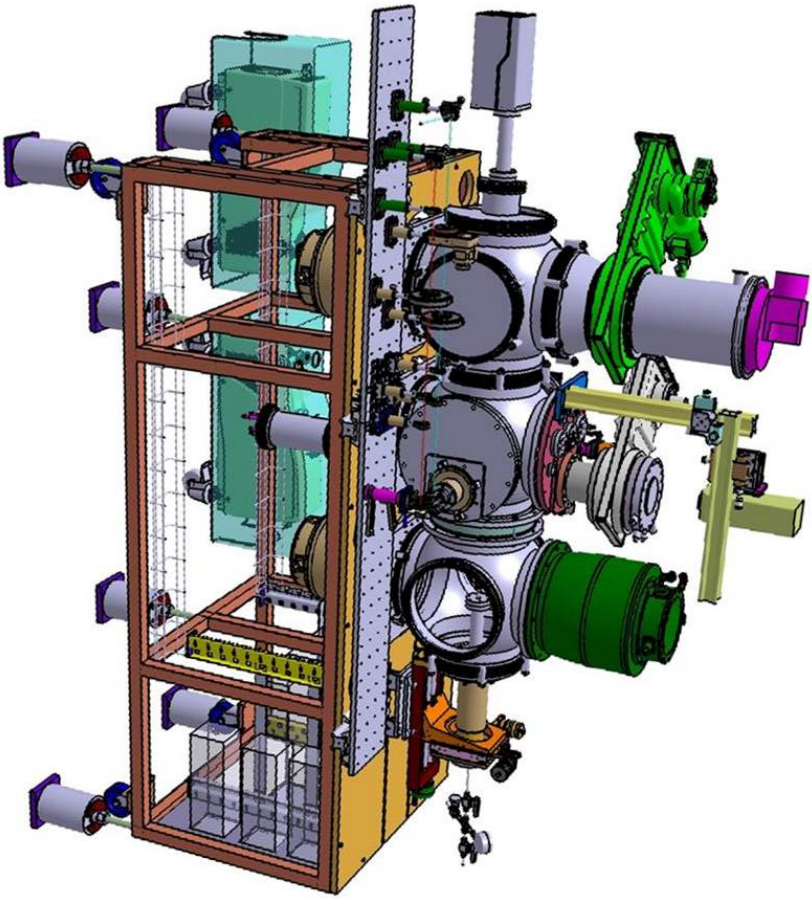

Figure 5.28: *Front view of the measuring apparatus in Saclay*[1]

In the molecular beam axis a quad mass spectrometer is mounted, which was not used in this thesis.

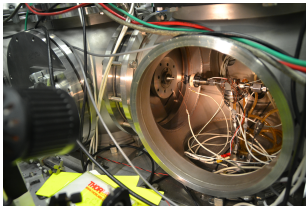

Figure 5.29: *Pictures of the source chamber*

The source chamber (see fig. 5.29 and fig. 5.30) consists of a round chamber with 6 DN 250 ISO-K flanges on the sides, with one of them connected to the main chamber. Contrary to the apparatus in Würzburg, one of the side flanges was opened to directly mount the source inside. The flange in prolongation to the source was fixed to a *Meca2000-Vinci Technologies* XYZ-manipulator consisting of three micrometer screws, allowing positioning the molecular beam on the skimmer. The cables for pyrolysis, thermocouple and heating were entered into the source chamber via a swagelock cross (see fig. 5.31). This cross was fixed on a DN 40 ISO-KF flange connection mounted on the flange opposite to the flange, which can be opened to access the source chamber.

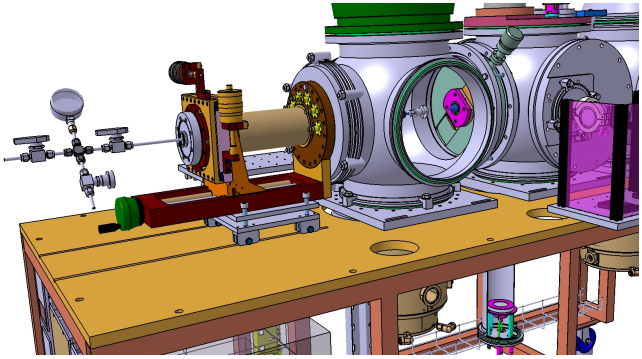

Figure 5.30: *3D scheme of the source chamber[1] with the positioning system of the molecular beam, the pulsed valve and the skimmer visible.*

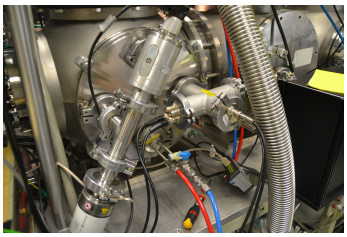

Figure 5.31: *Swagelock cross to enter the cables*

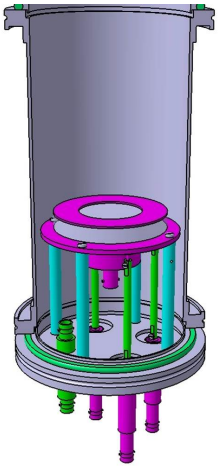

Figure 5.32: *TOF detector consisting of a MCP and an anode*[1]

The pulsed valve was a *First Sensor* series 9 pulsed valve, steered by an *IOTA ONE* Pulse Driver (*General Valve corporation*) and an *4455 Generateur d'impulsion synthetise (selfram instrument & systems)*. It was operated (just like the lasers) at 20 Hz with a typical opening duration of the valve of 180 µs. The cables for the pulsed valve pass via the front flange. The source and the main chamber are separated via a gate valve, allowing separate venting of the two chambers. On the upper and lower flange an *ATH 2300 M* and an *ATH 1600 M* turbopump were mounted respectively. The pressure in the source chamber was measured by a pfeiffer vacuum compact full range gauge.

The main chamber (see fig. 5.27 left and fig. 5.28 right) consists of two connected round chambers of the same type as the source chamber. On the upper flange on the first chamber the electrostatic optics and the VMI detection is fixed. The electrostatic optics is described later in the text. The VMI spectrometer consists of a 25 cm long DN 63 ISO-F flight tube connected to a VMI detector via a *VAT 14044* gate valve. The gate valve keeps the detector isolated, thus under vacuum and waterfree conditions even when the main chamber is vented. The VMI detector consists of two micro-channel plates in chevron configuration and a phosphorous screen. Charged particles arriving on the first micro-channel plate lead to electrode cascades. These are then accelerated to the second micro-channel plate by typical voltages of 1700 V, causing even more electron cascades. The micro-channel plates serve as signal amplifiers. Via a typical voltage of around 4600 V these electrons are then accelerated in direction of the phosphorous screen, causing it to glow upon hitting it. The resulting

light is photographed by a *PCO.1600* CCD camera mounted above the phosphorous screen. The second MCP is gated to allow mass-selective ion images. Gating means that 600 V are added to a constant voltage of 1200 V when detection is desired. This allows to reduce noise from other charged particles, like electrons produced by the laser as it passes through the window into the main chamber or electrons emitted by the gauges.

On the lower flange of the first round chamber, opposite to the VMI detector, a 55 cm long DN 63 ISO-F time-of-flight tube is mounted, with a microchannel plate connected to a *LeCroy Waverunner 62Xi* oscilloscope at its end (see fig. 5.32). Ions are accelerated (by applying the correct voltages on the electrostatic optics; see below) and arrive on the detector, which is typically kept at voltages of -1850 V. There they cause a drop in voltage, which is detected by the oscilloscope.

The other two flanges of the first main chambers have inlaid windows for the lasers. Both lasers enter on one side under a small angle, cross each other in the middle of the ion optics and exit the main chamber on the opposite side. There the pump laser is reflected on an *OceanOptics USB 400* spectrometer so that its spectrum can be recorded in real time during measurements. The spectrum of the probe laser is measured on the optical tables of the laser (see section 5.4.2.4).

The second main chamber's purpose is to keep the vacuum. On the lower and upper flange it is connected to an *ATH 1600 M* turbopump and an Edward Cryo Drive pump respectively. Both are connected to a primary pump. On the flange in direction of the molecular beam a *SRS RGA 300* quad mass spectrometer is mounted. A sky hot

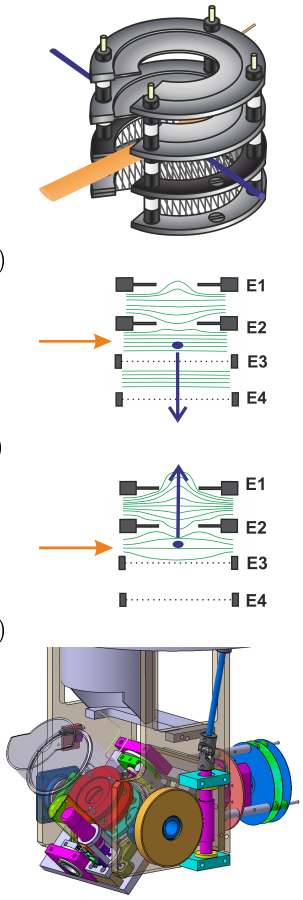

Figure 5.33: *a) ion optics in Saclay b) field lines in tof mode c) field lines in ion/photoelectron imaging mode d) 3D-scheme of ion optics*[1]

a)

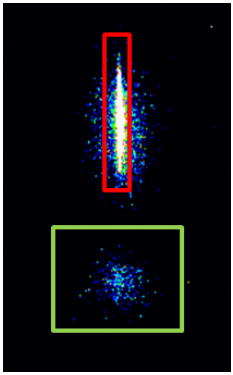

b)

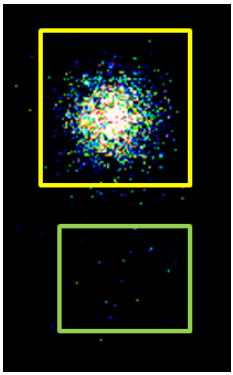

Figure 5.34: *Typical ion images. a) The molecular beam (red rectangle) b) dissociative photoionization (yellow rectangle). The green rectangle shows the background signal.*

combi pressure gauge and two inlets are connected to one of the side flanges. One inlet can be used to vent the main chamber with nitrogen, whereas the other is connected to a tetrakis(dimethylamino)-ethylene reservoir. This molecule can be used to find the spatial and temporal overlap (pump-probe signal) of the lasers.

During the course of the thesis, the primary pumps of the source chamber and the main chamber were changed from *Pascal 2063SD* and *Pascal 2033 SD* pumps to *Adixen ACP 40/28* pumps.

The ion optics is optimized to allow good mass resolution and to be used as an electrostatic lens for ion or photoelectron imaging. As can be seen in fig. 5.33 a), it consists of 4 electrodes. E1 and E2 are electrostatic lenses, whereas E3 and E4 are grids. The molecular beam (depicted in orange) and the lasers (depicted in blue) pass between E2 and E3, for minimizing reflections these are painted in black with graphite. The electrodes are thicker on the outside, this minimizes field perturbations from the spacers between the electrons, which are made out of PTFE (polytetrafluoroethylene), a nonconductive plastic. Moreover, the ion optics can be mechanically turned inside the apparatus (see fig. 5.33-d), which allows optimal flight paths and detection on the upper/lower detector. It can also be turned in direction of the quad mass spectrometer to extract in this direction. A μ-metal tube is placed around the ion optics and in the flight tube of the VMI setup, to obtain a field-free flight region and an undistorted photoelectron image.

To have a good imaging resolution, we use the ions optic as an electrostatic lens (see fig. 5.33-b). The lower grid E4 is grounded, the upper grid E3 is typically at 2000 V, E2 at 1388 V and the

upper lens at 0 V. The resulting electromagnetic lines form a lens, so that ions/electrons formed at different points in space arrive on the same radius around the center on the imaging detector.

These electric field lines, however, are not optimal for a good mass resolution. For a good mass resolution they should be as parallel as possible, the voltages consequently need to be adapted (see fig. 5.33-c). On E1 and E2 a voltage of 2400 V and 2000 V is applied respectively, on E3 and E4 voltages of 1806 V and 0 V are applied.

In contrast to ion imaging in Würzburg, the ions are extracted orthogonal to the molecular beam. Since the molecular beam [43, 132] has a high velocity, the ions produced from the molecular beam continue to move in the direction of the molecular beam while they are being extracted. Thus the molecular beam is directly visible as a horizontal line (fig. 5.34-a in the red rectangle), contrary to background molecules (molecules present in the main chamber moving randomly, green rectangle), which appear as a diffuse circle. If, however, the ions in the molecular beam are formed via dissociative processes, the resulting ions obtain velocity components in x and y direction. The line is blurred out, a more or less circular blotch is visible (fig. 5.34-b, yellow rectangle).

5.4.2 The fs-laser system in Saclay

The production of the desired wavelengths with a fs-time resolution can be divided into two parts: The generation of 800 nm by the Luca Laser Server (section 5.4.2.1) and, using this laser as the light source, the frequency conversion setup for the generation of either 266/400 nm (section 5.4.2.2) or variable wavelengths using the NOPA setup (section 5.4.2.3). Those will be described briefly in the following, included the entry of pump and the probe laser into the detection chamber (section 5.4.2.4).[2]

5.4.2.1 Luca Laser Server

The Luca Laser Server is built on two tables: The table 'Ampli REGENERATIVE' (fig. 5.35) and the table 'AMPLI and NOPAS' (fig 5.37).

On the Ampli Regenerative table (see fig. 5.36) a *VERDI* laser (532 nm) pumps the *MIRA* Ti:Saphire Laser (800 nm, 30 fs, red lines) at a repetition rate of 76 MHz. Using a pockels cell its repetition rate is brought down to 20 Hz. An Offner Stretcher streches the beam temporally, allowing chirped pulse amplification without damaging the equipment. It passes Ti-Saphir crystals in a regenerative amplifier (gain: x10^6) and in a multipass amplifier(gain: x20) setup, which are both pumped with 532 nm 7 ns long pulses (green lines) produced by a Surelite Continuum laser at 20 Hz. The resulting beam is splitted into a 9 mJ beam and a 6mJ beam. The 9 mJ beam is used for other experiments, whereas the 6 mJ continues to the second table 'AMPLI and NOPAS'.

[2] Many thanks to Michel Perdrix for the schemata of the lasers

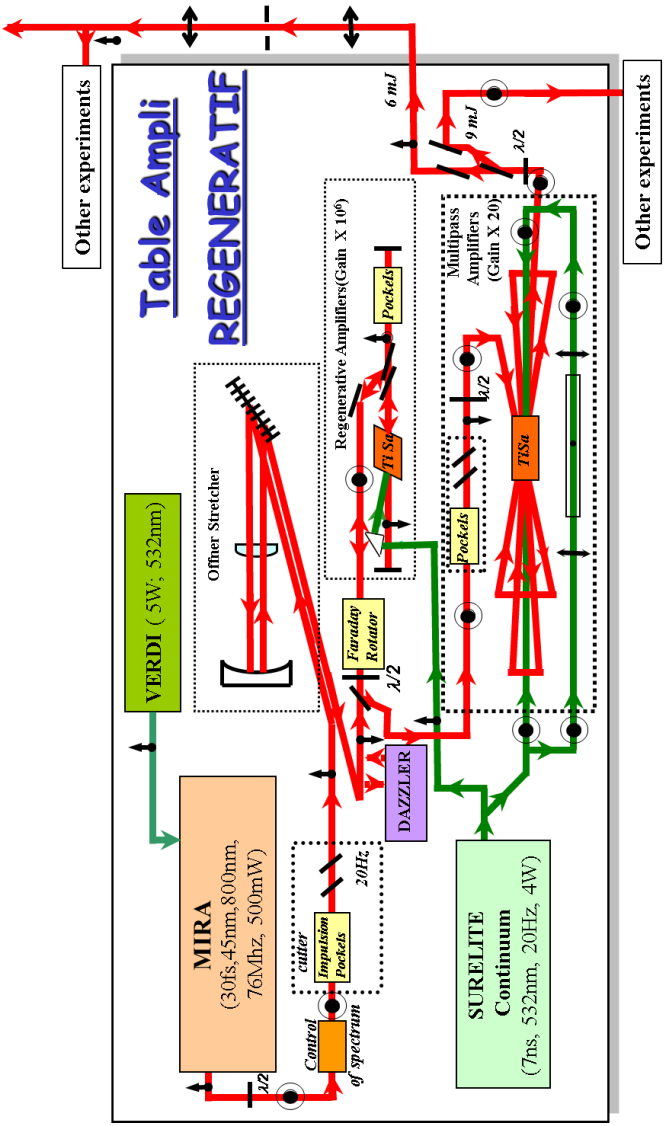

Figure 5.35: *Scheme of the Luca Laser Server, part 1*[2]

On the second table 'AMPLI and NOPAS' two different operation modes are possible: either using the NOPA/800 nm or 266/800(400) nm. In the 266/800(400) nm mode (see fig,5.37) the 800 nm beam (red line) arriving from the Ampli Regenerative table is temporally shortened by a grating compressor. Using a $\lambda/2$-plate and polarisators it is then split up into two parts: One for the frequency conversion setup (to generate 266/400/(200) nm) and one for the delay line. The frequency conversion setup is detailed in the next section. By turning the polarisator the relative intensities of the two parts can be adjusted. The 800 nm then passes a delay line, which is controlled by a *Universal Motion Controller Model ESP300*, delaying the two laser pulses relative to each other in time. After the delay line it is possible to insert a BBO type I crystal to double the 800 nm beam to 400 nm (light blue line); and via dichroic mirrors the remaining 800 nm is eliminated before it enters into the main chamber.

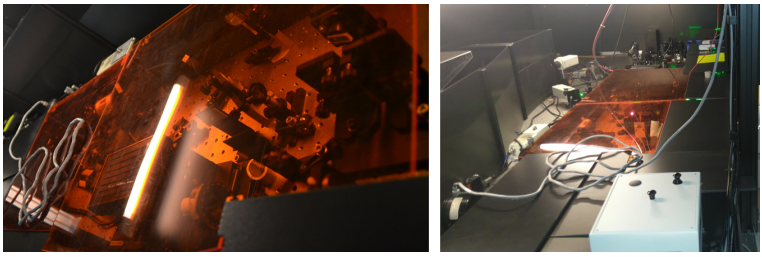

Figure 5.36: *Pictures of the Ampli Regenerative table*

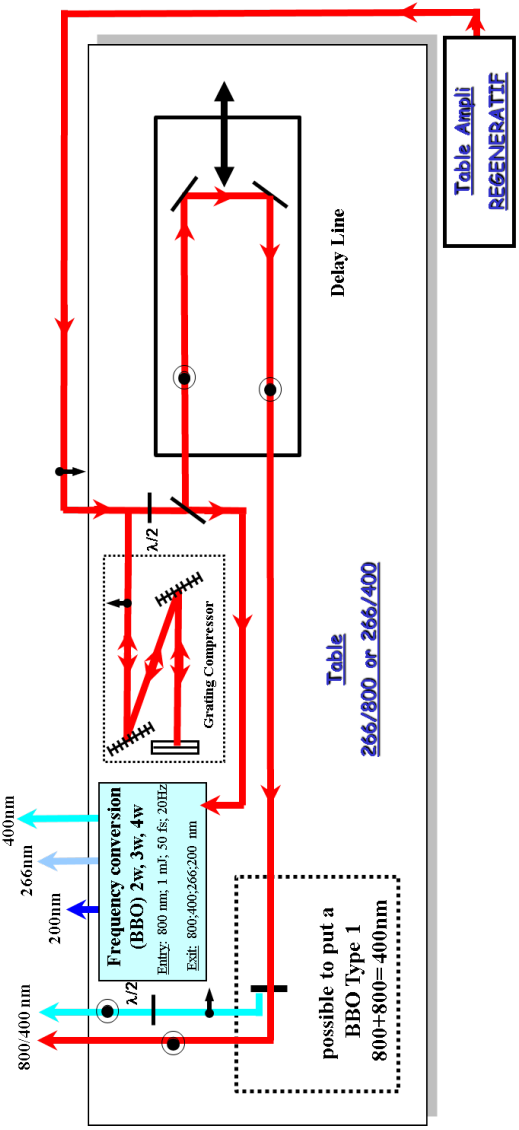

Figure 5.37: Table 'AMPLI and NOPAS', mode 266/800(400)²

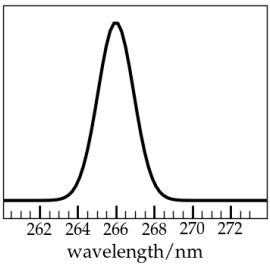

Figure 5.38: *Typical spectrum for the 266 nm pump laser*

5.4.2.2 Generation of 266 and 400 nm

To generate 266 or 400 nm pump pulses (see fig. 5.39 and fig. 5.40), the part of the 800 nm pulse (red line) for the frequency conversion setup passes a $\lambda/2$ plate to turns its polarization before it is doubled by a BBO type I crystal. Via a dichroic mirror the 400 nm pulse (light blue line) is then separated from the 800 nm pulse. The 800 nm passes a delay stage and its polarization is turned vertically before it mixes with the 400 nm pulse in another BBO type I crystal to produce 266 nm (blue line). A typical spectrum of 266 nm is shown in fig. 5.38. The delay stage for the 800 nm is used to assure that both beams arrive on the BBO crystal on the same time. Another dichroic mirror separates 266 nm from the 400/800 nm before both are propagated towards the entry of the detection chamber (see section 5.4.2.4). It is also possible, though it was not used during this thesis, to mix 266 nm in an BBO type I crystal again with 800 nm to obtain 200 nm pulses (dashed blue line).

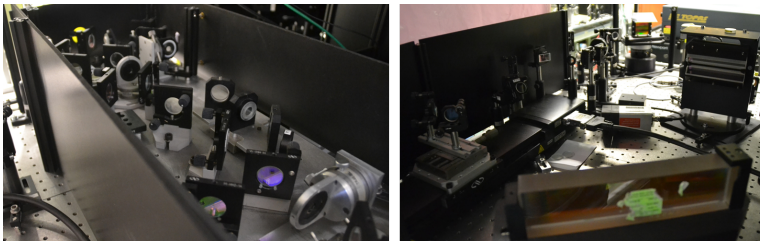

Figure 5.39: *Pictures of the generation of 266/400 nm (left picture) and of the delay line and the compressor (right picture)*

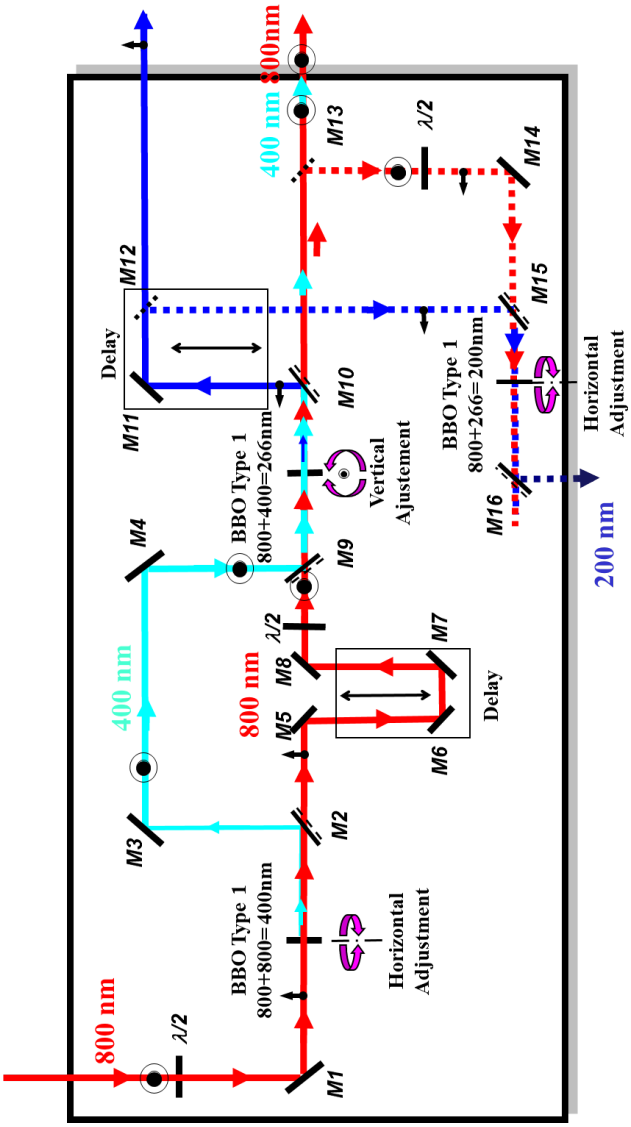

Figure 5.40: Generation of 266 and 400 nm^2

5.4.2.3 NOPA

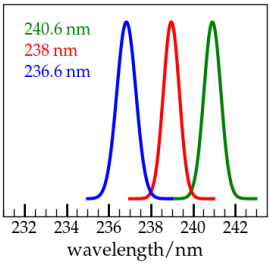

Figure 5.41: *Typical spectrum for NOPA output around 250 nm*

Having only 266 nm as a pump laser seriously limits the variety of molecules that can examined. Therefore a NOPA (Nonlinear Optic Parametric Amplifier) was set up by the LUCA laser team and is described briefly in the following. Two setups were used, one to produce wavelengths around 250 nm and one for wavelengths around 325 nm.

For generating wavelengths around 250 nm (see fig. 5.42), 800 nm enter a *HE-TOPAS-Prime Light convertion* (model TH8U1) to generate tunable wavelengths between 1100-1400 nm via parametric amplification of chirped signal produced by supercontinuum (white-light) generation. The ω_{Idler} (orange line), parallel polarized, is filtered from the vertically polarized ω_{signal} (light green line), which is then doubled by a LBO type I crystal (dark green line). By passing a semi-reflectant mirror ω_{signal} is eliminated from 2 ω_{signal}. $2\omega_{\text{signal}}$ is then filtered and focused in a BBO SFG type crystal. The 800 nm (red line), leaving the TOPAS light conversion, is filtered spatially, passes a delay line to adjust the temporal overlap between both lasers and is then doubled via a BBO type I crystal. The 400 nm pulse (light blue line) is reflected by a dichroic mirror (to eliminate the remaining 800 nm) and then also focused into the BBO SFG type crystal. There both lasers mix and light between 230 to 254 nm is generated. Possible spectra are shown in fig. 5.41.

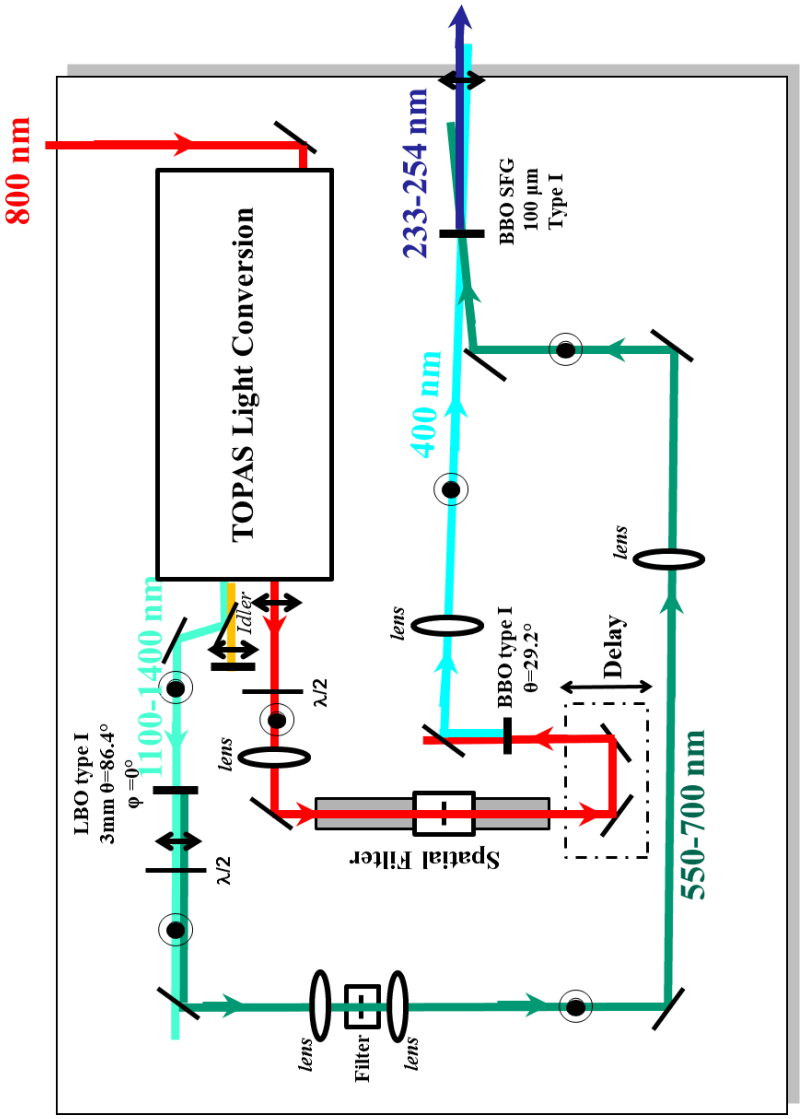

Figure 5.42: Setup for generating wavelengths around 250 nm

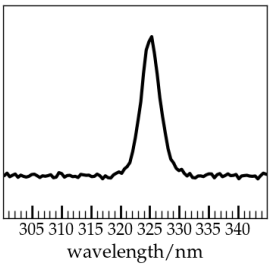

Figure 5.43: *Typical spectrum for NOPA output around 325 nm*

As for generating a pump laser around 325 nm, the setup shown in fig. 5.45 was used. The heart of this scheme is again the TOPAS Light conversion, but both ω_{Idler} (orange line) and 800 nm (red line) coming out of the TOPAS light conversion are blocked. ω_{signal} (light green line) is doubled using a LBO type I crystal, and the resulting $2\omega_{\text{signal}}$ (dark green line) is, after reflecting from a semi-reflective mirror to eliminate the remaining fundamental, doubled again by a BBO type I to 325-350 nm. It then passes a prism compressor to compress our pulse. A typical spectrum of the pump laser generated this way can be seen in fig. 5.43.

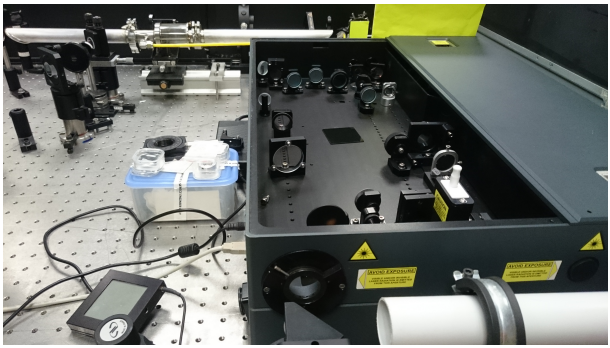

Figure 5.44: *Pictures of the NOPA (mode 250 nm)*

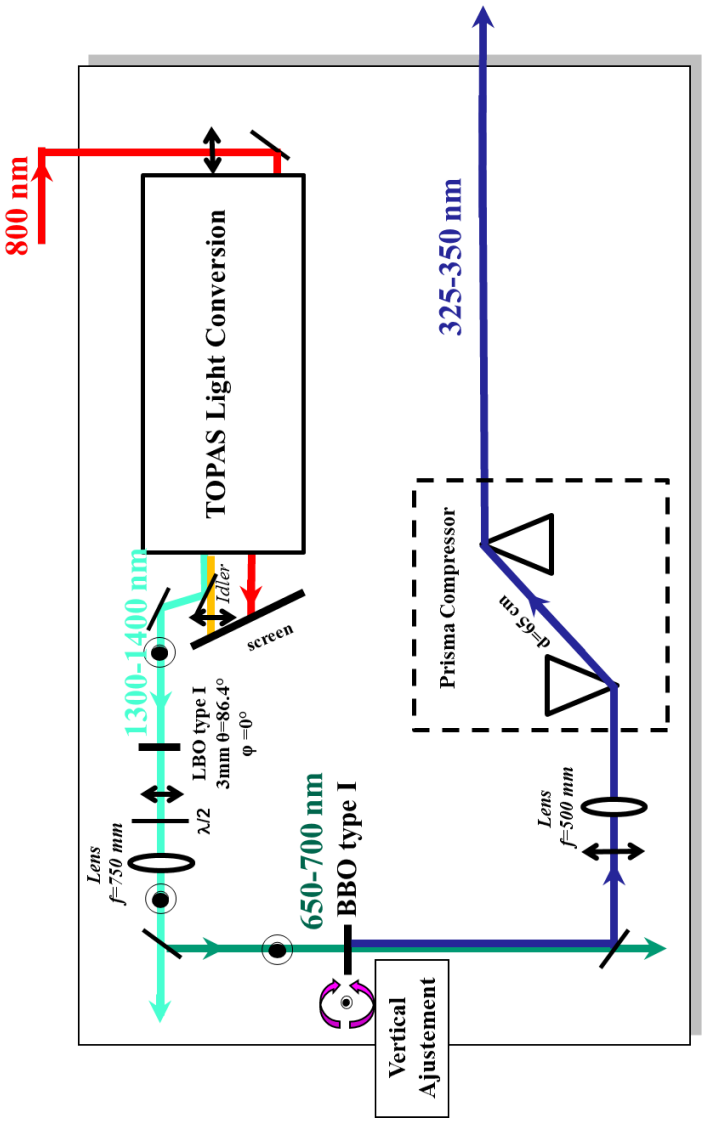

Figure 5.45: *NOPA setup for generating wavelengths around 325 nm*

5.4.2.4 Entry of the beams into the main chamber

The paths of the laser beams when in the 288/800 or 266/400 nm mode is displayed schematically in fig. 5.46 and as a 3D Design in fig. 5.47.

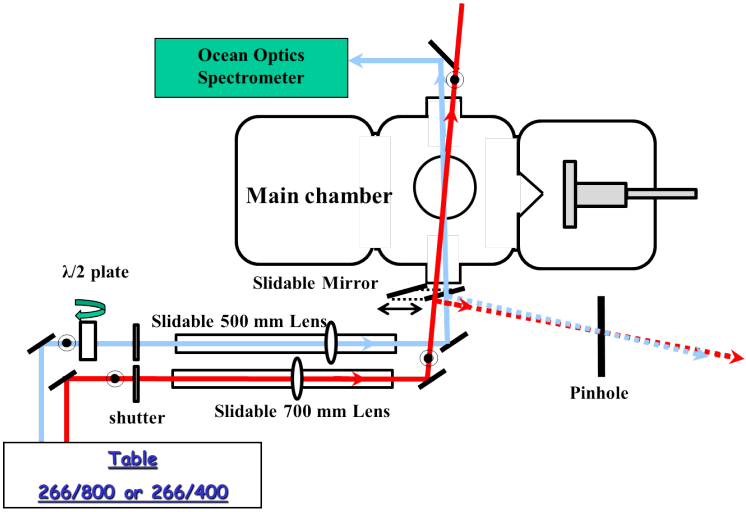

Figure 5.46: *When using the 266/800 nm or 266/400 nm setup: scheme of the entries/exits of the lasers*

As for the following text, 266 nm is designed as pump (blue line) and 800/400 nm as the probe laser (red line).

The pump laser passes a remote controlled λ/2 plate, allowing to change the polarization of the pump laser from horizontal to vertical. This is used to measure the rotational anisotropy. Both pump and probe then pass remote-controlled shutters, which permit automatic measurements of pump only/probe only signals during the time delay scans.

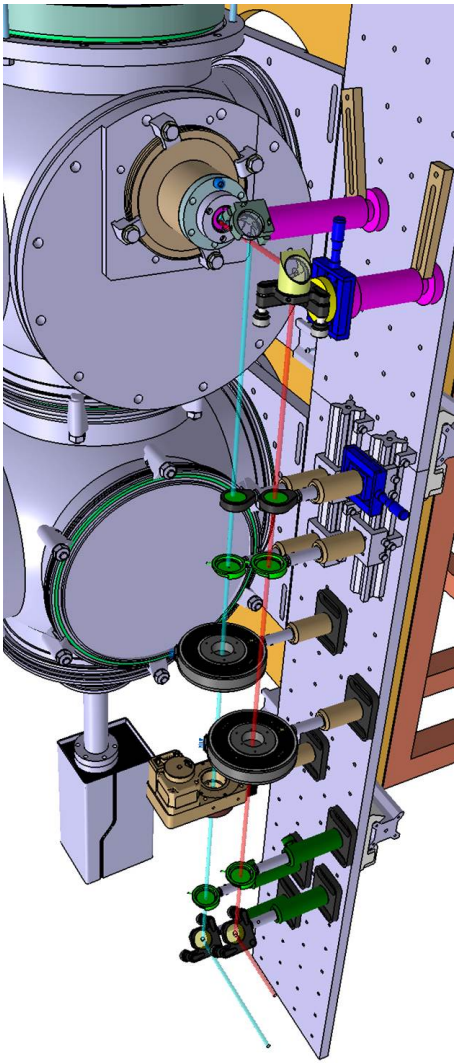

Figure 5.47: *When using the 266/800 nm or 266/400 nm setup: 3D design of the entry of the laser system*[1]

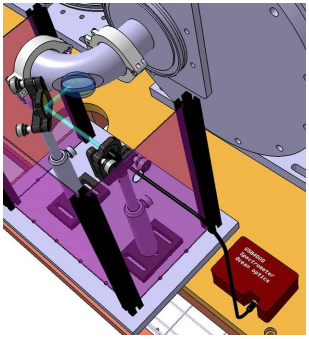

Figure 5.48: *Exit of the laser beams out of the main chamber and directed to the Ocean Optics Spectrometer*[1]

i Vertical adjustment was correct when by changing the Rep/Extr voltage ratio the background ion signal did not change its height. Horizontal adjustment was correct when the molecular beam was as fine as possible. This can also be obtained by adjusting the Rep/Extr voltage ratio.

The pump and the probe laser are focused by a 500 mm and a 700 mm lens respectively into the main chamber. Both lenses are fixed on slidable rails, allowing to adjust the size of the focal point and the fluency of the respective laser beam. To overlap both laser beams spatially a mirror was slid in front of the entry of the apparatus, reflecting both beams in direction of a pinhole. This pinhole was fixed in the distance corresponding to spatial overlap of both lasers with the molecular beam. When both beams passed the pinhole and were visible on a screen behind, the beams also overlapped in the apparatus when the mirror was removed. In practice, first one of the lasers was focused and overlapped with the molecular beam in the middle of the ions optic. Then the other laser was overlapped spatially using the pinhole. Lastly the first beam was defocalized or its power deattenuated, as to minimize pump only/probe only signal. On exiting the apparatus the pump laser is redirected via a mirror towards an *OceanOptics* spectrometer. (see fig. 5.48) This was used to routinely measure remotely the pump wavelengths during time delay scans.

With the NOPA as the pump laser, the changes in the setup are illustrated in fig. 5.49. The probe laser (800 nm, red line) now uses the path of the 266 nm pump laser in the 266/800(400) nm setup. The NOPA pump laser (green line) arrives from the other side, passes a fixed 500 mm lens, the remote controlled shutter and is reflected by a mirror into the main chamber. The procedure for aligning the lasers onto the molecular beam and their spatial overlap is the same as with 266 nm as a pump laser and 800 nm as probe. The pump laser spectrum is again measured using an Ocean Optics spectrometer.

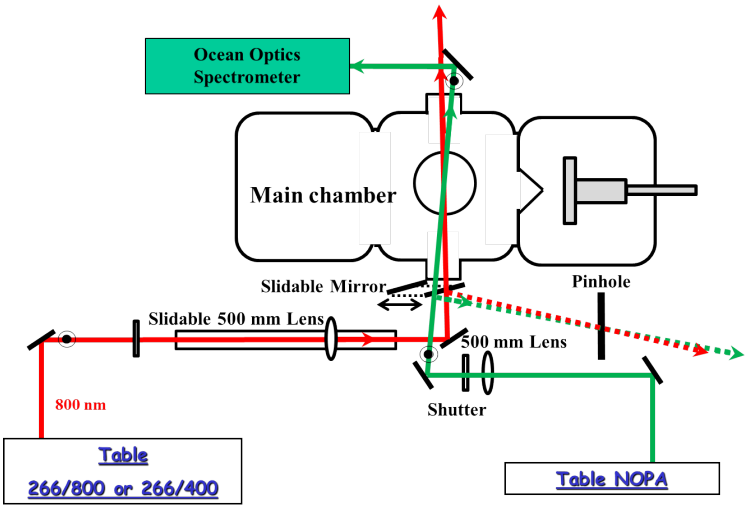

Figure 5.49: *When using the 800 nm/NOPA setup: scheme of the entries/exits of the lasers*

5.4.3 Data aquisition

The data was measured using *General Interface 3D*, a programm written in LabView by Lionel Poisson. It allows measuring photoelectron-, photoion- and mass spectra, while piloting the delay line, the remote controlled shutters and half-wave plate. It also allowed simultaneously measurement of several experimental parameters, like temperature, pressure and the spectra of both lasers.

5.5 Calibrations

5.5.1 PE-spectra and Ion images

The calibration of the photoelectron spectra is detailed in chapter 4.4.1, the calibration of chlorine ion imaging in chapter 4.4.2.

5.6 Mass spectra

The mass is correlated to the square of the arrival time:

$$m \sim t^2 \tag{5.1}$$

To calibrate a mass spectra, in theory only one reference point would be required, if the time of ionization (corresponding to the point of ionization) were known exactly. Since this is not the case, two (eq. 5.2) or for a better calibration three (eq. 5.3) calibration masses are used:

$$m = at^2 + b \tag{5.2}$$

$$m = at^2 + bt + c \tag{5.3}$$

with t the time of detection, m the molecular mass and a, b and c constants derived from the calibration masses. It is noteworthy that due to the procedure described in chap. 5.4.2.4, the ionization point in Saclay was very similar each time, and new calibrations were often unnecessary, in contrast to experiments done in Würzburg.

Part III

Results and Discussion

Chapter 6 Methylallyl radicals

Part of the research on the methyl allyl radicals described in this chapter has been published under the title "Femtosecond Dynamics of the 2-Methylally Radical: A Computational and Experimental Study" in the Journal of Chemical Physics [147].

6.1 State of knowledge

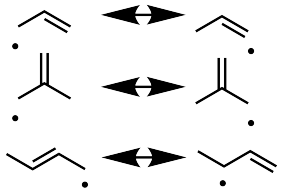

Figure 6.1: *Resonance structures of the allyl, 2-methylallyl and 1-methylallyl radical, from top to bottom*

The allyl radical, with its three carbon atoms, one double bond and radical center, is the smallest molecule to show the phenomena of resonance stabilization (see fig.6.1, top). Numerous studies were thus carried out on this benchmark system [148–157], including pump-probe experiments [154], Raman spectroscopy [152, 153] and several theoretical investigations [149–151]. The allyl radical is an important intermediate in combustion processes [158–160], and has also been postulated as a carrier of diffuse interstellar bands [161].

Its simplest derivatives are the methylallyl radicals, where a hydrogen atom has been replaced by a methyl group in either 1-position (1-methylallyl or 1-MA, see fig. 6.1, middle) or in 2-position (2-methylallyl radical or 2-MA, see fig. 6.1, bottom). These derivatives have also been identified as combustion intermediates [162], especially in the combustion chemistry of biofuels, which often contain branched or non-branched unsaturated fatty acid esters [163, 164].

The 2-MA radical can be considered to have the same symmetry as the allyl radical: bent with C_{2v} symmetry [148]. This is especially true at higher

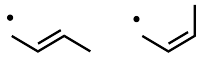

Figure 6.2: *(E)-1-MA and (Z)-1-MA*

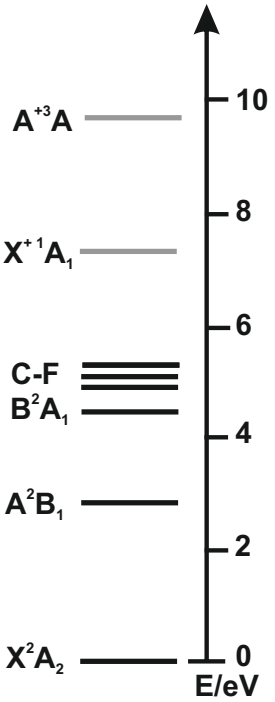

Figure 6.3: *Scheme of the excited states of the 2-MA radical*

temperatures, where the methyl group can rotate freely. Otherwise it has C_s symmetry. The 1-MA radical has two stereoisomers: (E)- and (Z)-1-MA (see fig. 6.2). *Ab initio* MO calculations showed that the (E)-isomer is 0.13-0.15 eV lower in energy than the (Z)-isomer [165]. Both methylallyl radicals were first observed 1968 by Callear et al. [157], who measured their absorption spectra in the gas phase, showing several transitions from the ground $^2A_2$ to higher lying $^2B_2$ states.

Looking at the excited states of the **2-MA radical** in detail (summarized in table 6.1 and fig. 6.3), it has been postulated that all states higher than the A^2B_1 possess Rydberg character [150].

Indeed, a 3s $B(1^2A_1)$ Rydberg state has been observed at 260.55 nm by Hudgens et al. [167] and by Chen et al. [166] using multiphoton ionization spectroscopy. Apart from calculating the seven lowest-lying states using MRCI, Chen et al. also observed the $C(1^2B_2) \leftarrow X(1^2A_1)$ and the $E(2^2A_2) \leftarrow X(1^2A_1)$-transitions. The 3s and 3p-Rydberg states of the 2-MA were examined in more detail using REMPI spectroscopy by Gasser et al. [168], who observed more than 30 vibrational levels of the 3s Rydberg state. They showed in another experiment [170] that after electronic excitation at 258 nm, an hydrogen atom is ejected isotropically, in agreement with statistical theories. More recently Herterich et al. [171] examined the dynamics of $B^2A_1$of the 2-MA using a tunable ps laser, showing a mono-exponential decay of 14 ps for the 0^0 origin and faster mono-exponential decays for the vibronic transitions of the B-state to the ground state via an internal conversion (IC).

state	energy/eV	wavelength/nm
$X(1^2A_2)$		
$A(1^2B_1)$ (theo) [166]	3.08	402.55
3s B $^2A_1$ Rydberg [166–168]	4.76	260.55
$C(1^2B_2)$ [166]	4.78	259.09
$E(2^2A_2)$ [166]	4.807	257.88
$D(2^2B_2)$/ $F(3^2B_2)$ [166]	5.08-5.39	243.9-229.9
N.A. [157,169]	5.16/5.15	240.2/240.6
$3p_z$ and $3p_x$ Rydberg [168]	5.17	239.5
N.A. [157]	5.20	238.5
N.A. [157]	5.25	236.0
$X^{+1}A_1$	7.88	157
$A^{+3}A$	9.85	126

Table 6.1: *Experimentally observed and previously calculated excited states of the 2-MA radical (N.A. = not attributed), the attribution will be partly revised during this chapter.*

As for the electronic states of the **1-MA radical** (summarized in table 6.2), Callear et al. [157] measured 8 quite broad and diffuse bands between 226 and 238 nm. Tarrant et al. postulated based on the vibrational spectrum of 1-MA and previously reported vibrational spectra of the 2-MA radical [172] that its excited state dynamics should differ significantly from its isomer 2-MA [173]. Gasser et al. [174] excited it with 415 nm in its lowest-excited state, and detected the loss of an hydrogen atom. This result was explained as a statistical non-radiative decay followed by an H-loss in the ground electronic state.

As for the adiabatic/vertical ionization energies of both methylallyl radicals, they were first determined using photoelectron spectroscopy by Schultz et al. [175] in 1984 (1-MA (7.49 ± 0.02 / 7.67 ± 0.02 eV) and 2-MA (7.90 ± 0.02 / 7.95 ± 0.02 eV)). Using threshold photoelectron spectroscopy the values for the adiabatic ionization energies were refined by our group to 7.48 ± 0.01 (1-E-methylallyl), 7.59 ± 0.01 (1-Z-methylallyl) and 7.88 ± 0.01 (2-methylallyl) [137].

state	energy/eV	wavelength/nm
A [174]	2.93eV	415 nm
N.A. [157]	5.21	237.8
N.A. [157]	5.25	236.0
N.A. [157]	5.28	234.9
N.A. [157]	5.32	233.2
IE(E) [137]	7.48	165.8
IE(Z) [137]	7.59	163.4

Table 6.2: *Experimentally observed bands of the 1-MA radical (N.A. = not attributed)*

To extend the already existing work on the excited-state dynamics of both 1-MA and 2-MA, we examined them using fs pump-probe spectroscopy, with mass spectra and photoelectron spectra as the detection methods. Both radicals were excited into the maxima of the absorption bands measured by Callear et al. [157], and for 2-MA the interpretation was supported by non-adiabatic dynamic on the fly calculations carried out by K. Issler, R. Mitrić and J. Petersen [147, 176].

6.2 Experimental

Both radicals were examined in Saclay using the source for liquids (see chapter 5.1 and 5.4). They were produced via pyrolysis from their nitrite precursors (see fig. 6.6), their synthesis is described in the appendix. Pyrolysis of 2-methyl-3-buten-1-nitrite produces only the 2-methylallyl radical (m/z=55, see fig. 6.4). Note that no precursor is visible neither with pyrolysis off nor on, which has already been observed in previous experiments on the methylallyl radicals [177].

Pyrolysis of (z)-3-Penten-1-yl-nitrite also shows m/z=30 (NO or formaldehyde) beside the dominant 1-MA-peak (m/z=55, fig. 6.5), but no precursor is visible without pyrolysis. The experimental conditions for both molecules are summarized in table 6.3.

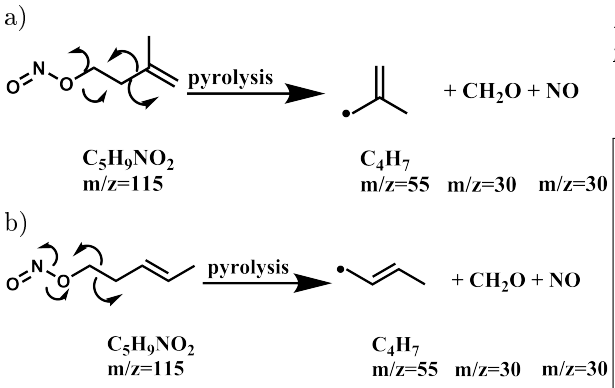

Figure 6.6: *Production via pyrolysis of a) 2-methyallyl radical from 2-methyl-3-buten-1-nitrite b) 1-methylallyl radical from (Z)-3-Penten-1-ylnitrite*

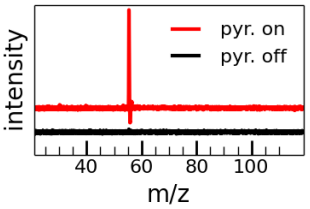

Figure 6.4: *Mass spectra at pump-probe conditions for 2-MA with pyrolysis off and Pyrolysis on*

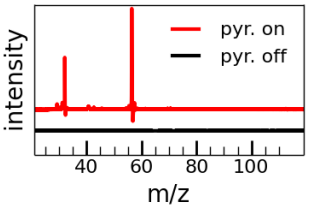

Figure 6.5: *Mass spectra at pump-probe conditions for 1-MA with pyrolysis off and Pyrolysis on*

i
The freshly synthesized precursors were clear blue liquids, after some time the color changed to green and finally to yellow, indicating deterioration of the precursor.

radical	pyrolysis power /W	carrier gas	backing pressure /bar, abs
1-MA	27	Ar	2.5
2-MA	33	He	1.5

Table 6.3: *Experimental conditions*

Both the 2-MA and 1-MA radical were excited to the maxima of their respective absorption spectra [157], for 2-MA at 240.6, 238.0 and 236.0 nm, for 1-MA at 238.0 nm. The pump laser was produced using the NOPA setup (see chapter 5.4.2.3), both molecules were probed using 800 nm multiphoton ionization. A pump-probe signal with 400 nm probe was not observed neither for the 2-MA nor for the 1-MA. The NOPA was focused slightly using a 700 mm lens; the 800 nm probe laser was focused using a 500 mm lens. The focal points were adjusted as to minimize pump only/probe only ionization.

During each scan the signal of pump only/probe only was recorded automatically and subtracted from the pump/probe signal, resulting in a baseline with zero intensity before the pump-probe signal. The slight distortion of the photoelectron images due to a slightly magnetized CF flange around the photoelectron flight tube was corrected by software before inversion. The photoelectron spectra were inverted using the pBasex algorithm implemented in the *Analyse*-program. The polarization of the pump in respect to the probe laser was varied during measurements between horizontal and parallel. No rotational anisotropy could be observed (see fig. 6.7 for 240.6 nm probe), the rotational mean of the obtained data was therefore analyzed. Decays were

fitted using the procedure described in chapter 13, all uncertainties plotted correspond to fitting uncertainties.

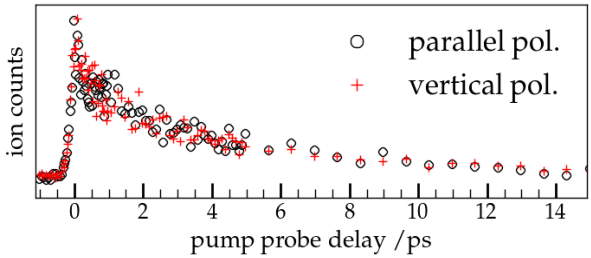

Figure 6.7: *Time-delay of the 2-MA mass spectra signal for 240.6 nm pump with parallel and perpendicular pump-probe laser polarizations*

6.3 2-Methylallyl

6.3.1 Experimental results

TOF spectra

All decays of the 2-methylallyl radical signal (m/z= 55) for the three different pump wavelengths can be fitted using a bi-exponential function, though for 236.0 and 240.6 nm the IRF has to be held fixed to obtain meaningful values (see fig. 6.9). The IRF reproduces well the rise-time. The S/N-ratio, however, is not very good, especially for 240.6 and 238.0 nm pump wavelengths the spectra are quite noisy. Excited with 240.6 and 238.0 nm 2-MA shows similar decays, meaning the short time-constant (τ_1 = 100 – 131 fs) and the long time-constant (τ_2 = 3.9–4.3 ps) have comparable values.

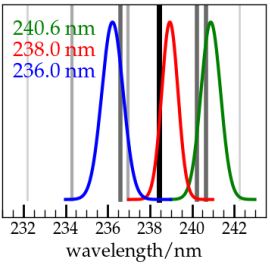

Figure 6.8: *Averaged spectra of the three pump wavelengths for the time-resolved mass spectra, the black, dark grey, light grey and silver lines correspond to very strong, strong, medium and weak lines in the absorption spectrum measured by Callear et al. [157]*

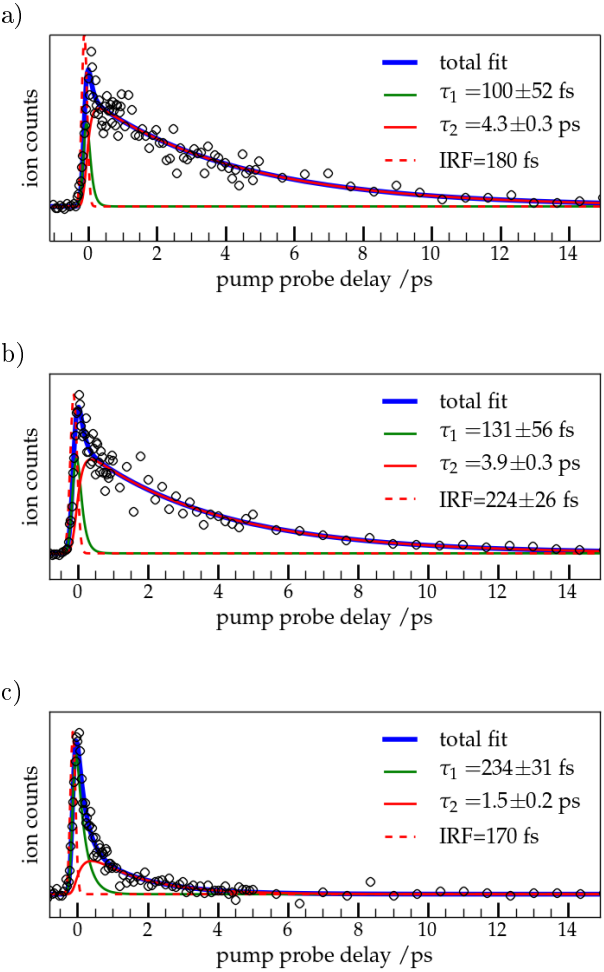

Figure 6.9: *Bi-exponential fits of the m/z=55 mass spectra decays for a) 240.6 nm pump b) 238.0 nm c) 236.0 nm pump laser wavelength. No sensible fit could be achieved with the IRF as a fit parameter, the IRF was therefore held constant to the value issued out of a mono-exponential fit.*

For 236.0 nm pump wavelength the decay is considerably shorter ($\tau_2 = 1.5$ ps). This is visible directly in the raw data, where at 4 ps the signal in fig. 6.9 c) has returned to the baseline, which is not the case for 240.6 and 238.0 nm pump wavelengths (fig. 6.9-a and -b).
The pump laser spectra for 240.6 and 238.0 nm overlap slightly on a strong band (see fig. 6.8), but overall all three spectra excite different bands. The black to silver lines in the background correspond to the position of the absorption bands measured by Callear et al. [157], correlated with their relative absorption strengths from very strong (black) to weak (silver).
In the time-resolved mass spectra only the methylallyl signal m/z=55 was observed, consequently photoelectron spectra should give more information about the underlying processes.

Photoelectron inversion

The photoelectron images were inverted using the pBasex algorithm implemented in the *Analyse*-program. Since the S/N ratio was quite low for all measurements, the maxEntropy method (see chapter 4.3) was administered on the series as well. This method was applied recently to velocity map imaging by B. Dick, and should perform better than pBasex for noisy data [109]. This method was applied in the images in addition to the pBasex algorithm. Both methods will be compared in the following.

The program MEVELER1.1.exe and F2Q.exe provided by B. Dick were used to invert the images with the maxEntropy method [178]. In fig. 6.10 the 2D-TRPES for maxEntropy (a) and pBasex (b) are plotted.

a)

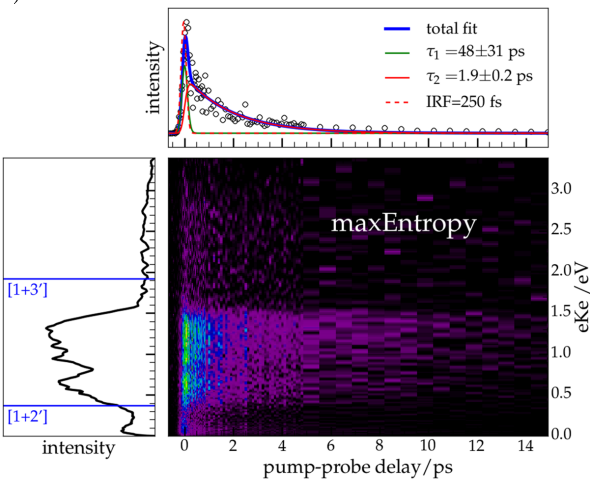

b)

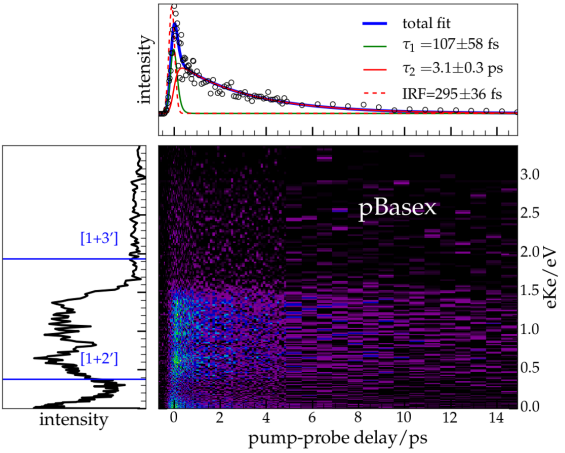

Figure 6.10: *Time-resolved photoelectron spectra for 240.6 nm pump wavelength reconstructed using a) the maxEntropy method and b) pBasex. In both figures the upper panel corresponds to the photoelectron signal summed over all energies, and the left panel corresponds to the photoelectron spectrum summed over all times. No fit was possible with the IRF as a fit parameter, the IRF was therefore held constant to the value issued out of a mono-exponential fit.*

The maxEntropy 2D map is smoother than pBasex 2D map, just as is the photoelectron spectrum summed over all times (left panel for both figures). Both photoelectron spectra show the same band structure: two large, overlapping bands between 1.55-0.8 eV and 0.8-0.25 eV.

The photoelectron spectra are comparable for both methods, but the maxEntropy method results in less noisy spectra. The time-depent photoelectron signal (upper panel for both figures), however,

shows a clear difference. With the pBasex method the observed time-constants are longer than for the maxEntropy method.

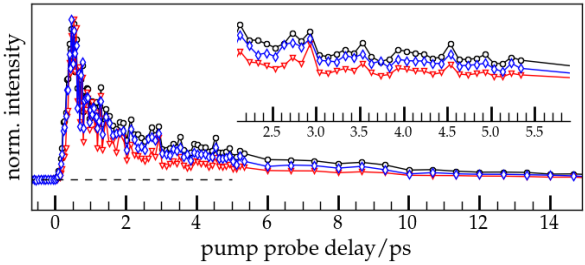

Figure 6.11: *Comparison of the total photoelectron decay for the inversion methods pBasex (—◇—) and maxEntropy (—▽—) to the direct integration (—○—) from the images*

In fig. 6.11 the normalized decays for the maxEntropy, pBasex and for the total photoelectron signal obtained directly from the images are compared. The pBasex algorithm recovers much better the time-dependence than the maxEntropy algorithm. It seems that the maxEntropy algorithm either over-estimates too intense data or underestimates noisy data.

Since a small difference between the pBasex algorithm and direct integration remains visible, the time-dependence of the total photoelectron signal will be analyzed.

Photoelectron images

a)

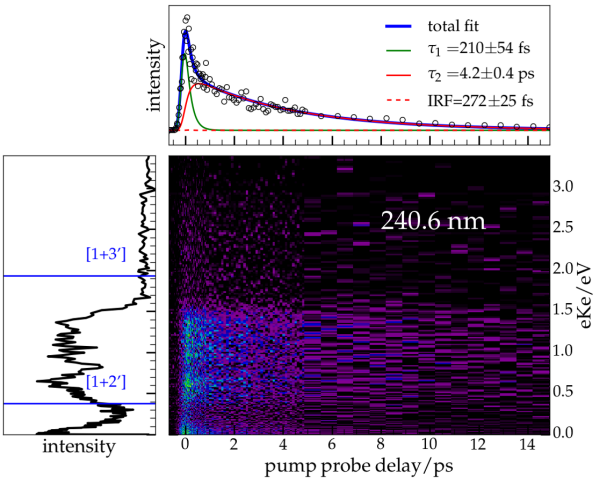

b)

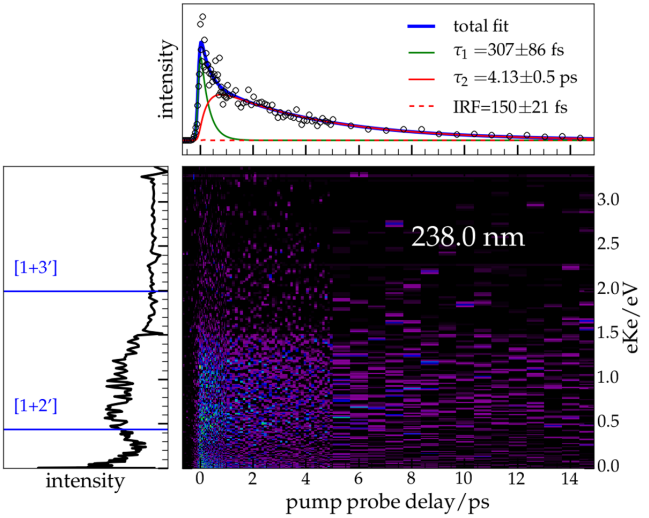

c)

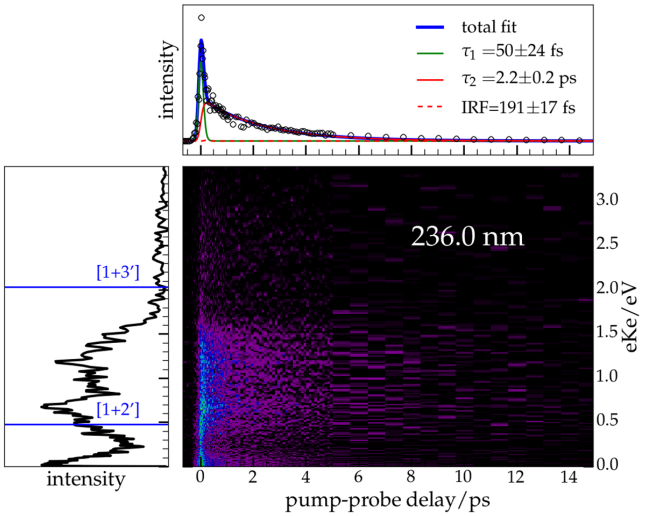

Figure 6.12: *TRPES of 2-methylallyl at a) 240.6 nm pump, b) 238.0 nm pump and c) 236.0 nm pump wavelength. The upper panel shows a bi-exponential fit of the total photoelectron signal decay. The side panel shows the photoelectron spectrum summed over all times, where the ionization limits [1+2'] and [1+3'] are drawn in as blue lines. The ionization limit of 2-MA is 7.88 eV [137].*

The time-resolved photoelectron spectra for 240.6 nm, 238.0 nm and 236.0 nm are shown in fig. 6.12 a), b) and c) respectively. The decay of the total photoelectron signal (upper panel) is well reproduced using a bi-exponential fit. The time-constants of the time-resolved photoelectron spectra for all three wavelengths are summarized in table 6.4.

The IRF is different from one TRPES experiment to another (just as it was the case for the time-resolved mass spectra). The reason for this is the same for both: the NOPA had to be newly

pump wavelength/nm	τ_1/fs	τ_2/ps	IRF/fs
240.6	210 ± 54	4.2 ± 0.4	272 ± 25
238.0	307 ± 86	4.13 ± 0.5	150 ± 21
236.0	50 ± 24	2.2 ± 0.2	191 ± 17

Table 6.4: *Overview of the time-constants for the total photoelectron signal decay for all three pump wavelengths*

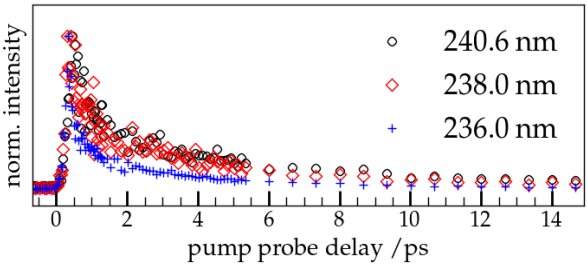

Figure 6.13: *Comparison of the decays of the total photoelectron intensity for the different wavelengths of the 2-MA*

aligned each day, thus the efficiency of the compression was also different from day-to-day. From 240.6 nm to 236.0 nm the first and the second time-constants shorten considerably, but 238.0 nm seems to fall out of line. The decay for 238.0 nm is, just as the mass spectra decay, similar to 240.6 nm.

This is best illustrated in fig. 6.13, where the decays at the different pump wavelengths are compared. The decays at 240.6 and 238.0 nm are nearly the same, whereas for 236.0 nm it is much shorter.

Their corresponding spectra of the pump laser, plotted as a Gaussian with the expected value (value at the maximum) and the FWHM averaged over the photoelectron spectra are the same as for the mass spectra (see fig. 6.14).

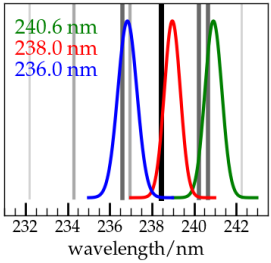

Figure 6.14: *Averaged spectra of the three pump wavelengths for the time-resolved photoelectron spectra, the black, dark grey, light grey and silver lines correspond to very strong, strong, medium and weak lines in the absorption spectrum measured by Callear et al.* [157]

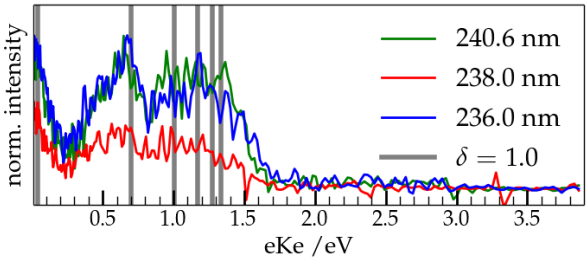

Figure 6.15: *Comparison of the photoelectron spectra for the three different pump wavelengths. The position of Rydberg bands (n=4,5,6,7,8,9) for a s-Rydberg state (δ=1.0) for 240.6 nm pump are shown in the background.*

The photoelectron spectra summed over all times (left panels in fig. 6.12) show the same two-band structure for all three pump wavelengths (see fig. 6.15), though not as clearly distinguishable for 238.0 nm due to the inferior S/N ratio. This indicates that the same excited state is pumped with all three wavelengths.
The attribution of the band structure is not evident at a first glance. They do not correspond to vibrations in the cation [137]. Ionizing in the first excited triplet state in the cation $A^+ {}^3A$ at 9.85 eV would correspond to 0.05 eV and 1.6 eV in a [1+3'] and [1+4'] process respectively. Only the electrons with low kinetic energy could correspond ionization in the first excited triplet state, the band structure can not be attributed to this state. Since the band structure neither originates from the initally excited state nor from the cation, it comes from intermediate resonances in the probe step.

These intermediate resonances are often Rydberg states, and the resulting spectra are called Rydberg fingerprint spectra. These Rydberg finger-

print spectra can help identify a molecule [179–181]. Rydberg states are diffuse states which derive from the electronic states of the hydrogen atom. Their position is determined according to [180]:

$$E_{electron} = E_{probe} - \frac{Ry}{(n-\delta)^2} \qquad (6.1)$$

where Ry is the Rydberg constant (13.606 eV), n the principal quantum number and δ the quantum defect. For s-orbitals the quantum defect is close to 1, for p-orbitals between 0.3-0.5, and smaller than 0.1 for d- and higher orbitals. Rydberg fingerprint spectra have been observed before in time-resolved photoelectron spectroscopy [182–184].

The observed band structure coincides with an s-Rydberg state (see fig. 6.15). Assuming a p-Rydberg state does not reproduce the peak at 0.7 eV in fig. 6.15. The resonant rydberg states are reached by exciting the initially excited state with two photons, therefore the initial state has either s-Rydberg or d-Rydberg character.

Comparison of photoelectron and mass decays

For the first time-constant no clear trend is visible, neither in the time-resolved photoelectron nor in the time-resolved mass spectra. They also don't coincide for different experiments using the same pump wavelength, like for example for 240.6 nm 100 ± 52 fs are obtained for τ_1 in the time-resolved mass spectra, but 210 ± 54 fs for the time-resolved photoelectron spectra. This is not surprising, since the first time-constant, fitted on only few points, is shorter than the IRF, and can therefore only be de-

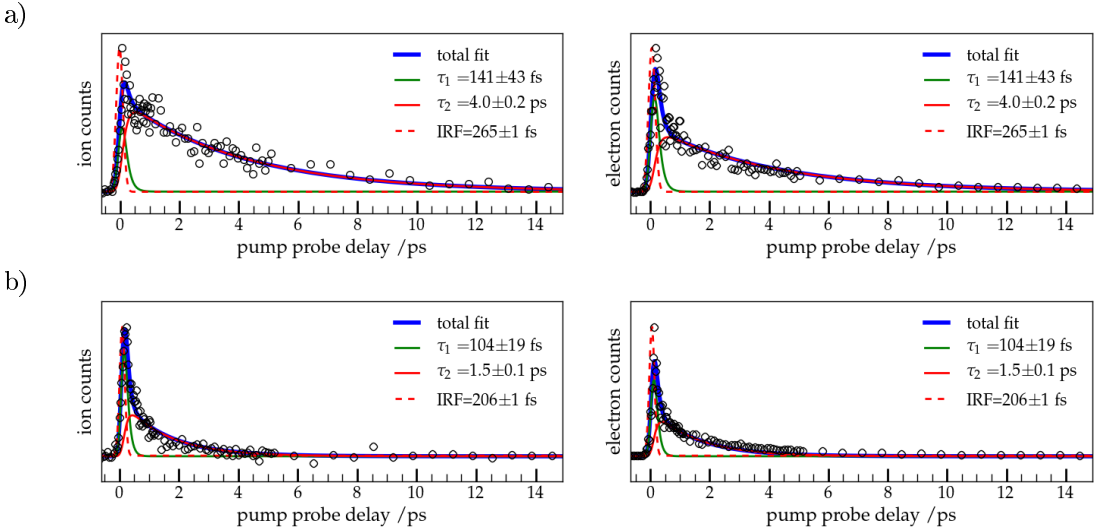

Figure 6.16: *Decays of mass/PE spectra fitted together for a) 240.6 nm pump and b) 236.0 nm pump. On the left is fitted the time-resolved mass spectra, on the right the time-resolved photoelectron signal.*

termined approximately. It is also highly dependant on the S/N-ratio. τ_2 is much more similar between photoelectron and mass spectra decays.

To confirm that this is not a real difference, the normalized photoelectron and mass spectra decay were fitted using the same fit constants (for 240.6 nm see fig. 6.16). Both decays are well reproduced with a bi-exponential decay using the same time-constants. For 240.6 nm $\tau_1 = 141 \pm 43$ fs and $\tau_2 = 4.0 \pm 0.2$ ps are obtained, for 236.0 nm the first time-constant $\tau_1 = 104 \pm 19$ fs is with very similar to 240.6 nm, but the second time-constant is with 1.5 ± 0.1 ps considerably shorter. Consequently we didn't observe a difference between time-resolved mass spectra and time-resolved photoelectron spectra, both can be well reproduced using the same fit constants.

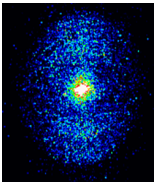

Figure 6.17: *Photoelectron image for 240.6 nm pump at around 300 fs*

Photoelectron anisotropy

The photoelectron images show a positive anisotropy (see in fig. 6.17). This is in agreement with an s-Rydberg orbital. Plotting the anisotropy as a 2D-map (P_0/P_2, as was done e.g. for the benzyl radical, see chapter 7.1) leads to many values which are not in [-1,2] - range (see fig. 6.18). This is due to the not good enough S/N ratio, which causes the anisotropy values to diverge. Therefore the average of the band from 1.1 to 1.5 eV was used to determine the anisotropy (sum(P_0)/sum(P_2)), plotted in fig. 6.19. Before the pump-pulse, the uncertainty is very high (no signal) and β is close to zero. After the pump-probe signal the photoelectron anisotropy is constant at +1.5, the uncertainties start to increase again with decreasing total signal intensity.

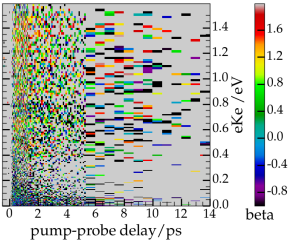

Figure 6.18: *Photoelectron anisotropy 2D map for 240.6 nm pump. The S/N ratio is not good enough to properly discern visually the positive anisotropy.*

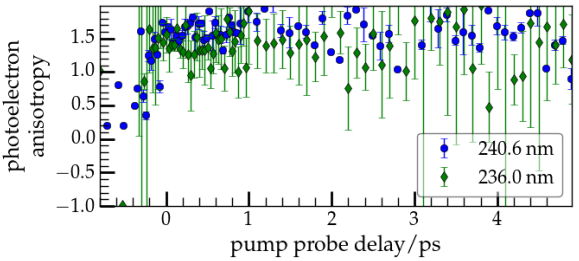

Figure 6.19: *Comparison of the photoelectron anisotropy parameter (β_2) for 240.6 nm pump and 236.0 nm pump, averaged between 1.1. and 1.5 eV. The positive anisotropy after the pump-probe pulse of about β_2 =1.5 can be seen, the uncertainties at earlier times are not displayed since they exceed the graph limits.*

To interpret the experimental results, the group of R. Mitrić performed non-adiabatic dynamic on the fly calculations.

6.3.2 Theoretical methods and results

All calculations on the 2-MA are the work of the group of R. Mitrić, specifically of R. Mitrić, J. Petersen, M. Wohlgemuth and K. Issler [147], who also discussed these calculations in detail in his bachelors thesis [176].

Electronic absorption spectrum

Before starting with dynamics calculations of a system, the different electronic states have to be calculated with computationally time-efficient methods and compared to a more exact one - to verify whether the character and energy of the relevant excited states is correctly reproduced with the computationally time-efficient method. Mitrić et al.

State	A^2A'' (D_1)	B^2A' (D_2)	$^2A''$ (D_3)	$^2A'$ (D_4)	$^2A'$ (D_5)
Character	πn	Ry-3s	Ry-3p_x	Ry-3p_z	Ry-3p_y
CAM-B3LYP/6-311++G	3.77 (0.01)	4.83 (0.0)	5.36 (0.23)	5.56 (0.02)	5.60 ($2 \cdot 10^{-4}$)
CAM-B3LYP/aug-cc-pVDQZ	3.74 (0.01)	4.83 (0.0)	5.21 (0.19)	5.49 (0.02)	5.56 (0.0)
ωB97XD/aug-cc-pVDQZ	3.66 (0.01)	4.90 (0.0)	5.21 (0.18)	5.51 (0.02)	5.62 (0.0)
EOM-CCSD	4.49 ($4 \cdot 10^{-3}$)	5.01 (0.0)	5.49 (0.20)	5.73 (0.02)	5.83 (0.0)
ADC(2)	4.04 (0.01)	5.27 (0.0)	5.60 (0.20)	5.94 (0.02)	6.06 (0.0)
exp	2.98 [174]	4.76 [167]	5.21 [169]		

Table 6.5: *Vertical excitation energies in eV (oscillator strengths in brackets for a one-photon excitation) for the five lowest excited states of the 2-methylallyl radical. C_s symmetry was used for characterization of the excited state, values are taken from ref. [147].*

compared the more exact methods *equation of motion coupled cluster with single and double excitation* (EOM-CCSD) [185,186] and *algebraic diagrammatic construction through second order* ADC(2) [187–189] to the more time-efficient *time-dependent density functional theory* (TDDFT) [190] method calculated with different basis sets and functionals. The excited states were calculated starting from the optimized ground state, for EOM-CCSD and ADC(2) this was the *coupled cluster with single and dou-*

ble excitation (CCSD) [191,192] optimized ground state using the turbomole [193] program package, for TDDFT the ground states were optimized using the respective functional and basis set with the Gaussian09 [194] program package. The functionals CAM-B3LYP [195], ωB97XD [196] with the basis set 6-311++G [197] and the larger basis set aug-cc-pVDQZ [198,199] were used in the TDDFT calculations.

The excited states for the different methods are compared in table 6.5. All different methods show the same energetic order of the excited states. The first excited state D_1 at 3.48-4.04 eV shows little oscillator strength and is attributed to the A band (2.98 eV, 415 nm) measured by Gasser et al. [174]. The second excited state is of Rydberg s-character, a dark state for a one-photon process, and has been measured by Gasser et al. [168]. D_3 is the brightest state of the first five excited states, and has p-Rydberg character. The other two higher-lying p-Rydberg states are dark. The D_3 is attributed to the band around 5.21 eV [157,166,168].

The electronic character and the relative ordering of the electronic states is comparable for all employed methods. In fig. 6.20 the simulated absorption spectrum with (CAM-B3LYP/6-311++G, blue line) is compared to the experimental spectra measured by Nakashima et al. [169] . The simulated spectrum is shifted slightly to higher energies than the experimental one, but the shape of the $D_3/D_4/D_5$ band is very well reproduced. Overall the simulated absorption spectrum and the experimental absorption spectrum are in excellent agreement.

Since CAM-B3LYP showed for both basis sets comparable results, and is in better agreement with

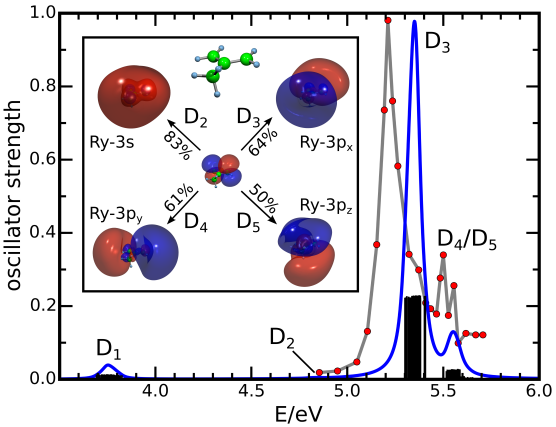

Figure 6.20: *Comparison of the simulated absorption spectrum (CAM-B3LYP/6-311++G, blue line) and the experimental absorption spectrum measured by Nakashima et al. [169] (red dots with gray line). The character of the electronic states with the orbital contributions of D_2-D_5 is shown in the inlet. The black, vertical lines correspond to the contributions of each individual geometry. Reproduced from [176] and provided by K. Issler.*

the EOM-CCSD and ADC(2) calculations than ωB97XD, CAM-B3LYP with the smaller basis set 6-311++G was used for the subsequent non-adiabatic dynamics on the fly calculations. Using the other methods EOM-CCSD and ADC(2) would have been too time-expensive.

Non-adiabatic dynamics on the fly

Non-adiabatic dynamics on the fly calculations used the *field-induced surface hopping* (FISH) [200] method, with TDDFT (CAM-B3LYP/G-31++G) to calculate the excited states. The FISH method was de-

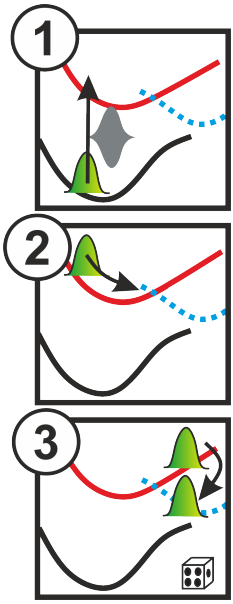

Figure 6.21: *Concept of the non-adiabatic dynamic calculations*

veloped 2009 by R. Mitrić, J. Petersen and V. Bonaćić-Koutecký and works as follows:

- Choose a suitable ensemble of geometries of the molecule for propagation. For the 2-MA 70 different geometries were propagated, sampled randomly from a propagated ground state trajectory.
- For each geometry a trajectory is obtained in the following way:
  - ▷ Interaction with laser (⊙ in fig. 6.21): The interaction of the geometry in the ground state (and in the excited state) with a laser is explicitly included, and described with field-induced surface hopping including non-adiabatic dynamics [200, 201]. The laser field has a certain energy, intensity and temporal length (in fig. 6.21 this is indicated as the gray pulse envelope). The energy of the laser corresponds to the excitation energy of a given electronic state, in fig. 6.21 from the ground state (black) to the excited state (red). This has the advantage - compared to just letting the dynamics start directly in the excited state - that different excited states for different starting geometries can be populated during the interaction with the laser field.
    For the 2-MA the electronic transition dipole moments and scalar non-adiabatic couplings were calculated as described in [202–204]; the laser field pulse envelope had a FWHM of 100 fs with an energy of 5.346 eV (corresponding to the computed $D_0 \rightarrow D_3$ transition) and a peak intensity of $1.4*10^{10}$ W/cm^2. The laser-field is treated classically. The electric dipole couplings (the interaction of the molecule with the laser field) were calculated by solving the time-dependent Schrödinger equation in the

manifold of the electronic ground and first five excited states.

- ▷ Evolution (② in fig. 6.21): The system evolves during and after the laser pulse. The dynamics of the nuclei are described using classical mechanics (Newtonian equations). The dynamics of the electron is described using quantum mechanics by solving the time-dependent Schrödinger equation in the manifold of the electronic ground state and the excited states. The potential surfaces are thus not calculated completely but 'on the fly', meaning only in the vicinity of the geometry defined by the dynamics of the nuclei (hence the name of the method).
  For 2-MA the newton equations were integrated using the velocity Verlet algorithm [205] with a time-step of 0.2 fs. The first five excited states were taken into account for the dynamic of the electron. The integration of the time-dependent Schrödinger equation employed the fourth order Runge Kutta procedure with a time step of $2x10^{-5}$ fs.
- ▷ 'Hopping' between excited states ((③ in fig. 6.21): At every time-step, a probability for a transition to another electronic state is calculated. If the electronic states are closer together (e.g. near a conical intersection) this probability will naturally be higher. The transition is treated statistically [206], symbolized by the dice in fig. 6.21. These surface-hopping probabilities are calculated from the time-dependent electronic state populations (which are in turn calculated by solving the time-dependent Schrödinger equation).

- Since hopping incorporates a statistical approach, drawing a meaningful conclusion implies interpretation of several trajectories; the evolution of the population in a given electronic state needs to be analyzed. For an easy comparison with experimental data the time-resolved photoelectron spectral intensities and anisotropies were calculated just as detailed in [207] for all trajectories. It should be noted that the probe laser in this simulation is approximated as a one-photon transition with E_{photon}=3*1.55=4.65 eV. The Dyson orbitals necessary for this method were calculated for the 2-MA using TDDFT (B3LYP [208–211] /6-311++G** [197]).

In fig. 6.22 the evolution of the electronic state populations for the 2-MA is shown. The gray shape in the background corresponds to the laser pulse envelope. The simulation starts at -100 fs, where all molecules are found in the ground state D_0 (black line). Then the laser starts to interact with the molecules, and we see a depopulation of the ground state and excitation into the D_3 (p-Rydberg) state (blue line). Via D_3 the two close-lying p-Rydberg states D_4 and D_5 are populated as well, the population transfer is observed. The D_3 and the higher-lying p-Rydberg states relax non-adiabatically in the first 100 fs, so already during the duration of the laser pulse in the D_2(s-Rydberg) state. This relaxation is almost complete at the end of the laser pulse.

From the D_2-state it relaxes more slowly via the D_1-state in the ground state. At the end of the 500 fs propagation time the population of the ground state is restored to a value of $\sim$60%, whereas at the time of maximum field intensity it was around 30%. When the molecules arrive in the ground state, they

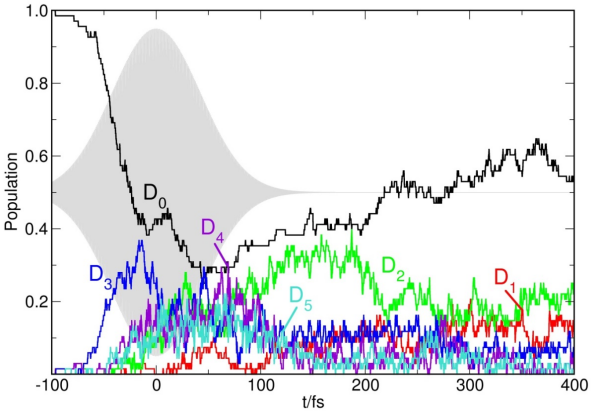

Figure 6.22: *Evolution of the electronic state populations of 2-MA after being excited by a laser pulse with an energy of 5.346 eV (corresponding to the computed* $D_0 \rightarrow D_3$ *transition). The laser pulse envelope is shown as gray in the background. Reproduced from [147] with the permission of AIP Publishing.*

are vibrationally highly excited. This leads in some cases to fragmentation (hydrogen loss or C-C bond breaking) as well as to cyclisation. The loss of an hydrogen after excitation into the p-Rydberg state has been observed by Gasser et al. [170], an observation which is reproduced in the simulations.

It should be noted that K. Issler calculated in his bachelor's thesis pure surface-hopping for 2-MA, meaning that all trajectories start directly in the excited state; the interaction between the molecule and the laser field is not taken into direct consideration. The trajectories were started from the D_3 and also from the D_5 state, and showed the same behavior. When the calculation is started in the D_5-state, a fast relaxation via the D_4 into the D_3 state is observed [176].

In summary, the following mechanism is postulated:

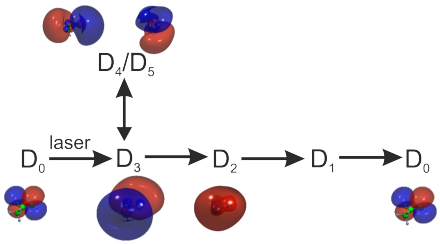

Figure 6.23: *Mechanism after excitation in the D_3 state. The orbital character of the excited states is shown as well.*

6.3.3 Comparison between experimental and theoretical results

To check whether the calculation capture the essential features of the experiment, the experimental observables were computed and compared. In the simulation a one-photon ionization (4.65 eV) was assumed, whereas in the experiment the ionization involves three 800 nm (3*1.55 eV) photons involving Rydberg resonances. The precise shape of the photoelectron spectra is therefore not comparable.

The total photoelectron signal depends, however, only on the total energy of the ionization process. The comparison of the FISH total photoelectron signal decay with the experimental decay for 236.0 nm is shown in fig. 6.24. The experimental curve (blue dots) is well reproduced by the simulated one (red lines). The decay in intensity corresponds to the relaxation from the D_2-state to the lower-lying D_1-state.

Another experimental observable is the photoelectron anisotropy, which gives an insight into the character of the involved electronic states. The calculated ionization mechanism (one-photon ionization) and the experimental ionization mechanism (three-photon ionization) are different. But the ionization from an s-Rydberg state passes via a p-Rydberg state to a s- or d-Rydberg state resonance, from which is finally ionized with the last photon. As can be seen in fig 4.12, an ionization from a 3p-Rydberg orbital in the range 1.1 -1.5 eV leads to a high beta parameter. The experimental probe scheme may reasonably be the same for higher quantum numbers. It can therefore be regarded as a one-photon ionization from a p-Rydberg state, and the computed (red line) and experimental (blue dots) anisotropy values (β_2) are compared in fig. 6.25 for a pump wavelength of 236.0 nm.
The simulated beta is positive and with a value of 1.8 very close to 2, reflecting the 3s Rydberg orbital character of D_2, which is populated very quickly

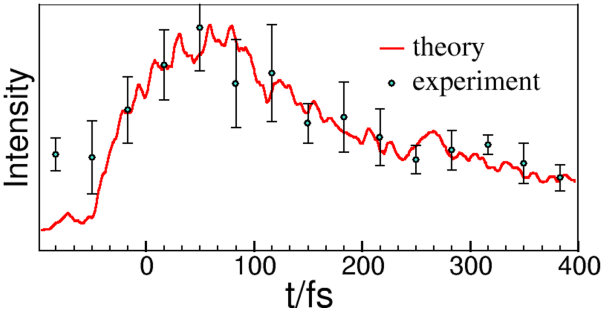

Figure 6.24: *Comparison of the time-resolved experimental (for 236.0 nm) and the simulated normalized photoelectron intensities. The simulated intensities have been averaged over a period of 33 fs. Reproduced from [147] with the permission of AIP Publishing.*

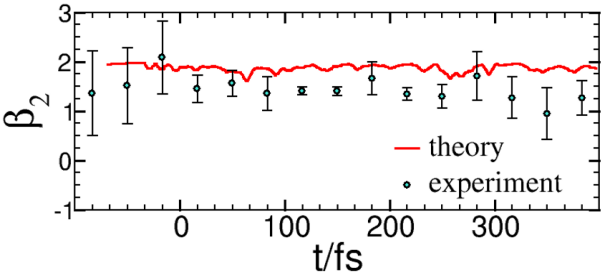

Figure 6.25: *Comparison of the time-resolved experimental (for 236.0 nm) and the simulated anisotropy parameter, averaged between 1.1 and 1.5 eV. The simulated anisotropy parameters have been averaged over a period of 33 fs. Reproduced from [147] with the permission of AIP Publishing.*

from the initially excited D_3 state with 3p character. The experimental points before t=0 have a large uncertainty (low total signal) and should not be considered. This large uncertainty is even better visible in fig. 6.19, where more points before t=0 is plotted. After t=0 the experimental uncertainty becomes small, and β_2 is highly positive, around 1.5. This is also the case when excited with 240.6 nm, showing that in both cases we pass via the same excited states.

6.3.4 Conclusion for 2-MA

The computed deactivation mechanism is in excellent agreement with the observed experimental data. In the photoelectron spectrum an s-Rydberg fingerprint spectrum is observed, moreover, the highly positive anisotropy β_2, characteristic for a s-Rydberg orbital, is well reproduced by the simulation. The first of the two experimental observed time-constants is attributed to the relaxation of three p-Rydberg

states (D_3, D_4, D_5) to the D_2-state on the order of 50-150 fs, whereas the second observed time-constant is attributed to the relaxation of the 3s Rydberg state D_2 towards the first excited state A^2B_1 of 2-methyl allyl radical, to finally arrive in the ground state.

This relaxation from the D_2 to D_1-state accelerates when more energy is deposited into the initial excited state (from 240.6 nm to 236.0 nm), the initial wave-packet can reach faster the conical intersection to the D_1-state.

6.4 1-Methylallyl - results and Discussion

Whereas the excited states of the 2-MA show an interesting dynamic, this was - just as postulated by Tarrant et al. - different for 1-MA [173]. The evolution of the mass spectra signal of 1-MA (m/z=55) is displayed in fig. 6.26.

The observed signal is Gaussian-shaped and can be reproduced using a FWHM of 242 ± 8 fs. This autocorrelation value is not surprising and similar values (considering the experimental uncertainty) were obtained with the phenyl radical (see chapter 11.3), measured previously to the 1-MA using the same setup. The NO/CH_2O at m/z=30 also showed only autocorrelation, but the signal was a lot weaker and noisier (289 ± 19 fs). No shift between those two signals was observed.

The TRPES displayed in fig. 6.27 shows only one peak at 0.431 eV (left graph). The temporal evolution of this peak, as displayed in the upper graph in fig. 6.27, shows only autocorrelation with a FWHM of 282 ± 14 fs, in agreement with the time-resolved mass spectra. Direct ionization into the cationic ground state with 238.0 nm gives an ion-

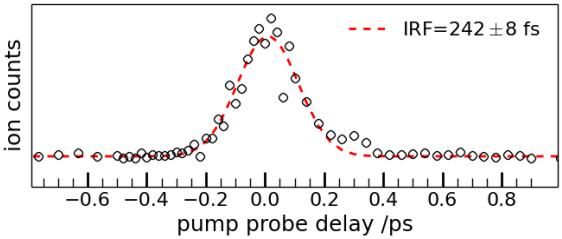

Figure 6.26: *Dynamics of the mass spectra signal of the 1-MA (m/z=55)*

ization limit of 0.837 eV and 0.727 eV for the (E)- and (Z)-1-MA respectively. No peak is observed in that region. Exciting a vibration in the cation is unlikely, since then cationic ground state should also be visible in the photoelectron spectrum. Possibly we also excite a Rydberg-state, but the dynamic is too fast for us to resolve.

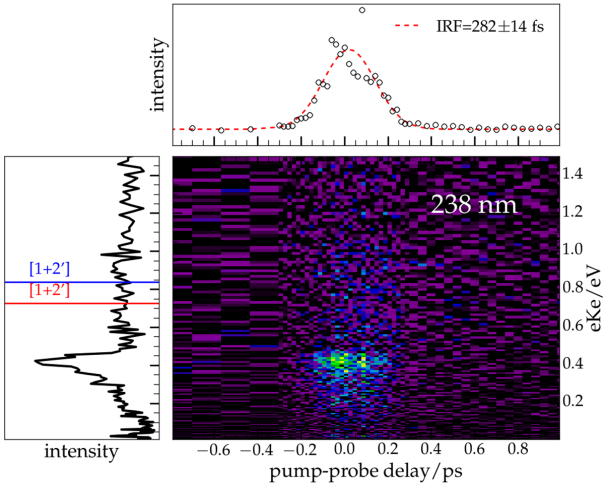

Figure 6.27: *TRPES of the 1-MA, the blue ionization limits correspond to the ionization energy of (E)-1-MA (IE=7.48 eV), the red ionization limits to the ionization energy of (Z)-1-MA (IE=7.59 eV).*

Chapter 7 C_7H_7 isomers

7.1 Benzyl radical

The work on the benzyl radical has been published in the Journal Physical Chemistry Chemical Physics under the title "Femtosecond Time-Resolved Photoelectron Spectroscopy of the Benzyl Radical" [212].

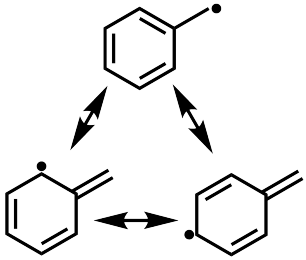

Figure 7.1: *Resonance structures of the benzyl radical*

7.1.1 State of knowledge

The benzyl radical is the simplest radical stabilized by an aromatic system (see fig. 7.1). This combustion intermediate can be formed by simple hydrogen abstraction from toluene, an important component in fuels with anti-knock properties. Other possible toluene combustion products are the tolyl radical (hydrogen abstraction from the ring) and the phenyl radical (methyl abstraction). The benzyl radical is, however, the dominant product compared to the other two [213–215]. As the main reaction product of isoprene with C_2 [216], both omnipresent in flames and in the interstellar medium, it plays a key role in combustion processes [217–219].

The benzyl radical is stabilized by the aromatic ring via delocalizion, as shown by the experimentally measured spin density of only 0.7-0.8 on the methylene group. The remaining spin density is found on the ortho and para positions of the ring. Consequently the benzyl radical is planar and has C_{2v} -symmetry [220, 221]. The aromatic resonance stability is also reflected in its heat of formation ($\Delta_f H_{298\,K} = 49.7 \pm 0.6$ kcal/mol [222]), which is about 15 kcal/mol lower than for its isomer tropyl ($\Delta_f H_{298\,K} = 64.7$ kcal/mol [223]).

State(radical)	Energy/eV	Excitation wavelength/nm
1^2B_2	ground state	
1^2A_2 [224–226]	2.76	450
2^2B_2 [227,228]	2.78	445
(2^2A_2) [228,229]	4.00	310
(3^2B_2) [230–232]	4.76	260
(4^2B_2) [229,232]	4.86	255
Rydberg [229]	5.4	229
$X^{+1}A_1$ [233]	7.252	
$a^{+3}B_2$ [233]	9.180	
$A^{+1}B_2$ [233]	9.62	
$b^{+3}A_1$ [233,234]	9.69	
$B^{+1}A_2$	11.2	

Table 7.1: *Overview of the different electronic states of the benzyl radical and its cation as determined previously in the literature, the states in brackets are reassigned during this chapter.*

Several electronic states of the radical and its cation have been identified and characterized (summarized in table 7.1 and fig. 7.2). The vibronic spectrum of the radical [235] and of the cation [236] in their electronic ground states are in excellent agreement with planar structures calculated with B3LYP. The benzyl radical fluoresces between 400 and 600 nm, showing a structured spectrum, which was attributed after a lot of discussion [237] to vibrations of the 1^2A_2-state [224–226]. Rotational constants of the $6a_1^0$ and $6b_1^0$ vibronic bands from this state fit well with an assymetric top model [227]. The 1^2A_2-state is also strongly coupled to the 2^2B_2-state [238], both are nearly isoenergetic. Two stretching modes are majorly responsible for this coupling: an in-plane skeletal deformation and an in-plane skeletal plus

CCH bending motion, both b_1-symmetric [239,240].

The benzyl radical absorbs strongly between 310 and 220 nm, showing several peaks with a maximum at 255 nm. This was attributed to the D-state, to which the 4^2B_2-symmetry was assigned [229].

This D-state decays after excitation with 255 nm in 150 ± 30 fs [241], examined using time resolved mass spectrometry in an [255+280 nm] excitation scheme. The 4^2B_2-state can also dissociate and eliminate an H-atom, which was examined with high-n Rydberg atom time-of-flight (HRTOF) spectroscopy. The nearly isotropic $P(E_T)$ distributions indicate the production of fulvenallene, most likely via an unimolecular decomposition in the ground state after internal conversion [242].

The adiabatic and vertical ionization energy coincide for this molecule and were first determined 1976 by Koenig et al. [243] using photoelectron spectroscopy (7.43 ± 0.06 eV). This value was corrected two years later by Houle and Beauchamp [244] (7.20 ± 0.02 eV) and refined further by Eiden et al. [245] (7.2491 ± 0.0006 eV) using threshold photoionization. In 2015, using threshold photoelectron spectroscopy, Savee et al. confirmed not only the adiabatic ionization energy (7.252(2) eV), but they also observed transition to at least three electronic states of the benzylium cation [233].

Despite its importance as a combustion intermediate, the dynamics of the benzyl radical are still not well understood. Therefore we examined it using femtosecond pump-probe mass and photoelectron spectroscopy with 265 nm as the pump and 798/398 nm as the probe pulse. These experiments were complemented with non-adiabatic dynamic on the fly calculations, leading to a reassignement of the electronic states.

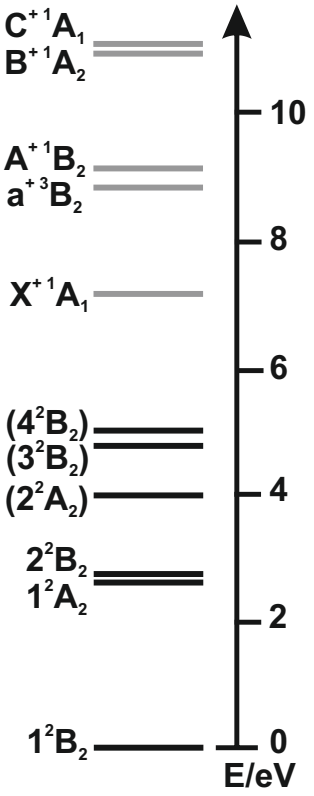

Figure 7.2: *Energy diagramm of the different electronic states of the benzyl radical as determined in the literature, states in brackets are reassigned later in this chapter.*

7.1.2 Experimental conditions and data treatment

The fs-setup in Saclay was described previously in section 5.4. The benzyl radical was produced via pyrolysis (see chapter 5.2) using the source for liquids with low boiling points (see chapter 5.1) and argon at 2 bar absolute pressure as a carrier gas. Phenylethylnitrite was the precursor of the benzyl radical, the synthesis is described in the appendix 12. Under pyrolysis the aliphatic C-C bond and the O-N bond in phenylethylnitrite are cleaved, producing the benzyl radical, NO and formaldehyde (see fig. 7.3).

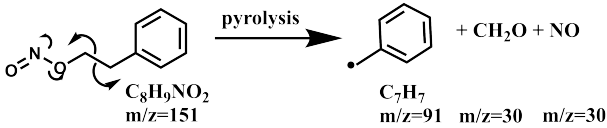

Figure 7.3: *Production of the benzyl radical via pyrolysis of phenylethylnitrite*

265/798 nm and 265/398 nm were used as the wavelengths, produced as described in section 5.4.2.1. The laser power and focalization were adjusted to minimize the signal of pump only/probe only and to maximize pump-probe signal. Decays were averaged over at least four scans. During each scan both the decays for the parallel pump/probe laser polarizations and perpendicular pump/probe laser polarizations were measured, the pump laser was turned via a $\lambda/2$-plate and the probe laser was polarized horizontally with respect to the optical table. No rotational anisotropy was observed, as can be seen exemplary in fig. 7.4 for the photoelectron yield with 265/798 nm.

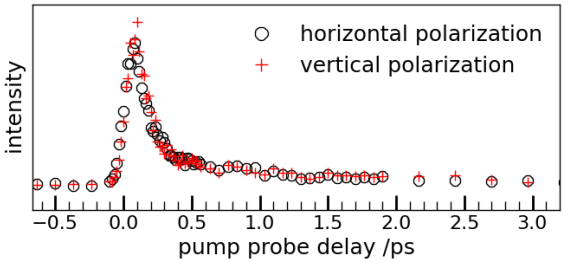

Figure 7.4: *Comparison of the total photoelectron decay with 265 nm pump and 798 nm probe for different polarizations of the pump wavelength with respect to the probe wavelength.*

Consequently the rotational mean are analyzed in the following. The signals pump only/probe only were measured at random during the scan using the remote shutters. These signals were removed from the mass spectra/PE decays after data treatment, leading to a zero baseline. The photoelectron spectra were inverted using the pBasex algorithm using P_0P_2 Legendre polynomial as implemented in the *Analyse*-program, the contribution of higher polynomials was negligible. The decays were fitted using the fit program whose procedure is described in chapter 13. The uncertainties shown in the figures correspond to the fit uncertainties and not to experimental uncertainties, which have to be estimated higher.

7.1.3 Experimental results

Pyrolysis conditions

As can be seen in fig. 7.5 the radical is produced cleanly by pyrolysis. All measured peaks are sharp, indicating that no dissociative photoionization of the precursor occurs.

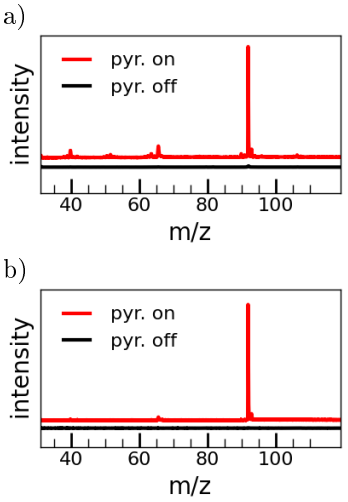

Figure 7.5: *Mass spectra with pyrolysis on and pyrolysis off a) with 265/798 nm b) 265/398 nm at pump-probe conditions*

With 798 nm (fig. 7.5-a) more side-products are visible than with 398 nm probe. The mass m/z= 65 corresponds to C_5H_5 (cyclopentadienyl), a typical combustion product of aromatic compounds [9], whereas the mass m/z =40 corresponds C_3H_4, another combustion side-product (see fig. 7.5-a).

The contrast between pyrolysis on and off is excellent, so time-resolved photoelectron spectra were recorded in addition to time-resolved mass spectra.

Time-resolved mass spectra

In fig. 7.6 the temporal evolution of the benzyl signal m/z=91 (∘) and the m/z=65 (◊) for 265 nm pump and 798 nm probe (a) and 398 nm probe (b) are displayed. The decay of the benzyl signal with 798 nm probe is well reproduced using a bi-exponential decay ($\tau_1 = 83 \pm 8$ fs, $\tau_2 = 1.68 \pm 0.16$ ps) with an IRF of 120 ± 5 fs.

The decay of cyclopentadienyl is quite different from the benzyl decay and can be adjusted reasonably well with a mono-exponential decay ($\tau_1 = 1.65 \pm 0.12$ ps, IRF $= 88 \pm 17$ fs). The cyclopentadienyl radical signal is about 25 times weaker than the benzyl radical signal and the S/N ratio is largely inferior, which is the most probable source of the different IRF. More photons are involved in ionizing cyclopentadienyl (IE=8.41 [246], at least [1+3']), which also leads to a shorter IRF. Consequently its time-decay was not investigated in detail. The time zero of the pump-probe signal is the same in both cases, indicating that this mass is a pyrolysis product and not a photodissociation product of the benzyl radical.

With 398 nm probe no second time-constant is visible, the decay can be well reproduced using a mono-exponential decay ($\tau_1 = 87 \pm 5$ fs) with an

IRF of 128±5 fs. The slightly longer IRF is not surprising, since the 398 nm probe pulse is produced by doubling the fundamental output of the Ti:Saphire laser, which leads to a slight temporal extension. The cyclopentadienyl radical signal shows again a mono-exponential decay (τ_1 = 499 ± 55 fs, IRF = 103±26 fs), 13 times weaker than the benzyl radical signal, extremely noisy and also shorter. Again the time zero of both the benzyl and the m/z=65 signal is the same, indicating that this mass is produced via pyrolysis.

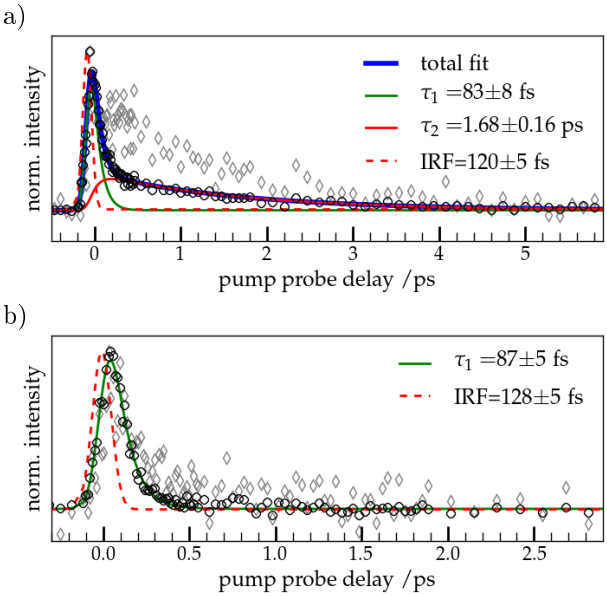

Figure 7.6: *Decay of the mass spectrum benzyl signal for a) 265 nm pump / 798 nm probe b) 265 nm pump / 398 nm probe. ○ corresponds to the benzyl signal, ◊ to the m/z=65 signal. Both signals were normalized.*

Time-resolved photoelectron spectra

Since mainly the benzyl radical in the mass spectra is observed (benyl radical: cyclopentadienyl radical=25:1 for 798 nm probe; 13:1 for 398 nm probe), photoelectron spectra at both probe wavelengths were measured. The TRPES with 798 nm probe wavelength is plotted in fig. 7.7. The photoelectron spectrum consists of a broad band, with signal stemming up to a [1+4']-process. Several peaks are visible, with the most prominent at 0.3 eV issued out of a [1+2']-process. These peaks do nei-

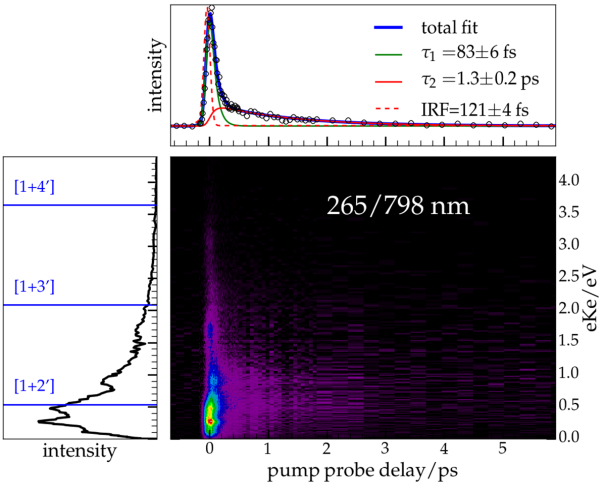

Figure 7.7: *TRPES of the benzyl radical for 265 nm pump and 798 nm probe. The decay plotted in the upper graph corresponds to the decay of the total photoelectron signal, in the left graph the photoelectron spectrum summed over all times is displayed. The blue lines in the left graph correspond to the ionization limits (IE=7.252 eV [233]).*

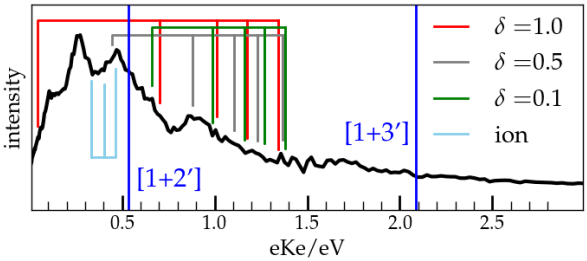

Figure 7.8: *Possible position of the Rydberg states and vibrations in the cation $X^+\ ^1A_1$-state drawn in the summed photoelectron spectrum of 265 nm pump/798 nm probe.*

ther correspond to a Rydberg fingerprint spectrum (see section 6.3.1 for details on Rydberg fingerprint spectra) nor to vibrations in the cation or excited states of the cation (see fig. 7.8).

A p-Rydberg fingerprint spectrum (gray lines, δ=0.5) coincides with the peaks at 0.45 and 0.8 eV, but assigning a Rydberg fingerprint spectrum based on two peaks is arbitrary. As for vibrations in the cationic ground state $X^+\ ^1A_1$ (light blue lines) only one peak coincides, the peak at 0.3 eV is again not reproduced. It also does not correspond to an excited cationic state. The known excited cationic state are the $a^+\ ^3B_2$-(9.18 eV) and the $A^+\ ^1B_2$ (9.62 eV)-state [233], ionizable in a [1+3']-and [1+4']-process with a electron kinetic energy (eKe) of 0.16 eV and 1.27 eV respectively. No prominent bands are observed in that region.

In the upper panel the whole photoelectron signal is reproduced with a bi-exponential decay ($\tau_1 = 83 \pm 6$ fs, $\tau_2 = 1.3 \pm 0.2$ ps) with an IRF of 121 ± 4 fs, in good agreement with the time-constants observed in the mass spectra. The rise-time and decay

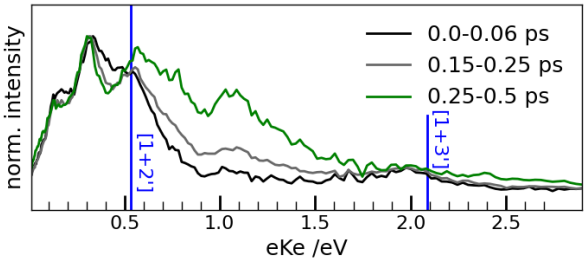

Figure 7.9: *Selected traces of the time-resolved photoelectron spectrum with 265 nm pump and 798 nm probe (see fig. 7.7).*

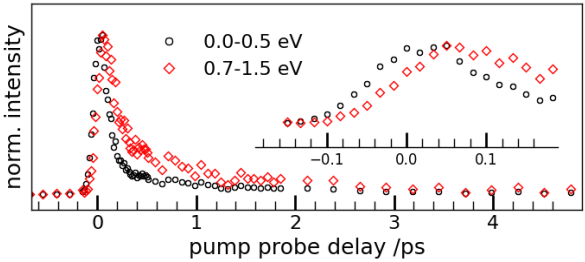

Figure 7.10: *Comparison of the decays for different energy ranges for 265 nm pump and 798 nm probe pulse of the TRPES*

of the different bands in the photoelectron spectrum (left panel in fig. 7.7) is not the same. In fig. 7.9 the photoelectron spectrum summed from 0-60 fs shows nearly no intensity at eKe≈1.0 eV, only a band centered at 0.3 eV and a less intense band centered at 1.8 eV are visible. At late times between 250 and 500 fs a new band centered at eKe≈1.0 eV arises, which at late times possesses nearly the same relative intensity as the band at 0.3 eV.

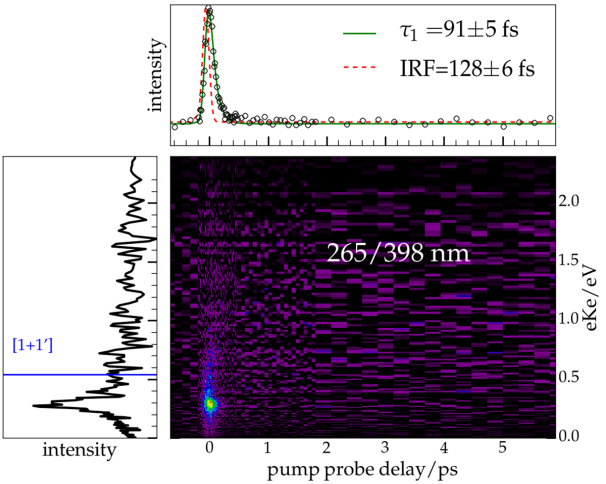

Figure 7.11: *TRPES of the benzyl radical for 265 nm pump and 398 nm probe. The decay plotted in the upper graph corresponds to the decay of the total photoelectron signal, in the left graph the photoelectron spectrum summed over all times is displayed. The blue lines in the left graph correspond to the ionization limits, with IE=7.252 eV [233].*

The decays of the band centered at 0.3 eV and of the band centered at 1.0 eV show different temporal evolutions (see fig. 7.10). The band centered at 1.0 eV is shifted towards later times, and the band centered at 0.3 eV decreases more rapidly than the higher energetic band.

Both time-components cannot be separated cleanly since the bands overlap, therefore the bi-exponential decay of the whole photoelectron spectrum is used for further discussion. The total photoelectron decay with 798 nm probe is well reproduced using a bi-exponential decay ($\tau_1 = 83 \pm 6$ fs, $\tau_2 = 1.3 \pm 0.2$ ps) with an IRF of 121 ± 4 fs. The first time-constant is identical with the one observed in the mass spectra,

but the second time-constant is slightly shorter in the photoelectron spectra. The first time-constant is predominantely attributed to the band centered at 0.3 eV, whereas the second time-constant corresponds to the growth of the second component centered at 1.0 eV.

The TRPES with 398 nm probe (see fig. 7.11) is quite different. Here only one peak at eKe=0.3 eV is visible, corresponding to a [1+1']-process. The difference to the [1+1'] ionization limit 0.262 eV (2113 cm^{-1}) does not correspond to any vibration in the cation. No signal from higher-order processes is visible. The decay of this peak is well reproduced with a mono-exponential fit (upper trace in fig. 7.11, $\tau_1 = 91 \pm 5$ fs, IRF $= 128 \pm 6$ fs), in excellent agreement with the mass spectra and is in the same order of magnitude as the first time-constant with 798 nm probe.

Comparison of photoelectron and mass spectra

Experiment		τ_1/fs	τ_2/ps	IRF /fs
265/798	tof	83 ± 8	1.68 ± 0.16	120 ± 5
	pe	83 ± 6	1.3 ± 0.2	121 ± 4
	both	84 ± 5	1.55 ± 0.12	120 ± 1
265/398	tof	87 ± 5	—	128 ± 5
	pe	91 ± 5	—	128 ± 6
	both	89 ± 5	—	128 ± 2

Table 7.2: *Overview of the time-constants from photoelectron (pe) and mass spectra (tof) decays*

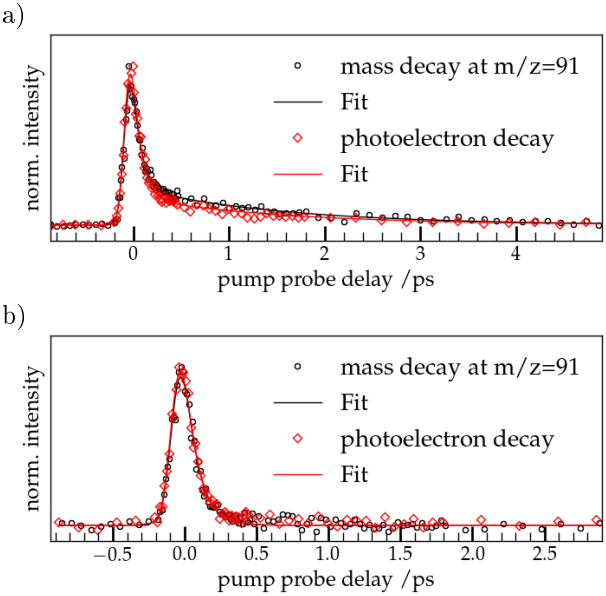

Figure 7.12: *Comparison of the mass spectrum benzyl decay and photoelectron decay for a) 265 nm pump and 798 nm probe ($\tau_1 = 84 \pm 5$ fs, $\tau_2 = 1.55 \pm 0.12$ ps, IRF=120 ± 0.01 fs) and for b) 265 nm pump and 398 nm probe ($\tau_1 = 89 \pm 5$ fs, IRF=128 ± 2 fs)*

The time-constants obtained in the photelectron spectra and mass spectra are slightly different (see table 7.2), but this is only due to an uncertainty in the fit itself.

This is best visible in fig. 7.12 a) and b), where both the photoelectron spectrum decay and mass spectrum decay at m/z=91 are fitted simultaneously, meaning with the same fit parameters. Both signals were normalized prior to fitting. The decay in both photoelectron and mass spectra is the same. The time-constants issued out of the fit for both at the same time will be taken for further discussion

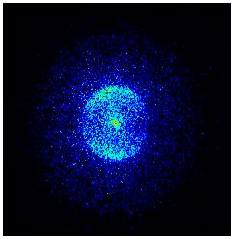

Figure 7.13: *Exemplary photoelectron image of 265 pump/398 probe. The outer circle corresponds to a pump only signal.*

and comparison with the experimental results (row 'both' in table 7.2).

Photoelectron anisotropy

The photoelectron anisotropy for 265 nm pump /398 nm probe is displayed in fig. 7.14 a), showing positive photoelectron anisotropy (β_2) of about 0.8. This positive beta can be seen directly in the photoelectron images (see fig. 7.13), the outer diffuse circle is signal from 265 nm only.

The photoelectron anisotropy values for 798 nm probe are in the same range (see fig. 7.14 b)).

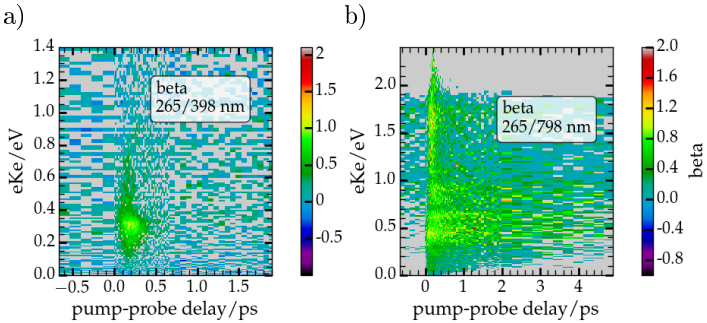

Figure 7.14: *Anisotropy for a) 265 nm pump and 398 nm probe b) 265 nm pump and 798 nm probe. Gray points correspond to data points where the intensity in the TRPES in fig. 7.11 is lower than 2000 counts.*

7.1.4 Theoretical methods and results

Theoretical methods

All calculations were carried out by Alexander Humeniuk from the Mitrić group. He used several methods including TDDFT, EOM-CCSD and CASSCF +MRCI. TDDFT calculations with the PBE [247], PBE0 [248], LC [249]-PBE, B3LYP [208,209], CAM-B3LYP [195] and ωB97XD [196] with the aug-cc-pVDZ basis set were performed using the Gaussian program package [194]. The orbitals of the active space of the benzyl radical for the *state-averaged complete active space SCF* (SA-CASSCF) calculations are displayed in fig. 7.15.

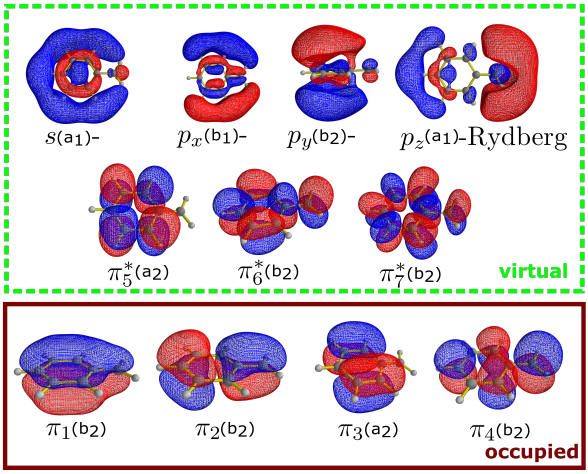

Figure 7.15: *Relevant valence orbitals of the benzyl radical calculated with CASSCF/(aug-cc-pVDZ,s-,p-Rydberg). The C_{2v} irreducible representations are given in brackets. Reproduced from [212] with the permission of AIP Publishing.*

The occupied valence orbitals consist of the three π-orbitals and one π*-orbital, whereas the virtual space consists of the remaining three unoccupied π*-orbitals, a s- and three p-Rydberg orbitals. The s-Rydberg orbital is energetically the lowest Rydberg orbital, followed by the p_x- and p_z-Rydberg orbitals.

For the SA-CASSCF calculations several basis sets were employed, including the aug-cc-pVDZ, 3-21 G and 6-31 G* basis sets, augmented by functions optimized for the description of the s- and p-Rydberg states. These were calculated according to the recipe by Kaufmann et al. [250], centered on the carbon atom next to the CH_2-group. In the SA-CASSCF calculations all states were given equal weights. Starting from the properly reordered RHF orbitals as the initial guess, the configuration coefficients and orbitals were optimized simultaneously.

With Molpro's conical program [251] the conical intersections of the benzyl radical were calculated and optimized, the Franck-Condon point served as the initial geometry. Intermediate geometries were linearly interpolated.

Non-adiabatic dynamic on the fly calculations were performed with the CASSCF(7,8)/(6-31G*, s-Ryd) method. The geometry of the benzyl radical at initial conditions was derived from a frequency calculation from an optimized PBE/6-311++G** [197] structure, whose normal modes were used to construct the Wigner distribution in the harmonic approximation at a constant temperature of 50 K. 100 trajectories lifted vertically to the $2\,^2A_2$ (ππ*-state) were propagated for 1 ps, the initial conditions were sampled randomly from the Wigner distribution. The motion of the nuclei on the current potential surface were described with Newton's equations and

integrated with a time step of 0.1 fs. The electronic amplitudes were integrated in the local diabatic basis [252] with a time step of $4 \cdot 10^{-5}$ fs, and were used to determine the hopping probabilities in an improved version [253] of Tully's hopping scheme [206]. The scalar non-adiabatic couplings were calculated from the wavefunction overlap between the consecutive time steps [254].

Electronic absorption spectrum

Just as for the non-adiabatic dynamic calculations for the 2-methylallyl radical (see chapter 6), the electronic states need to be characterized and a computationally time-efficient method needs to be found that still reproduces correctly the energetic order of the electronic states.

SA-9-CASSCF(7,11) + MRCI/(aug-cc-pVDZ,s-,p-Ryd) calculations was the most exact method used and its results are summarized in table 7.3. These results are in excellent agreement with previous experiments in the literature.

The first two excited states, $D_1(2\ ^2B_2)$ and D_2-$(^2A_2)$ are nearly degenerate. Though the order of these two states was discussed controversially in the literature [259, 260], the lowest excited must be long-lived since it fluoresces [224–226, 259]. The experimental observed C-band [257] at 4.06 eV is attributed to the D_3 $(^2A_1)$-state, the only energetically close bright electronic state at 4.16 eV. According to the new calculations, it has s-Rydberg character. The C-band is therefore just as the D-band reassigned. Ward [257] measured the rovibronic spectrum of the C-band, and the inexistant vibrational progressions were attributed to a small geometry change between the ground and excited state minima. The D-band from 4.7 to 5.1 with a maxi-

State	Sym.	E	Dominant config.	Exp.
D_0	$1\ ^2B_2$	0.0	$0.90\times$ $(\pi_1)^2(\pi_2)^2(\pi_3)^2(\pi_4)^1$	X
D_1	$2\ ^2B_2$	3.08 $(3\cdot10^{-3})$	$0.64\times$ $(\pi_1)^2(\pi_2)^1(\pi_3)^2(\pi_4)^2$	A 2.728 [255]
D_2	$1\ ^2A_2$	3.09 (0.0)	$0.64\times$ $(\pi_1)^2(\pi_2)^2(\pi_3)^2(\pi_5^*)^1$	B 2.886 [256]
D_3	$1\ ^2A_1$	4.16 $(2.5\cdot10^{-2})$	$0.91\times$ $(\pi_1)^2(\pi_2)^2(\pi_3)^2(s)^1$	C 4.06 [257]
D_4	$2\ ^2A_1$	4.65 $(3\cdot10^{-3})$	$0.91\times$ $(\pi_1)^2(\pi_2)^2(\pi_3)^2(p_z)^1$	D 4.9 [231]
D_5	$1\ ^2B_1$	4.72 (0.0)	$0.92\times$ $(\pi_1)^2(\pi_2)^2(\pi_3)^2(p_x)^1$	
D_6	$2\ ^2A_2$	4.75 (0.24)	$0.64\times$ $(\pi_1)^2(\pi_2)^2(\pi_3)^1(\pi_4)^2$	
D_7	$3\ ^2B_2$	4.76 (0.18)	$0.79\times$ $(\pi_1)^2(\pi_2)^2(\pi_3)^2(p_y)^1$	
D_8	$4\ ^2B_2$	4.89 $(3\cdot10^{-3})$	$0.65\times$ $(\pi_1)^2(\pi_2)^2(\pi_3)^1(\pi_4)^1(\pi_5^*)^1$	
S_0	$1\ ^1A_1$	6.61	$0.93\times(\pi_1)^2(\pi_2)^2(\pi_3)^2$	X^+ 7.24 [258]

Table 7.3: *Excitation energies of the benzyl radical calculated with SA-9-CASSCF(7,11) + MRCI/(aug-cc-pVDZ,s-,p-Ryd), excitation and ionization energies in eV, oscillator strengths in brackets*

mum at 4.9 eV [231] is attributed to the four excited states D_4-D_8.

The initially excited state with 265 has either $\pi\pi$-character (D_6), or is the p_y-Rydberg state (D_7). D_6 is flanked by two states with p_x- and p_y-Rydberg character, which are dark or have negligible oscillator strength. D_8 is almost dark and has $\pi\pi^*$-character. The calculated ionization energy is lower than the experimental ionization energy, for DFT

State	Sym.	E[a)]	B3LYP[b)]	CAS SCF(7,8)[c)]	EOM CCSD[d)]
D_0	$1\ ^2B_2$	0.0	0.0		
D_1	$2\ ^2B_2$	3.08 ($3\cdot10^{-3}$)	3.36 ($2.4\cdot10^{-3}$)	3.06 ($1.5\cdot10^{-2}$)	3.58 ($1.7\cdot10^{-3}$)
D_2	$1\ ^2A_2$	3.09 (0.0)	3.14 ($3\cdot10^{-4}$)	3.20 ($5\cdot10^{-4}$)	3.57 (0.0)
D_3	$1\ ^2A_1$	4.16 ($2.5*10^{-2}$)	4.21 ($3.4\cdot10^{-3}$)	4.35 ($1.5\cdot10^{-3}$)	4.65 ($4.1\cdot10^{-3}$)
D_4	$2\ ^2A_1$	4.65 ($3\cdot10^{-3}$)			
D_5	$1\ ^2B_1$	4.72 (0.0)			
D_6	$2\ ^2A_2$	4.75 (0.24)	3.77 ($2.6\cdot10^{-2}$)	5.00 ($3\cdot10^{-4}$)	4.67 ($4.67\cdot10^{-2}$)
D_7	$3\ ^2B_2$	4.76 (0.18)			
D_8	$4\ ^2B_2$	4.89 ($3\cdot10^{-3}$)			

Table 7.4: *Excitation energies of the benzyl radical calculated with different methods, excitation energy in eV, oscillator strength in brackets. a) SA-9-CASSCF(7,11)+MRCI/(aug-cc-pVDZ,s-,p-Ryd) b) TD-DFT B3LYP/aug-cc-pVDZ c) SA-5-CASSCF(7,8)/(6-31G*, s-Ryd) d) EOMCCSD/aug-cc-pVDZ*

the agreement between the calculated ionization energy and the experimental ionization is better.

The non-adiabatic dynamics on the fly calculations at CASSCF+MRCI level are not feasible. In table 7.4 computationally less demanding methods are compared to the CASSCF + MRCI calculations.

The results for B3LYP are shown exemplary for

the TDDFT calculations. All TDDFT functionals fail to reproduce the correct ordering of the excited states, the s-Rydberg state (D_3 in the CASSCF+MRCI calculations) is always energetically higher than the $\pi\pi$-state (D_6 in the CASSCF+MRCI calculations), probably due to charge-transfer influence from higher-lying electronic states. Therefore the computationally cheap TDDFT method can not be employed to simulate the dynamics of the benzyl radical.

The more expensive method SA-5-CASSCF(7,8)/(6-31G*,s-Ryd), still computationally less demanding compared to CASSCF+MRCI calculations, reproduces the correct order of the excited states. Especially the s-Rydberg state still lies below the initially excited $\pi\pi^*$-state. The excitation energies are higher than those from the CASSCF+MRCI-calculations since the dynamic correlation is not as well described, and due to the small basis set the oscillator strengths are not correct.

The EOM-CCSD method reproduces the correct ordering of the states, but the s-Rydberg state and the initially excited $\pi\pi$-state are separated only by 0.02 eV, simulating the dynamics with this method would therefore lead to a too fast relaxation between those two states.

Potential energy surfaces

The potential energy surfaces (fig. 7.16) illustrate qualitatively what happens after the benzyl radical is excited into the D_4-state with $\pi\pi$-character. The conical intersections were calculated with SA-5-CASSCF(7,8)/(6-31G*, s-Ryd); the character of $D_{1\text{-}3}$ is as discussed above for the CASSCF+MRCI calculations. D_4 corresponds to the initially excited state with $\pi\pi$-character, the states with p-Rydberg

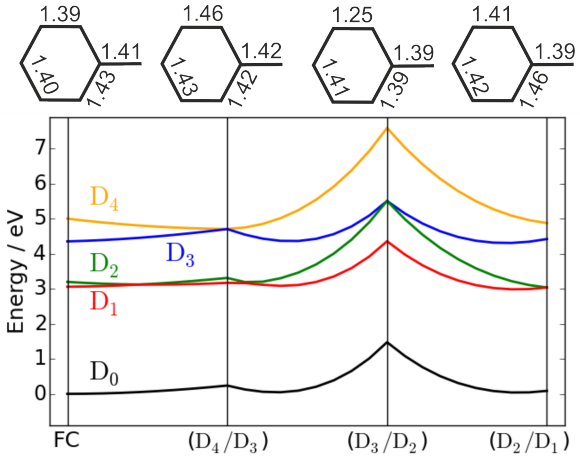

Figure 7.16: *Potential energy scan from the Franck-Condon point (FC) to different conical intersections with SA-5-CASSCF(7,8)/(6-31G*, s-Ryd). The key geometries have C_{2v} symmetry, their bond lengths in Å are depicted above. Reproduced from [212] with the permission of AIP Publishing.*

character are not incorporated in this calculation to bring the calculations down to a feasible length.

Starting in D_4 at the Franck-Condon point, the wave-packet will slide down the potential surface and cross into D_3. There it remains trapped, unless its kinetic energy is high enough to pass the barrier to the D_3/D_2 conical intersection. Therefore the kinetic energy of the wave-packet of the initially excited state should influence strongly the lifetime of the s-Rydberg state (D_3), since the conical intersection D_3/D_2 is energetically slightly higher compared to D_4 at the Franck-Condon point. If the wavepacket passes the D_3/D_2 barrier, it will slide down quickly towards the barrierless D_2/D_1 intersection and relax into D_1.

During all those conical intersections the molecule remains planar, only the bond lengths in the aromatic ring vary. For the in fig. 7.16 not-displayed conical intersection between D_1/D_0 this is not the case, here the planar symmetry is broken. This ring-puckered geometry has elongated (or broken) bonds, and lies -at the CASSCF-level with only π-electrons in the excited states- energetically very high. Including orbitals from the σ-framework would improve this description. But the aromaticity of the benzyl radical will enforce planarity, shifting this conical intersection to even higher energies.

A deactivation of the D_1-state via a D_1/D_0 conical intersection is therefore hindered. This results in a long life-time for the D_1-state, in agreement with fluorescence from the lowest excited state [259]. Deactivation from the D_1-state via a conical intersection will break the benzyl radical apart, as was observed experimentally when exciting the benzyl radical in the D-band [242].

The potential energy surfaces represent a qualitative explanation of the dynamics of the benzyl radical. A more quantitative picture is provided by non-adiabtic dynamic on the fly calculations.

Non-adiabatic surface hopping calculations

The methodology of non-adiabatic surface hopping calculations was already explained in detail for the 2-methylally radical (see section 6.3.2). For the benzyl radical, however, no interaction with the laser is taken into account, all populations started directly from the $\pi\pi$-state (D_4). The evolution of 100 trajectories, calculated with CASSCF(7,8)/(6-31G*, s-Ryd), is shown in fig. 7.17 (see beginning of this section for more details on the calculation procedure). p-Rydberg states were not included in this

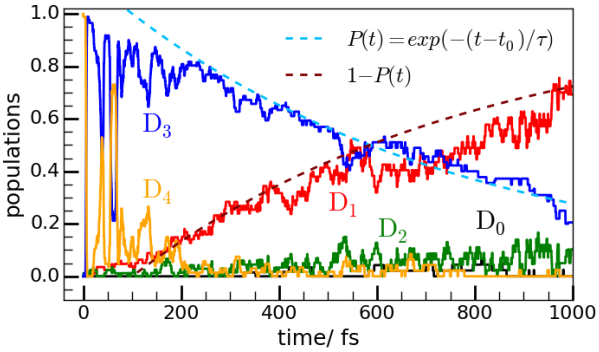

Figure 7.17: *Adiabatic state populations from non-adiabatic dynamics simulations with CASSCF(7,8)/(6-31G*, s-Ryd) after a vertical excitation of all trajectories into D_4 (2 $^2A_2$, ππ*). A fit considering only the transition of D_3 (1 $^2A_1$, s-Rydberg) to the D_1 (1 $^2A_2$) state resulted in a lifetime of the s-Rydberg state of τ≈700±100 fs (dotted thin blue and red curves). Reproduced from [212] with the permission of AIP Publishing.*

simulation, since this would be too time-consuming.

At t=0 all trajectories are in the ππ*-state D_4 (orange line). It is tempting to interpret the rapid cycling between D_4 (orange line) and D_3 (blue line) in the first 100 fs as the rapid relaxation of D_4 into the s-Rydberg state D_3. But the plotted populations are adiabatic ones, meaning that the character of a state may change but the color of the respective curve remains the same.

During those first 100 fs the D_4 and D_3 state are energetically very close and switch order, leading to the cycling seen in the first 100 fs. After about 100 fs the gap between those two states widens, meaning that now the conical intersection between D_4 and D_3 has been passed, and the D_3-population

has mainly s-Rydberg character. This is also nicely visible in fig. 7.18, where the adiabatic energies of a typical trajectory are shown. During the first 100 fs D_4 and D_3 are very close and sometimes even cross, then the gap widens.

Turning back to fig. 7.17, the wave-packet then relaxes from the D_3-state to the D_1-state (red line), where it remains, since the D_1-state is long-lived. The small population in the D_2-state (green line) is again attributed to switching in the energetic order of the D_2 and D_1-state. This switching of the order of D_1/D_2 as well as the relaxation into D_1 is also visible in fig. 7.18 for a typical trajectory. When the gap between two states widens, the conical intersection between those two has been passed.

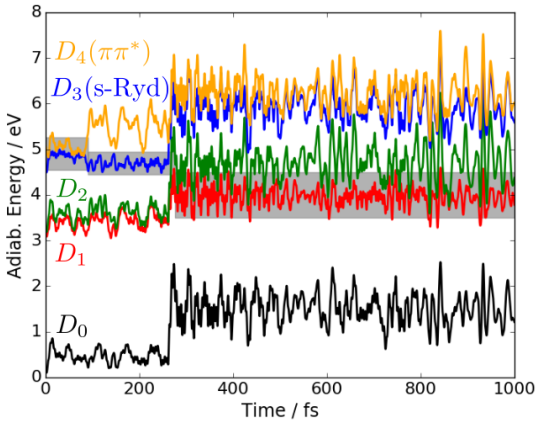

Figure 7.18: *Adiabatic energies along a typical trajectory, with the gray area highlighting the current electronic state. Reproduced from [212] with the permission of AIP Publishing.*

The relaxation from D_3 to D_1 can be described with a single exponential (blue and red dotted lines in fig. 7.17):

$$P(D_3) = e^{(-t-t_0)/\tau}$$

The inital delay t_0=100±50 fs corresponds to the time where the states D_4 and D_3 still switch their energetic order. The lifetime τ=700±100 fs describes the deactivation of the D_4-state to the lower-lying D_1-state. Both the lifetime τ and the initial delay t_0 are derived from a manual fit.
In summary, the following deactivation mechanism is postulated:

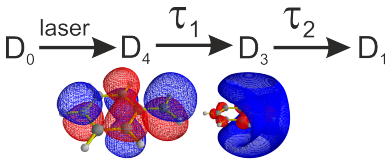

7.1.5 Discussion of theoretical and experimental results

This postulated deactivation mechanism is in excellent agreement with the experimental results.

The first time-constant $\tau_1 = 84 \pm 5$ fs with 798 nm probe and the time-constant $\tau_1 = 89 \pm 5$ fs with 398 nm probe are attributed to the relaxation of the initially excited state to the s-Rydberg state, which takes place in the first 100 fs. The initally excited state is mainly the $\pi\pi$-state, but probably has also some p_y-Rydberg character. Ionizing from p_y-Rydberg states is very efficient. This results in photoelectrons with an eKe≈0.3 eV, the only band observed in the 398 nm photoelectron spectra and

the band observed at early times in the photoelectron spectra with 798 nm probe.

The second time-constant visible with 798 nm probe, corresponding to the decay of the second band in the photoelectron spectra around eKe≈1.0 eV, is attributed to the relaxation of the s-Rydberg-state to the lowest excited state D_1. The experimentally observed time-constant $\tau_2 = 1.55 \pm 0.12$ ps and the computed time-constant of $\tau = 700 \pm 100$ fs are in reasonable agreement. The s-Rydberg state lies energetically lower than the initially excited $\pi\pi^*$-state and cannot be ionized by one single 398 nm photon. With 798 nm ionization occurs via resonant Rydberg states, resulting in the observed [1+3']-signal. Ionization via resonant Rydberg states has been observed before [182–184]. This interpretation is in perfect agreement with the delayed formation of the band in the photoelectron spectrum at eKe≈1.0 eV.

S-Rydberg states are characterized by a highly positive photoelectron anisotropy of $\beta = 2$ for one-photon ionization. The observed anisotropy in the photoelectron spectrum with 798 nm probe is about 0.8 for all observed signal, but this anisotropy stems from a multiphoton process, involving probably resonant states. Both processes are therefore not comparable, and will not be discussed further.

In the 398 nm probe photoelectron spectra only one-photon ionization is observed with a photoelectron anisotropy of 0.8. This photoelectron anisotropy might stem from the initially excited $\pi\pi$-state, but also from the p-Rydberg states, which are energetically quite close (but were not included in the dynamic simulations since too time-expensive).

Since the photoelectron anisotropy for states other than s-Rydberg states varies with the kinetic en-

ergy of the photoelectron (see section 4.2), a clear identification is only possible if the probe energy is varied. This measurement cannot be performed with the experimental setup, so no conclusion can be drawn as to whether the observed anisotropy is in agreement with the postulated mechanism.

Ionization from D_1 with 798 or 398 nm cannot be observed, since the probe energy is too low in both cases. The simulation as well as previous experiments [259] show that this state is long-lived, since it fluoresces when excited directly. Song et al. observed that the benzyl radical excited in the D-Band (230-270 nm) leads to dissociation to fulvenallene and a hydrogen atom [242], which is in agreement with the analysis of the potential energy surface (see section 7.1.4).

This mechanism is different from the one observed by Zierhut et al., who excited benzyl with 255 nm and probed with 280 nm. Time-resolved mass spectrometry showed a mono-exponential decay ($\tau = 150 \pm 30$ fs) with a final offset [241]. Their observations are probably compatible with to our postulated mechanism, since the time-dependant signal of Zierhut et al. was only recorded until 1.25 ps delay and the signal had not yet returned to the base-line.

Figure 7.19: *Tropyl radical (cycloheptatrienyl radical)*

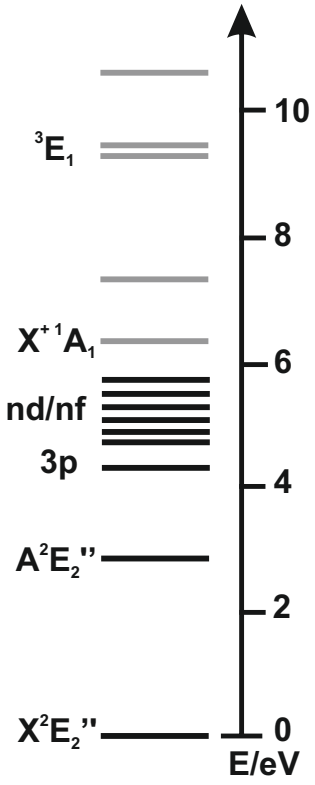

Figure 7.20: *Electronic states of the tropyl radical*

7.2 Tropyl radical

The tropyl (cycloheptratrienyl) radical (see fig. 7.19 is a fascinating structure. With 7 electrons it is not aromatic (it doesn't obeys Hückel's rule for [4n+2] electrons); but the cation with its 6 electrons is aromatic. The non-aromatic radical, however, is still extensively resonance stabilized, even better than the triphenylmethyl radical [261].

The cation has D_{7h} symmetry [262], in agreement with calculations [263], but it has been unclear for quite some time whether the radical is symmetric (D_{7h}) or distorted by the Jahn-Teller (JT) effect to a lower symmetry, caused by the electron in the antibonding orbital.

A symmetric or near-symmetric geometry was postulated by Johnson [264], but IR measurements of the radical tell a different tale. The IR spectrum of the radical measured in a supersonic expansion in the gas-phase is not reproduced by calculations which do not take into account the Jahn-Teller distortion from the D_{7h} symmetry to lower symmetry C_{2v} [235]. Recently Kaufmann et al. measured the C-H stretch vibrations in helium droplets, confirming that the Jahn-Teller-interaction strongly influences the intensity of the vibrational bands [265]. These results contradict electron spin resonance (ESR) measurements of the tropyl radical in crystals, where the tropyl radical is to possess seven equivalent hydrogen atoms at room temperature (no JT distortion), anisotropic spectra in low temperature crystals were attributed to effects of a different crystalline environment [266].

Even though the tropyl radical is Jahn-Teller distorted, it is still normally treated in the framework of a D_{7h} symmetry group, therefore its ground state has E_2" symmetry. The transition into the

first excited state A^2E_3'' at 25 719 cm^{-1} shows a large vibronic progression; covering over 6000 cm^{-1}, revealing a large geometry change due to the JT effect (distorting it from the D_{7h} geometry) [267]. The Jahn-Teller distorted potential energy surfaces of the first excited state and the ground state were calculated in detail, revealing conical intersections [268] as confirmed by laser-excited dispersed fluorescence spectra [269].

The ionization energy of the tropyl radical is very low compared to other organic molecules, which reflects the stability of the aromatic cation. Harrison et al. were the first to measure the ionization energy of the radical (6.60 ± 0.1 eV) [273], which was refined three years later by Trush et al. via absorption spectra measurements. The one-photon absorption spectrum revealed a Rydberg series with a δ of 0.046, converging to an ionization energy of 6.237 ± 0.01 eV [270]. 1969 Elder et Parr remeasured the adiabatic IE to be 6.236 ± 0.005 eV [274]. Using He(I)-photoelectron spectroscopy, the first two excited states of the tropyl cation were determined and the ionization energy measured to be 6.28 eV [272]. By measuring two Rydberg series with δ(np)=0.35 and δ(nf)=0.05, an ionization energy of $50\,177 \pm 86$ cm^{-1} (6.22 eV) was determined. The vibrations in the Rydberg series are quite similar to the cation [264].

Recently our group determined an ionization energy of 6.23 ± 0.02 eV in a photoelectron-photoion coincidence (PEPICO) experiment [271]. The cation shows a strong vibrational progression. Several states of the cation were also observed, but their symmetry was not determined. At wavelengths higher than 10.55 eV the cation dissociates to $C_5H_5^+$ and C_2H_2. The electronic states of the tropyl radical

state	energy /eV
X^2E_2'' [267]	0
A^2E_3'' [267]	3.1887
3p [264]	4.3625
nd (δ= 0.046) [270]	4.773
	5.4124
	5.7022
nf (δ= 0.05) [264]	5.3481
	5.6656
	5.8347
	5.9374
$X^{+1}A_1$ [271]	6.23
N.A. [271]	7.25
$^3E_1$ [272]	9.63 eV
N.A. [271]	9.85
N.A. [271]	10.7
$^1A_2''$ [234]	11.79

Table 7.5: *Electronic states of the tropyl radical, N.A. means not attributed.*

and cation are summarized in table 7.5 and fig. 7.20.

An isomer of the tropyl radical is the benzyl radical, which has already been discussed in the previous section 7.1. The benzyl radical is about 0.65 eV more stable than the tropyl radical. For their cations this is different, here the tropyl cation is 0.24 eV more stable than the benzyl cation [235]. The rearrangement from the benzyl cation to the tropyl cation needs an activation energy of 2.81 eV, passing through a single intermediate minimum [275].

Since we already examined one C_7H_7 isomer, the benzyl radical, it is interesting to examine the tropyl radical using the same experimental method, namely fs pump-probe spectroscopy.

7.2.1 Experimental conditions and data treatment

The tropyl radical was examined with the fs-setup in Saclay using 266 nm as a pump pulse and 800 or 400 nm as the probe pulse (see chapter 5.4). Tropyl was produced via pyrolysis from the precursor bitropyl (see figure 7.21, for the synthesis see appendix). It was seeded into gas phase in the T-filter source at 60-70°C (see chapter 5.1) with argon as carrier gas at 2 bar absolute pressure.

The pyrolysis was kept at 30 W. The experimental parameters of the lasers are summarized in table

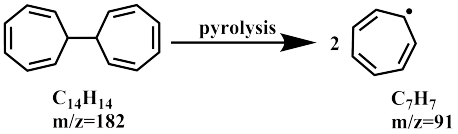

Figure 7.21: *Pyrolysis of the precursor bitropyl leads to the formation of the tropyl radical*

7.6. For 266/800 nm the polarization of the lasers was varied during the measurement between horizontal/horizontal and horizontal/vertical. No rotational anisotropy (see fig. 7.22) was observed, consequently the rotational mean are analyzed for 800 nm probe. For 266/400 nm both lasers were horizontally polarized. Photoelectron images were inverted using the pBasex algorithm as implemented in the *Analyse*-program. The fit program detailed in chapter 13 was used to fit the decays, the plotted uncertainties correspond to fit uncertainties and not to experimental uncertainties.

λ/nm	energy	lens/mm	focus/cm
266	8 µJ	500	+18
800	1.0 mJ	700	-2
266	18 µJ	500	+16
400	38 µJ	700	-5

Table 7.6: *Laser parameters of the tropyl experiments with 800 and 400 nm probe pulse. A positive (negative) focus correspond to a focal point behind (before) the interaction region.*

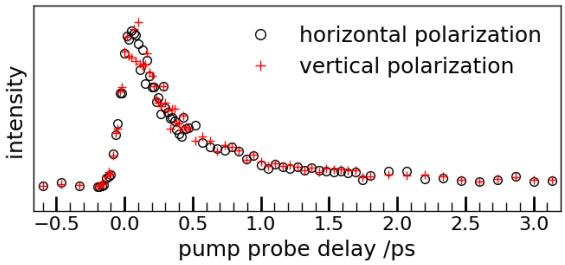

Figure 7.22: *Total photoelectron decay for 266/800 nm with different polarizations of the pump laser in respect to the probe laser.*

7.2.2 Results

Pyrolysis conditions

The tropyl radical (m/z=91) is produced cleanly from the precursor bitropyl, as can be seen in fig. 7.23 a) for 266/800 nm and in fig. 7.23 b) for 266/400 nm at pump-probe conditions.

Without pyrolysis no precursor (m/z=182) is visible in either case, but the tropyl radical itself is. The ion image with 800 nm probe gated on the tropyl radical without pyrolysis shows a diffuse blotch (see fig. 7.24), confirming that the tropyl radical can be formed by dissociative photoionization of bitropyl. The M+1-peak at mass 92 corresponds to $^{13}CC_6H_6$-peak.

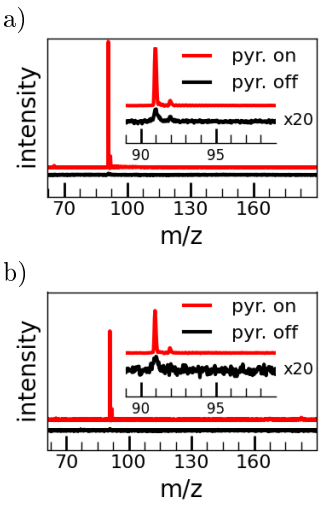

Figure 7.23: *Pyrolysis on vs pyrolysis off for a) 266/800 nm b) 266/400 nm*

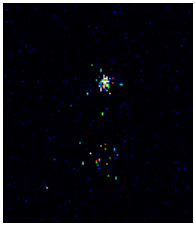

Figure 7.24: *Ion image gated on tropyl without pyrolysis*

Time-resolved mass spectra

The evolution of the tropyl signal (m/z=91) for 800 nm probe with pyrolysis on is displayed in fig. 7.25. A mono-exponential fit ($\tau_1 = 432 \pm 23$ fs, IRF=106±11 fs) reproduces the data, and the IRF issued from the fit is in agreement with previous experiments using the same experimental setup.

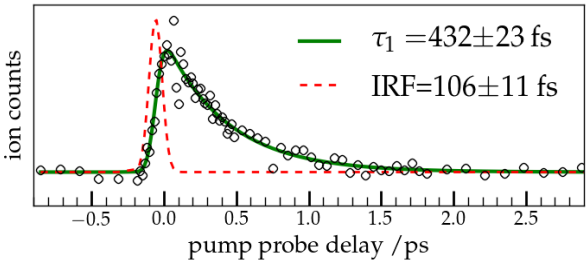

Figure 7.25: *Mono-exponential fit of the decay of the m/z=91 signal with 266/800 nm pump-probe*

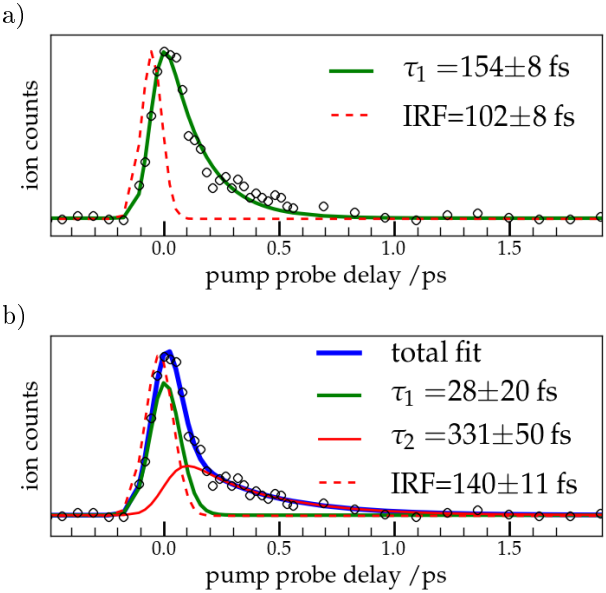

Figure 7.26: *Mono-exponential (a) and bi-exponential (b) fit of the decay of the m/z=91 signal with 266/400 nm pump-probe*

With 400 nm probe this situation is different. A mono-exponential and bi-exponential fit with 400 nm probe are shown in fig.7.26 a) and b) respectively. Fitting with only one time-constant doesn't reproduce the signal after 0.5 ps. A second time-constant is necessary, but this leads to an IRF that is too large and a first time-constant which is too short to be realistic. This only means that the first time-constant is too short to be resolved with the experimental IRF.
It is striking, however, that the decay with 400 nm probe is shorter than with 800 nm probe. With 400 nm probe no intensity remains after 1.0 ps, whereas for 800 nm probe signal is still visible.

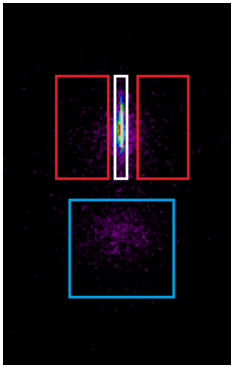

Figure 7.27: *Typical ion image of the tropyl radical with 266/800 nm and pyrolysis on*

To clarify whether the observed signal and dynamics stem from the tropyl radical itself or from dissociative photoionization from the precursor, time-resolved ion images gated on the tropyl radical were recorded.

Time-resolved ion images

In fig. 7.27 a typical ion image gated on the tropyl radical (T(A)=8.68 µs, T(B)=300 ns) at pump-probe conditions with 800 nm probe and pyrolysis is shown. The molecular beam (white rectangle) is visible as a fine line. But signal on the side of the molecular beam (red rectangles) is also visible, indicating dissociative processes. Background signal (blue rectangle) corresponds to molecules in the detection chamber with no velocity in direction of the molecular beam.

The decays of these different regions of interest is shown in fig. 7.28. In a) the decay of the molecular beam (○) is fitted, the decay of the dissociative photoionization signal (◇) and the background (▽) is also shown. Both the molecular beam (○) and the dissociation signal (◇) show the same decay, which is well reproduced with a mono-exponential decay. The observed time-constant ($\tau_1 = 262 \pm 9$ fs) is shorter than the time-constant in the mass spectra ($\tau_1 = 432 \pm 23$ fs). This is due to insufficient detector voltage and will be detailed later when comparing the time-constants from mass spectroscopy, ion and photoelectron imaging.

The background molecules show a different behavior, the signal converges to an offset. A mono-exponential fit with offset (fig. 7.28-b upper panel) does not reproduce well the background decay around

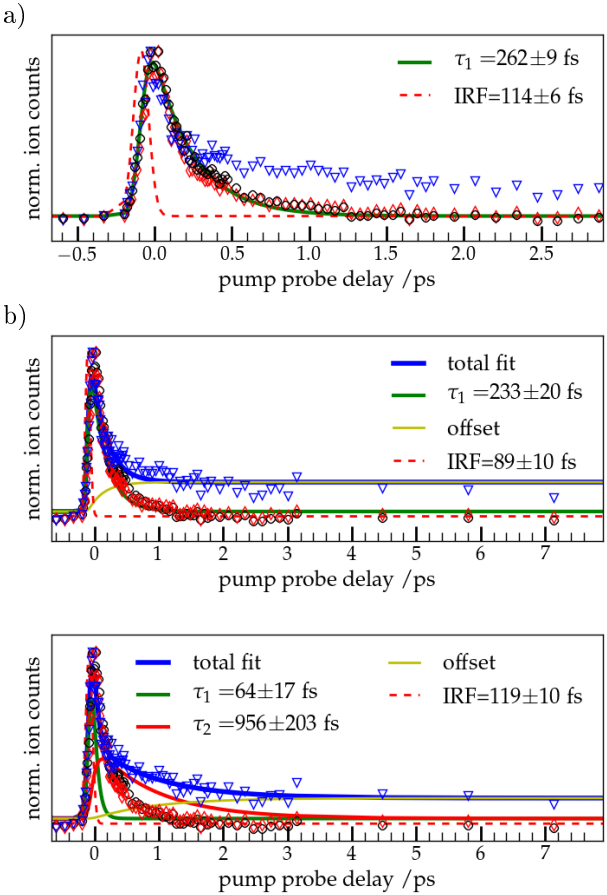

Figure 7.28: *Ion image decays for 266/800 nm with different fits for different regions of interest, gated on the tropyl radical.* ○ *is the decay of the tropyl radical in the molecular beam (white rectangle in fig. 7.27),* ◊ *the dissociative processes around the molecular beam (red rectangles in fig. 7.27), and* ▽ *the background (blue lower rectangle in fig. 7.27). In a) the molecular beam is fitted, in b) the background.*

0.6 ps. A bi-exponential fit with offset (fig. 7.28-b lower panel) reproduces well the complete background signal, and also leads to a more realistic IRF.

The background signal intensity is 13% compared to the molecular beam signal summed up to 1.5 ps, so its influence should be visible in the photoelectron spectra. In the mass spectra the background signal is of no consequence, since it is experimentally excluded. When switching from imaging mode into mass mode, the electrostatic optics is turned (see section 5.4) to capture the ions on the bottom detector. The size of the mass detector is only 25.4 mm, compared to 80 mm for the imaging detector, the background signal is not captured with time-of-flight mass spectrometry.

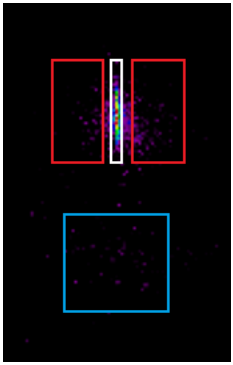

Figure 7.29: *Typical ion image of the tropyl radical with 266/400 nm and pyrolysis on*

The ion image gated on the tropyl radical at pump-probe conditions with 400 nm probe (fig. 7.29) is noisier, but the same processes are distinguishable, namely the molecular beam (white rectangle), dissociative processes (red rectangles) and the background signal (blue rectangle). The decays of these three regions of interests are shown in fig. 7.30.

Again dissociative processes (◊) and the molecular beam (○) show similar decays. For the molecular beam a mono-exponential fit represents well the observed decay (fig. 7.30-a), and the observed time-constants and the mono-exponential time-constant of the time-of-flight decay are in agreement. The background signal (▿ , fig. 7.30-b) shows again an offset. It can be fitted with a mono-exponential fit including an offset, but the background signal is so noisy that a bi-exponential fit with offset is equally valid. Summing all images up to 1.5 ps leads to a background-to-signal ratio of 14% with respect to the molecular beam signal.

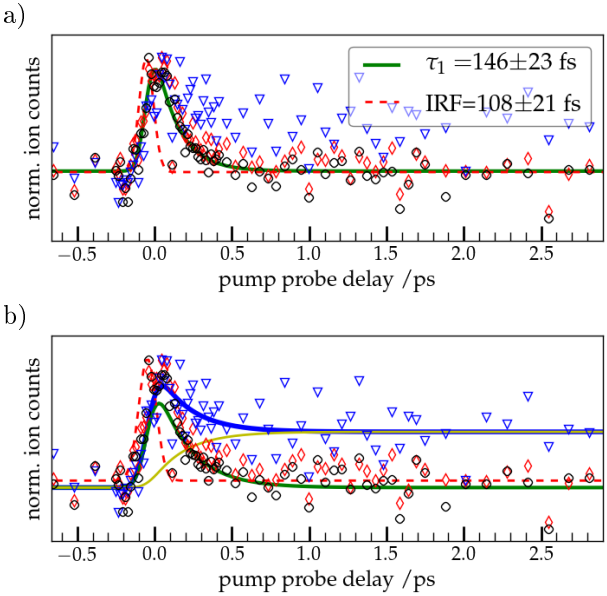

Figure 7.30: *Ion image decays for 266/400 nm with different fits for different regions of interest, gated on the tropyl radical.* ○ *is the decay of the tropyl radical in the molecular beam (white rectangle in fig. 7.29),* ◇ *the dissociative processes around the molecular beam (red rectangles in fig. 7.29), and* ▽ *the background (blue lower rectangle in fig. 7.29). In a) the molecular beam is fitted, in b) the background* ($\tau_1 = 213 \pm 100$ *fs, IRF*$=133 \pm 40$ *fs).*

The offset of the background signal is a very interesting pheomena. The image is gated on the tropyl radical (m/z=91), but the minimum width of the experimental gate is ±1 mass unit. If the background molecules were also tropyl radicals, their temperatures are expected to be higher (not cooled in the molecular beam), and a shorter decay is expected. Instead an offset is observed. Therefore

the background signal cannot be the tropyl radical, but another molecule of roughly the same mass ($\pm^1$H). Cycloheptatriene or toluene are the most likely candidates. Cycloheptatriene absorbs in the region around 266 nm, and even though in solution the decay was fast (110 ± 10 fs) [276], this can differ dramatically without the interaction with solvent molecules. The S_1-state of toluene also absorbs at 266 nm, and since this state fluoresces [277], it is long-lived on the ps-time scale. That no large M+1-peak (other than the tropyl-^{13}C-peak) was observed in the mass spectra is not in disagreement with this analysis, since with the experimental setup the mass spectra do not incorporate the background signal, as was explained above.

The dissociative signal shows the same temporal behavior as the molecular beam signal, and stems therefore also from the tropyl radical and not from the bitropyl precursor. The dissociative signal corresponds most likely to the loss of a hydrogen, giving the fragment velocity orthogonal to the molecular beam direction.

Time-resolved photoelectron spectra

Consequently the photoelectron spectra should be composed mainly of the tropyl radical signal. In fig. 7.31 the time-resolved photoelectron spectrum with 800 nm pump pulse is displayed. A mono-exponential fit with or without offset is not sufficient to fit the total photoelectron decay (upper panel in fig. 7.31). A bi-exponential fit reproduces well the observed decay (middle panel). The decay is the same for all kinetic energies (see fig. 7.32). This observed bi-exponential decay ($\tau_1 = 229 \pm 39$ fs, $\tau_2 = 1.1 \pm 0.3$ ps, IRF=124 ± 7 fs) is in disagreement with the mono-exponential fit seen in the mass

spectra ($\tau_1 = 432 \pm 23$ fs). This is treated later on in detail, when the time-constants of all tropyl experiments are compared.

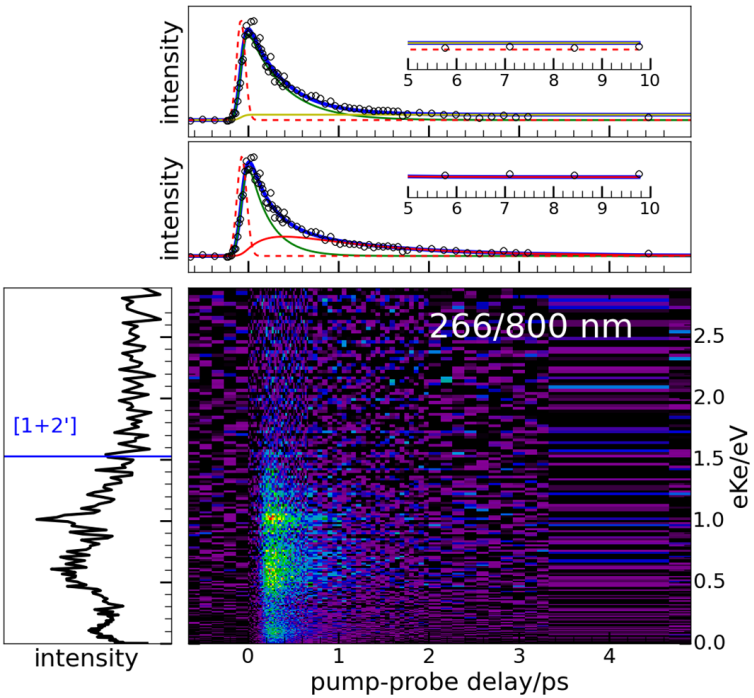

Figure 7.31: *TRPES of the tropyl radical at 266 nm pump and 800 nm probe wavelength. The upper panel shows a mono-exponential fit with offset ($\tau_1 = 394 \pm 16$ fs, IRF=111 ± 7 fs), the middle panel a bi-exponential fit ($\tau_1 = 229 \pm 39$ fs, $\tau_2 = 1.1 \pm 0.3$ ps, IRF=124 ± 7 fs) of the total photoelectron signal decay. The blue line corresponds to the total fit, the green, red, and yellow lines to the population of the first, second state and offset respectively. The red dotted line represents the IRF. The side panel shows the photoelectron spectrum summed over all times, where the ionization limit [1+2'] is drawn in as blue lines. The ionization limit of the tropyl radical is 6.23 eV [271].*

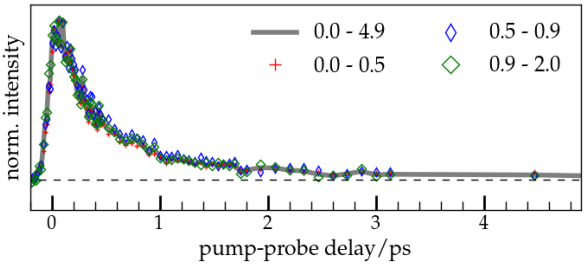

Figure 7.32: *Comparison of the decays summed over different parts of the photoelectron spectrum with 800 nm probe*

The photoelectron spectrum shows two peaks at 0.60 and 1.05 eV, both stem from a [1+2']-process. It is very different from the photoelectron spectrum of the benzyl radical at 265/798 nm (see section 7.1), consequently isomerization to the benzyl radical during the pyrolysis is excluded.

These two observed peaks do not fit an obvious well-defined Rydberg fingerprint spectrum, nor do they correspond to vibrations in the cation. The first excited electronic state in the cation measured by Fischer et al. is at 9.65 eV [271] , which ionized in a [1+4']-process would correspond to an excess energy of eKe=1.21 eV. No peak is observed in that region. In fig. 7.33 the time-resolved photoelectron spectrum with 400 nm probe is displayed with different fits for the total photoelectron signal (upper three panels). A mono-exponential fit only (top panel) does not take into account the observed offset. Including this offset (middle panel) in a mono-exponential fit leads to a better agreement, but including another time-constant for a bi-exponential decay (lower panel) leads to the best fit and to a realistic IRF. Just as for 800 nm probe, the decay is the same over the whole energetic range.

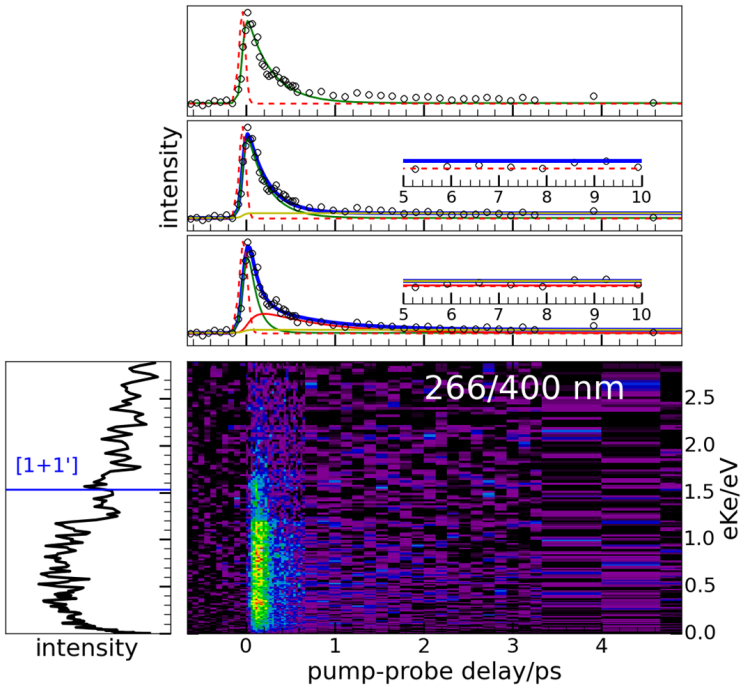

Figure 7.33: *TRPES of the tropyl radical at 266 nm pump and 400 nm probe wavelength. The upper panel shows a mono-exponential ($\tau_1 = 272 \pm 16$ fs, IRF=80 ± 10 fs), the second upper panel a mono-exponential fit with offset ($\tau_1 = 224 \pm 12$ fs, IRF=84 ± 8 fs) and the lower upper panel a bi-exponential fit with offset ($\tau_1 = 99 \pm 18$ fs, $\tau_2 = 693 \pm 167$ fs, IRF=104 ± 8 fs) of the total photoelectron signal decay. The side panel shows the photoelectron spectrum summed over all times, where the ionization limit [1+2'] is drawn in as blue lines. The ionization limit of the tropyl radical is 6.23 eV [271].*

But the photoelectron spectrum (left panel) shows no discernible structure, only a broad band up to [1+1'] is visible. The observed offset is attributed to background signal, from molecules in the detection chamber with no velocity in direction of the molec-

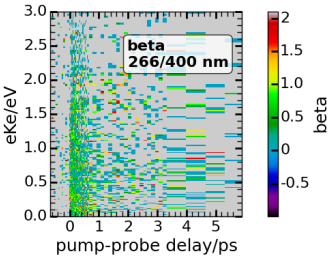

Figure 7.34: *Anisotropy of the tropyl radical at 266/400 nm*

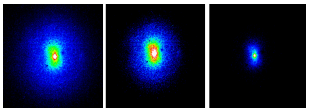

Figure 7.35: *Sum over all photoelectron images for tropyl radical at 266/400 nm with different intensity scaling*

ular beam (see the time-resolved photoion images of tropyl).

Photoelectron anisotropy

The photoelectron anisotropy for 400 nm probe of the tropyl radical is shown in fig. 7.34. It is positive (0.5-1.0), where electrons with low kinetic energies (between 0 and 0.25 eV) have slightly higher anisotropy (1.0).

Overview of the time-constants

In table 7.7 the time-constants of the different experiments are compared. For 800 nm the mono-exponential time-constant for the mass spectra is not in agreement with the bi-exponential photoelectron spectra decay, nor with the decays observed in the photoion images gated on tropyl.

A graphic comparison of all three experiments (fig. 7.32) show that photoelectron and mass spectra are in agreement up to 1 ps, but the photoelectron spectra show a slower decay than the mass signal. These signals stem from background molecules, which are also imaged with photoelectron images but excluded from the mass spectra. The mono-exponential decay of the tropyl radicals in the molecular beam in the photoionimages is shorter than the decays in the mass or photoelectron experiments. This is attributed to wrong experimental conditions: the detector voltage was probably not high enough during this experiment, and the non-linearity of the detector caused that weak signals to be underestimated, resulting in a shorter observed time-constant.
As for the experiments with 400 nm probe, all observed time-constants are shorter than the time-

λ_{probe}		τ_1/fs	τ_2/fs	offset	IRF/fs
800	tof	432 ± 23	—	—	106 ± 11
	pi_{beam}	262 ± 9	—	—	114 ± 6
	pi_{dpi}	217 ± 9	—	—	110 ± 7
	pi_{bg}	64 ± 17	956 ± 203	yes	119 ± 10
	pe	229 ± 39	1100 ± 300	—	124 ± 7
400	tof	28 ± 20	331 ± 50	—	140 ± 11
	tof	154 ± 8	—	—	102 ± 8
	pi_{beam}	146 ± 23	—	—	108 ± 21
	pi_{dpi}	118 ± 35	—	yes	176 ± 31
	pi_{bg}	213 ± 100	—	yes	133 ± 40
	pe	99 ± 18	693 ± 167	yes	104 ± 8
	pe	224 ± 12	—	yes	84 ± 8

Table 7.7: *Summary of the fit constants for the different experiments with 800 and 400 nm probe at m/z=91 (with the exception of the photoelectron experiments). ms=mass spectra, pe=photoelectron spectra, pi=photoion spectra, beam=molecular beam and dpi=halo around the beam*

constants with 800 nm probe. Mono-exponential fits of the mass spectra and of the molecular beam are in excellent agreement; but the mass spectra decays are better reproduced with a biexponential decay, the mono-exponential time-constant for the photoelectron spectrum is about 60 fs longer. A bi-exponential fit of the ion images does not converge due to the bad S/N ratio. The biexponential fits of the photoelectron and mass spectra do not agree, but extracting a time-constant of 30 fs with an IRF of 140 fs is not realistic.

All three decays are compared graphically in fig. 7.37, showing that the differences in the time-constants can be attributed the fitting procedure and to the inferior S/N ratio. But no matter whether the decay with 400 nm probe is best reproduced by a bi-exponential or mono-exponential decay, it is

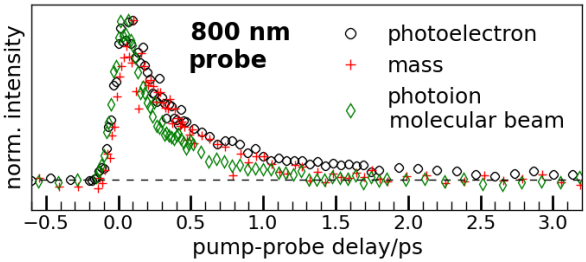

Figure 7.36: *Comparison of the decays of the tropyl radical for 266 nm pump and 800 nm probe for the photoelectron experiments, the time-resolved mass spectra (tropyl radical signal m/z=91) and the photoion signal of the tropyl radical in the molecular beam.*

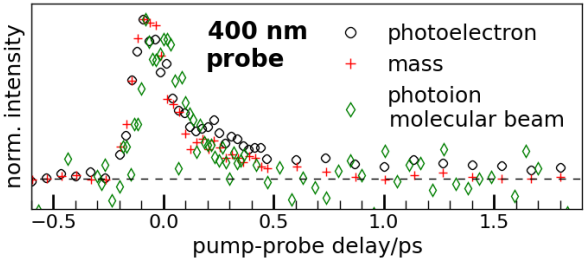

Figure 7.37: *Comparison of the decays of the tropyl radical for 266 nm pump and 400 nm probe for the photoelectron experiments, the time-resolved mass spectra (tropyl radical signal m/z=91) and the photoion signal of the tropyl radical in the molecular beam.*

substantially shorter than the decay with 800 nm probe.

7.2.3 Interpretation

With 266 nm we excite tropyl in a region where Rydberg series have already been measured. Trush et al. reported Rydberg bands at 259.7, 229.0 and 217.4 nm, excited in a one-photon transition, attributed to a d-series with δ=0.046 [270]. The observed band-width of 150 cm^{-1} for the 3d-Rydberg band at 259.7 nm is too small to be excited with 266 nm (spectrum displayed in fig. 7.38). Johnson also measured several Rydberg series [264] (see table 7.8). These Rydberg series were excited in a two-photon transition and are dark with one 266 nm photon.

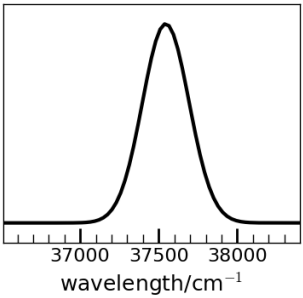

Figure 7.38: *Spectrum of the pump laser*

The electron in the tropyl radical is resonance-stabilized and is therefore expected to have p-character. With one 266 nm we can either excite into a s- or into a d-Rydberg state. The d-Rydberg-states measured by Trush cannot be reached with the pump laser. Most likely we excite therefore into an s-Rydberg orbital, which explains the unstructured photoelectron spectra. S-Rydberg bands have not been observed yet for the tropyl radical. This does not explain the difference in the observed decays with 800 and 400 nm probe. With 400 nm probe the decay is shorter. Since in both cases

assignment	energy/cm^{-1}
3p 0_0^0	34 521
3p 2_0^0	35 186
3p 20_0^2	36 051
3p 18_0^2	36 481
4p 0_0^0	36 736
4p 2_0^1	41 920

Table 7.8: *Rydberg states close to 266 nm as measured by Johnson with a two-photon transition.* [264]

the same amount of energy is used in ionization, and the same initial state is excited with 266 nm, the observed difference has to stem from the ionization step. Assuming the initially excited s-Rydberg states moves very fast out of the Franck-Condon-region, with 800 nm we could still ionize via intermediary Rydberg states, which increase the ionization cross section.

This could be confirmed by calculations of the excited states of the tropyl radical, which are far from trivial for this open-shell molecule with Jahn-Teller distortion. K. Issler is currently working on them.

Chapter 8 Xylylenes

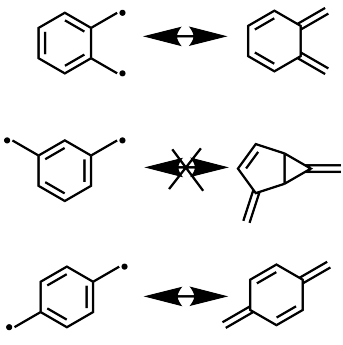

Figure 8.1: *Ortho-, meta-, and para-xylylene*

Biradicals play just like radicals a premordial role in combustion processes. The xylylenes are the first example of a species with biradical character examined in this thesis.

Three xylylene isomers exist, *ortho*-, *meta*-, and *para*-xylylene, named after the position of one of the methylene groups in respect to the other (see fig. 8.1). The *ortho*- and the *para*-xylylene can be easily regarded as having a diene structure, for the *meta*-xylylene a true biradical character is expected [278]. Thus it is not surprising that calculations show a thermal decomposition of the *ortho*-methylbenzyl radical and *para*-methylbenzyl to the corresponding xylylenes, whereas *the meta*-methylbenzyl radical rearranges to *para*-xylylene [279]. Their saturated parents, the xylenes, are like many alkylated aromatic hydrocarbons an important component in liquid fuels due to their anti-knock properties. In the following an overview on the literature for all three xylylene isomers will be presented, then the experimental results of the *para*-xylylene and finally the preliminary results of the *ortho*-xylylene will be discussed.

***Ortho*-xylylene, (or o-quinodimethane)** is an important reaction intermediate [280], since it can be seen as a diene (see fig. 8.1, top). The diene structure has been confirmed by IR and Raman spectra in an argon matrix [281]. The ground state of *ortho*-xylylene is a planar singlet state [282,283], in accordance with its diene structure. As a diene it can react with dienophiles in typical pericyclic Diels-Alder-like reactions, [284–286] and has

Figure 8.2: *Benzocyclobutane, an isomer of o-xylylene*

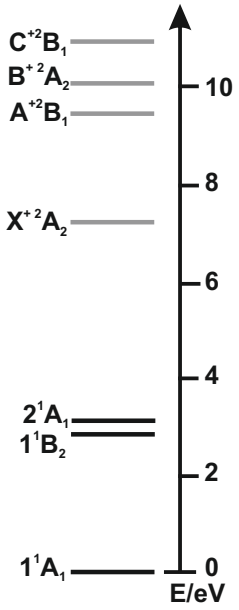

Figure 8.3: *Known electronic states of the ortho-xylylene, see table 8.1*

proven to be especially useful in the synthesis of six-membered ring systems like alkaloids, steroids and terpenes [280,287]. This reactive molecule has been postulated for quite some time and was first observed directly 1973 by Flynn and Michl in an argon matrix [282] and some years later by Roth et al. in solution [288]. In absence of other molecules it dimerizes quickly [283,289]. Another possible reaction is isomerization to benzocyclobutane (see fig. 8.2), which is more stable than *ortho*-xylylene (ΔH_f (*ortho*-xylylene) = 54.2 kcal/mol, ΔH_f (benzocyclobutane) = 49.2 kcal/mol). The activation barrier of this reaction is 25.6 kcal/mol [290].

Both isomers have different ionization energies. Benzocyclobutane as an ionization energy of 8.65 ± 0.015 eV [291], higher than the ionization energy of *ortho*-xylylene (IE= 7.70 eV [292]).

The excited states of *ortho*-xylylene are summarized in table 8.1 and in fig. 8.3. When excited from the planar ground state into the first excited state, it undergoes quite some geometrical change [293]. Tseng et al. measured an absorption spectrum of *ortho*-xylylene in an argon matrix, showing absorption from 400 to 294 nm, and another band which starts at 285 nm and increases up to their limit of measurement, 278 nm. They also showed that it fluoresces between 400 - 600 nm [281]. Miller et al. also measured the absorption spectrum of *ortho*-xylylene between 670-220 nm [294]. They reported only absorption/emission between 670-420 nm, in agreement with the fluorescence spectrum measured by Tseng et al. We tried to excite *ortho*-xylylene in this non-attributed band by Tseng et al. using 266 nm.

***Para*-xylylene** (see fig. 8.1, middle) was first proposed 1942 by Szwarc as a pyrolysis product of

symmetry	energy/eV	wavelength/nm
$S_0\,^1A_1$ [283, 293]	ground state	
$S_1\,^1B_2$ [283, 293]	2.99 eV	414
$S_2\,^1A_1$ [293]	3.09 eV	401
$X^{+2}A_2(\pi)$ [292]	7.70 eV	
cation $^2B_1(\pi)$ [292]	9.6 eV	
cation $^2A_2(\pi)$ [292]	10.05 eV	
cation $^2B_1(\pi)$ [292]	10.49 eV	
cation $^2A_1(\sigma)$ [292]	11.44 eV	
cation $^2B_2(\sigma)$ [292]	12.14 eV	

Table 8.1: *Overview of the different electronic states of the ortho-xylylene and its cation as can be found in the literature.*

para-xylene [295,296]. As a Chichibabin hydrocarbon it is an intermediate in many organic reactions [297]. Whereas *ortho*-xylylene only dimerizes, *para*-xylylene can polymerize, forming parylene N. This polymer is commonly synthesized from the precursor [2.2]paracyclophane [298] by heating it over 500°C in a vacuum, creating the *para*-xylylene as an intermediate, which polymerizes [298]. Parylene N is used as an isolating coating in e.g microwave electronics or as barrier layers for filters [299].

Para-xylylene can also be formed photochemically from *para*-xylene by irradiation with 193 nm. Absorption of two 193 nm photons lead to the elimination of two hydrogen atoms and formation of *para*-xylylene [300].

Just like *ortho*-xylylene, it can exist in two me-

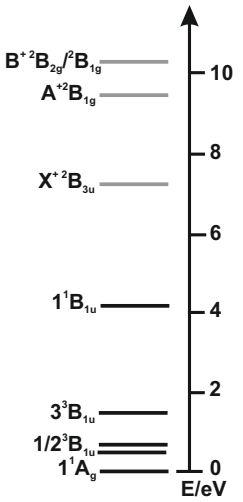

Figure 8.4: *Known electronic states of the para-xylylene, see table 8.2*

someric, uncharged structures (see fig. 8.1). The quinone structure seems the best simplistic representation of the *para*-xylylene instead of the double radical form; its bond lengths indicate that a simple assembly of conjugated double and simple bonds is not the correct representation for this molecule [301]. UV and IR spectra further consolidate the quinone structure over the biradical structure [302]. *Para*-xylylene is more stable than its *ortho*-isomer, which is shown by its lower heat of formation (49.3 kcal/-mol [303]).

In accordance with the quinone structure the ground state is a singlet state [304], and its UV spectrum show a first absorption band with a maximum at 301 nm [302]. All electronic states of *para*-xylylene and its cation are summarized in table 8.2 and in fig. 8.4. Several theoretical studies were performed on this molecule [295, 304, 305], most recently Bobrowski et al. calculated several triplet and singlet states using CASSCF/MRMP2 [304]. They concur with several other studies that the singlet ground state of *para*-xylylene is more stable than its first triplet state, with the symmetry of the ground state being D_{2h}.

Koenig et al. [306] determined the ionization energy of *para*-xylylene as 7.87 ± 0.05 eV using He I photoelectron spectroscopy, measuring also the position of the first three ionic states. They showed that some ionic states mixed strongly, which is also the case for a *para*-xylylene derivate [307]. The value of the ionization energy of *para*-xylylene was confirmed recently using threshold photoelectron spectroscopy [308]. Under irradiation of an ArF-excimer laser [2.2]-paracylclophane dissociates to *para*-xylylene in a fast (faster than ns) 2-photon process, with the reaction rates well reproduced by a statistical reaction theory [309].

symmetry	energy/eV
^1A_g [304]	0
$^3B_{1u}$(theo) [304]	1.65
$^1B_{1u}$(theo) [304]	4.38
$^1B_{1u}(\pi\pi*)$ [302,305]	4.12
$X^{+2}B_{3u}$ [306]	7.87
$A^{+2}B_{1g}$ [306]	9.7
$B^{+2}B_{2g}/^2B_{1g}$ [306]	10.2-10.5

Table 8.2: *Overview of the different electronic states of the para-xylylene and its cation as can be found in the literature, own TDDFT calculations which show that the S_1/S_2 states are very close are presented later in this chapter.*

***Meta*-xylylene** is, in contrast to the other xylylene-isomers, expected to be a true biradical [278]. ESR-spectroscopy confirm that the ground state of *meta*-xylylene is a triplet state [278], as do calculations of the lowest triplet and singlet states [310]. The triplet ground state and two higher excited singlet states were observed by anion photoelectron spectroscopy, which also allowed the measurement of the electron affinity of the triplet ground state [311]. The fluorescence spectrum of *meta*-xylylene is structured, showing peaks at 988, 530 and 440 nm [293].

The xylylene isomers are important intermediates in combustion processes, where they are excited by thermal energy. But the dynamics of their excited states is largely unknown, we therefore try to fill that void by examining their dynamics of their excited states after excitation with 266 nm. First the results of the *para*-xylylene will be described. Then the results of two possible *ortho*-xylylene precursors will be compared to benzocy-

clobutane, revealing that producing *ortho*-xylylene via pyrolysis is problematic. For the *meta*-xylylene no suitable precursor was found during the time of this thesis.

8.1 *para*-Xylylene

8.1.1 Experimental conditions and data treatment

Para-xylylene was produced via pyrolysis from the precursor [2.2]paracyclophane (*Sigma-Aldrich*, used without further purification, see fig. 8.5) using the T-filter setup (see chapter 5.1) and examined using the fs-setup in Saclay (see chapter 5.4).

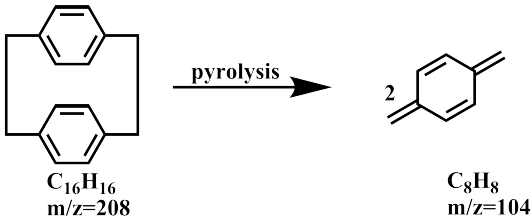

Figure 8.5: *Production of para-xylylene by pyrolysis of [2.2]paracyclophane*

266 nm was used as a pump laser and it was probed with either 800 nm or 400 nm. The 266 nm pump beam was focalized with a 500 mm lens, the 800/400 nm laser beam with a 700 mm lens. All other experimental conditions are summarized in table 8.3.

All decays were averaged for at least four scans, and the polarization of the pump/probe laser was varied between horizontal/horizontal and vertical/horizontal. No rotational anisotropy was observed for any of the measurements (see fig. 8.6), so the ro-

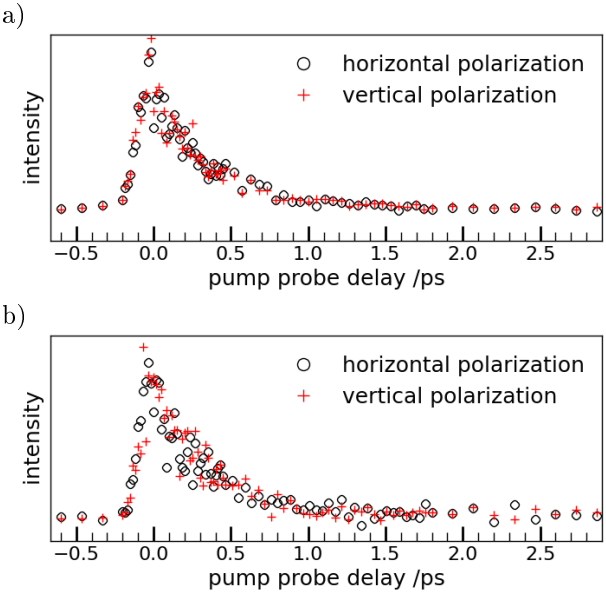

Figure 8.6: *Total photoelectron signal with different polarizations of the pump laser of para-xylylene for a) 266/800 nm and b) 266/400 nm*

tational mean ((2*$\text{Signal}_{\text{ortho}}$+$\text{Signal}_{\text{para}}$)/3) was used in further analysis. The points were selected randomly in each time sequence. The mass spectra decays were analyzed by integrating over the respective signal. Photoelectron spectra were inverted using the pBasex algorithm as implemented in the *Analyse*-program with a $P_0P_2P_4$ basis set. Decays were fitted using the fit program as described in chapter 13, uncertainties correspond to the uncertainties of the fit itself and are not experimental uncertainties. A sequential fit A $\rightarrow$ B ($\rightarrow$ C) was used to fit the data. An offset (static signal after the laser autocorrelation) was included in the fit if reasonable.

precursor	pyrolysis power/W	T/°C	laser	power	focus /cm
[2.2]para-cyclophane	22.5	115	266	8 μJ	+16
			800	1.0 mJ	+3

Table 8.3: *Laser focalization and powers of the experiments on para-xylylene, a positive focus corresponds to a focal point after the laser spatial overlap, a negative focus to a focal point before laser spatial overlap*

8.1.2 Experimental results

Pyrolysis conditions

The pyrolysis on/pyrolysis off ratio was excellent (see fig. 8.7). Only two side-products of *para*-xylylene (m/z=104) are visible: m/z=103 (800 nm probe: 7%; 400 nm probe: 21%) and m/z=78 (800 nm probe: 0.05%; 400 nm probe: 6%; for the percentages the m/z=104 peak corresponds to 100%). M/z=105 is with 11% (9% for 400 nm probe) mostly $^{13}CC_7H_8$, corresponding to the ^{13}C *para*-xylylene.

The m/z=78 peak (probably benzene) is quite broad, indicating formation from dissociative processes. The m/z=103 peqk is quite sharp, however.

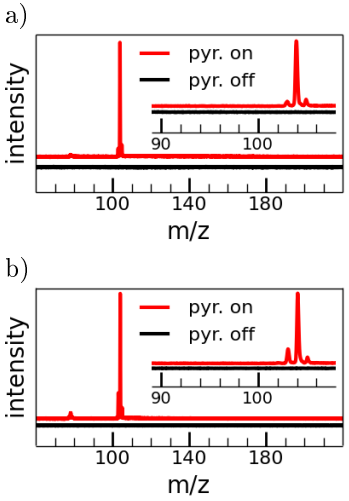

Figure 8.7: *Paracyclophane pyrolysis on versus pyrolysis off at pump-probe conditions for a) 266/800 nm and b) 266/400 nm*

Time-resolved mass spectra

For both probe wavelengths the decay of the m/z=104 signal (○) is well reproduced with a mono-exponential fit with similar time-constants (τ_1=339-299 fs, see fig. 8.8). The IRF is, with 86 ± 6 and 89 ± 6 fs for 800 and 400 nm probe wavelength respectively, reasonable as well. The decay of m/z=103 (◇) and m/z=78 (▽) are plotted in the background.

For both probe wavelengths it is apparent, though for 800 nm probe especially striking, that the onset and maximum of the m/z=103 and m/z=78 decays is shifted in respect to the m/z=104 decay. For 800 nm probe a shift of roughly 80 fs is visible, for 400 nm probe the shift is about 30 fs, though the 266/400 nm signal is noisier. Both masses m/z=103 and m/z=78 show the identical temporal behavior.

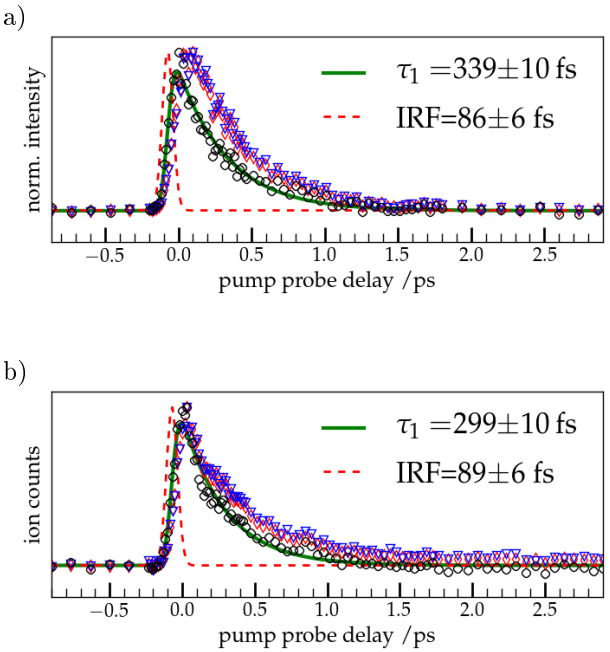

Figure 8.8: *Mono-exponential fit of the m/z=104 signal of the TOF decay with a) 800 nm probe and b) 400 nm probe. ○ represent the experimental points for m/z=104, ◊ of m/z=103 and ▽ of m/z=78.*

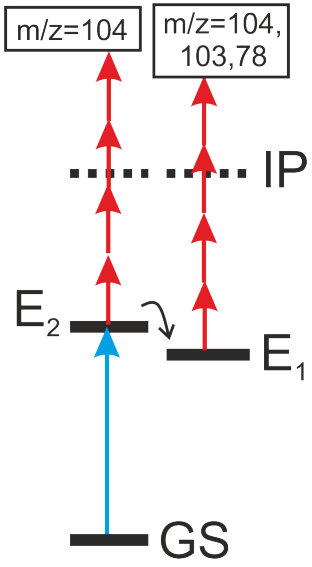

Figure 8.9: *Scheme for the excitation of para-xylylene with 800 nm*

Several explanations are possible:

These lower masses could be produced via dissociative photoionization, and the observed offset stems from a lower effective IRF since only a high multiphoton process leads to a dissociative photoionization. For 400 nm probe this hypothesis still seems reasonable, but for 800 nm a shift of 80 fs for an IRF of 86 fs is not.

Another hypothesis is that the lower masses could be formed independently in pyrolysis. As pyrolysis side-products their IRF and in particular the time zero (see the fit procedure chapter 13) should be identical to those from the fit of *para*-xylylene. Keeping these parameters fixed does not allow reasonable fits.

A valid picture of the origin of these lower masses from *para*-xylylene is represented schematically in fig. 8.9: The pump laser (blue arrow) excites *para*-xylylene into the excited state E_2, from which it can be ionized directly with the multiphoton ionization (red arrows representing 800 nm probe). E_2 then relaxes into E_1, which upon ionization dissociates, and the molecules at m/z=103 and 78 are formed. It is unlikely that the state E_1 is just a different vibronic state and not another electronic state, since E_1 is formed too fast for vibrational relaxation. E_1 can then relax either to the ground state GS or to another lower-lying electronic state, which can no longer be ionized. A similar process has been observed in the case of decatetraene [312].

The proposed model is $E_2 \xrightarrow{\tau_1} E_1 \xrightarrow{\tau_2}$GS/ dark state, with the m/z=103/78 signals reflecting the population of the E_1-state. This model is used to fit both m/z=104 and m/z=103 simultaneously, and it reproduces well the observed data (see fig. 8.10).

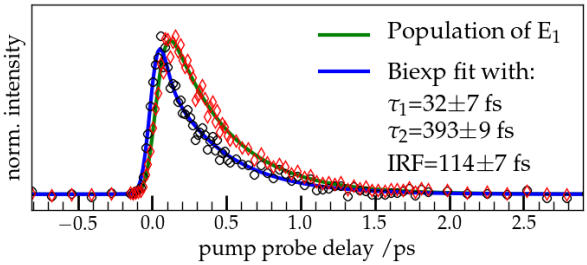

Figure 8.10: *Fitting both the para-xylylene signal (m/z=104, ○) and m/z=103 (◇) with the model depicted in fig. 8.9.*

The time-constants from the same model with a simultaneous fit of m/z=104 and m/z=78 are within the limits of uncertainty (τ_1 = 38±7 fs, τ_2 = 407±9 fs and IRF = 115 ± 7 fs).

Using the same model for 400 nm probe leads to an unreasonable value of τ_1 = 2 ± 723 fs (τ_2 = 354 ± 9 fs and IRF = 107 ± 72 fs). The S/N ratio is worse than with 800 nm probe, which is likely the reason why the fitting of such a model fails for 400 nm probe.

Time-resolved photoelectron spectra

In fig. 8.11 and fig. 8.12 the time-resolved photoelectron spectra for 800 and 400 nm probe wavelength are plotted respectively. The total photoelectron decay is plotted in the upper panel, and is well reproduced for both by a mono-exponential fit with $\tau_1 \approx$ 330 fs. But the model established with the mass spectra data shows a bi-exponential decay. Fitting the total photoelectron decay of either 800 or 400 nm probe leads to unrealistic values of the first time-constant. This stems from the fact that no evolution of the second state is fitted simultane-

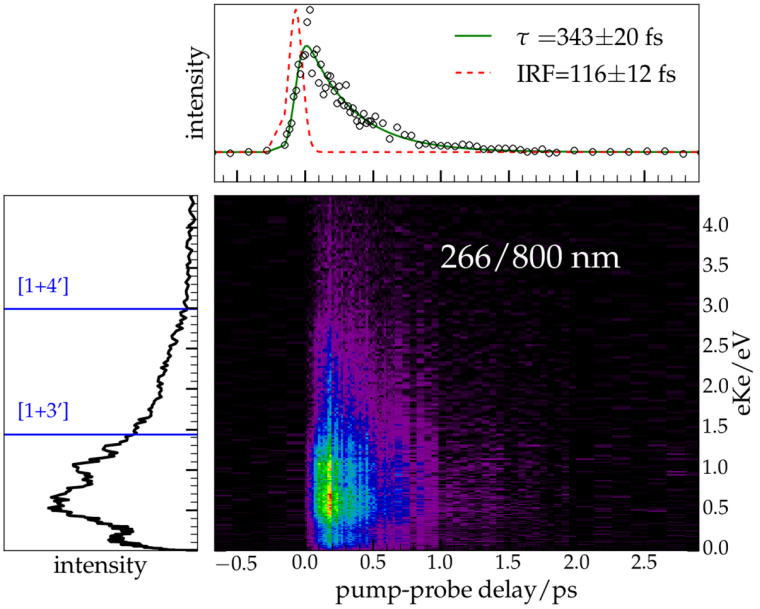

Figure 8.11: *Rotational mean TRPES for para-xylylene with 266 nm pump and 800 nm probe. The upper panel shows the decay summed over all photoelectron energies with a mono-exponential fit, the black circles correspond to the experimental data points. In the left panel the photoelectron spectrum summed over all times is displayed, the ionization limits for para-xylylene (IE=7.87 eV [306]) are depicted in blue.*

ously with the total photoelectron decay, since the photoelectron spectra are dominated by the signal from *para*-xylylene.

Therefore in fig. 8.13 the total photoelectron decay (◊) and mass spectra (m/z=104, ○) are compared for both probe wavelengths. Mass and photoelectron signals show the same decay, but the photoelectron decays are noisier than the decay of the

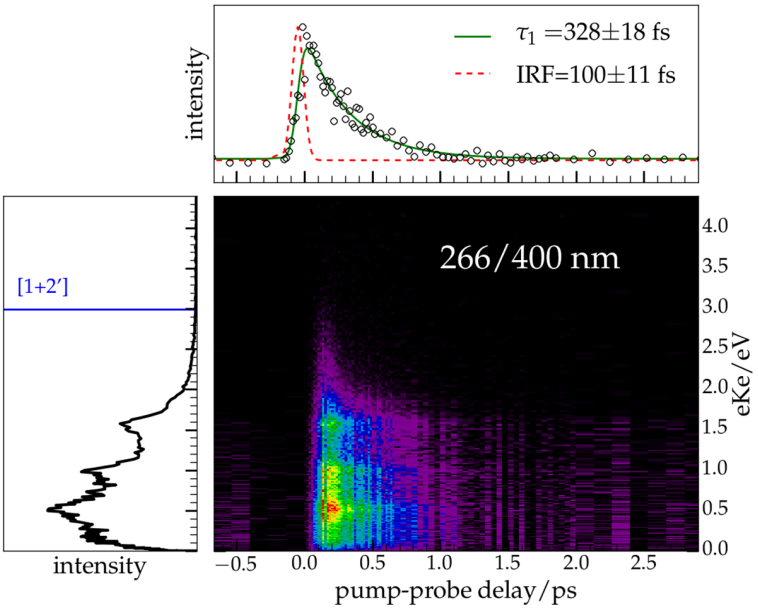

Figure 8.12: *Rotational mean TRPES for para-xylylene with 266 nm probe and 400 nm pump. The upper panel shows the decay summed over all photoelectron energies with a mono-exponential fit, the black circles correspond to the experimental data points. In the left panel the photoelectron spectrum summed over all times is displayed, the ionization limits for para-xylylene (IE=7.87 eV [306]) are depicted in blue.*

para-xylylene mass spectra signal. The inherent assumption in fig. 8.13 is that photoelectrons with different kinetic energies show the same temporal evolution, and that therefore the total photoelectron decay can be used for comparison.

This is true for the bands in the photoelectron spectrum with 800 nm probe (see fig. 8.11), but not for the bands in the photoelectron spectra with 400 nm probe. Looking closely at the 2D-map in fig. 8.12, the band above 2.0 eV shows a different

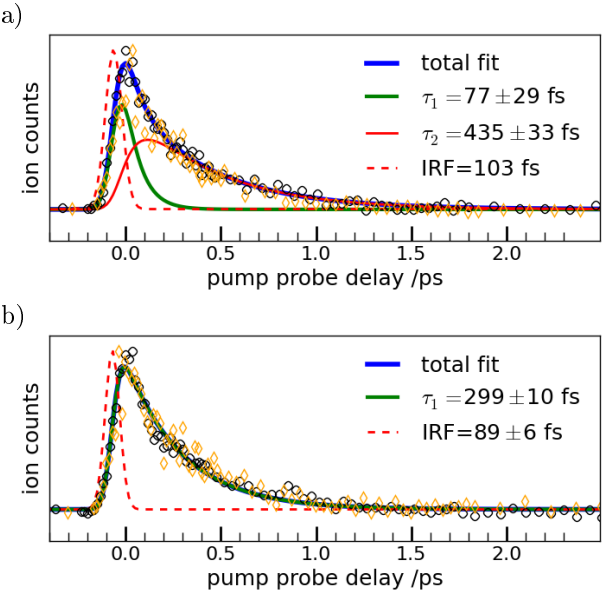

Figure 8.13: *Comparison between mass spectra (m/z=104, ○) and photoelectron spectra (all energies, ◇) for a) 800 nm probe and b) 400 nm probe.*

temporal evolution than the other bands at lower energies (see fig. 8.14). The three overlapping peaks from 0 to 1.9 eV are well reproduced using the same mono-exponential fit parameters ($\tau_1 = 115 \pm 7$ fs; IRF $= 72 \pm 6$ fs), whereas the diffuse band from 2.0 to 2.5 eV shows a shorter, different temporal behavior.

A mono-exponential fit of this signal is not sufficient; a bi-exponential decay reproduces the signal ($\tau_1 = 50 \pm 21$ fs; $\tau_2 = 256 \pm 90$ fs; IRF $= 90 \pm 9$ fs). The first time-constant is - within the uncertainties - in agreement with the bi-exponential model parameters from the mass spectra fit with

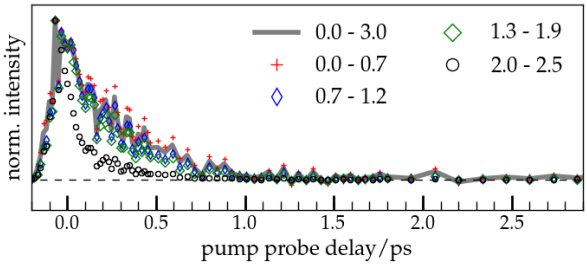

Figure 8.14: *Comparing the decays of the photoelectron bands for 266 nm pump and 400 nm probe. All energy regions are in eV.*

800 nm probe ($\tau_1 = 38 \pm 7$ fs, $\tau_2 = 407 \pm 9$ fs and IRF $= 115 \pm 7$ fs), but the second time-constant is about 100 fs shorter. This difference is attributed to an insufficient S/N ratio. It is possible to fit satisfactorily the two decays of both energy ranges using the same time-constants (see fig. 8.15), but the first time-constant and the IRF has to be held fixed for the fit to converge.

So both bands show the same temporal evolution, but the different populations have different ionization cross sections at different photoelectron kinetic energies. For the peaks with eKe<1.9 both populations have nearly the same weight, which is

a)

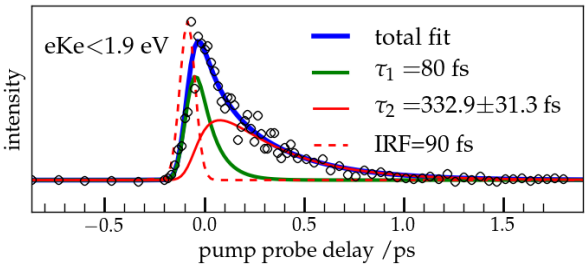

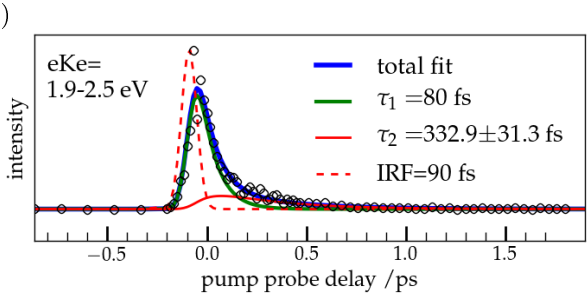

Figure 8.15: *Simultaneous fit of the two photoelectron bands with 400 nm probe, a) the band from 0 to 1.9 eV b) the band from 1.9 to 2.5 eV. The first time-constant and the IRF had to be held fixed for the fit to converge.*

also the reason why a mono-exponential can satisfactorily fit the observed decay.

For the band above 1.9 eV the second population has less weight. So with 800 nm probe the bi-exponential decay is visible in the mass spectrum, whereas for 400 nm probe it is also visible in the photoelectron spectrum. The proposed mechanism $E_2 \xrightarrow{\tau_1} E_1 \xrightarrow{\tau_2}$ GS/darkstate is the same for both probe wavelengths, but the ionization cross sections differ with a different probe wavelength, which explains the slightly different photoelectron spectra.

The photoelectron spectra with 800 nm probe shows up to [1+4']- signal, so one more photon is used for ionization than necessary. With 400 nm probe a [1+2']-process is at least necessary to ionize *para*-xylylene, and no signal with higher eKe was observed.

A comparison of the summed photoelectron spectra for both probe wavelengths is given in fig. 8.16. In the 400 nm probe photoelectron spectrum four peaks are discernible (0.1, 0.5, 0.9, 1.55 eV), whereas

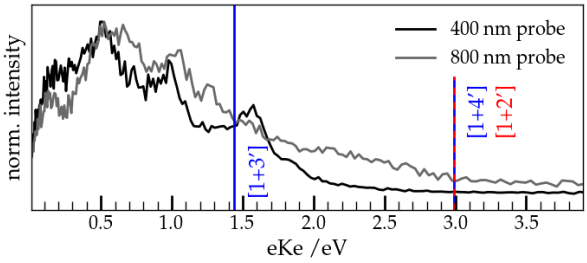

Figure 8.16: *Comparison between the sum of the photoelectron spectra over all times for probe 400 and 800 nm*

the last peak at 1.55 eV is not visible with 800 nm probe.
The attribution of these bands is tricky: Their positions do not match Rydberg series, nor do the photoelectron spectra show a cutoff at the energy of one probe photon as it would be the case for a Rydberg fingerprint spectrum.

The first excited state of the *para*-xylylene cation is located at 9.7 eV. With 800 nm probe it could be reached in a [1+3'] process, resulting in an excess energy eKe=0.4 eV; whereas for 400 nm ionization requires an [1+2']-process with a resulting eKe of 1.9 eV. No prominent peaks are observed in these regions for the corresponding probe wavelength. The observed peaks also cannot correspond to vibrations in the cation, since the band structure is so large that for 400 nm probe the difference between the ionization limit and the highest energetic peak is more than 9 600 cm^{-1}. The measued spectra also does not correspond to vibrations in the cation as measured in the treshold phtoelectron spectra by Hemberger et al. [308].

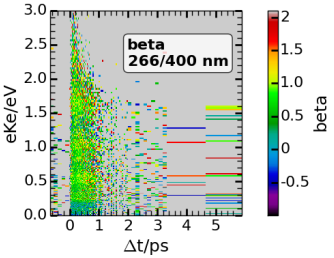

Figure 8.17: *Anisotropy of p-xylylene 266/400 nm*

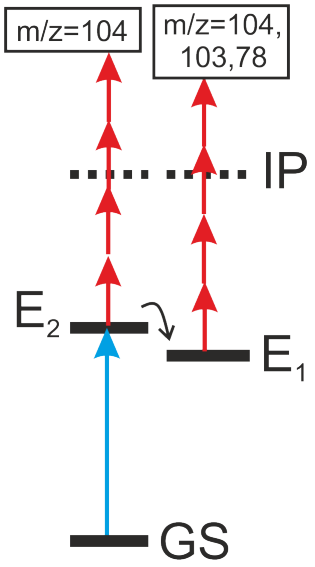

Figure 8.18: *Scheme for the excitation of para-xylylene with 800 nm*

Photoelectron anisotropy

The photoelectron anisotropy with 400 nm probe is positive (0.8-1.2 between 0.25-2.5 eV; see fig. 8.17) and doesn't change during the decay. The anisotropy between 0 and 0.25 is less positive (0.4), which for electrons with low kinetic energies is not surprising. Photoelectron anisotropies of multiphoton processes are complicated to interpret, since states with different electronic character can show the same photoelectron anisotropy. The photoelectron anisotropy is therefore not considered.

8.1.3 Conclusion

The proposed model (see fig. 8.18) is in agreement with the experimental data: *para*-xylylene is initially excited into the state E_2. This state relaxes fast to a lower-lying state, whose population is directly observed in the dissociative photoionization products.

An attribution of the initially excited state E_2 based on the literature is not straightforward. With 266 nm we excite into the band from 350 to 250 nm observed (in matrix) by Pearson et al., with a maximum at 295 nm [302]. Ha attributed this band to the first excited singlet state $^1B_{1u}(\pi\pi*)$ using *ab initio* configuration interaction. With an oscillator strength of 0.846 this state is very bright, higher-lying states are dark.

The next bright singlet state is $^1B_{1u}(\pi\pi*)$=8.69 eV, which lies above his calculated ionization energy. Two triplet states are in the vicinity of the first singlet state: $^3B_{3g}(\pi\pi*)$ =4.79 eV and $^3B_{1u}(\pi\pi*)$ =4.88 eV, one triplet states lies substantially lower $^3B_{1u}(\pi\pi*)$ =2.27 eV [305]. These excited-state calculations are in agreement with CASSCF calcula-

state	B3LYP[a)]	B3P86[a)]	CAM-B3LYP[b)]	ωB97xD[c)]
1	$^1B_{1u}$ 4.14 (0.74) ππ*	$^1B_{1u}$ 4.17 (0.74) ππ*	$^1B_{1u}$ 4.37 (0.86) ππ*	$^1B_{1u}$ 4.45 (0.84) ππ*
2	$^1B_{3g}$ 4.47 (0.0) ππ*	$^1B_{3g}$ 4.51 (0.0) ππ*	$^1B_{3g}$ 4.93 (0.0) ππ*	$^1B_{3g}$ 5.03 (0.0) ππ*
3	$^1B_{3g}$ 4.73 (0.0) ππ*	$^1B_{3g}$ 4.77 (0.0) ππ*	$^1B_{3g}$ 5.11 (0.0) ππ*	$^1B_{3g}$ 5.11 (0.0) ππ*
4	$^1B_{3u}$ 4.88 (0.0035) π-s-Ryd	$^1B_{3u}$ 4.36 (0.0035) π-s-Ryd	$^1B_{1g}$ 6.28 (0.0) **σπ***	$^1B_{1g}$ 6.24 (0.0) **σπ***
5	$^1B_{2g}$ 5.21 (0.0) π-p_x-Ryd	^1A_g 5.57 (0.0) π-p_y-Ryd	^1A_g 6.37 (0.0) π-s-Ryd	^1A_g 6.59 (0.0) **σπ***

Table 8.4: *Vertical excitation energies of the first five excited singlet states of para-xylylene in eV (oscillator strength). The major contribution is given below the oscillator strength.* [a)] *6-311++G** [197]* [b)] *Def2TZVP [313, 314]* [c)] *cc-pVDZ [198, 199]*

tions by Boboski et al., who calculated the first triplet state $^3B_{1u}$ at 1.65 eV and the first singlet $^1B_{1u}$ state at 4.38 eV [304]. It is tempting to attribute now E_2 to the singlet state $^1B_{1u}(\pi\pi*)$, and E_1 to the triplet states in the vicinity. But all triplet states have ππ*-character, and $^1\pi\pi^* \rightarrow {}^3\pi\pi^*$ transitions are slow according to the El Sayed rules [40].

The first five excited singlet states, calculated with TDDFT[1] and different functionals [195, 196, 208–211] using the Gaussian09 program package [194], are sum-

[1] Thanks to Florian Hirsch for providing the TDDFT calculations.

marized in table 8.4. The excited states were calculated from a singlet ground state geometry (D_{2h}) optimized in a first step with B3LYP [208,209] followed by a Gaussian-4 [315] calculation. The geometry was optimized with an imposed D_{2h}-symmetry.

All four functionals agree on the nature of the first three excited states, namely that the first excited singlet state is very bright $\pi\pi^*$-state, corresponding to the $^1\pi\pi^*$-excitation as proposed in the literature [304,305]. For the fourth and higher-lying electronic states this is no longer the case. B3LYP and B3P86 predict a bright $^1B_{3u}$-state, which corresponds to a s-Rydberg state. CAM-B3LYP and ωB97xD predict a dark $^1B_{1g}$-state, corresponding to a $\sigma\pi*$-transition. All higher-lying states up to the tenth excited state are dark.

Correctly describing Rydberg states with TDDFT is not easy and can fail for open-shell species (see chapter 7.1 for the benzyl radical), since charge transfer states are also possible, which are not well described with TDDFT. But it can be used for a first hypothesis until higher-level calculations are on hand[2]. With 266 nm the $^1B_{3u}$ s-Rydberg state could be excited. It can then either deexcite to a lower-lying singlet state via a conical intersection, and since the first - third excited states are energetically very close, this hypothesis is valid. Passing via a Rydberg state can accelerate the dynamics, since it allows a localized electron to interact with the other end of the molecule, as was observed in the case of tetrakis(dimethylamino)ethylene [316].

It could also deexcite via an intersystem crossing into a triplet state. The first five excited triplet

[2] Higher-level calculations on the excited states of the *para*-xylylene are currently undertaken by K. Issler of the research group of R. Mitrić.

state	B3LYP[a)]	B3P86[a)]	CAM-B3LYP[b)]	ωB97xD[c)]
1	$^3B_{1u}$ 1.47 ππ*	$^3B_{1u}$ 1.40 ππ*	$^3B_{1u}$ 1.05 ππ*	$^3B_{1u}$ 1.19 ππ*
2	$^3B_{3g}$ 3.44 ππ*	$^3B_{3g}$ 3.41 ππ*	$^3B_{3g}$ 3.36 ππ*	$^3B_{3g}$ 3.47 ππ*
3	^3A_g 4.16 ππ*	^3A_g 4.14 ππ*/π-p_y-Ryd	^3A_g 4.02 ππ*/π-s-Ryd	^3A_g 4.16 ππ*/π-s-Ryd
4	$^3B_{3g}$ 4.45 ππ*	$^3B_{3g}$ 4.48 ππ*	$^3B_{1u}$ 4.48 ππ*	$^3B_{1u}$ 4.92 ππ*
5	$^3B_{1u}$ 4.72 ππ*	$^3B_{1u}$ 4.68 ππ*	$^3B_{3g}$ 4.99 ππ*	$^3B_{3g}$ 5.02 ππ*

Table 8.5: *The excitation energies of the first five excited triplet states of para-xylylene in eV. The ground triplet state lies 1.39 eV higher in energy (B3LYP) than the ground singlet state. The major contribution(s) is given below the oscillator strength.* [a)] *6-311++G** [197]* [b)] *Def2TZVP [313, 314]* [c)] *cc-pVDZ [198, 199]*

states calculated just as for the singlets are summarized in table 8.5. Several triplet states lie very close to the initially excited singlet state. But $^1\pi\pi^* \rightarrow {}^3\pi\pi^*$ intersystem crossings are forbidden by the El-Sayed rules, and the time constant is very fast for an intersystem crossing, making this process unlikely.

Another hypothesis is that with 266 nm we excite vertically into the S_1-state, which is in the adiabatic picture the S_2-state (see fig. 8.19). In the adiabatic picture we excite into S_2, which then relaxes to S_1(first time-constant). The (adiabatic) S_1-state then relaxes to the electronic ground state (second time-constant). Since the (adiabatic) S_1-state could be ionized into a different ionic state, which shows fragmentation, the population of the adiabatic S_1-state could thus be followed directly

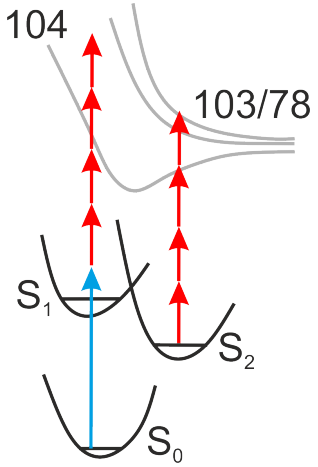

Figure 8.19: *Adiabatic/vertical excitation picture of para-xylylene, the numerotation of the excited states follows the vertical excitatition energies. The cationic states (gray) are labeled with the corresponding masses of the cations.*

in the mass spectra fragments of benzene and *para*-xylylene-H. This postulated mechanism is in agreement with the high oscillator strength of the S_1-state in the TDDFT calculations (0.7-0.8), which is two orders of magnitude higher than the next bright state found with the B3LYP and B3P86 functionals. For those two functionals the excitation energy of S_1 is about 0.5 eV below our excitation energy, but the excitation energies calculated with TDDFT are not that precise.

8.2 Examination of two *Ortho*-Xylylene precursors

Two potential *ortho*-xylylene precursors were examined with the fs-time-resolved Saclay setup; photoelectron spectra, photoion and mass spectra were measured for both. These were compared to photoelectron and mass spectra of benzocyclobutane, an isomer of *ortho*-xylylene. Since the time-resolved spectra of the pyrolysis products of both potential *ortho*-xylylene precursors were qualitatively identical, only the results of 2-indanone will be presented in detail.

8.2.1 Experimental conditions and data treatment

Two potential precursors for *ortho*-xylylene were examined: 2-indanone and 3-isochromanone (*Sigma-Aldrich*, used without further purification). During pyrolysis they can eject carbon monoxide or carbon dioxide respectively, forming *ortho*-xylylene. It is also possible that during pyrolysis *ortho*-xylylene isomerizes to benzocyclobutane. Since the rearrangement of the molecule is small, the activation barrier for this process is with 25.6 kcal/mol [290] quite low (see fig. 8.20).

Benzocyclobutane is commercially available (*Sigma-Aldrich*, used without further purification). All substances were seeded into gas phase using the T-filter setup (see chapter 5.1). 266 nm was used as the pump laser and 800 nm as the probe laser. No signal could be obtained with 400 nm probe laser for 2-indanone and 3-isochromanone, for benzocyclobutane no experiments with 400 nm as the probe laser were carried out. The laser focal points and

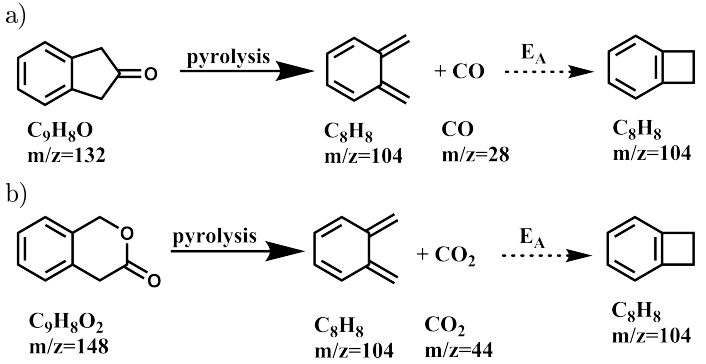

Figure 8.20: *Production of ortho-xylylene and subsequent isomerization to benzocyclobutane by pyrolysis of a) 2-indanone and b) 3-isochromanone*

other experimental parameters are summarized for 2-indanone and 3-isochromanone in table 8.6. For the 266 nm pump beam a 500 mm lens was used, the 800 nm laser beam was focalized using a 700 mm lens.

At least four scans were averaged for every decay, the polarization of the pump/probe laser was varied between horizontal/horizontal and vertical/horizontal. The spectra did not show any rotational anisotropy, as can be seen exemplary in fig. 8.21 for the decay of the total photoelectron signal for 2-indanone. Consequently all represented measurements are the rotational mean ((2*$\text{Signal}_{\text{ortho}}$+ $\text{Signal}_{\text{parallel}}$)/3). The photoelectron spectra were inverted using the pBasex algorithm with a $P_0P_2P_4$ basis set as implemented in the *Analyse*-program, decays were fitted in the same way as for *para*-xylylene (see section 8.1).

precursor	py rolysis /W	T/ °C	p_{He}/ bar abs.	λ/ nm	P/ µJ	focus /cm
2-indanone	38	85	2	266	8	4
				800	830	10
3-iso-chromanone	43	95	2	266	10	-2
				800	800	4
Benzo-cyclo-butane	variable	25	2.5			

Table 8.6: *Laser focalization and powers of the experiments concerning ortho-xylylene, a positive focus corresponds to a focal point after the laser spatial overlap, a negative focus to a focal point before laser spatial overlap*

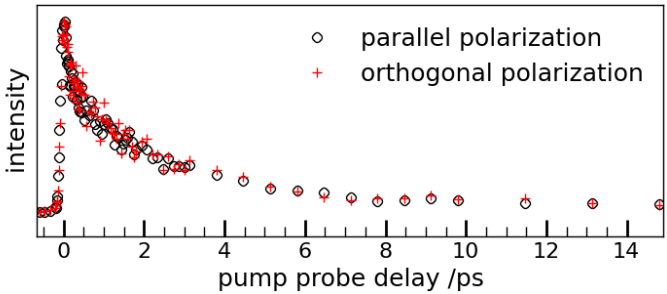

Figure 8.21: *Decay of the total photoelectron signal of 2-indanone for parallel laser polarization and orthogonal laser polarization*

8.2.2 Experimental results of the two *ortho*-xylylene precursors

Pyrolysis conditions

i

All masses present in the time-resolved mass spectra showed the same temporal behavior.

Both 2-indanone and 3-isochromanone show a satisfactory pyrolysis on/pyrolysis off ratio (see fig. 8.22 and fig. 8.23), but for the 2-indanone it is cleaner. Without pyrolysis (black line) the precursor (m/z=132) and also a large peak at m/z=104 is visible for 2-indanone. The width of the m/z=104 peak indicates that it is formed by photodissociation from the precursor. With the pyrolysis on, the precursor peak disappears, and m/z=104 increases. The smaller peak visible with pyrolysis on at m/z=105 corresponds not only to $^{13}CC_7H_8$ (theoretically 8%, measured 15% of m/z=104), but also contains C_8H_9. Possibly C_8H_8 abstracted a hydrogen atom from another molecule during pyrolysis. Therefore only the m/z=104 peak is analyzed in the time-resolved mass spectra. The small peak at m/z=91 stems from previous experiments with tropyl (see chapter 7.2).

Without pyrolysis (black line, fig. 8.23) 3-isochromanone shows only a very large peak centered

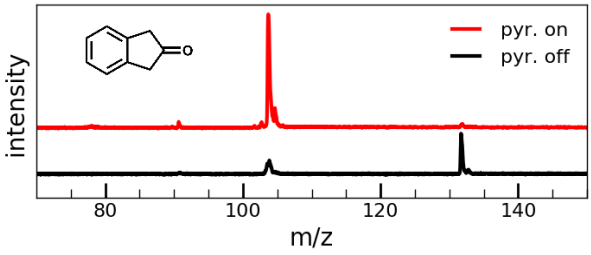

Figure 8.22: *Mass spectra at pump-probe conditions with pyrolysis on and pyrolysis off for 2-indanone*

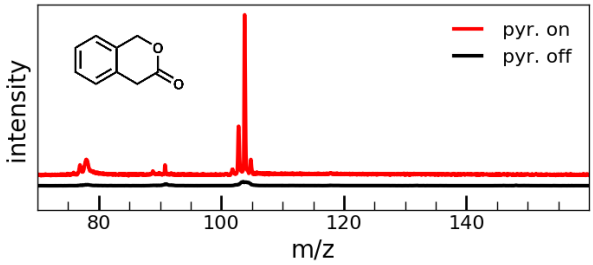

Figure 8.23: *Mass spectra at pump-probe conditions with pyrolysis on and pyrolysis off for 3-isochromanone*

at m/z=104, the peak at m/z=91 again stems from previous tropyl experiments. Once the pyrolysis is turned on (red line), m/z=104 appears as the largest, sharp peak along with several other peaks.

M/z=103 is the second strongest peak (C_8H_7), and even m/z=102 is clearly visible. M/z=105 has an intensity of 10% compared to m/z=104, and corresponds thus to $^{13}CC_7H_8$. The other mass visible is m/z=77, most likely the phenyl radical. The large peak indicates that it is formed by dissociative photoionization.

In the following only the time-resolved experimental results for 2-indanone will be discussed, these are qualitatively identical with the results for 3-isochromanone.

Time-resolved mass spectra

In fig. 8.24 a mono- and a bi-exponential fit with offset are used to fit the m/z=104 of 2-indanone (pyrolysis on). A bi-exponential fit reproduces better the data at short times, and the IRF is in better agreement with previous experiments. The first time-constant, however, is much shorter than the

IRF, so we can only say that one time-constant shorter than the IRF is involved.

a)

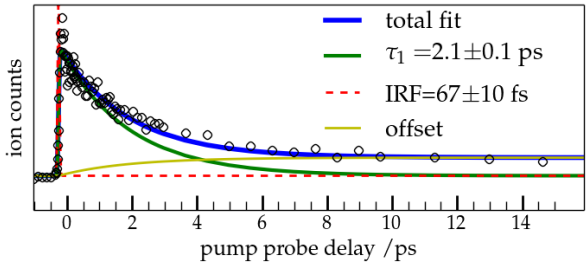

b)

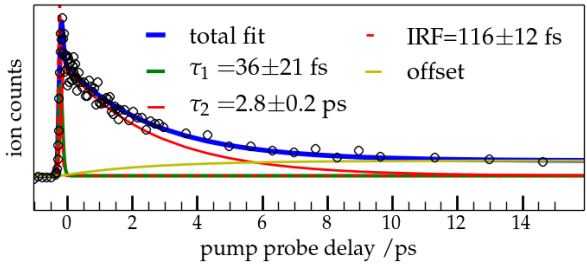

Figure 8.24: *Mono-exponential (a) or bi-exponential (b) fit with offsets of the m/z=104 signal of the TOF decay of 2-indanone with pyrolysis on*

Time-resolved ion images

In time-resolved mass spectra (and in time-resolved photoelectron spectra), a distinction between signal from molecules in the molecular beam, signal from dissociative photoionization and molecules in the background (leftover molecules in the detection chamber) is not possible. With ion-images those

three processes are distinguished easily (see section 5.4).

In ion images (fig. 8.25) gated on the m/z=104 pyrolysis product (of 2-indanone) the molecular beam (red box) is about a factor of 1000 more intense than the background signal (yellow box). No dissociative processes are visible.

Just as in the mass spectra, a mono-exponential fit is insufficient to reproduce the molecular beam decay (fig. 8.26-a). A bi-exponential fit (fig. 8.26-b) reproduces well the decay and also leads to a reasonable IRF. The signal from the background molecules (fig. 8.26-c) shows a different temporal behavior. Despite it being so noisy, it shows clearly a different dynamic, namely a long-lived offset after a mono-exponential decay. Just as for the tropyl radical (see chapter 7.2) the offset might stem from

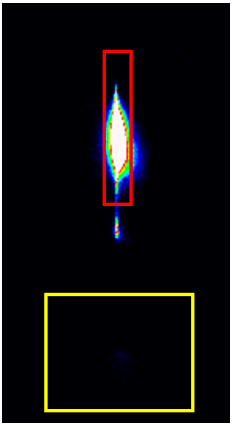

Figure 8.25: *Ion image of 2-indanone with pyrolysis on gated on m/z=104 with regions of interests whose decays are displayed in fig. 8.26.*

a)

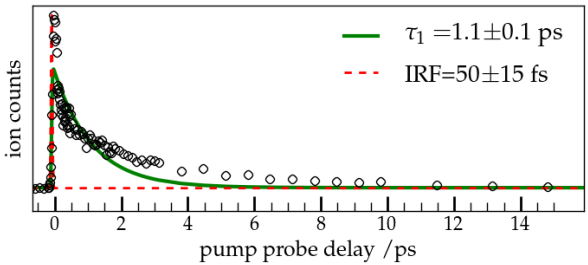

b)

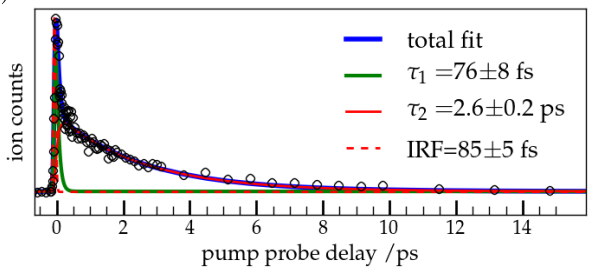

c)

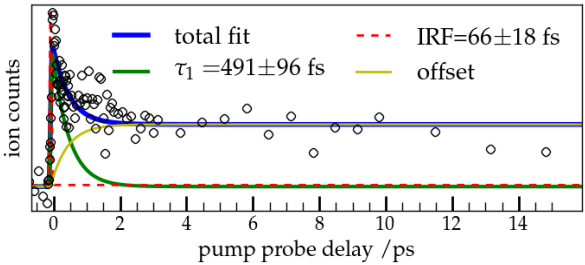

Figure 8.26: *Mono-exponential (a) or bi-exponential (b) fit of the molecular beam decay (red square in fig. 8.25) of the time-resolved ion images for m/z=104 (T(A)=9.22 µs, T(B)=300 ns), and (c) mono-exponential fit with offset of the background signal (yellow square in fig. 8.25).*

a stable molecule with roughly the same mass, benzocyclobutane is the most probable candidate.

Time-resolved photoelectron spectra

Since the mass spectra showed predominately only m/z=104, time-resolved photoelectron spectra were measured.

In fig. 8.27 the time-resolved photoelectron spectrum of 2-indanone is displayed, which is - within the uncertainties - identical to the time-resolved photoelectron spectrum of 3-isochromanone. In the upper three panels different fits of the total photoelectron signal are shown. A mono-exponential fit (upper panel) is insufficient at long times (8 ps), a bi-exponential (middle panel) reproduces better the experimental data at longer times (12 ps). The best agreement is with a bi-exponential fit including an offset (lower panel).

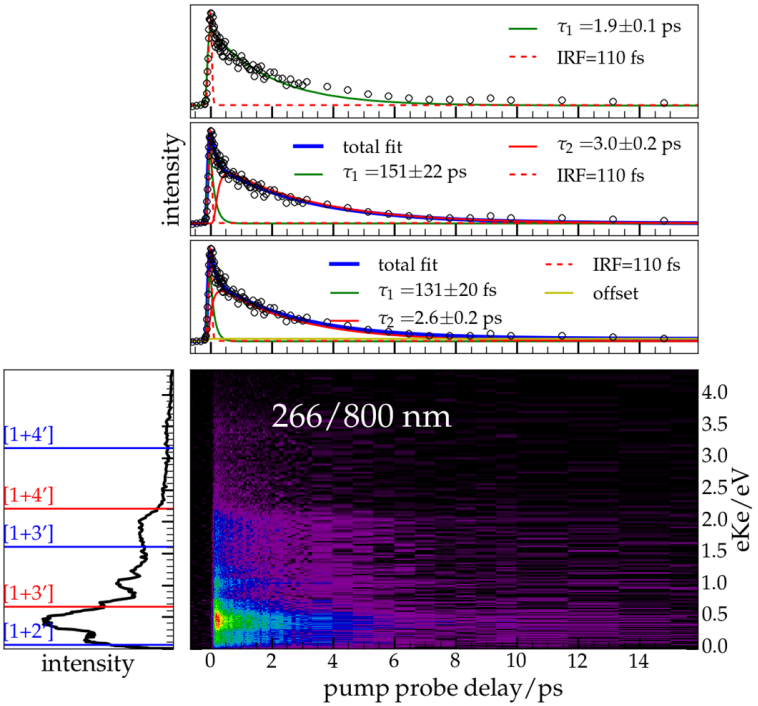

Figure 8.27: *Rotational mean TRPES for 2-indanone with pyrolysis on. The upper panel shows the decay summed over all photoelectron energies with a mono-exponential fit; the second panel shows the decay summed over all photoelectron energies with a bi-exponential fit; and the third shows a bi-exponential fit with an offset. The IRF was held fixed, because otherwise no meaningful fit could be achieved. In the left panel the photoelectron spectrum summed over all times is displayed. The ionization limits for ortho-xylylene (IE=7.70 eV [292]) are depicted in blue, those for benzocyclobutane in red (IE=8.65 eV [291]).*

This is in agreement with the observed photoion images, and corresponds to the sum of the observed processes there. The IRF for the fits of the photoelectron spectrum was held fixed and issued out

of the mono-exponential fit, since fitting the IRF and a bi-exponential fit at the same time resulted in non-realistic values (τ_1=5 fs). All bands in the photoelectron spectrum showed the same temporal behavior. In table 8.7 the time-constants of 2-indanone and 3-isochromanone for all experiments are summarized. Both show similar time-constants, with the exception of the mass spectrum decay of 2-indanone. The decay of the photoelectron signal is a sum over all signal issued out of different processes, may those be molecular beam, dissociative photoionization or background.

Precursor		IRF/fs	τ_1/fs	τ_2/ps	offset
2-indanone	ms	97 ± 10	112 ± 29	1.4 ± 0.3	no
	pi_{beam}	85 ± 5	76 ± 8	2.6 ± 0.2	no
	pi_{bg}	66 ± 18	491 ± 96	—	yes
	pe	110	131 ± 20	2.6 ± 0.2	yes
3-isochromanone	ms	90 ± 6	81 ± 11	2.6 ± 0.1	no
	pi_{beam}	85	90 ± 13	2.5 ± 0.1	no
	pi_{bg}	85 ± 7	10.34 ± 2.3 ps	—	yes
	pe	85	80 ± 35	2.2 ± 0.2	no

Table 8.7: *Summary of the fit constants for the different experiments of the different precursors 2-indanone and 3-isochromanone for m/z=104 (with the exception of the photoelectron experiments). If no deviation is given for the IRF, it was held fix to achieve a meaningless fit. The guess issued out of a fit with less constants, meaning for a mono-exponential fit instead of a bi-exponential fit. ms=mass spectra, pe=photoelectron spectra, pi=photoion spectra with beam=molecular beam and bg=background*

The question still remains whether the observed mass m/z=104 corresponds to the pyrolysis product *ortho*-xylylene or to its isomer benzocyclobutane (for the equations see fig. 8.20). The activation

energy between those two isomers is small, since only minor rearrangements of the molecule are necessary. In the photoelectron spectrum summed over all times (left panel in fig. 8.27) the blue lines represent the ionization limits of *ortho*-xylylene, the red those of its isomer benzocyclobutane. The fall-off of the photoelectron signal at 2.2 eV is in better agreement with the ionization limits of benzocyclobutane than those of *ortho*-xylylene.
To verify the origin of the observed signals, benzocyclobutane without pyrolysis as well as with pyrolysis on was examined.

8.2.3 Experimental results of benzocyclobutane

In fig. 8.28 the time-resolved photoelectron spectrum of benzocyclobutane with no pyrolysis has a superb pump-probe signal. It shows a step-function with no change up to 400 ps. The photoelectron spectrum summed over all times, displayed in the left panel of fig. 8.28, shows two (three) peaks, situated each time just below the ionization limit. Comparing this to the photoelectron spectrum of 2-indanone, shown as the gray area, the major peaks and the cutoff coincide nicely. The side-peaks are weaker in the photoelectron spectrum of benzocyclobutane with the pyrolysis off.

This changes once benzocyclobutane is heated with the pyrolysis. The offset disappears with the pyrolysis at 20 W (see fig. 8.29) and instead a decay appears, which is reproduced with a bi-exponential decay (middle panel). A mono-exponential decay does not fit as cleanly the peak at t=0.0 ps, and the obtained IRF is not in good agreement with previous values for the same setup. All bands in

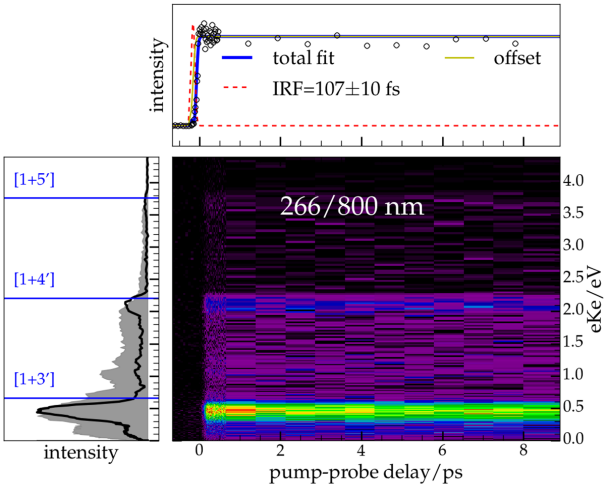

Figure 8.28: *Rotational mean TRPES for benzocyclobutane with pyrolysis off. The upper panel shows the decay summed over all photoelectron energies fitted with an offset; in the left panel the photoelectron spectrum summed over all times is displayed. The gray area corresponds to the photoelectron spectrum of 2-indanone with pyrolysis on. The ionization limits for benzocyclobutane (IE=8.65 eV [291]) are depicted in blue.*

the photoelectron spectrum show the same temporal behavior.

The photoelectron spectrum, displayed in the left panel, shows now an even better agreement in shape with the photoelectron spectrum of 2-indanone (gray area). Not only are the major peaks reproduced, but also the smaller side-peaks appear with almost the same relative intensities. The measured photoelectron spectra from the precursors 2-indanone and 3-isochromanone are therefore attributed to benzocyclobutane. Apparently the transformation of ortho-xylylene to benzocyclobutane during pyroly-

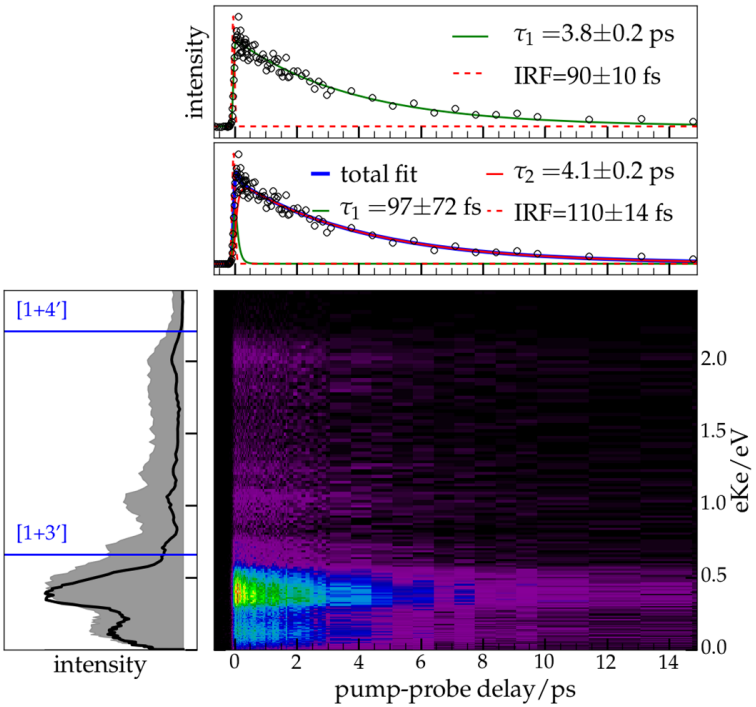

Figure 8.29: *Rotational mean TRPES for benzocyclobutane with pyrolysis on=20W. The upper two panels show the decay summed over all photoelectron energies with a mono-exponential and a bi-exponential fit respectively; in the left panel the photoelectron spectrum summed over all times is displayed. The gray area corresponds to the photoelectron spectrum of 2-indanone with pyrolysis on. The ionization limits for benzocyclobutane (IE=8.65 eV [291]) are depicted in blue.*

sis is very efficient, which is considering the small activation barrier of 25.6 kcal/mol (1.1 eV) [290] not surprising.

In fig. 8.30 the decays of the mass spectrum signal m/z=104 at different pyrolysis powers are compared. The corresponding time-constants are

summarized in table 8.8. With increasing pyrolysis power the signal decays faster, since the molecule has a higher internal energy, and conical intersections are reached faster in vibrationally excited molecules.

Pyrolysis power/ W	IRF/fs	τ_1/ps	τ_2/ps	offset
off	107 ± 10	—	—	yes
14	121 ± 10	0.7 ± 0.3	16 ± 1	yes
20	112 ± 10	0.9 ± 0.3	11.8 ± 0.9	no

Table 8.8: *Summary of the fit constants of the mass spectrum signal m/z=104 of benzocyclobutane at different pyrolysis powers.*

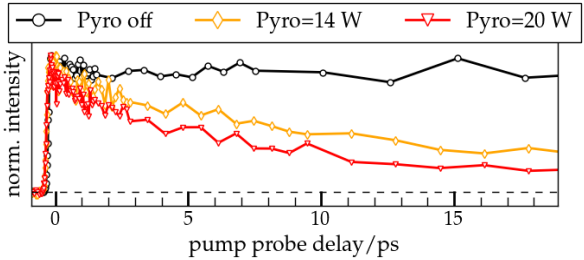

Figure 8.30: *Comparison of the mass spectra decays of benzocyclobutane (m/z=104) at different pyrolysis powers. With increasing pyrolysis power the decays shorten.*

8.2.4 Conclusion

With 266 nm benzocyclobutane is excited into the $S_1(\pi\pi^*)$-state, which is known to show a vibrationally resolved UV absorption spectrum from 269-258 nm. This state fluoresces as well, and is therefore long-lived [317]. *Ortho*-xylylene itself does either not ab-

sorb at this wavelength (in accordance with the absorption spectrum measured by Miller et al. [294]), or the isomerization of *ortho*-xylylene to benzocyclobutane under flash pyrolysis conditions is very efficient. It is most likely both. The isomerization from *ortho*-xylylene to benzocyclobutane has a small activation barrier, so it is not surprising that it is formed from *ortho*-xylylene precursors during high pyrolysis temperatures. *Ortho*-xylylene was successfully produced from the precursor 2-indanone by using flash photolysis [284], where the intermediate temperatures are much lower.

Comparing computed absorption spectra of *ortho*-xylylene and benzocyclobutane (fig. 8.31), the absorption spectrum of *ortho*-xylylene is dominated by the first excited state at 400 nm. At 266 nm only a very small absorption is visible for *ortho*-xylylene, whereas for benzocyclobutane its first excited state absorbs very well in that region. Even if *ortho*-xylylene is created during pyrolysis, benzocyclobutane absorbs better and, by its strong absorption, would obscure absorption *ortho*-xylylene. REMPI experiments with 400 nm with these two precursors

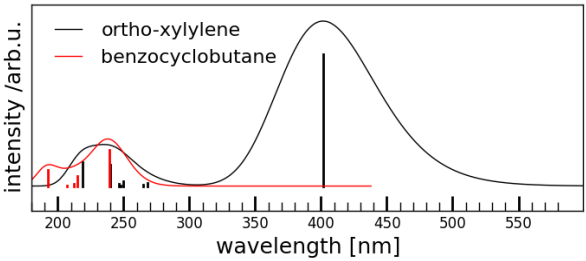

Figure 8.31: *Absorption spectrum of ortho-xylylene and benzocyclobutane calculated TDDFT/B3LYP/6-311++g(d,p) using the program package Gaussian09* [194]

are planned in Würzburg, to finally examine *ortho*-xylylene using IR/UV ion dip spectroscopy, as was done recently with the propargyl radical [318]. It would also be interesting to examine the same possibly presursors in a 400 nm pump/800 nm probe setup. If 400 nm acts as a pump laser for *ortho*-xylylene, it is not surprising that no 266 nm pump/ 400 nm probe signal could be obtained, since 266 nm pumps the benzocyclobutane, and 400 nm the *ortho*-xylylene.

Another conclusion that can be drawn from this experiment concerns the cooling of the pyrolysis products in the molecular beam. It is likely that benzocyclobutane is formed directly in the SiC-tube, and should be cooled down in the supersonic beam expansion. But we still observe a decay in the mass spectra, which was not observed for benzocyclobutane without pyrolysis, showing that a supersonic beam expansion cannot completely compensate the heating from the pyrolysis (see section 3.2).

Chapter 9 Halogen-containing radicals

9.1 Trichloromethyl radical

Halogen atoms and halogen-containing radicals act as catalysts leading to stratospheric ozone depletion. They are especially devastating considering the long lifetimes until they are washed out of the atmosphere: CCl_4, for example has a lifetime of 42 years [17]. Halogen-containing radicals are often toxic, but their precursors are chemically inert and have long residence times. Another example is 2,3,7,8-tetrachlorodibenzodioxin, a carcinogen contaminant in the herbicide Agent Orange, which was released during the Vietnam war and is still persisting in the environment [323].

The combustion of hazardous waste, which often contains chlorinated hydrocarbons [324], can lead to the formation of the trichlormethyl radical, as proposed recently via chlorine abstraction of CCl_4 [325]. As one of the simpler chlorinated methyl radical derivatives, its kinetics, including the formation from various precursors and its reactions with other molecules/radicals such as CH_3 and NO have received considerable interest. They have been studied extensively over the years [325–335].

Spectroscopic studies of the CCl_3 radical, however, are less abundant. Its pyramidal structure (C_{3v}) was confirmed by infrared spectroscopy [336], ESR studies [337] and theoretical calculations [338]. The cation has a planar D_{3h}-symmetry [322] instead. As for the excited states of the CCl_3 radical, a broad emission band between 420 and 700 nm with a max-

state [319–322]	E/ nm	E/ eV
X^2A_1		
A^2A_2	390	3.0
B^2A_1	400	3.1
$C^2A_1'(3s)$	210	5.90
D^2E	227	5.4
$E^2E'(3p)$	212.0	5.848
$F^2A_2''(3p)$	208.9	5.935
G(3d)	195.2	6.350
$K^2E'(4p)$	177.8	6.972
$L^2A_2''(4p)$	177.3	6.994
M(4d)	173.2	7.158
$X^{+1}A_1'$	153.8	8.06

Table 9.1: *Known electronic states of the* CCl_3 *radical and cation. Energies written in italic correspond to estimates and not to experimental values*

imum at 490 nm measured in an electrical discharge of $CCl_4$was attributed to the CCl_3 radical [339]. This claim was, however, contested. Three years later the same authors showed that CCl_4 emits in the same range [340], and Ibuki et al. attributed the band in this region to CCl_2 [341].

Hintsa et al. examined the photodissociation of CCl_3 with 308 nm to CCl_2 and Cl in a molecular beam, showing that an average of 13 kcal/mol is released in translation. They did not, however, identify the electronic state from which dissociation occurs [326], but it is probably the first excited electronic state.

At lower wavelengths the UV absorption spectrum shows a band between 190 and 270 nm, peaking at 210 nm [320, 342]. This band exhibits considerable fine structure, attributed to the $X^2A_1 \rightarrow C\ ^2A_1'(3s)$ Rydberg state transition [319]. Various other planar Rydberg states (summarized with other electronic states of the CCl_3 radical and cation in table 9.1) were observed by Hudgens et al., out of which they extracted the adiabatic ionization energy 8.109 ± 0.005 eV [321]. This value is considerably lower than the earlier determined values (8.28 eV) obtained via monoenergetic electron impact [343]. From photoelectron spectra an adiabatic ionization energy of 8.06 ± 0.02 eV was obtained [322], which was reproduced by DFT calculations (8.05 eV) [344].

In conclusion even though the ionization energy of CCl_3 is well characterized experimentally, its electronic states are not. This gap will therefore be closed by characterizing the different electronic transitions examined in the literature using TDDFT. This will allow interpretation of time-resolved experiments on the $X^2A_1 \rightarrow C^2A_1'$transition into a 3s Rydberg state.

9.1.1 Experimental

The trichloromethyl radical was produced using pyrolysis from the precursor bromotrichloromethane (*Sigma-Aldrich*, used without further purification, see fig. 9.1), and examined using the Saclay setup (see section 5.4) with 266/800 nm (see section 5.4.2.1).

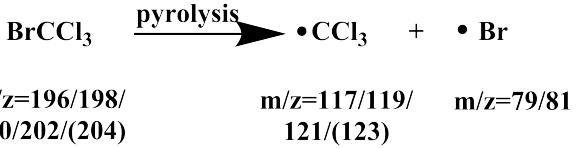

Figure 9.1: *Production of the trichlormethyl radical by pyrolysis of bromotrichloromethane*

The precursor was put in the source for liquids (see section 5.1), and seeded into the gas phase using argon as a carrier gas at 2 bar absolute pressure. 30 W were applied to the SiC tube. The angle of the pump laser polarization was varied for the time-resolved photoelectron spectra (pump-probe polarization parallel-parallel and pump-probe polarization vertical-paralel). The photoelectron spectra were inverted using the pBasex algorithm, decays were fitted using the fit program as detailed in section 13, the plotted uncertainties correspond to fit uncertainties and not to experimental uncertainties.

9.1.2 Excited states of the CCl_3 radical

All calculations were performed with the program package Gaussian09 [194]. In table 9.2 the parameters for the optimized ground state with DFT using the functionals B3LYP [208–211], CAM-B3LYP [195] and ωB97xD [196] with a 6-311++g(d,p)) [197] basis set are compared to known experimental values.

a)

b)

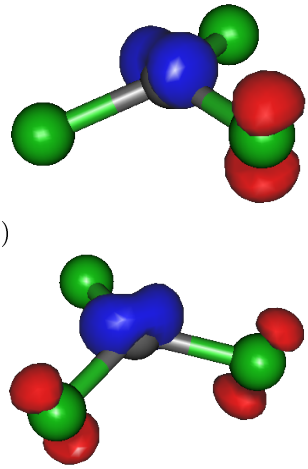

Figure 9.2: *Excited state difference for the third (a) and fourth (b) excited states. Red corresponds to decreasing electron intensity during the transition, blue to increasing electron density.*

	B3LYP	CAM-B3LYP	ωB97xD	Exp
symmetry	C_{3v}	C_{3v}	C_{3v}	C_{3v} [336]
∡(ClCCl)/°	116.82	117.28	117.03	116.7 [321]
r(CCl)/Å	1.73	1.71	1.72	
∡(ClClClC)/°	20.15	18.68	19.50	10.6 [321]

Table 9.2: *Optimized geometries of the CCl_3 radical in its ground state calculated with DFT using different functionals (basis set: 6-311++g(d,p))*

a)

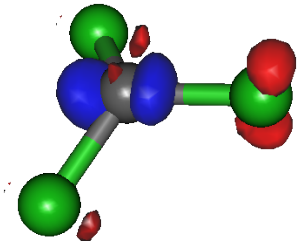

b)

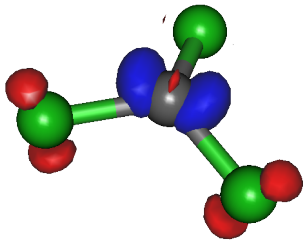

Figure 9.3: *Excited state difference for the fifth (a) and sixth (b) excited states. Red corresponds to decreasing electron intensity during the transition, blue to increasing electron density.*

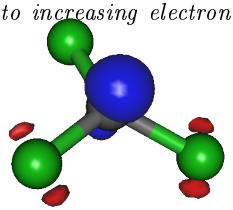

Figure 9.4: *Excited state difference for the seventh excited states. Red corresponds to decreasing electron intensity during the transition, blue to in-*

The correct symmetry is reproduced with all three functionals. The Cl-C-Cl angle deviates from the experimental values only with maximal deviations of 0.5 %, with the B3LYP functional performing best. The C-Cl bond lengths are similar (maximal difference between the different functionals of 1%), which is not the case for the dihedral angle. All three functionals considerably overestimate this dihedral angle compared to the experimental value (76-90%). The experimental values were, however, obtained by taking into account *ab inito* bond lengths.

In table 9.3 the excited states calculated with TDDFT [190] and different functionals for CCl_3 are listed with their symmetry attribution, energy, oscillator strength and spin expectation value. For B3LYP and ωB97xD the spin-contamination is negligible, only for CAM-B3LYP the deviation from the expected value (0.75) exceeds slightly 10 %.

The first excited state is dark for all three functionals, and the second excited state symmetry-forbidden. In a molecular orbital scheme calculated for B3LYP/6-311++g(d,p), displayed in fig. 9.5, they correspond to the SOMO→LUMO and HOMO-1→SOMO transition. The third/fourth and fifth/sixth excited states are degenerated, optically active and dominated by the orbital transition of two electrons. This two-transition character is dis-

state	TDDFT/ B3LYP	TDDFT/ CAM-B3LYP	TDDFT/ ωB97xD
0	$^2A_1$	$^2A_1$	$^2A_1$
1	$^2A_1$ 3.38 (0.0, 0.78)	$^2A_1$ 3.74 (0.0, 0.80)	$^2A_1$ 3.71 (0.0, 0.79)
2	$^2A_2$ 4.55 (0.0, 0.77)	$^2A_2$ 5.01 (0.0 , 0.78)	$^2A_2$ 4.93 (0.0, 0.78)
3	^2E 5.11 ($2.5 \cdot 10^{-3}$, 0.79)	^2E 5.48 ($1 \cdot 10^{-4}$, 0.85)	^2E 5.48 ($2.5 \cdot 10^{-3}$, 0.82)
4	^2E 5.11 ($2.4 \cdot 10^{-3}$, 0.79)	^2E 5.48 ($1 \cdot 10^{-4}$, 0.85)	^2E 5.48 ($2.5 \cdot 10^{-3}$, 0.82)
5	^2E 5.33 ($3.2 \cdot 10^{-2}$, 0.79)	^2E 5.71 ($4.2 \cdot 10^{-2}$, 0.80)	^2E 5.70 ($3.6 \cdot 10^{-3}$, 0.82)
6	^2E 5.33 ($3.2 \cdot 10^{-2}$, 0.79)	^2E 5.71 ($4.2 \cdot 10^{-2}$, 0.80)	^2E 5.70 ($3.62 \cdot 10^{-2}$, 0.82)
7	^2E 5.62 ($3.0 \cdot 10^{-2}$, 0.78)	$^2A_1$ 5.98 ($9.5 \cdot 10^{-3}$, 0.81)	^2E 6.03 (0.33, 0.79)

Table 9.3: *Excited states of CCl_3 calculated with TDDFT (basis set: 6-311++g(d,p)) using different functionals from optimized ground state structures, energy in eV (oscillator strength, $<S>^2$)*

played schematically in fig. 9.5 as two arrows with the same color, the more intense arrow corresponds to the transition with slightly more weight. For these transitions two electrons and show considerable two-transition character. It makes therefore more sense to look at the excited state difference of the transition instead of the multiple initial and

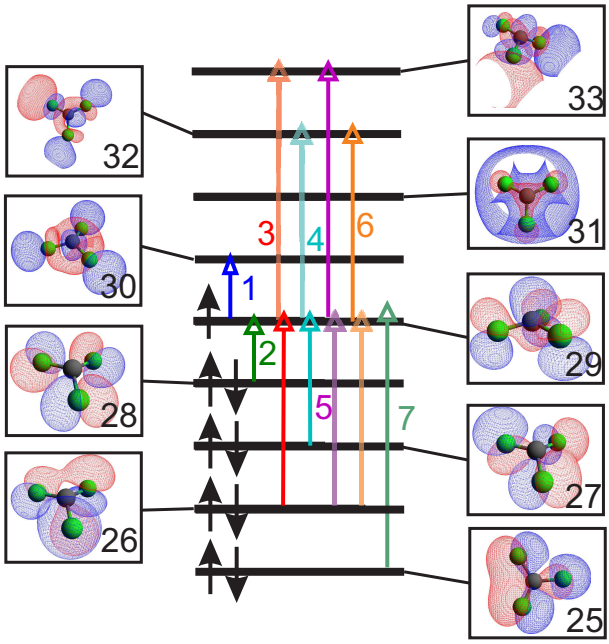

Figure 9.5: *The four highest occupied and three lowest unoccupied molecular orbitals of CCl_3 for the optimized ground state with B3LYP/6-311++g(d,p). The colored arrows correspond to the transitions of the respective excited state. When two arrows are shown, the state exhibits considerable (>35%) two-transition character. The transparent arrow corresponds to the transitions with less weight.*

final orbitals. These are displayed for the third and fourth excited state in fig. 9.2 a) and b) respectively, calculated with B3LYP/6-311++g(d,p). Red corresponds to decreasing electron intensity during the transition, blue to increasing electron density. Electron density transfers from the one and two chlorine atoms to the carbon atom for the third and fourth electronic state respectively.

The excited state difference for the fifth and sixth excited states are displayed in fig. 9.3, showing a similar situation: electron density transfer from the chlorine atoms to the central carbon atom.

The seventh electronic state, a bright state as well, is depicted in fig. 9.4. It gains electron intensity mainly in a p_z-like orbital centered on the carbon atom and is thus attributed to a p-Rydberg state. For completeness of the discussion of the excited state difference, the former are displayed in fig.9.6 for the first and second excited state.

With 266 nm we excite into the third/fourth excited state; the bright states which are energetically the closest to our pump energy (energy difference of 1.55 eV). An excitation into the fifth/sixth excited states is unlikely, since those states lie at least 0.7 eV energetically higher.

a)

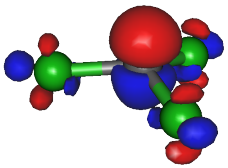

b)

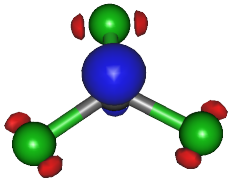

Figure 9.6: *Excited state difference for the first (a) and second (b) excited states. Red corresponds to decreasing electron intensity during the transition, blue to increasing electron density.*

9.1.3 Experimental results and Discussion

Pyrolysis on and off

As can be seen in fig. 9.7, the CCl_3 radical is produced predominantly (m/z= 117/119/121/123; easily identifiable via the typical chlorine isotope intensity distribution of 0.43:0.41:0.13:0.01). The precursor could not be observed, the small peaks at high masses (m/z=162/164/166/168) correspond to $BrCCl_2$, easily identifiable as well by the typical isotope pattern. The small peaks at low masses (m/z= 79/81) correspond to atomic bromine (m/z=79/81), the large peaks (m/z=82/84/(86)) to dichlorocarbene out of dissociative photoionization. The sum of these small peaks is about a factor of 6 weaker than the sum of the CCl_3 radical signal, measuring

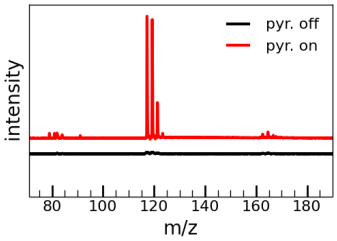

Figure 9.7: *Bromotrichloromethane, mass spectra with pyrolysis on and pyrolysis off*

time-resolved photoelectron spectra in addition to time-resolved mass spectra is thus justified.

Time-resolved mass spectra

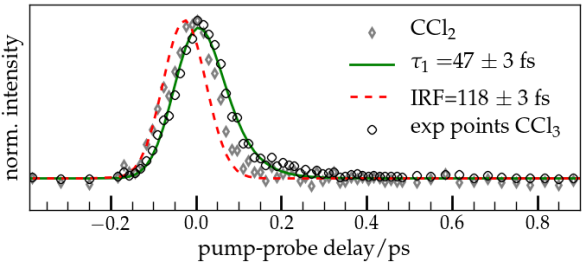

Figure 9.8: *Decay of the mass signal of CCl_3 (black circles) with the corresponding mono-exponential fit, the decay of the mass signal of CCl_2 is depicted as gray diamonds. Both signals are normalized.*

In fig. 9.8 the decay trace of the CCl_3 signal is displayed. A very short mono-exponential decay is visible, shorter than the IRF. This is really a mono-exponential decay, as can be seen in comparison with the CCl_2 decay trace (◊). The CCl_2 decay trace shows an even shorter decay (mainly auto-correlation) and is visibly shifted towards negative times. The decay traces of the other mass signals are depicted in fig. 9.9. The bromine signal shows an offset, whereas the CCl_2 signal can be fitted well using a Gaussian function with a FWHM of 110 fs. The bromine signal could either stem from a dissociative photoionization of $BrCCl_2$, or from ionization of atomic bromine produced in the pyrolysis. It is probably a combination of both: if the bromine signal were only from dissociative photoionization of $BrCCl_2$, we would see the same temporal evolu-

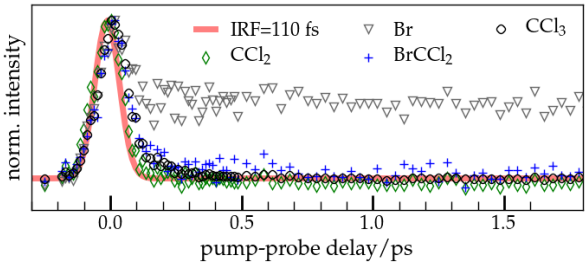

Figure 9.9: *Decay traces of the mass signals of CCl_2 (m/z=82/84), atomic bromine (m/z=79/81), $BrCCl_2$ (m/z=162/164/166/168) and CCl_3 (m/z=117/119/121/123)*

tion as for the $BrCCl_2$-signal. If the bromine signal were only from atomic bromine produced in the pyrolysis, an offset is expected. Instead a combination of both evolutions, meaning a temporal evolution similar to the $BrCCl_2$-signal combined with an offset is observed. The origin of the bromine signal in the offset from direct ionization of atomic bromine is confirmed by time-resolved photoelectron spectroscopy.

CCl_3 and $BrCCl_2$ show the same mono-exponential decay with a time constant of $\tau_1 < 50$ fs. Even though both CCl_3 and $BrCCl_2$ show the same temporal behavior, the intensity of the $BrCCl_2$ signal is of a factor of 14 smaller. Consequently the photoelectron spectrum should be dominated by the CCl_3 signal.

Time-resolved photoelectron spectra

For the time-resolved photoelectron experiments (contrary to the time-resolved mass spectra) the polar-

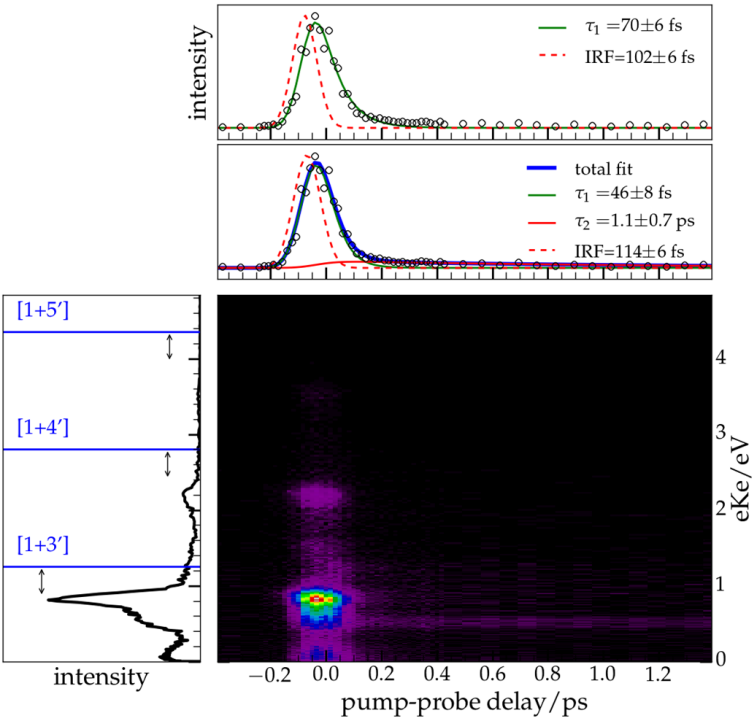

Figure 9.10: *Rotational mean TRPES of the trichlormethyl radical. The upper panel shows the decay summed over all photoelectron energies with a mono-exponential fit; the middle panel shows the decay summed over all photoelectron energies with a bi-exponential fit. In both fits the black circles correspond to the experimental data points. In the left panel the photoelectron spectrum summed over all times is displayed. The ionization limits for CCl_3 are depicted in blue (with an ionization energy of 8.06 eV [322])*

ization of the pump laser was varied between horizontal and parallel. First the time-resolved photoelectron spectrum of the rotational mean will be discussed ((Signal$_{parallel}$+2*Signal$_{ortho}$)/3), then the rotational anisotropy in the photoelectron spectrum will be treated.

In fig. 9.10 the rotational mean of the time-resolved photoelectron spectrum is displayed. The photoelectron spectrum summed over all times is displayed in the left panel, the ionization limits are displayed as blue lines. Three peaks with the same distance to their respective ionization limit are visible (see the black arrows), one for [1+3'], [1+4'] and [1+5'] signal (for [1+5'] it is very weak and hardly visible). This distance to the maximum of the peak is 0.39 eV (3145.6 cm^{-1}), but the peaks themselves are quite large.

Horn and Boschwina calculated the vibrational structure of the first band of the photoelectron spectrum of CCl_3 for one-photon ionization from the ground state and published all the vibrational term energies and the corresponding Franck-Condon factors [345]. The Franck-Condon spectrum is inlaid in fig. 9.11. The observed bands are well reproduced, even though the assumed temperature of 10 K is unrealistic with pyrolysis (see section 3.2) and even though we ionize in a multiphoton process instead of a one-photon process.

The upper panel shows the decay of the total photoelectron intensity. It can be fitted using only one time-constant (τ_1=70 $\pm$ 6 fs) just as the mass spectrum CCl_3 (and $BrCCl_2$) signal, though the observed time-constant is slightly longer. A mono-exponential fit alone, however, does not reproduce the 'shoulder' around 0.4 ps. Fitting it using a bi-exponential fit (see middle panel in fig.9.10) repro-

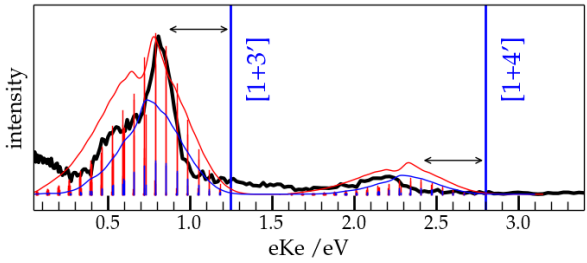

Figure 9.11: *Photoelectron spectrum with an inlaid Franck-Condon fit, assuming a temperature of 10 K. The red-line spectra corresponds to a Franck-Condon fit where all vibrational term energies are plotted with their corresponding Franck-Condon factors, for the blue-line spectra only those issued out of v"=0-state are plotted. The lines are convoluted with a Gaussian function.*

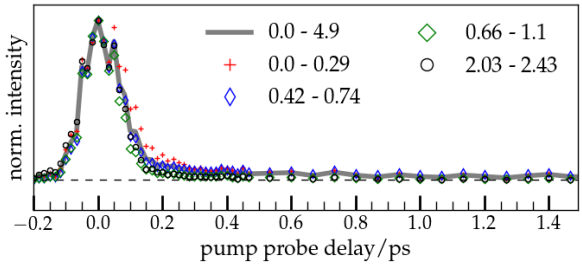

Figure 9.12: *Normalized decays for different peaks (in eV) for the rotational mean TRPES*

duces well the whole decay and leads to a more reasonable first time constant (τ_1=46 ± 8 fs). Summing over all energies, however, is not reasonable. Looking closely at the 2D-map of the TRPES, not all photoelectron bands show the same temporal behavior. Looking at the temporal evolution of the different peaks, the peak around 0.5 eV in fig. 9.10 shows an offset. Decays for different integration zones are shown in fig. 9.12, the gray line corresponds to the total photoelectron signal as dis-

played in the upper panel in fig. 9.10. The shoulder between 0.3-0.4 ps comes from a combination of the slow photoelectrons (eKe <0.29 eV, ◆) and of the peak between 0.42-0.74 eV (◆). This one shows a small offset, though no near as large as the offset seen in the bromine signal (fig. 9.9). This is probably due to an overlap of the bromine signal and the CCl_3 signal, which increases the autocorrelation signal.

Bromine has an ionization energy of 11.81381 eV [346]. Eight 800 nm photons (or a [1+5']/[2+2']) are necessary to ionize bromine and would give a maximal excess energy of 0.57 eV - which corresponds exactly with the position of the offset band. The observed bromine signal therefore originates either from a [1+5'] or from a [2+2'] process and not out of a photodissociation from $BrCCl_2$. Looking at the excited states of atomic bromine [347], there is no state excitable with only one 266 nm (37 594 cm^{-1}) photon (the first excited state $^2P^0_{1/2}$= 3 685 cm^{-1}; the next at $^4P_{5/2}$ = 63 436 cm^{-1}). With two 266 nm photons (75 171 cm^{-1}), however, two states are energetically close, the $^4P^0_{3/2}$ state = 75 009.13 cm^{-1}(266.66 nm) and the $^4P^0_{5/2}$= 74 672.32 cm^{-1}(267.84 nm). The spectrum of the pump laser is depicted in fig. 9.13, averaged over the continuously measured spectrum during the TRPES. The pump laser spectrum is large enough to reach both the $^4P^0_{3/2}$ and $^4P^0_{5/2}$states, resulting in excess energies between 0.58 - 0.54 eV. The bromine signal originates therefore from a [2+2']-process, where the bromine is excited into the $^4P^0_{3/2}$ and $^4P^0_{5/2}$ state, both long-lived.

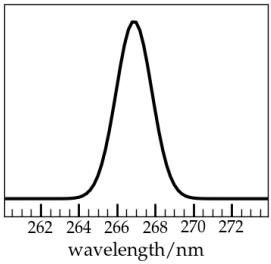

Figure 9.13: *Spectrum of the pump laser, mean of the spectra measured continously during the TRPES*

The decay from 0.42-0.74 eV is therefore a mixture of the bromine and CCl_3 signal. The decays

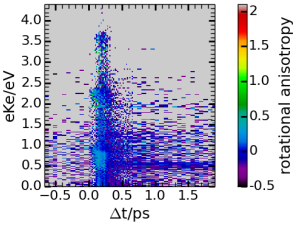

Figure 9.14: *Rotational anisotropy, gray corresponds to points with no experimental intensity*

of the other peaks at higher energy, at 0.66-1.1 eV (◇) and 2.03-2.43 eV (○), are attributed to CCl_3 only, and can be fitted - in accordance with the time-resolved mass spectra - using one very short time-constant ($\tau_1 = 44 \pm 5$ fs, IRF $= 102 \pm 5$ fs and $\tau_1 = 37 \pm 7$ fs, IRF $= 128 \pm 7$ fs respectively).

Rotational Anisotropy

A positive rotational anisotropy is observed in the TRPES (see fig. 9.14). This rotational anisotropy is a combination of anisotropy in the energy spectra and in the temporal decay. The observed intensity is significantly lower if the pump laser is polarized orthogonally with respect to the probe laser. The angles were not varied for the mass spectra, so no conclusion as to the rotational anisotropy in the mass spectra decays can be made. The decay of the rotational anisotropy (fig. 9.15) can be fitted with a mono-exponential decay, showing a change in electronic character.

This also indicates that the excited state presents some asymmetry. The third/fourth initially excited

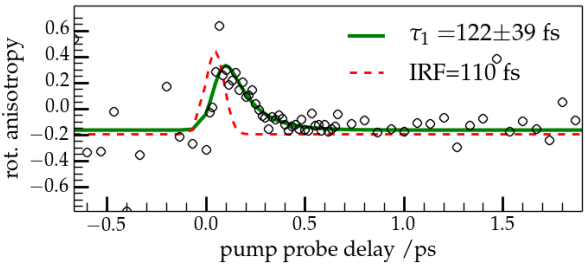

Figure 9.15: *Mono-exponential fit of the rotational anisotropy of the total photoelectron decay. The IRF was held fixed for the fit to converge to reasonable values.*

states (see fig. 9.2) show decreasing electron density in p-like orbitals going out of plane centered on the chlorine atoms, and increasing electron density on the central carbon atom and on three (two) chlorine atoms in plane. In the context of a molecular orbital scheme (see fig. 9.5) both show excitation into MO 29, which shows out-of-the plane symmetry. It is thus not surprising that a rotational anisotropy is visible.

9.1.4 Interpretation

With 266 nm we excite into the third/fourth initially excited states, which show rotational anisotropy. The initially excited states relax via a conical intersection into a lower-lying electronic state, the deposited wavepacket moves out of the Franck-Condon region. This change of electronic character is reflected in the rotational anisotropy. The different ionization cross sections of the different electronic states can be understood following the Koopman's theorem: The ionic ground state should have the electron configuration of SOMO-1. When the excited state no longer corresponds to the SOMO-LUMO-transition, the ionic state formed by the removal of an electron is not the ionic ground state. This is the case for example for the second electronic state in fig. 9.5.

All these three different formulations - conical intersection, move-out of the Franck-Condon region, Koopman's theorem - describe the same relaxation process.

9.2 Monobromomethyl radical

As mentioned in the previous section, halogen atoms and halogen-containing radicals are one of the key participants in the catalytic reactions leading to stratospheric ozone destruction [348–351]. Bromine atoms are even more effective at destructing ozone than chlorine atoms [352], bromine and chlorine radicals even exhibit a synergistic effect which efficiently destroys catalytically the ozone layer [353,354].

The smallest hydrocarbon radical containing a bromine atom is CH_2Br, the monobromomethyl radical, which constitutes an important source of atomic bromine in the atmosphere [355]. Hence the continued interest in its kinetics [354,356–358] and its spectroscopy [358–368].

In contrast to the other halogen-containing radical CCl_3 examined in this thesis, the CH_2Br radical is planar in its ground state [359–364] and its ionized state [365] with C_{2v} symmetry for both. The properties of the ground state of the CH_2Br anion and the radical were examined with *ab initio* methods, yielding a computed electron affinity of 0.917-0.927 eV [369] for the radical (compared to an experimental value of 1.0 ± 0.3 eV [366]) and an ionization energy of 8.45 eV [370]. Its ionization energy was first determined experimentally in 1958 (8.34 ± 0.11 eV) [367]. This was refined in 1983 by Andrews et al. [371], who determined the adiabatic (8.61 ± 0.01 eV) and vertical (8.72 ± 0.01 eV) ionization energies of the monobromomethyl radical using photoelectron spectroscopy. The value of its adiabatic ionization energy was confirmed by Ma et al. [366]. Recently Steinbauer et al. [372] reexamined the monobromomethyl radical using mass-selective threshold photoelectron spectra, resulting in an adiabatic ion-

ization energy of 8.62 ± 0.01 eV, in accordance with the result from Andrews et al. [371].

Spectroscopic studies of the excited states of the monobromomethyl radical are still sparse. The UV spectrum measured by Villenave et al. [358] shows one broad band between 270 and 210 nm, peaking at 230 nm, whereas Nielsen et al. [373] measured a band between 340 and 220 nm, peaking at 270 nm. Their measured absorption spectrum looks very similar to the absorption spectrum of CH_2BrO_2 which they measured as well, a contamination of their spectrum is thus likely. Villenave et al. [358] stated strongly that CH_2Br does definitely not absorb at wavelengths longer than 270 nm.

The first five excited states were calculated using CASSCF and MRCI [374] (see table 9.4). The lowest electronic excited state $2^2A'$ lies at 4.45 eV (4.73 eV for CASSCF) and has an oscillator strength of 0.08, whereas the second electronic excited state is symmetry forbidden. The third electronic excited state has an oscillator strength higher than one, which is questionable, and lies with 5.62 eV (6.01 eV for CASSCF) too high to be excited with 266 nm (4.66 eV). Bromine introduces a large spin-orbit coupling effect in the molecule, which makes calculations complicated, but the gap between $3^2A'$ and $2^2A'$ is still large, so they can be considerated as seperate states.

The dynamics of the first excited state has been examined using transient resonance Raman spectroscopy [368], concluding with the support of DFT calculations that the first excited state exhibits motion mostly along the C-Br bond in the Franck-Condon region. We therefore looked at the fs-dynamics of this first excited state in a 266 nm pump/800 nm probe experiment.

state	energy/eV (oscillator strength)
$1^2A'$ [374]	0.0
$2^2A'$ [374]	4.45(0.08)
$1^2A''$ [374]	4.80(0.0)
$3^2A'$ [374]	5.62(1.53)
$2^2A''$ [374]	6.96(0.13)
$3^2A''$ [374]	7.87(0.02)

Table 9.4: *Calculated electronic states of* CH_2Br *with MRCI*

9.2.1 Experimental

The monobromomethyl radical was examined using the Saclay setup (see section 5.4) with 266 nm as the pump laser and 800 nm as the probe laser. It was produced via pyrolysis at 30 W from bromonitromethane (*Sigma-Aldrich*, *technical grade*, used without further purification, see fig. 9.16), which was transferred into the gas phase using the source for liquids (see section 5.1) with argon at 2 bar absolute background pressure.

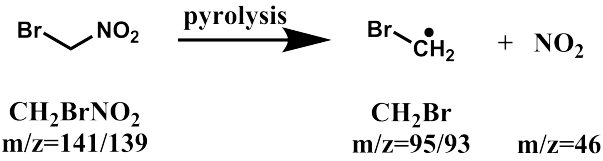

Figure 9.16: *Scheme of production of the bromomethyl radical via pyrolysis from bromonitromethane*

TOF delay scans were averaged over 2 series and PE delay scans over 5 series. The probe laser was polarized horizontally, the polarization of the pump laser was varied between horizontal and vertical polarization. The photoelectron spectra were inverted using the pBasex algorithm as implemented in the *Analyse*-program, fit constants were extracted as described in section 13, the plotted uncertainties correspond to fit uncertainties and not to experimental uncertainties.

9.2.2 Results and Discussion

Pyrolysis on and pyrolysis off

As can be seen in fig. 9.17 in the mass spectrum at pump probe conditions, the bromomethyl rad-

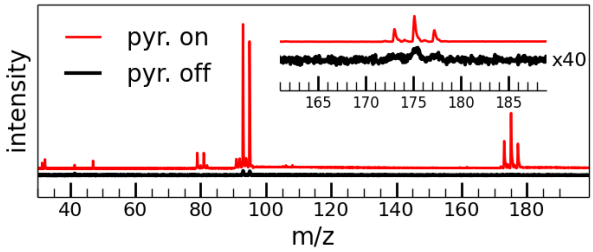

Figure 9.17: *Mass spectra of bromonitromethane with pyrolysis on and pyrolysis off*

ical at m/z=93/95 is the most intense peak, but $CHBr_2$ at m/z=173/175/177 is also formed and is about 40% as intense as the bromomethyl radical. Both are easily identifiable via their typical isotopic pattern (for CH_2Br: m/z= 93/95 with an intensity distribution like those of atomic bromine of 1:0.98; $CHBr_2$: m/z=173/175/177 with an intensity distribution of 1:2:1).

$CHBr_2$ could be formed by an addition of bromine in the pyrolysis tube to the bromomethyl radical and a loss of a hydrogen atom. Looking closely at the mass spectrum without pyrolysis, however, a small $CHBr_2$ signal is still visible. The $CHBr_2$ signal consequently originates from an impurity (for example $CHBr_2NO_2$ or $CH_2Br_2NO_2$) already present in the precursor. Bromine (at m/z=79/81, intensity distribution 1:1) is also visible with the pyrolysis on. The precursor is not visible neither with pyrolysis on nor off. H_2BrCNO_2 shows dissociative photoionization to CH_2Br^+ above 10.95 eV [372], which can be reached with three pump photons. This explains the weak, yet broad CH_2Br peaks visible without pyrolysis.

Time-resolved mass spectra

In fig. 9.18 the time-decay traces for CH_2Br, $CHBr_2$ and for Br are displayed. Fitting the CH_2Br and $CHBr_2$ signals using only autocorrelation (blue curve) does not reproduce the experimental data between 0.1-0.2 ps pump-probe-delay. Including one time-constant τ_1 leads to a good agreement and to a more reasonable IRF (previously measured IRFs were between 100-120 fs, see other experiments using 266/800 nm in this thesis). The obtained time-constants are very short, 37 and 52 fs for CH_2Br and $CHBr_2$ respectively. For CH_2Br the difference between the decay with orthogonal laser polarization ($\perp$) and parallel laser polarization ($\parallel$) is negligible (rot. anisotropy=-0.1), whereas for $CHBr_2$ it is much more pronounced (rot. anisotropy=+0.40).

For atomic bromine signal, even though weak it is weak compared to the CH_2Br and $CHBr_2$ signals, this difference is even more pronounced (rot. anisotropy=0.8-1.0). Its dynamic is also very interesting; on the observed timescale it converges to an offset with a visible damped oscillation. A fourier transform reveals that this oscillation is composed of two oscillations ($\sim$100 cm^{-1} and $\sim$340 cm^{-1}).

The atomic bromine signal can have two possible origins: either from free bromine present in the molecular beam produced via pyrolysis, or via dissociation of a bromine-containing molecule.

Several arguments are in favour of the ionization of free atomic bromine:

Just as in the CCl_3 experiments (see section 9.1), atomic bromine can be ionized in a [2+2'] resonant ionization via the $^4P^0_{3/2}$ and $^4P^0_{5/2}$ states [347]. The energy difference between those two states is 337 cm^{-1}, which corresponds to one of the oscillations. The oscillation could therefore be partly ex-

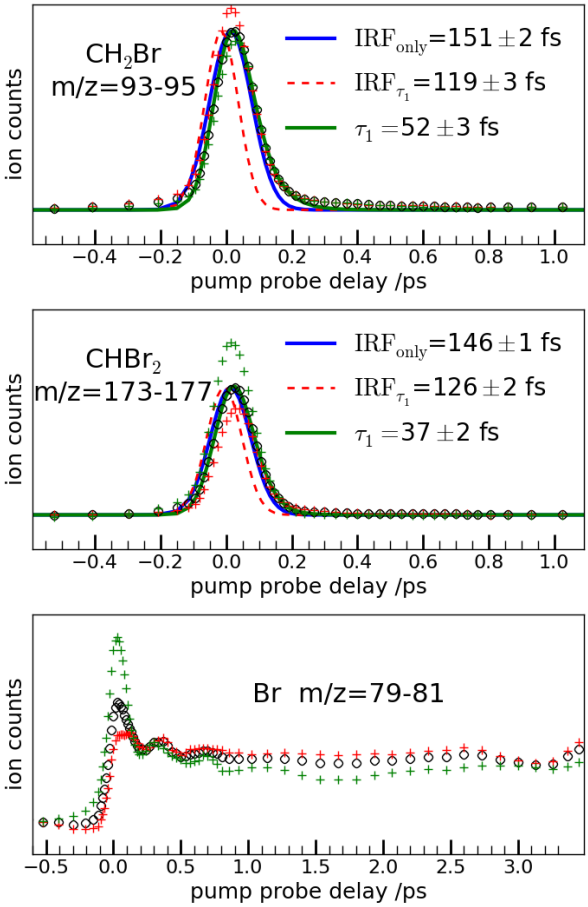

Figure 9.18: *Fitted time-decay traces of the mass signals of (in order) CH_2Br, $CHBr_2$ and Br. ○: rotational mean experimental data points +: pump laser and probe laser orthogonal polarized +: pump laser and probe laser parallel polarized.*

plained via oscillation of the wavepacket in atomic bromine between these two states. This phenomena should then also be present in the CCl_3 experiments. No vibrations were observed, but this could be attributed to an insufficient S/N ratio.

A photodissociation of a bromine-containing molecule or dissociative photoionization is also possible. Velocity map imaging techniques can help answer the question of the origin. Ion imaging of atomic bromine could answer this question, but no ion images of bromine were recorded. But the photoelectron spectrum alone should give insight into this process. If the atomic bromine signal stems exclusively from pyrolysis, the photoelectron spectrum should exhibit a narrow band centered at 0.54-0.58 eV analogous to the CCl_3 photoelectron spectrum (see fig. 9.10). In the case of a dissociative process, a broad offset is expected.

Time-resolved photoelectron spectra

In fig. 9.20 the rotational mean of the photoelectron spectrum is displayed, which, considering the mass spectrum, is essentially a mixture of CH_2Br and $CHBr_2$. The rotational anisotropy in the photoelectron spectrum is treated later.

The time-resolved photoelectron spectrum (left panel) shows two broad bands centered at 0.6 and 0.9 eV, which show the same fast decay (see fig. 9.21). The band centered at 0.5 eV shows an offset, which extends over the whole energy range (see fig. 9.21), which was not the case in the the CCl_3 photoelectron spectrum. The excitation spectrum is identical in both cases (see fig. 9.19). Therefore the bromine signal can not stem exclusively from free atomic bromine produced in the pyrolysis, but

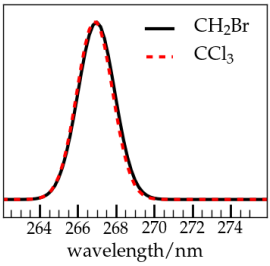

Figure 9.19: *Spectrum of the pump laser, mean of the spectra measured continously during the TRPES*

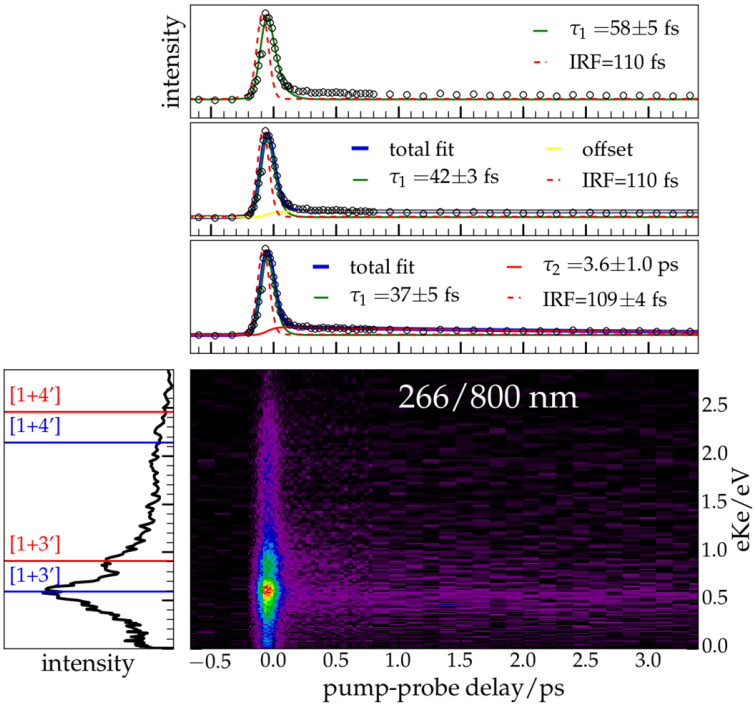

Figure 9.20: *Rotational mean time-resolved photoelectron spectra of $CH_2Br/CHBr_2$. The blue ionization limits correspond to the ionization limits of CH_2Br (IE=8.72 ± 0.01 eV [371]), whereas the red ionization limits correspond to the ionization limits of $CHBr_2$ (IE=8.40 ± 0.03 eV [371]). The upper panels show the total photoelectron decay with different fits, whereas the left panel represent the photoelectron spectrum summed over all times.*

also has to stem from photodissociation processes in the excited state of either $BrCH_2$ or Br_2CH.

The attribution of the peaks in the photoelectron spectrum is relatively straightforward. The first peak at 0.6 eV in the photoelectron spectrum in fig. 9.20 is attributed to the photoelectron spec-

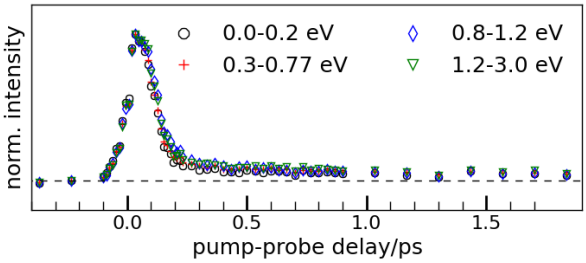

Figure 9.21: *Decay traces of the photoelectron spectrum over different energy ranges*

trum of CH_2Br, whereas the second smaller peak at 0.9 eV is attributed to the photoelectron spectrum of $CHBr_2$. This is in agreement with their intensities in the mass spectra (CH_2Br : $CHBr_2$= 2:1). The two peaks cannot correspond to the two atomic states of bromine, $^4P^0_{3/2}$ and $^4P^0_{5/2}$, since they are seperated only by 0.04 eV.

Fitting the time-decay of the total photoelectron signal using only one time-constant (top time-decay trace in fig. 9.20) does not reproduce the observed offset. This can be corrected by including either an offset (middle time-decay trace in fig. 9.20) or by using a bi-exponential decay (lower time-decay trace in fig. 9.20). Since the photoelectron spectrum was recorded only up to a pump-probe delay of 3.5 ps, fitting it using a bi-exponential decay results in a second time-constant of τ_2=3.6 ps, which is equivalent to an offset on the measured timescale. This offset corresponds to the mass spectrum bromine signal, and the small mono-exponential decay with a time constant of $\tau_1 \approx 40$ fs is comparable to the time constant of the CH_2Br and $CHBr_2$ signal. A marked oscillation is not observed in the photoelectron spectrum, but considering the relative intensities in the mass spectra (see fig. 9.17),

this is not surprising.

Rotational anisotropy

For the photoelectron spectra a positive rotational anisotropy (+0.5) at the autocorrelation (see fig. 9.22) is observed, just as in the mass spectra. This is an indication that a σ state is initially excited, since the rotational constants to randomize a σ-state are very big compared to a π state (see fig. 9.23).

As to understand what happens after the excitation of $CHBr_2$ and CH_2Br with 266 nm, their excited states and the potential energy surface along the C-Br bond were calculated using TDDFT as implemented in Gaussian09 [194].

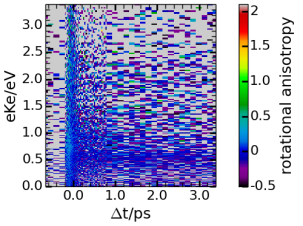

Figure 9.22: *Rotational anisotropy, gray corresponds to points with no experimental intensity*

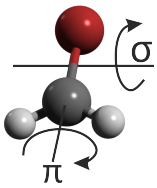

Figure 9.23: CH_2Br

9.2.3 Excited states of the CH_2Br radical

Concerning the $CHBr_2$ radical, Li et al. [374] computed the first five electronic excited states using CASSCF and MRCI. They characterized their states in accordance with C_S symmetry, in a lower symmetry than the experimentally confirmed C_{2v}-symmetry [359–364]. In the following the calculations of Li et al. [374] are compared with TDDFT [190] calculations with the functionals B3LYP [208–211], CAM-B3LYP [195] and ωB97xD [196] using the basis set 6-311++g(d,p) [197].

In table 9.5 the geometrical parameters of DFT calculations with different functionals for the ground state are compared with experimental values obtained from rotational spectra [362]. The correct symmetry is obtained each time and the agreement with the experimental values is excellent ($\Delta < 1\%$). In table 9.6 the first five excited states for the CH_2Br

	B3LYP	CAM-B3LYP	ωB97xD	exp [362]
symmetry	C_{2v}	C_{2v}	C_{2v}	C_{2v}
∡HCH/°	124.83	124.43	124.42	124.5
r(CBr)/Å	1.864	1.851	1.850	1.848
r(CH)/Å	1.078	1.077	1.079	1.084

Table 9.5: *Optimized geometries of the CH_2Br radical calculated with DFT using different functionals (basis set: 6-311++g(d,p))*

radical calculated with TDDFT using three different functionals (B3LYP, CAM-B3LYP and ωB97xD) and the MRCI calculations by Li et al. [374] are compared. All TDDFT calculations were started from the optimized ground state. It should be noted that the spin-orbit coupling of the bromine atom is not included in the TDDFT calculations. These transitions are visualized in fig. 9.24. The displayed orbitals correspond to the optimized ground state orbitals; the contribution of the displayed transition is higher than 95%.

The excited states calculated with different functionals are energetically very close. But compared to the MRCI calculations they are all lower in energy. In the TDDFT calculations the first electronic ground state has a small oscillator strength, whereas the second and third excited states are dark. The fourth excited state is very bright, whereas the fifth is dark again. This is in contrast to the MRCI calculations.

Whereas for the first two excited states the oscillator strength is comparable, in the MRCI calculations the third electronic state is the brightest with an oscillator strength of 1.53. Both the fourth and the fifth excited state have a small oscillator strength. Probably in the MRCI calculations the third and fourth excited states are switched as compared to the TDDFT calculations. But even

state	B3LYP	CAM-B3LYP	ωB97xD	MRCI [374]
0	$^2B_1$	$^2B_1$	$^2B_1$	$^2A'$
1	$^2B_1$ 4.00 ($2.2 \cdot 10^{-3}$, 0.80)	$^2B_1$ 4.27 ($1.9 \cdot 10^{-3}$, 0.83)	$^2B_1$ 4.05 ($2.5 \cdot 10^{-3}$, 0.80)	$^2A'$ 4.45 (0.08)
2	$^2A_2$ 4.25 (0.0, 0.77)	$^2A_2$ 4.54 (0.0, 0.78)	$^2A_2$ 4.25 (0.0, 0.77)	$^2A'$ 4.80 (0.0)
3	$^2B_1$ 5.09 (0.0, 0.81)	$^2B_1$ 5.41 (0.0, 0.84)	$^2B_1$ 5.06 (0.0, 0.77)	$^2A'$ 5.62 (1.53)
4	$^2A_1$ 5.15 ($6.4 \cdot 10^{-2}$, 0.78)	$^2A_1$ 5.43 ($6.5 \cdot 10^{-2}$, 0.78)	$^2A_1$ 5.20 ($6.7 \cdot 10^{-2}$, 0.77)	$^2A''$ 6.96 (0.13)
5	$^2A_2$ 5.86 (0.0, 0.80)	$^3B_2$ 6.14 (0.0, 2.67)	$^2A_2$ 5.81 (0.0, 0.80)	$^2A''$ 7.87 (0.02)

Table 9.6: *Excited states of CH_2Br calculated with TDDFT (basis set: 6-311++g(d,p)) using different functionals from optimized ground state structures, energy in eV(oscillator strength, $<S>^2$). The last column corresponds to MRCI calculations by Li et al [374] (energy in eV($<S^2>$)), they assumed a C_S symmetry for their characterization of the electronic states, even though it has been shown in literature that this molecule has C_{2V} symmetry [359–364].*

that does not explain why the symmetry of the fourth excited state is A_1 in the TDDFT calculations, which corresponds to A' in the C_S-symmetry. Combined with their obtained oscillator strength greater than one for the third excited state (in contrast to the definition of the oscillator strength [39]) makes the quality and validity of the MRCI transitions questionable.

The TDDFT calculations are mostly not significantly spin-contaminated, since the expectation value of the total spin (ideal: 0.75) differs from the

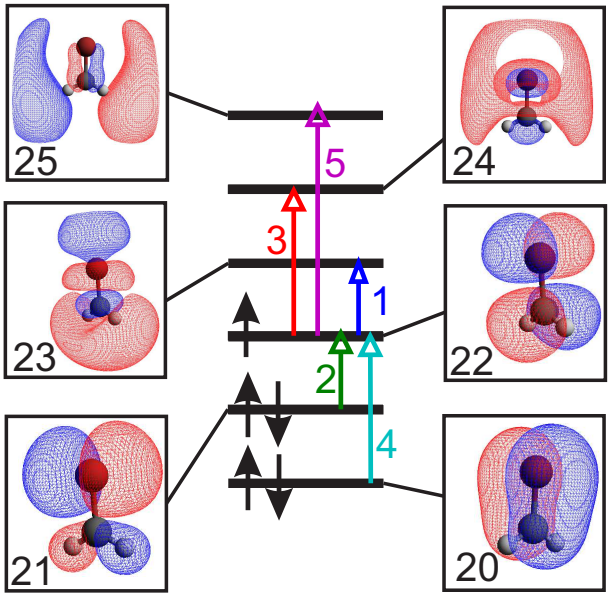

Figure 9.24: *The three highest occupied and three lowest unoccupied molecular orbitals of CH_2Br for the optimized ground state with B3LYP/6-311++g(d,p). The colored arrows correspond to the transitions of the respective excited state, where the contribution of the respective molecular orbital is at least 95%. The color-code is the same as in fig. 9.27.*

obtained values by less than 10 %. The only exception are the fifth excited state calculated with CAM-B3LYP, which is very strongly spin-contaminated, and the first and third excited state calculated with CAM-B3LYP, where the value of the total spin slightly exceeds the 10% limit. CAM-B3LYP performs worse than B3LYP and wB97xD based on the spin-contamination. All transitions, as displayed in fig. 9.24 for B3LYP/6-311++g(d,p), have only one major contribution (calculated as de-

tailed in the supplementary in ref. [375]). The two transitions with the major oscillator strength, the first and fourth excited state, are SOMO→LUMO and HOMO-2→SOMO transitions.

With respect to our TDDFT calculations the excitation with 266 nm is attributed to the fourth most intense excited state, even though the calculated energy maximum is above the energy of 266 nm=4.66 eV. The calculated excitation energies range between 5.15-5.43 eV, which corresponds to a deviation of 10-16 %. Since even between the different functionals the difference is about 6%, the attribution of the fourth excited state as the initially excited state is valid. The excited state difference for the fourth excited state is shown in fig. 9.25. For the fourth excited state electron density transfers from the bromine atom towards the carbon atom.

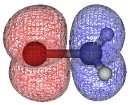

Figure 9.25: *Excited state difference for the fourth excited state. Red corresponds to decreasing electron intensity during the transition, blue to increasing electron density.*

To understand the dynamics of the fourth excited state, the energies of the excited states during elongation of the C-Br bond were calculated with B3LYP/6-311++g(d,p). This is depicted in fig. 9.27, where states with no oscillator strength have a ◊ symbol. The gray line corresponds to the position of the optimized ground state.

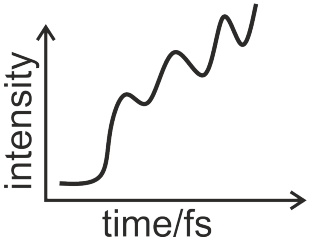

Figure 9.26: *Excepted intensity increase with oscillations in the bromine mass signal after photodissociation.*

Starting from the optimum in the ground state (following the gray line), with 266 nm the fourth excited state is not excited in its minimum. This state shows two minima separated by a barrier and crosses the third excited state, which is a dissociative. If the wavepacket were to oscillate in the first minimum, this oscillation should also be observed in the CH_2Br mass signal, which was not the case. If the wavepacket, however, oscillates in the second minimum, CH_2Br could no longer be ionized due to diagonal Franck-Condon factors. If the observed

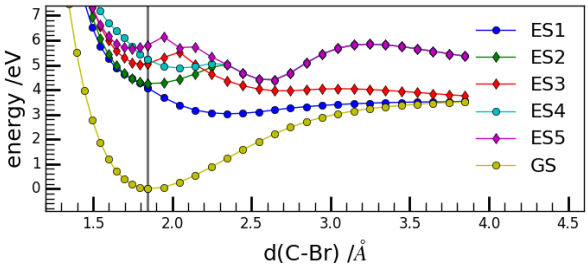

Figure 9.27: *PES of the CH_2Br radical during elongation of the C-Br bond, calculated with TDDFT/B3LYP. All other parameters were held fixed. Lines with ◊ correspond to electronic states with no oscillator strength. The gray line corresponds to the equilibrium geometry in the ground state.*

oscillations in the bromine mass signal were from a dissociation in the excited state, an increase in the intensity is to be expected (see fig. 9.26), which is not observed.

The fourth excited state could show dissociative photoionization, which explains the observed oscillations in the mass spectra as well as the energetically broad offset in the photoelectron spectrum. The short time-constant observed in the photoelectron spectrum and in the CH_2Br mass signal corresponds to the time it takes for the wave packet to phase out of the Franck-Condon-region with the ion and towards the minimum of the fourth excited state.

9.2.4 Excited states of the $CHBr_2$ radical

$CHBr_2$

To the best of our knowledge, only a few studies on the $CHBr_2$ radical can be found in literature. 1992 Moc [370] calculated the ground state using *ab inito* and hybrid UB3LYP DFT method. Experimentally it has been observed as a 267 nm photolysis product of bromoform [376]. Pyrolysis was used to produce $CHBr_2$, so bromoform pyrolysis is negligible.

	B3LYP	CAM-B3LYP	ωB97xD
symmetry	C_S	C_S	C_S
∡(BrCBr)/°	120.80	121.04	120.80
r(CBr)/Å	1.874	1.857	1.858
r(CH)/Å	1.808	1.079	1.081
∡(BrBrHC)/°	18.85	15.27	16.72

Table 9.7: *Optimized geometries of the $CHBr_2$ radical in its ground state calculated with DFT using different functionals (basis set: 6-311++g(d,p))*

Just as for the CH_2Br radical, the ground state of $CHBr_2$ was optimized with DFT (basis set: 6-311++g(d,p)) using the three functionals B3LYP, CAM-B3LYP and ωB97xD. The parameters for the optimized ground states are summarized in table 9.7. All three calculations agree that $CHBr_2$ is pyramidal, in contrast to the planar CH_2Br. The obtained values are in good agreement with those calculated by Moc, with exception of the out-of-plane angle (∡(BrBrHC)), which is higher (25.8-33.4°) in the calculations by Moc [370]. Based on these optimized ground states TDDFT calculations were performed, using again the three functionals B3LYP, CAM-B3LYP and ωB97xD. The results are summarized in table 9.8.

state	TDDFT/ B3LYP	TDDFT/ CAM-B3LYP	TDDFT/ ωB97xD
0	$^2A'$	$^2A'$	$^2A'$
1	$^2A'$ 3.16 ($5 \cdot 10^{-4}$, 0.79)	$^2A'$ 3.43 ($3 \cdot 10^{-4}$, 0.82)	$^2A'$ 3.47 ($3 \cdot 10^{-4}$, 0.81)
2	$^2A''$ 4.16 ($3 \cdot 10^{-4}$, 0.78)	$^2A''$ 4.59 ($7 \cdot 10^{-4}$, 0.78)	$^2A''$ 4.53 ($1.0 \cdot 10^{-3}$, 0.78)
3	$^2A'$ 4.41 (0.0, 0.77)	$^2A'$ 4.82 ($1 \cdot 10^{-4}$, 0.78)	$^2A'$ 4.76 (0.0, 0.78)
4	$^2A''$ 4.52 ($4.0 \cdot 10^{-2}$, 0.80)	$^2A''$ 4.89 ($4.0 \cdot 10^{-2}$, 0.86)	$^2A''$ 4.84 ($5.0 \cdot 10^{-2}$, 0.81)
5	$^2A''$ 4.79 ($3.1 \cdot 10^{-2}$, 0.86)	$^2A''$ 5.05 ($3.6 \cdot 10^{-2}$, 0.96)	$^2A''$ 5.10 ($2.4 \cdot 10^{-2}$, 1.00)

Table 9.8: *Excited states of $CHBr_2$ calculated with TDDFT (basis set: 6-311++g(d,p)) using different functionals from optimized ground state structures, energy in eV(oscillator strength, $<S>^2$).*

The first three excited states are not spin-contaminated. The fourth and fifth excited states are moderately spin-contaminated (6-33 %), for the B3LYP functional this contamination is the lowest and exceeds just barely the 10 % limit (14% for the fifth excited state). Higher electronic states were also calculated, those were severely spin-contaminated. The first three electronic states have negligible oscillator strength for all three functionals, whereas the fourth and fifth excited state are not only energetically very close, but also very bright.

The transitions of $CHBr_2$ are displayed in fig. 9.29, with the molecular orbitals of the optimized

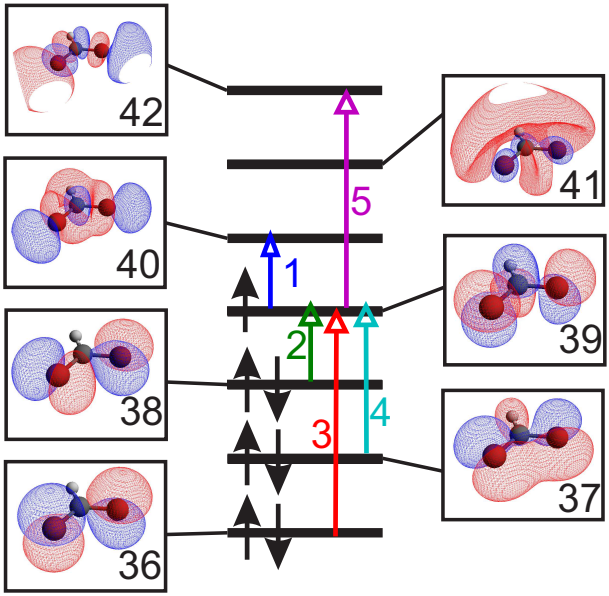

Figure 9.29: *The four highest occupied and three lowest unoccupied molecular orbitals of CH_2Br for the optimized ground state with B3LYP/6-311++g(d,p). The colored arrows correspond to the transitions of the respective excited state, where the contribution of the respective molecular orbital is at least 97% for the first three excited states, and at least 80% for the fourth and fifth excited state. The color-code is the same as in fig. 9.31.*

ground state with B3LYP/6-311++g(d,p). The fourth excited state is majorly a HOMO-2-SOMO excitation, the fifth majorly a SOMO-LUMO+3 excitation. Both show considerable character from another molecular orbitals (see table 9.9). Both excited states are shown in fig. 9.30. Red corresponds to decreasing electron intensity (where they come from) and blue to increasing electron inten-

N	contribution	%
4	37B →42A	85
	39A →42B	10
5	39A →42A	80
	37B →39B	10

Table 9.9: *Transition contributions for the fourth and fifth excited state for* $CHBr_2$ *exceeding 10 %*

a)

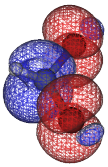

b)

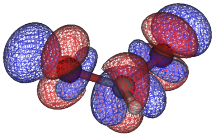

Figure 9.30: *Excited state difference for the fourth excited state (a) and the fifth excited state (b). Red corresponds to decreasing electron intensity during the transition, blue to increasing electron density.*

sity (where they go to). For the fourth state electron density mostly goes towards the carbon atom, wheras for the fifth excited state electron density also goes to the bromine atoms. With 266 nm (4.55 eV) both the fourth and the fifth excited state (4.52-4.89 eV and 4.79-5.10 eV respectively) could be excited.

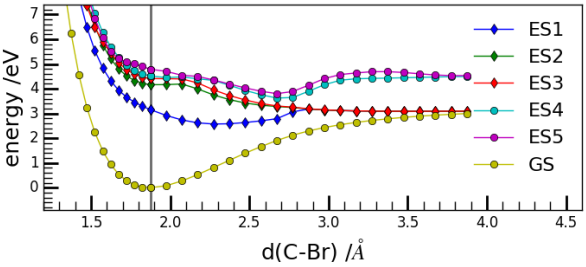

Figure 9.31: *PES of the $CHBr_2$ radical during elongation of the C-Br bond, calculated with TDDFT/B3LYP. All other parameters were held fixed, so with execption of the ground state minima the symmetry is C_1. Lines with ◊ correspond to electronic states with no oscillator strength. The gray line corresponds to the equilibrium geometry in the ground state.*

Just as for the CH_2Br radical the excited state potential surface of $CHBr_2$ along the C-Br elongation with B3LYP/6-311++g(d,p) (see fig. 9.31) was examined as to understand what happens after excitation with 266 nm. The symmetry is hereby broken, while for the ground state minima it is C_s, elongation of the C-Br leads to C_1-symmetry. Lines with ◊ symbolize states with very low or zero oscillator strength. Both the fourth and fifth excited state show a minimum near 2.6 Å, quite far away from the equilibrium geometry at 1.9 Å. If the wavepacket oscillates in this minimum, and the excited state

shows dissociative photoionization, it leads to an oscillation as well. The short time-constant corresponds to the time it takes for the wave packet to move out of the Franck-Condon region for ionization to $CHBr_2$.

9.2.5 Conclusion

The observed decay can be interpreted as follows: With 266 nm CH_2Br is excited in the first minimum of the fourth excited state, which shows a double minima seperated by a barrier. The wavepacket rapidly moves into the second minimum and out of the Franck-Condon region, this corresponds to the first observed time-constant $\tau_1 \approx 50$ fs. It then oscillates and an dissociative ionic state can be reached - which corresponds to the oscillations visible in the bromine mass signal.

$CHBr_2$ is also excited in its fourth or fifth excited state with 266 nm, which show both a minimum far from the equilibrium geometry. The observed time-constant $\tau_1 \approx 40$ fs corresponds to the move of the wavepacket in this minimum and out of the Franck-Condon region. Here it oscillates and an dissociative ionic state can be reached - which corresponds to the second oscillation frequency observed in the bromine mass signal.

The hypothesis of dissociative photoionization is in agreement with the observed offset over the whole photoelectron instead of an offset of the band between 0.54-0.58 eV.

The rotational anisotropy can be explained with the excited state difference of the fourth excited state for CH_2Br (fig. 9.25) and of the fourth/fifth excited state of $CHBr_2$ (fig. 9.30): Both show symmetry out of the C_s-plane, with the fourth excited state showing nearly no electron density in the C_s-

plane. It is thus consistent that both show rotational anisotropy. $CHBr_2$ shows more rotational anisotropy than CH_2Br, since its momentum of inertia is bigger.

Further experiments, especially ion imaging of bromine are necessary as to elucidate the origin of the bromine, since with this method bromine from the background (pyrolysis) and from dissociation processes can be distinguished. It would also be interesting to examine these dynamics on longer timescales ($>$3.5 ps).

Chapter 10 *Ortho*-benzyne

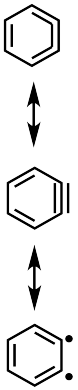

Figure 10.1: *Structure formula of ortho-benzine*

Ortho-benzyne (see fig. 10.1) is just like the xylylenes another molecule with a biradical resonance structure, and has fascinated many chemists over the years [377]. Known to every organic chemist primarily as a reactive intermediate in nucleophilic aromatic substitution [378–380], its formation has even been suggested in molecular clouds like TMC-1 [381] as an important intermediate in the formation of interstellar polycyclic aromatic hydrocarbons [381,382]. But during a detailed search using the Green Bank Telescope of the Westbrook nebula (CRL 618) it hasn't been detected [383]. As an unimolecular decomposition product of the phenyl radical [384,385] it is also an intermediate in the formation of polycyclic aromatic hydrocarbons [386].

Numerous spectroscopic studies were undertaken to characterize this molecule; including NMR [387], thermochemical [388,389] and theoretical investigations [390–400]. Several different mesomeric structures can be formulated for *ortho*-benzyne, including a cumulene-like structure, a triple bond structure and a biradicaloid structure (top to bottom, fig. 10.1). According to NMR studies the cumulene-structure (top formula) is dominant in the liquid phase [387]. Microwave studies [401–406] and IR measurements [407,408] show that in gas phase the triple bond structure (middle formula) dominates.

Its excited electronic states were characterized in an Ar matrix [409]. The electronic absorption spectrum was very broad and contains little information. Five electronic states were assigned to these overlapping absorption bands based on semi-

SE [409]	CASPT2D [399]	CCSD [398]	CASPT2 [392]
A $^1B_2$ ($\sigma\sigma*$)	$^1B_1$	$^1A_2$	$^1A_2$
3.26	4.03	4.32	4.33
C $^1A_1$ ($\pi\pi*$)	$^1A_2$	$^1B_1$	
4.09	4.05	4.45	
D $^1B_2$ ($\pi\pi*$)	$^1A_1$	$^1B_2$	
5.03	4.33	5.40	
F $^1A_1$ ($\pi\pi*$)	$^1B_2$	$^1A_1$	
6.69	4.91	5.45	
G $^1B_2$ ($\pi\pi*$)	$^1B_1$	$^1B_1$	
6.64	5.28	5.67	

Table 10.1: *Vertical excitation energies of different electronic states of ortho-benzyne as known in the literature (SE are the semi-empirical valence electron calculations). Revised values are presented later in the discussion.*

empirical valence electron calculations [390, 409], summarized in table 10.1.

Wheras semi-empirical valence electron calculations [390, 409] predict a $^1B_2$-state at 3.26 eV as the first excited state, CASPT2D predicts $^1B_1$-symmetry for the first excited state at 4.03 eV [399]. CCSD and CASPT2, however, state that the first excited state is of $^1A_2$-symmetry. From the difference in the symmetry and energetic position of the first excited electronic state it is apparent that calculations of the excited states of *ortho*-benzyne are due to its unusual structure and low singlet-triplet gap by no means trivial.

The first electronic state of the *ortho*-benzyne cation is nearly degenerate with the cation ground state, measuring the ionization energy of the *ortho*-benzyne proved therefore no easy task [410–414]. Dewar and Tien [411] attributed three bands in the photoelectron spectrum at 9.24, 9.75 and 9.87 eV to the *ortho*-benzyne-cation. Simon et al. [413], how-

ever, attributed the band at 9.24 eV to an impurity, and concluded that the first three peaks at 9.65 eV, 9.9 eV and 10.00 eV correspond to three different ionization processes of *ortho*-benzyne, into the first $B_1(\pi)$; $A_2(\pi)$ and $A_1(\sigma)$ respectively. This in contrast to the attribution of Zhang and Chen [414], who reported to ionization potentials at 9.03±0.03 eV and 9.77±0.03 eV to the removal of an electron of the out-of-plane π-orbitals and the in-plane σ-orbitals respectively. The attribution of the 9.24 eV band to ortho-benzyne was also contested by Chrostowska et al. [410], who assigned it to benzene. All these different experiments to determine the ionization energy were not mass-selective, and contamination by impurities are difficult to exclude.

Therefore our group measured recently the threshold photoelectron spectrum, of *ortho*-benzyne mass-selective with photoelectron-photoion coincidence measurements [415]. *Ortho*-benzyne was produced via pyrolysis from the precursor benzocyclobutendione. The attribution of the 9.24 eV band to benzene could be confirmed. *Ortho*-benzyne showed two ionization energies at 9.06±0.05 eV and 9.65±0.05 eV, attributed to the ionization from the π-orbitals and from the σ-orbitals respectively, in agreement with the measurements and attributions by Zhang and Chen [414]. The precursor benzocyclobutendione showed dissociative photoionization to *ortho*-benzyne at an appearance energy of 12.96 eV [415].

The dynamics of of the electronic states of *ortho*-benzyne hasn't been examined yet, though such knowledge is necessary to understand its role in combustion chemistry and to gain insight in its reactivity under astrochemical conditions. Therefore we examined ortho-benzyne with fs-pump-probe spectroscopy after excitation with 266 nm. Time-resolved

mass spectra and ion images of *ortho-benzyne* were recorded, via which we can distinguish between *ortho*-benzyne produced in pyrolysis and *ortho*-benzyne produced via dissociative photoionization. These experiments are complemented by calculations of the vertical and adiabatic excitation energies using different methods, allowing to assign the initially excited state and to interpret the observed decay. All calculations were carried out by D. Kaiser and E. Welz of the research group of Prof. Dr. Engels.

10.1 Experimental

All described experiments used the fs-setup in Saclay (see section 5.4) with 266 nm as a pump pulse and 800 nm as a probe pulse (see section 5.4.2.1). Ortho-

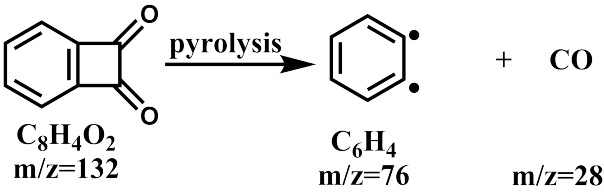

Figure 10.2: *Scheme of the production of ortho-benzyne via pyrolysis of benzocyclobutendione*

benzyne was produced via pyrolysis from benzocyclobutendione[1] (see fig. 10.2), synthesized as described in the master's thesis of Engelbert Reusch [415]. The benzocyclobutane was kept in the T-filter solid source at about 100 - 108 °C. The signal of 266 nm only and 800 nm only were recorded automatically

[1] Many thanks to Engelbert Reusch for providing the benzocyclobutendione sample and to Hans-Christian Schmitt for the help with the experiments.

during each scan and subtracted from the obtained data. Decays were fitted as described in section 13, the obtained uncertainties are uncertainties from the fit program and not from the experimental data.

10.2 Results and Discussion

Comparison of mass spectra at different pyrolysis powers

In fig. 10.3 mass spectra at different pyrolysis powers are displayed.

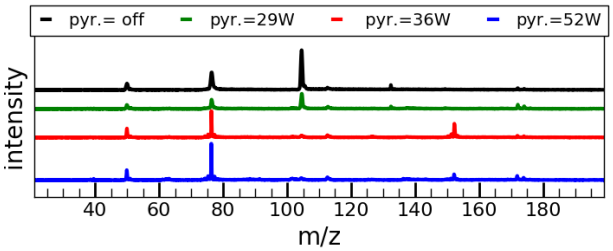

Figure 10.3: *Mass spectra at different pyrolysis powers*

With the pyrolysis off (black line), the precursor at (m/z)=132 is not the only visible peak, but also products out of dissociative photoionization, namely m/z =104, m/z=76 and m/z=50 are seen. The dissociative photoionization has already observed [415] and happens sequentially, meaning that at low photon energies benzoyclobutendione loses one CO (9.35 eV), and at higher photon energies two CO units (12.19 eV) [415]. M/z=50 is attributed to buta-1,3-diine (see fig. 10.4), which has been proposed previously as a possible fragmentation product of *ortho*-benzyne [394]. The peaks visible at m/z=

Figure 10.4: *Structure formula of buta-1,3-diine*

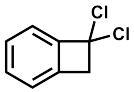

Figure 10.5: *Structure formula of 1,1-dichlorobenzocyclobutane*

172/ 174 (176) with the intensity distributions of 1.5:1.0:0.2 correspond to 1,1-dichlorobenzocyclobutene (see fig. 10.5), an intermediary product in the synthesis of benzocyclobutendione [415].

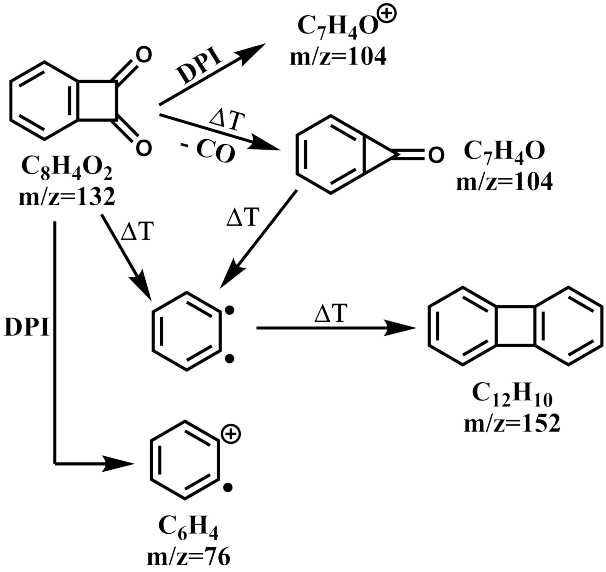

Figure 10.6: *Overview of the differen masses out of pyrolysis and dissociative photoionization of benzocyclobutendione and its pyrolysis products*

Increasing the pyrolysis power to 29 W (green line) leads to a change in relative intensities of m/z=104 and 76. With pyrolysis powers at 36 W (red line) the peak at m/z = 104 (benzocyclopropenone [415]) has disappeared, and the peaks have sharpened considerably; showing that the signals come out of the molecular beam and not out of dissociative photoionization processes. Another signal at m/z=152 appears, corresponding to the mass of the dimer.

Increasing further the pyrolysis power leads to a more favorable intensity ratio between m/z=76 and 152.

The structural formula and the different formation possibilities for the different components are summarized in fig. 10.6. The *ortho*-benzyne mass signal (m/z=76) can therefore be formed not only via pyrolysis, but also via dissociative photoionization of the precursor and also out of dissociative photoionization of the pyrolysis product m/z=104, which has been identified as benzocyclopropenone [415]. This has to be considered when interpreting the time-resolved mass spectra, and to distinguish those two processes, time-resolved ion images of *ortho*-benzyne were recorded. Time-resolved photoelectron spectra were not recorded since the multitude of different masses would make interpretation of these spectra ambiguous.

The small peak at m/z=112, present for all pyrolysis settings, could not be identified.

Time-resolved mass spectra at high pyrolysis power

In fig. 10.7 the sum over all time-resolved mass spectra at 60 W is displayed. Buta-1,3-diine (m/z = 50), *ortho*-benzyne (m/z = 76), benzocyclopropene (m/z = 104), hydrogen abstraction products of benzyne (m/z = 74-75), biphenylene (m/z = 152) and 1,1-dichlorobenzocyclobutane (m/z = 172/174) are visible. The broadness of the peak at m/z=112-114 is a hint at a photodissociative ionization process, but the question remains from which molecule. It does not correspond to any intermediary product in the synthesis of benzocyclobutane [415]. The difference between biphenylene and the unknown mass is

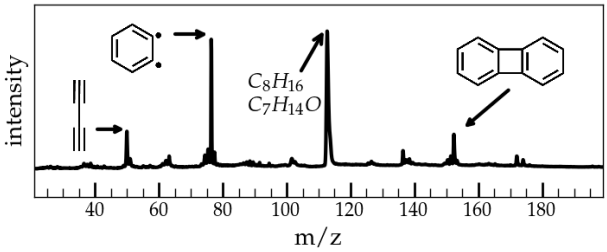

Figure 10.7: *Sum over all time-resolved mass spectra with pyrolysis at 60W, the decays of m/z=76 (benzyne), m/z=112 and m/z=152 (biphenylene) are plotted in fig. 10.8*

about m/z = 40-42, corresponding to C_3H_4-C_3H_6, a possible fragment.

The decays of m/z=50, 76, 112-114 and 152 are shown in fig. 10.8, and their respective time-constants are summarized in table 10.2.

The *ortho*-benzyne signal is well reproduced with a bi-exponential decay including an offset. The benzyne hydrogen abstraction products, however, show a longer second time constant and no offset. Benzocyclopropene shows just like *ortho*-benzyne a bi-exponential decay with an offset, though the observed time constants are considerably longer. The large peak at m/z=114 is well reproduced with a mono-exponential decay including an offset.

As stated previously, time-resolved mass spectra do not allow to unambiguously distinguish between products from pyrolysis and dissociative photoionization, and in the case of *ortho*-benzyne, we have a superposition of these two process. Therefore time-resolved ion images of *ortho*-benzyne were recorded, via which those two processes can be distinguished.

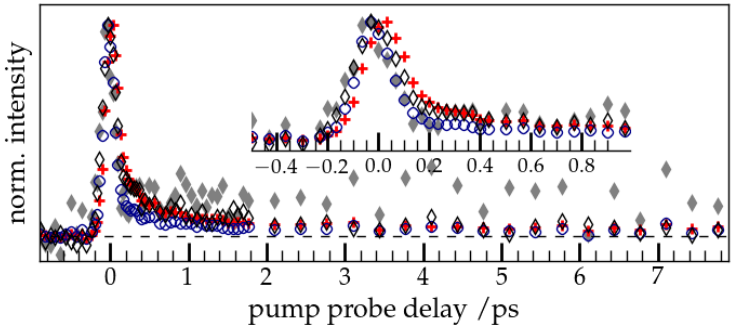

Figure 10.8: *Mass spectra decays of selected signals at a pyrolysis power = 60 W (see mass spectra in fig. 10.7).* + *: m/z=50* ○ *: m/z=76* ♦ *: m/z=112* ◇ *: m/z=152*

m/z	IRF/fs	τ_1/fs	τ_2/ps	offset?
50	123 ± 12	258 ± 19		yes
74-75	129 ± 4	62 ± 4	3.6 ± 0.6	no
76	143 ± 5	73 ± 8	1.5 ± 0.2	yes
104	144 ± 7	154 ± 12	3.9 ± 0.3	yes
112-114	125 ± 16	216 ± 23		yes
152	158 ± 8	93 ± 9	6.4 ± 0.7	no

Table 10.2: *Overview of the different time constants out of the fit for the mass spectra at 60W (see fig. 10.7 and fig. 10.8). If no second time-constant is listed, a mono-exponential fit was sufficient to fit the data.*

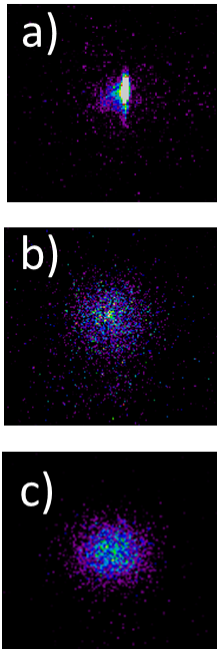

Figure 10.9: *Ion images at zero pump-probe delay for a) o-benzyne with high pyrolysis (50 W) b) o-benzyne with low pyrolysis(30 W) c) m/z=104 with low pyrolysis power(30W)*

Time-resolved ion imaging of benzyne and benzocyclopropene

In fig. 10.9 a) the ion image at pump-probe conditions for *ortho*-benzyne with high pyrolysis (50 W) shows not only signal from the molecular beam (pyrolysis), but also signal from dissociative processes like dissociative photoionization. At lower pyrolysis powers (30 W, fig. 10.9-b) the molecular beam signal dissapears and only dissociative photoionization remains visible. Dissociative photoionization is also visible in the m/z=104 channel at low pyrolysis powers (30 W, fig. 10.9-c), this signal completely dissapears with high pyrolysis power.

In fig. 10.10 the temporal evolution of the molecular beam signal and dissociative processes at high pyrolysis powers (corresponding to the ion image in fig 10.9-a) is shown, both are markedly different. *Ortho*-benzyne out of pyrolysis (°) shows a very fast decay. While it is possible to fit the observed signal using just a Gaussian function with an IRF of 151 ± 3 fs, this IRF is too large compared with previous values obtained in other experiments (see for example chapter 7). Therefore *ortho*-benzyne shows a fast decay $\tau_1 = 31 \pm 8$ fs, which convoluted with an IRF of 138 ± 7 fs reproduces the observed data.

The dissociative processes show a different behavior. The temporal evolution at high pyrolysis power is well reproduced with a bi-exponential decay (see fig. 10.11) with no visible offset. The evolution of m/z=76 in the mass spectra is therefore a superposition *ortho*-benzyne produced via pyrolysis and of *ortho*-benzyne produced via dissociative photoionization. At low pyrolysis power (corresponding to the evolution of the signal in fig. 10.9-c) only the second time constant gets longer.

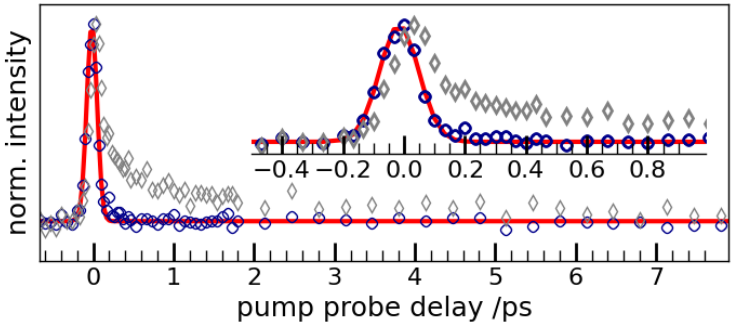

Figure 10.10: *Comparison of the decays of the ortho-benzyne ion image (m/z=76), a representative ion image at time zero is displayed in fig. 10.9 a). ○ corresponds to the decay of ortho-benzyne in the molecular beam; ◊ to the diffuse dissociative photoionization signal around the molecular beam. The red line corresponds either to a Gaussian function (IRF=*151 ± 3 *fs) or to a very fast mono-exponential decay (IRF=*138 ± 7 *fs and* $\tau_1 = 31 \pm 8$ *fs).*

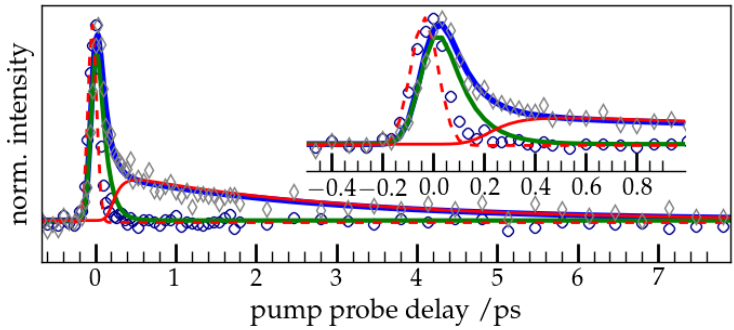

Figure 10.11: *Fitted temporal evolution of the ion images gated on ortho-benzyne (m/z=76), a representative ion image at time zero is displayed in fig. 10.9 a). ○ corresponds to the decay of ortho-benzyne in the molecular beam; ◊ to the diffuse dissociative photoionization signal around the molecular beam. The signal corresponding to the diffuse dissociative photoionization signal for high pyrolysis power ◊ is fitted (*$\tau_1 = 98 \pm 11$ *fs,* $\tau_2 = 2.8 \pm 0.3$ *ps, IRF=*126 ± 8 *fs), the blue line corresponds to the total fit, the green, red and red dotted line to the population of the first state, to the population of the second state and to the IRF respectively.*

This is not surprising, a faster decay is expected at higher temperatures as has been previously observed by Noller with styrene [139] and also in the case of benzocyclobutane (see section 8.2.3).

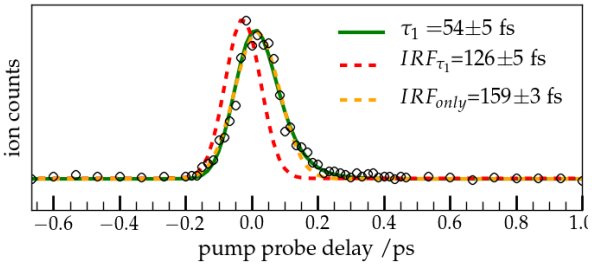

Figure 10.12: *Fitted temporal evolution of the ion image at m/z=104 (of all signal displayed in the representative image in fig.10.9c))*

In fig. 10.9 c) the ion image of m/z=104 at low pyrolysis power is dominated by dissociation. Its temporal evolution is shown in fig. 10.12. Fitting it with only the autocorrelation (159 ± 5 fs) does not reproduce the experimental points near 0.2 ps, which are reproduced using a mono-exponential decay (τ_1 = 54 ± 5 fs, IRF=126 ± 5 fs). This short decay is surprising, since the decay of the ortho-benzyne signal from dissociative photoionization shows a biexponential decay. Probably only the initally excited state of the precursor shows dissociative photoionization to the m/z=104 channel, whereas the lower channels and the initally excited states show dissociative photoionization to the m/z=76 channel.

10.3 Excited States of *ortho*-benzyne

Which state is initially excited with 266 nm? The vertical excitation energies of the first four excited state of *ortho*-benzyne calculated with different methods are summarized in table 10.3.

	ωB97xD	CC2	CASPT(2) (10-10)
$^1A_2$	3.96 (x)	4.05 (3.52) [0.0]	4.10 (3.49)
$^1B_1$	4.16 (3.12)	4.10 (3.49) $[1.4 \cdot 10^{-3}]$	4.17 (3.68)
$^1A_1$	5.67 (5.34)	5.26 (x) $[7.7 \cdot 10^{-3}]$	4.94 (x)
$^1B_2$	4.76 (4.05)	5.15 (x) $[2.2 \cdot 10^{-2}]$	5.23 (4.56)

Table 10.3: *Vertical (adiabatic) excitation energies of the first four excited states of ortho-benzyne in eV with different computational methods. x symbolizes calculations that did not converge for that state/method. Oscillator strengths are given for the CC2 calculations in square brackets.*

All calculations were carried out by D. Kaiser and E. Welz of the research group of Prof. Dr. Engels. The hybrid *second-order approximate coupled cluster* (CC2) [416] using the def2-cc-pVTZ [313,314] basis set was calculated with turbomole [193] , *complete active space perturbation theory* 2^{nd} *order* (CASPT2) [417,418] calculations (cc-pVDZ [198,199] basis set) used MOLCAS 7.8 [419]. Time-dependent

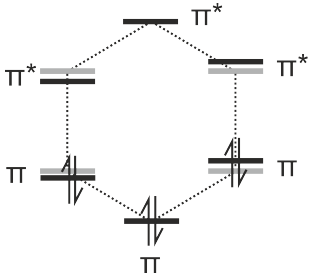

Figure 10.13: *Molecular orbital scheme of the π-orbitals of ortho-benzyne, the grey lines correspond to the positions for benzene.*

density functional theory (TDDFT) calculations with the ωB97xD [196] functional (6-311++g(d,p) [197] basis set) were done with Gaussian09 [194]. All excited-state calculations started from the optimized ground state.

All three methods agree that the first two excited states are nearly degenerate. These correspond to an excitation of an electron in the two highest π-orbitals, to a ππ* transition. In fig. 10.13 a molecular orbital scheme of the π-orbitals of *ortho*-benzyne is displayed, the gray lines correspond to the molecular orbitals of benzene. Due to the triplet bond *ortho*-benzyne is no longer as symmetric as benzene, the degeneracy of the π-orbitals is lifted. Therefore it is not surprising that the first two excited states are energetically very close.

The $^1A_1$-state, whose order switches with the $^1B_2$-state for CASPT(2), also corresponds to a ππ*-excitation. The $^1B_2$-state corresponds to a σσ*-transition out of the biradicaloid molecular orbitals.

The first excited state is dark, whereas all other three show non-negligible oscillator strength. All these states are quite close in energy and can be reached with 266 nm (4.66 eV), if not in a vertical transition, than at least in an adiabatic transition. It is also interesting that no adiabatic excitation energy could be obtained for the $^1A_1$-state, hinting that it might be dissociative. The oscillator strength for the $^1B_2$-state is one order of magnitude higher than of the two lower-lying states, so we therefore assume that we initially excite this state, though it is probably coupled with the $^1B_1$- and $^1A_1$-state.

10.4 Conclusion

So in conclusion *ortho*-benzyne shows a very short mono-exponential decay of about 50 fs after excitation with 266 nm into the $^1B_2$-state. This state is probably dissociative, or it relaxes very rapidly to the energetically close lower-lying states. In both cases the wave-packet leaves the Franck-Condon region, so *ortho*-benzyne can no longer be ionized.

Chapter 11 Further projects

In this chapter the results of experiments on other radicals and biradicals are presented. These experiments were either riddled with experimental difficulties, showed non-conclusive results or are preliminary results. They are summarized here to provide a guide and reference for future experiments on these systems.

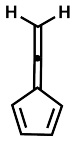

Figure 11.1: *Structure formula of fulvenallene*

11.1 Fulvenallene

Fulvenallene (see fig.11.1) is an important intermediate in the combustion of toluene [420–424], an octane number booster in fuels [425]. It is also involved in the formation of soot [426–428] and its existence has been postulated in the interstellar medium [429]. Over the years it has thus evoked considerable interest which resulted in numerous studies, including matrix isolation studies [430], photoelectron spectra studies [431,432], kinetic [433] and theoretical [434–438] investigations. The photodissociation dynamics of fulvenallene [59,118] to fulvenallenyl after excitation in the D $^1A_1$-state with 250 nm have been examined recently.

Since it is a major photodissociation product of the benzyl radical [242], and since thermal decomposition of toluene [219] and of the benzyl radical [429,439,440] also lead to the fulvenallene/fulvenallenyl radical, we decided to examine the femtosecond dynamics of these molecules, exciting them in the same electronic state as in the previous experiment.

11.1.1 Experimental conditions and results

Fulvenallene/fulvenallenyl were produced via pyrolysis from the precursor phthalide (*Sigma-Aldrich*, used without further purification, see fig. 11.2) using the Saclay setup (see section 5.4) with the sample in front of the pulse valve (see section 5.1). The pyrolysis alone at 36 W was enough to sufficiently heat the oven, seeding phthalide into the gas phase. Helium was used as the carrier gas with 3.0 bar absolute backing pressure. The NOPA at 250 nm (see section 5.4.2.3) was used as the pump laser and 800

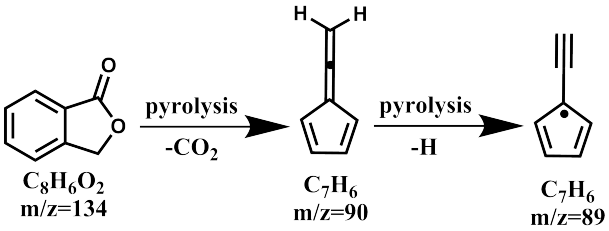

Figure 11.2: *Production of fulvenallene via pyrolysis from phthalide*

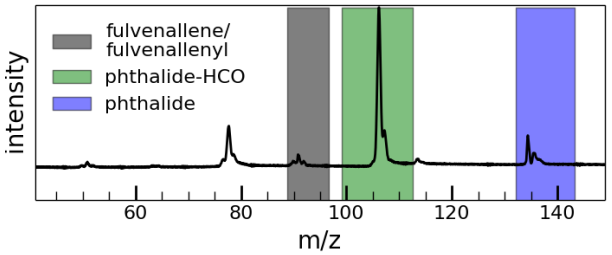

Figure 11.3: *Mass spectrum of phthalide with pyrolysis on*

nm as the probe laser (see section 5.4.2.1). Both lasers were polarized horizontally in respect to the ground.

Even though the mass spectra (see fig. 11.3) showed that fulvenallene is produced, it is not a clean mass spectrum. Significant precursor signal is still visible, as well as the loss of HCO (m/z=105). This peak is very broad and originates most likely out of dissociative photoionization, as has been observed in synchrotron experiments with energies higher than 10.5 eV [142]. No fulvenallene/fulvenallenyl signal out of dissociative photoionization between 7-13.9 eV was observed, so this signal really originates from pyrolysis. The peak at m/z=77 cor-

responds to phenyl, an impurity from previous experiments with diazobenzene. The different mass decays represented by the rectangles in fig. 11.3 show the same temporal evolution (fig. 11.4). Some (very noisy) decay is visible, but overall it is quite short compared to the instrument response function (IRF), which was estimated from previous experiments (ex. 1-methylallyl, see section 6.4).

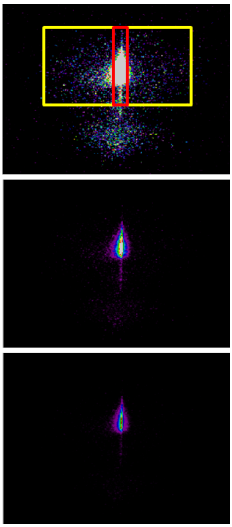

Figure 11.5: *Ion imaging of fulvenallene/fulvenallenyl at different intensity scales. The red rectangle corresponds to the 'molecular beam', the yellow one to 'dissociative photoionization' in fig. 11.6.*

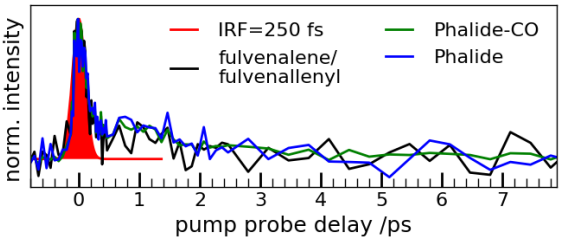

Figure 11.4: *Decays of the different masses as indicated in fig. 11.3*

Ion images of the fulvenallene/fulvenallenyl signal (T(A) = 8.71 µs, T(B) = 300 ns) show that the molecular beam (see fig. 11.5) is surrounded by a 'halo', indicating formation by dissociative photoionization. The precursor for the dissociative photoionization formation can either be phthalide, but since this was not observed [142] between 7-13.9 eV. It is more likely formed by dissociative photoionization of m/z=105. The temporal evolution of the molecular beam (red rectangle in fig.11.5) and of the dissociative photoionization processes (yellow rectangle in fig. 11.5, without the signal in the red rectangle) is plotted in fig. 11.6. The molecular beam signal only shows autocorrelation, whereas the fulvenallene/fulvenallenyl signal formed by dissociative photoionization shows a time decay.

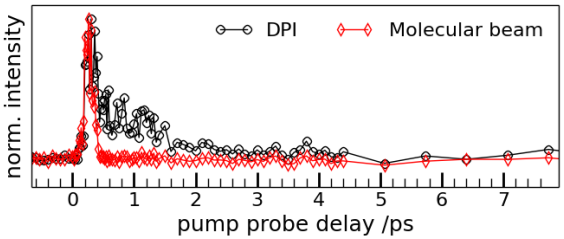

Figure 11.6: *Decay of the PI images, with the areas of interested depicted in fig. 11.5*

In conclusion although we could produce fulvenallene, the ovserved signal was partially due to dissociative photoionization. The employed solid source source did not permit to increase the pyrolysis to high enough temperatures as to fully convert our precursor to fulvenallene/fulvenallenyl. Through time-resolved ion imaging we were able to distinguish the fulvenallene/fulvenallenyl signal produced by pyrolysis from the one produced via dissociative photoionization. Only autocorrelation was observed, though an excited state lifetime < 50 fs can not be excluded. Excited in the D $^1A_1$-state with 250 nm, fulvenallene is known to eject a hydrogen atom [118], so we probably move out of the Franck-Condon region faster than our temporal resolution and can no longer ionize fulvenallene.

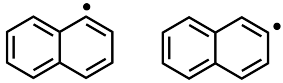

Figure 11.7: *The two isomeric naphthyl radicals: 1-naphthyl (left) and 2-naphthyl (right) radical*

11.2 Naphthyl radicals

The naphthyl radical has two isomers: the 1-naphthyl and 2-naphthyl radical (see fig. 11.7). Both are derivatives of the simplest polycyclic aromatic hydrocarbon (PAH) naphthalene, which is involved in the formation of soot [10]. In computational kinetic studies naphthyl radicals are incorporated to account for the formation of aromatic species in laminar flames [441]. The potential energy surface of their reaction with molecular oxygen has been examined, showing that the addition of O_2 to the respective radical site is barrier-less and leads to the formation of naphthoxy radicals [442].

Since the naphthalene cation was found recently in the Perseus molecular cloud [443], it is not surprising that the naphthyl radicals and naphthyl cations are also possible candidate carriers of the diffuse interstellar bands, resulting in a number of computational studies of IR spectra [444, 445] and their excited-state energies [446].

The naphthyl anions were studied quite extensively. Neumark et al. studied the vibronic structure of both radicals by doing slow photoelectron VMI spectroscopy of their anions, which allowed them to measure their electron affinities and vibrational frequencies. Their determined value of the electron affinity for 1-naphthyl is in good agreement with earlier measurements by Lineberger et al. using negative ion photoelectron spectroscopy [447]. The 1-naphthyl has has a higher electron affinity than the 2-naphthyl isomer [448], in agreement with earlier calculations [449]. Neumark et al. also measured the lowest excited state of the naphthyl radicals (389 nm for the 1-naphthyl radical and 370 nm for the 2-naphthyl radical) [448].

Less clear is situation for the ground state of the naphthyl cations. CCSD(T) studies yield singlet ground states for both naphthyl cations. These studies also predict that the energetically higher lying triplet states are different types for both isomers, $\pi\sigma$ for the 1-naphthyl, $\sigma\sigma$' for the 2-naphthyl cation [450,451]. Experimentally, however, IR spectra indicate a triplet ground state for both naphthyl cations [452].

To pave the way for future experiments on the naphthyl radicals, two different precursors of the 1-naphthyl radical have been examined and the production conditions optimized. No experiments on a precursor for the 2-naphthyl radical were performed, but an analogous behavior to the 1-naphthyl radical precursors is expected.

11.2.1 Experimental conditions and results

Using the setup in Würzburg (see section 5.3.1) two precursors for the 1-naphthyl isomer were examined using 118 nm, naphthalen-1-ylmethylnitrite and 1-iodonaphthalene (*Sigma-Aldrich*, used without further purification). The synthesis of naphthalen-1-ylmethylnitrite is described in the appendix 12. Both precursors were seeded into gas phase with the T-filter source with the pyrolysis setup mounted (see chapter 5.1). Pyrolysis of naphthalen-1-ylmethylnitrite produces the 1-naphthyl radical, formaldehyde and NO (see fig. 11.8, top), whereas pyrolysis of 1-iodonaphthalene simply cleaves the carbon-iodide bond (see fig. 11.8, bottom). Helium at 1.4 bar absolute pressure was used as a carrier gas. Signals for naphthalen-1-ylmethylnitrite and 1-iodonaphthalene were measured at temperatures of 140

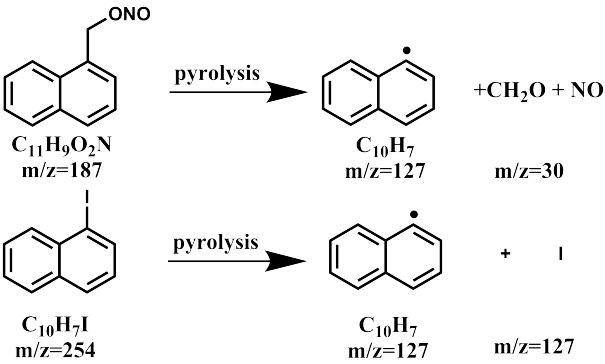

Figure 11.8: *Pyrolysis of naphthalen-1-ylmethylnitrite (top) and 1-iodonaphthalene (bottom) produces the 1-naphthyl radical*

and 134°C respectively.

In fig. 11.9 the mass spectrum for naphthalen-1-ylmethylnitrite at different pyrolysis powers is plotted. With pyrolysis off (black line) two peaks at m/z=127 and m/z=157 are visible, corresponding to the 1-naphthyl radical and the precursor -30 (probably NO) product out of dissociative photoionization by 118 nm. No precursor at m/z=187 is visible. With pyrolysis on the ratio between the m/z=127 and m/z=157 changes, both peaks grow more intense. For higher pyrolysis powers the m/z=157 peak (precursor-NO) decreases again in intensity, indicating that less precursor is available.

In fig. 11.10 the mass spectrum for 1-iodonaphthalene at different pyrolysis powers is displayed. With the pyrolysis off (black line), the precursor (m/z=254) and also the radical at m/z=127 are both visible. The peak at m/z=157 corresponds to the precursor (naphthalen-1-ylmethylnitrite) minus NO, which was in the source just before. Increasing the pyrolysis decreases the precursor m/z=254

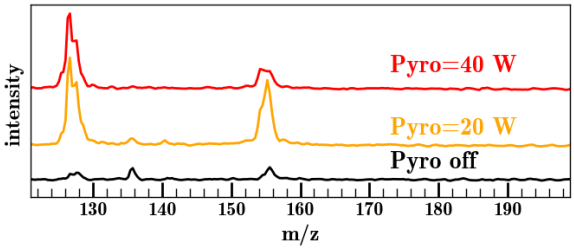

Figure 11.9: *Mass spectra for different pyrolysis powers of naphthalen-1-ylmethylnitrite*

signal, at 50 W it has completely disappeared. The radical signal visible with no pyrolysis stems from the nitrite precursor from previous experiments, since synchrotron measurements at the Swiss light source conducted recently showed no dissociative photoionization below 12 eV [453].

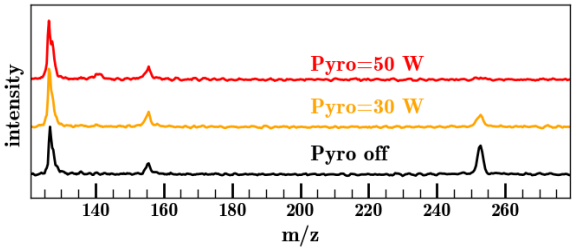

Figure 11.10: *Mass spectra for different pyrolysis powers of 1-iodonaphthalene*

Since for 1-iodonaphthalene the precursor signal disappeared completely, contrary to naphthalen-1-ylmethylnitrite, where the precursor-30 remained even at high pyrolysis, the 1-iodonaphthalene precursor is to be preferred. Both precursor are suitable for the production of the 1-naphthyl radical and it is very likely that the mass spectra for the 2-naphthyl

isomer will look similar. Measurements with PEPICO to determine the ionization energy of the 1-naphthyl radical were conducted successfully and are to be published shortly [453].

11.3 Phenyl radical

Figure 11.11: *Structure formula of the phenyl radical*

The phenyl radical (see fig. 11.11) is one of the central intermediates in the formation of soot [9] and polycyclic aromatic hydrocarbons (PAH) [454–456]; it is the first aromatic molecule formed by the addition of acetylene to n-C_4H_3 [457]. For the formation of polycyclic aromatic hydrocarbon (PAH)-like molecules in extraterrestrial conditions like carbon stars it is also one of the key participants [458, 459].

The phenyl has thus suscited considerable interest over the years, resulting in studies of its kinetics with small inorganic molecules such as NO [460], Cl, Br, Cl_2 and O_2 [461] and organic molecules [462] as well as in numerous spectroscopic studies. The phenyl radical is planar with C_{2v} symmetry. The geometry of the ground state was characterized via rotational spectroscopy [463, 464], ESR spectra [465, 466], infrared spectrum of the phenyl radical in the gas phase [467, 468] and in an argon matrix [469, 470] as well as the Raman spectrum in the argon matrix [471].

Its absorption spectra was measured in aqueous solution [472], in the gas phase [460, 461, 473, 474]and in solid argon [475], and the excited states calculated using different methods [476–478], showing (in order) a $^2B_1 \leftarrow^2 A_1$ n $\leftarrow \pi$ transition between 535 -490 nm [461, 474], a $^2A_1 \leftarrow^2 A_1$ transition with λ_{max}=235.1 nm [474] and a $^2B_2 \leftarrow^2 A_1$transition with the origin at 211.5 nm [474]. Its vertical ionization energy is 9.20 eV [479], nearly 1 eV above its adiabatic ionization energy 8.32 ± 0.04eV [480].

The $^2B_1 \leftarrow^2 A_1$ transition was measured rotationally resolved [454, 481] and its rotational spectrum simulated using a B3LYP/TD-B3LYP//N07D model [482]. The dynamics of the photodissociation between 215-268 nm to hydrogen and ortho-

benzyne were examined by Song et al., showing an isotropic distribution in excellent agreement with RRKM predictions [385]. Neumark et al. examined the photodissociation to C_4H_3 and C_2H_2 at 193 nm [483]. The results were at first in disagreement with theoretical calculations [484], but agreed later when slightly different experimental conditions were applied [485].

But no information on the lifetime of this deactiation is known, which is a prerequisition ofor the understanding of its dynamics. We were therefore examined the photodissociation in the A $^2A_1$-state with 245 nm using pump-probe fs spectroscopy, hoping to observe via which electronic states this dissociation occurs.

11.3.1 Experimental

The phenyl radical was examined with the fs-pump-probe setup in Saclay (see chapter 5.4) using the NOPA at 245 nm as the pump laser and 800 nm as the probe laser (see section 5.4.2.2 and 5.4.2.3). Diazobenzene (purchased from *Sigma-Aldrich* and used without further purification) in the solid source with the sample in front of the pulse valve (see chapter 5.1) was used to produce the phenyl radical using pyrolysis (see fig. 11.12). The solid source was

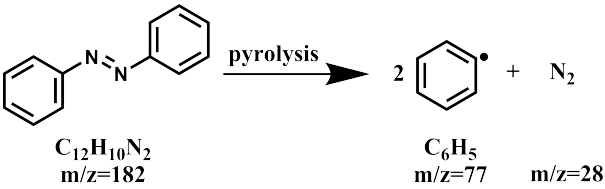

Figure 11.12: *Scheme of the production of the phenyl radical via pyrolysis of diazobenzene*

kept at temperatures between 60-70°C, the pyrolysis power typically employed was 17 W. Helium at 1.8 bar absolute pressure was used as a carrier gas. Both lasers were polarized parallel to each other.

11.3.2 Results and Discussion

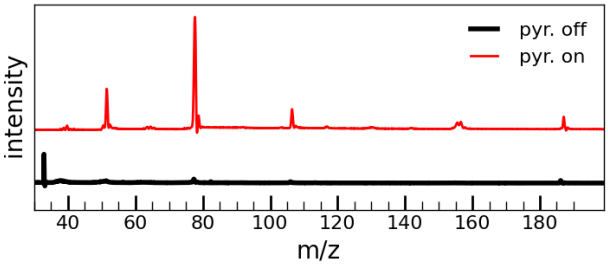

Figure 11.13: *Mass spectra with pyrolysis on and pyrolysis off for diazobenzene*

The mass spectra with pyrolysis on and pyrolysis off are displayed in fig. 11.13. The phenyl radical is the main peak with pyrolysis on (m/z=77), but several other masses are present with non-negligible intensities. The peaks at higher masses correspond to $C_6H_5N_2$ (m/z=105), the dimer of the phenyl radical (which was shown to be biphenyl [486], m/z=154, see fig. 11.15) and to the precursor molecule (m/z=182). This indicates an insufficient pyrolysis (not all precursor molecules are completely pyrrolized) and a too high concentration of phenyl radicals (presence of biphenyl). Unfortunately the pyrolysis power could not be increased further, since that lead to a rise in the temperature of the sample oven, and consequently to more dimerization. At lower masses C_4H_4 (m/z=52) is visible. Several isomers (see fig. 11.14) are possible, for example cyclobutadiene,

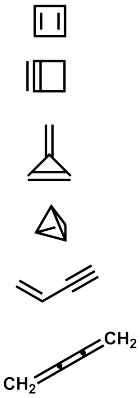

Figure 11.14: *Structure formula of (from top to bottom) cyclobutadiene, cyclobutyne, methylenecyclopropene, tetrahedrane, vinylacetene and butatriene*

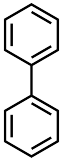

Figure 11.15: *Structure formula of biphenyl*

cyclobutyne, methylenecyclopropene, tetrahedrane, vinylacetene and butatriene. Though we cannot distinguish in our experiments between the different isomers, in other experiments vinylacetene was identified as a combustion product of the phenyl radical [487].

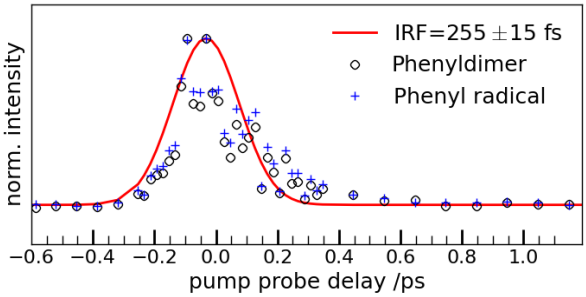

Figure 11.16: *Temporal evolution of the mass spectrum signals of the phenyl radical and the phenyl dimer*

The normalized temporal evolution of the phenyl radical signal and of the dimer signal are displayed in fig. 11.16. The signal has a Gaussian shape and can be fitted using just the instrument-response function IRF=255 ± 15 fs. Observing this autocorrelation with ion imaging (see fig. 11.17), the observed phenyl radical signal does not originate from the molecular beam, but from a dissociative process.

Most likely the observed phenyl radical signal originates from dissociative photoionization of biphenyl. Increasing the background pressure as to dilute the precursor and as to decrease the dimer formation did not lead to the appearance of a molecular beam signal in ion imaging. Most likely the dimer has a much better absorption cross section.

In conclusion the phenyl radical could not be examined successfully, only phenyl produced by dissociative photoionization from the biphenyl was observed. The oscillator strength of the phenyl radical at 245 nm is probably a lot weaker compared to the oscillator strength of biphenyl.

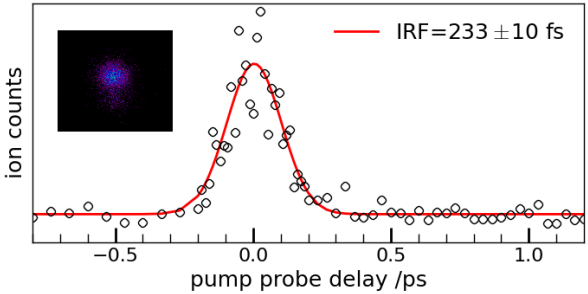

Figure 11.17: *Temporal evolution of the ion image (T(A)=8.08 µs, T(B)=300 ns), corresponding to the phenyl signal. The inlet image displays the ion image at time zero.*

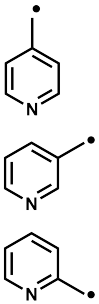

Figure 11.18: *Picolyl isomers (top to bottom): para-, meta-, and ortho-picolyl*

11.4 Picolyl radicals

Picolyl radicals (see fig. 11.18) are isoelectronic to C_7H_7, whose isomers benzyl and tropyl have been examined during this thesis (see chapter 7). The six-membered pyridinic rings are, along with the five-membered pyrrolic rings one of the main sources of nitrogen in fuels. Combustion of these ring systems lead to nitrogen oxides (NO_x), whose production is severely limited in several countries [488] since they are pollutants [489].

Research on these isomers is still sparse. Mackie et al. modeled experimentally data on the pyrolysis of 2-picoline [490], showing that the decomposition product 2-picolyl is not as much resonance stabilized as the benzyl radical [491]. The pyrolysis of 2-picoline leads to important formations of soot [492]. The combustion of its isomer 3-picoline, with 3-picolyl as one of the principal initial decomposition routes, resembles more the combustion of toluene [493]. The lifetime of the D_1-state of the 3-picolyl radical has been shown to be much shorter than the lifetime of the benzyl radical D_1 state [494].

Our group recently determined the ionization energies of all three isomers using threshold photoelectron spectroscopy [495, 496], with 8.01 ,7.59 and 7.70 eV for 4-,3- and 2-picolyl respectively.

No work has been published so far on the higher electronic excited states, be it an experimental or calculated absorption spectrum. But the similarities and discrepancies to the benzyl radical should provide a fascinating insight in the changes of the electronic structure by the nitrogen group. We therefore examined this isoelectronic molecule using pump-probe spectroscopy with 266 nm as a pump laser.

11.4.1 Experimental difficulties

The 3- and 2-picolyl radical were examined using the Saclay setup (see chapter 5.4) with 266 nm as a pump laser and 800 nm as a probe laser (see chapter 5.4.2.2). They were produced via pyrolysis from their amine analogues (see fig. 11.19), purchased from *Sigma-Aldrich* and used without further purification.

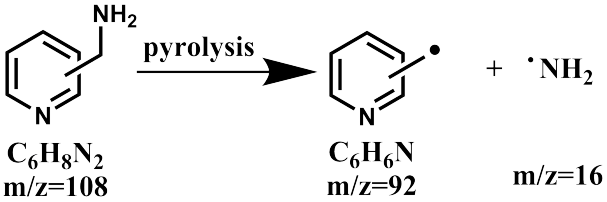

Figure 11.19: *Pyrolysis of the amine precursor to produce the corresponding picolyl radical*

For the 2-picolylamin the source for liquids (see chapter 5.1) with helium as a carrier gas at 2.2 bar absolute pressure and pyrolysis at 40 W was used. With 800 nm slightly focused (see fig. 11.20), the picolyl radical (m/z=92) is produced once the pyrolysis is turned on. Other masses like pyridine

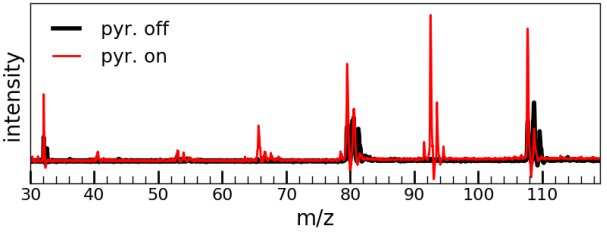

Figure 11.20: *2-Picolylamine in source for liquids, pyrolysis off and pyrolysis on*

(m/z=79) and the precursor (m/z=108) are still present, so only time-dependent mass spectra were recorded.

In the upper panel in fig. 11.21, the sum of all recorded tof-spectra for a time delay of 7 ps is plotted. The masses 79 (pyridine) and 80 (pyridine+H) dominate the spectrum, the masses 108 (2-picolylamine) and 109 (2-picolylamine+H) are also very intense. All four peaks show the same time-dependent behavior ($\tau_1 = 130 \pm 40$ fs, $\tau_2 = 3.2 \pm 0.2$ ps, IRF = 110 fs), indicating that pyridine is formed from the picolylamine by dissociative photoionization. The small picolyl peak shows a slightly different behavior ($\tau_1 = 160 \pm 50$ fs, $\tau_2 = 2.5 \pm 0.8$ ps, IRF = 110 fs), but the error bars are so large that this difference was not further explored. But the decay of the picolyl signal is also bi-exponential, as observed for the benzyl radical with 265 nm pump/ 798 nm probe.

The synthesis of another precursor, 2-picolyleth-

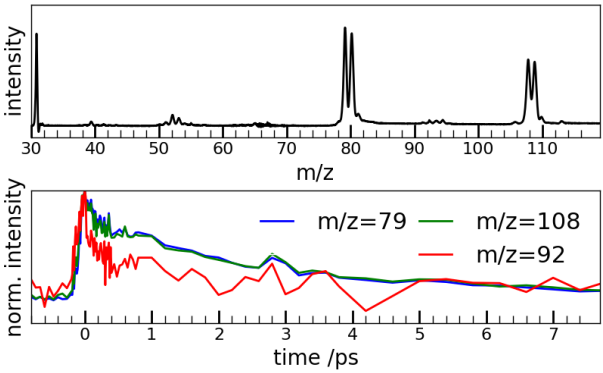

Figure 11.21: *Upper panel: Sum of all mass spectra recorded. Lower Panel: TOF decays for different masses, the intensities are normalized*

annitrite, using the same synthetic protocol as for the other nitrite precursors (see chapter 12) was unsuccessful.

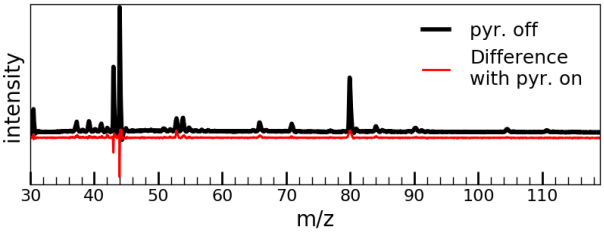

Figure 11.22: *3-Picolylamine in source for liquids, pyrolysis off and the difference with pyrolysis on*

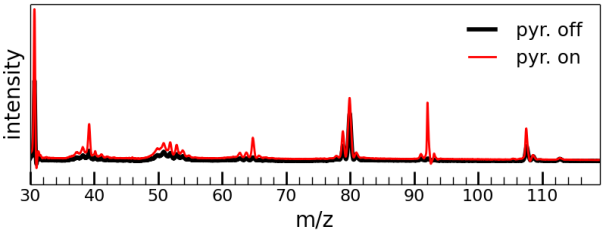

Figure 11.23: *3-Picolylamine in solid source, pyrolysis off and with pyrolysis on*

For the 3-picolylamine two different sources were used: the source for liquids and the oven in front of the pulse valve (see chapter 5.1), both with helium as the carrier gas at 2.1 bar absolute pressure and 52 W pyrolysis power. With the source for liquids and 800 nm slightly focused (fig. 11.22), the contrast between pyrolysis on and off is poor. The most intensive signal at m/z=79 corresponds to pyridine.

With the solid source mounted in front of the pulse valve a new peak at m/z=92 appears with pyrolysis on(fig. 11.23), which is attributed to the

i
The T-filter source was not used because it was not at disposition at that time.

3-picolyl radical. Mounting the pyrolysis on the oven heats the oven very strongly, causing strong signal intensities changes, and a rapid emptying of the oven. No time-dependent scans could be obtained with the oven in front of the pulse valve as the source.

11.5 Propargylene

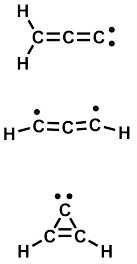

Figure 11.24: C_3H_2 isomers (from top to bottom): propadienylidene, propargylene and cyclopropenylidene

Propargylene (see fig. 11.24, middle) is one of three stable C_3H_2 isomers, all three of astrochemical importance. Propadienylidene and cyclopropenylidene, the other two isomers (fig. 11.24 top and bottom structure formula respectively) have already been identified via characteristic absorption lines in the interstellar medium [497, 498]. Hints exist for the existence of propargylene in interstellar medium, but its existence has not yet been definitely proven [499].

The structure of propargylene - whether it is a linear or bent chain, a singlet or triplet in its ground state - was object of several theoretical investigations [500–502]. This discussion was resolved experimentally by Seburg et al., combining IR, UV-Vis and EPR spectroscopy. Propargylene is a biradical has a triplet ground state with bent geometry, just as depicted in fig. 11.24, middle [503]. The adiabatic ionization energy of propargylene has been determined recently using mass selective photoelectron threshold spectra (8.99 ± 0.02 eV) [504], a more precise value than the one determined previously using photoionization efficiency (8.96 ± 0.04 eV) [505].

Propargylene loses an hydrogen atom after excitation with 250 nm. This photodissociation was examined by Giegerich et al. using photofragment velocity-map imaging [119]. The hydrogen distribution remained nearly isototropic even at high kinetic energies of the hydrogen fragment, which are higher than expected for a pure statistical dissociation. Non-adiabatic trajectory surface hopping calculations attribute this to a predissociation in the T_6-T_4, where the triplet state T_6 is initially excited with 250 nm. This predissociation happens

on the fs-time scale, several orders of magnitude faster than the ns-time resolution of the setup used by Giegerich et al., therefore the same process was examined using fs pump-probe spectroscopy.

11.5.1 Experiment

The experiment was carried out using the fs-pump-probe setup in Saclay (see section 5.4). Propargylene was produced via pyrolysis from the precursor diazopropyne, see fig. 11.25.

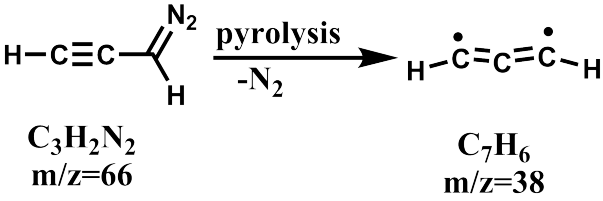

Figure 11.25: *Pyrolysis of the precursor diazopropyne produces propargylene.*

Since the precursor is unstable at room temperature and decomposes after 4-6 hrs, diazopropyne was freshly synthesized from *N*-nitroso-*N*-(2-propinylurea) each day prior to each experiment[1]. It was synthesized directly into a liquid precursor container (see section 5.1), which was cooled using with an ethanol-liquid nitrogen bath. The synthesis is described in detail elsewhere [59, 506]. The pump laser was the NOPA at 250 nm (see section 5.4.2.3) with 800 nm as a probe laser (see section 5.4.2.2). Argon at an absolute pressure of 1.5 bar was used as carrier gas, the pyrolysis was kept at about 30 V,

[1] Here again I humbly thank Engelbert Reusch for the help with the synthesis

which was more than sufficient for a complete conversion of the precursor in experiments in Würzburg. A complete conversion is quintessential for this experiment, since the diazopropyne precursor also absorbs at 250 nm [59, 119].

11.5.2 Results and Discussion

In fig. 11.26 mass spectra at pump-probe conditions with different pyrolysis powers are shown. With pyrolysis off (upper trace) a clean mass spectrum consisting of two peaks at m/z= 66 and 38 is obtained.

These correspond to diazopropyne and propargylene out of dissociative photoionization, which has been observed before [504]. With the pyrolysis at 18 W (middle panel), some precursor is still visible. At 31 W pyrolysis power the precursor peak has completely disappeared (lower trace), but no propargylene peak has appeared. Instead many

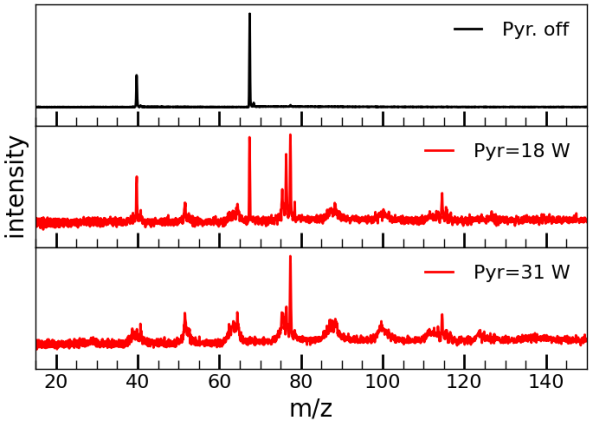

Figure 11.26: *Mass spectrum at pump-probe conditions at different pyrolysis powers*

other peaks, notably at m/z=76,77,78 are visible. These are already visible with the pyrolysis off, but are much weaker than the precursor peak. The observed peaks with pyrolysis on could correspond to impurities in the apparatus, like long C_n-chains.

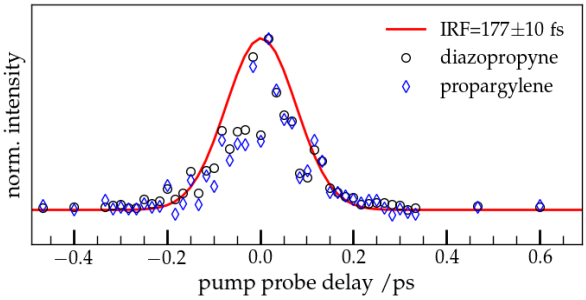

Figure 11.27: *Time-resolved mass spectra of diazopropargylene without pyrolysis*

Several experimental conditions were optimized as to obtain a pump-probe radical signal, including different bath temperatures and carrier gases (He and Ar). The observed mass spectra did not change. On the precursor a pump-probe signal was easily identifiable, but with pyrolysis on this signal disappeared and no propargylene signal appeared. Adjusting the laser intensities also did not allow to observe a propargylene signal out of pyrolysis. Once it seemed as if there was a pump-probe propargylene signal out of pyrolysis visible on the oscilloscope, but in the subsequent time-resolved mass spectra it could not be reproduced.

A time-resolved mass spectra over the precursor only (no pyrolysis on) showed only autocorrelation, as is depicted in fig. 11.27. The autocorrelation is realistic for the NOPA.

In conclusion propargylene could not be examined successfully using fs-pump-probe spectroscopy. The synthesis of the precursor was successful, but production of the radical via pyrolysis and pump-probe signal could not be obtained. It is likely that the dissociation of propargylene is very fast, so that the molecule moves out of the Franck-Condon region too fast to be ionized and to be detectable with a fs-pump-probe laser scheme.

Part IV

Appendix

Chapter 12 Synthesis

All nitrite precursor synthesis were performed according to a literature-known procedure [174].

If not otherwise stated, chemicals were purchased from the 'Chemikalienausgabe' of the University of Würzburg.

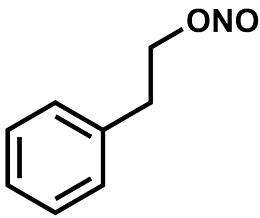

2-Phenylethylnitrite

In a 100 ml flask equipped with a dropping funnel with pressure equalizing tube a solution of 12 g (174 mmol, 1.5 eq) sodiumnitrite in 20.5 ml water was cooled to 0°C in an ice-bath. 13.9 ml (14.17 g, 116 mmol, 1.0 eq) 2-Phenylethanol was added, the flask is covered with aluminum foil to exclude light. 26.5 ml 30% sulfuric acid, prepared from 22.6 ml water and 5.3 ml conc. sulfuric acid, was slowly added via the dropping funnel over 40 minutes. Nitrose gases form and are evacuated via the pressure equalizing tube of the dropping funnel. After stirring for 90 min in the dark at 0°C, 20 ml of a saline solution (20 ml water with 3.75 g NaCl and 0.5 g $NaHCO_3$) is added via the dropping funnel to the yellow reaction mixture. After stirring for another 20 minutes at room temperature the organic and aqueous phases are separated, the yellow organic phase is washed two times with 20 ml and 25 ml of a saline solution (20 ml water with 3.75 g NaCl and 0.5 g $NaHCO_3$; 25 ml water with 4.6 g NaCl and 0.5 g $NaHCO_3$) . **Yield:** 10.5 g (60%) of a yellow liquid **IR (ATR):** no O-H peak between 3500-3200 cm^{-1}, $\nu(C_{sp^2}\text{-H})$ = 3064 cm^{-1}, $\nu(C_{sp^3}\text{-H})$ = 2947 cm^{-1}, $\nu(\text{R-O-N=O})_{syn}$= 1643 cm^{-1},$\nu(\text{R-O-N=O})_{anti}$ = 1605 cm^{-1}

2-Methyl-3-buten-1-nitrite

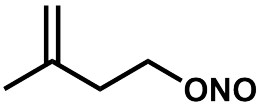

In a 250 ml three-necked flask equipped with a thermometer and a reflux condenser with a dropping funnel with pressure equalizing tube mounted on top 18.0 g (261 mmol, 1.5 eq) sodiumnitrite in 31 ml water was cooled in an ice-bath to 0°C. 17.6 ml (15 g, 174 mmol, 1.0 eq) 3-Methyl-3-buten-1-ol (*Sigma-Aldrich*, CAS: 763-32-6) was added, the flask was then covered with aluminum foil. 39.7 ml 30% sulfuric acid, prepared from 33.9 ml water and 7.6 ml conc. sulfuric acid, was slowly added via the dropping funnel over one hour. Nitrose gases are formed and are evacuated via the pressure equalizing tube. After stirring for 90 min in the dark at 0°C, 30 ml of a saline solution (30 ml water with 5.6 g NaCl and 0.75 g $NaHCO_3$) were added via the dropping funnel to the blue solution. The phases were separated and the organic phase was washed two times with 30 and 37 ml of a saline solution (30 ml water with 5.6 g NaCl and 0.75 g $NaHCO_3$; 37 ml water with 6.9 g NaCl and 0.94 g $NaHCO_3$). **Yield:** 17.2 g (85%) of a blue-turquoise liquid, which is stable for about a week at room temperature. The decay can be seen visually as the solution turns green and then yellow. **IR(ATR):** no O-H peak between 3500-3200 cm^{-1}, $\nu(C_{sp^2}\text{-H})$ = 3087 cm^{-1}, $\nu(C_{sp^3}\text{-H})$ = 2989-2906 cm^{-1}, $\nu(\text{R-O-N=O})_{syn}$ = 1643 cm^{-1},$\nu(\text{R-O-N=O})_{anti}$ = 1566 cm^{-1}

(Z)-3-Penten-1-ylnitrite

In a 100 ml three-necked flask equipped with a thermometer and a reflux condenser with a dropping funnel with pressure equalizing tube mounted on top, 8.8 g (127 mmol, 1.4 eq) sodiumnitrite in 17 ml water was cooled to 0°C in an ice-bath. 9.2 ml

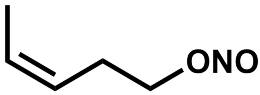

(7.85 g, 89 mmol, 1.0 eq) cis-3-Penten-1-ol (*ABCR*, CAS: 764-38-5) was added and the flask covered with aluminum foil. 19.1 ml 30% sulfuric acid, prepared from 19.0 ml water and 4.26 ml conc. sulfuric acid, were slowly added via the dropping funnel over an hour, then stirred in the dark for 90 min at 0°C. 17 ml of a saline solution (17 ml water with 3.13 g NaCl and 0.42 g $NaHCO_3$) was added via the dropping funnel, the phases separated and the yellow organic phase was washed two times with 17 and 19 ml of the same saline solution (17 ml water with 3.13 g NaCl and 0.42 g $NaHCO_3$; 17 ml water with 2.80 g NaCl and 0.38 g $NaHCO_3$). **Yield:** 7.2 g (75%) of a yellow liquid **IR(ATR):** no O-H peak between 3500-3200 cm^{-1}, $\nu(C_{sp^2}\text{-H})$ = 3077 cm^{-1}, $\nu(C_{sp^3}\text{-H})$ = 2992-2905 cm^{-1}, $\nu(\text{R-O-N=O})_{syn}$= 1643 cm^{-1},$\nu(\text{R-O-N=O})_{anti}$ = 1567 cm^{-1}

Naphthalen-1-ylmethylnitrite

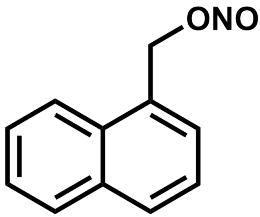

In a 100 ml flask equipped with reflux condenser and a dropping funnel with pressure equalizing tube mounted on top 3.3 g sodiumnitrite (47.4mmol, 1.5 eq) in 12 ml water were cooled in an ice-bath to 0°C. 5.0 g (31.6 mmol, 1.0 eq) of naphthalen-1-ylmethanol (*Sigma-Aldrich*, CAS: 225-324-1) was added, the flask was then covered with aluminum foil. 7.65 ml 30% sulfuric acid, prepared from 6.2 ml water and 1.45 ml conc. sulfuric acid, was slowly added via the dropping funnel over ten minutes. Nitrose gases form and the solution changes color to whitish-yellow. After stirring for 90 min in the dark, 20 ml of a saline solution (30 ml water with 5.6 g NaCl and 0.75 g $NaHCO_3$) is added via the dropping funnel. The phases are separated and the

organic phase is washed once with 7 ml of the saline solution. **Yield:** 1.4 g (23%) of a yellow-orange oil **^{1}H-NMR (400 MHz, $CDCl_3$):** [ppm] =6.02 (s, 2H, CH_2), 7.11-7.46(m, 4H, CH naphthyl), 7.73-7.78 (m, 2H, CH naphthyl), 7.83-7.85(m, 1H, CH naphthyl)

Tropyliumbromide

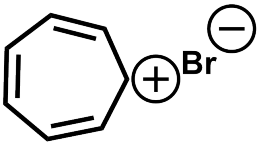

Both the synthesis of tropyliumbromide and of ditropyl were carried out as described in the literature [507] with some minor changes. In a three-necked 500 ml flask equipped with reflux condenser and dropping funnel 26.1 ml (23 g, 250 mmol, 1.0 eq) cycloheptatriene (*Sigma-Aldrich*, CAS: 544-25-2) in 200 ml dichloromethane was cooled in an ice-bath to 0°C. Over 3.5 h a solution of 12.8 ml (40 g, 250 mmol, 1.0 eq) bromine in 50 ml dichloromethane was added under cooling via the dropping funnel. The solvent was removed via a rotary evaporator and the dark-brown (red) oil was heated at 90°C over 24 hours at a pressure <1 mbar. The solution turns into an ocher-brown solid. The solid was pestled and washed with dichloromethane until the dichloromethane ran clear. The ocher-green solid was dried for several days under reduced pressure in an dessicator. **Yield:** 25.7 g (30%) **^{1}H-NMR (400 MHz, $CDCl_3$):** [ppm]=9.31 (s, 7H)

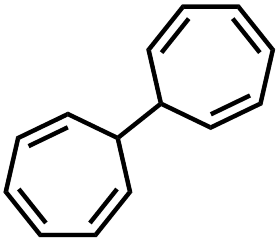

Ditropyl

In a one-necked 100 ml round flask 5.0 g (29.2 mmol, 1.0 eq) tropyliumbromide were dissolved in 40 ml water. To the dark solution 2.0 g zinc powder was added and the solution was shaken vigorously. The solution turns yellow. In a waterbath the solution was heated at 40°C for three hours, the solu-

tion turns colorless. The solution was then filtered and the aqueous phase extracted four times with 20 ml dichloromethane. The solvent was removed. **Yield:** 2.127 g (40%) of a brown crystalline solid **^{1}H-NMR (400 MHZ, $CDCl_3$):** [ppm]=1.89 (s, 2H, CH), 5.20-5.24 (dd, 4H,4.36 Hz, 9.51 Hz, CH), 6.17-6.22 (dt, 4H, 10.0Hz, 3.1 Hz,CH), 6.62-6.64 (t, 4H, 3.1Hz, CH)

Chapter 13 Fitting decay curves

13.1 Two-state model

A two state model of the form A $\xrightarrow{\tau_1}$ B, where only A is detectable, is described by the differential equation

$$\lambda[A] = -\frac{d[A]}{dt} \tag{13.1}$$

Solving this equation leads to

$$A(t) = A_0 e^{-\lambda t} \tag{13.2}$$

If the physical impulse (here the two lasers) were a Dirac delta-function-like impulse, the following decay could be modeled very simply using this equation. But in reality the physical impulse, meaning the two lasers, has a Gaussian temporal profile:

$$y(t) = Be^{-\frac{(t)^2}{2\sigma^2}} \tag{13.3}$$

For the evolution of the measured signal the two functions A(t) and y(t) need to be convoluted.

$$S(t) = \int_0^\infty A(x) \cdot y(t-x)dx = A_0 B \int_0^\infty e^{-\lambda x} \cdot e^{-\frac{(t-x)^2}{2\sigma^2}} dx \tag{13.4}$$

The expression in the exponent is rewritten to its canonical form

$$-(\lambda x + \frac{(t-x)^2}{2\sigma^2}) = (\frac{\sigma^2}{2}\lambda^2 - \lambda t) - \frac{(x-t+\sigma^2\lambda)^2}{2\sigma^2} \tag{13.5}$$

The time-independent part can be factored out of the integral, and only the time-dependent part needs to be integrated. Performing a change of variables with $s = \frac{x-t+\sigma^2\lambda}{\sqrt{2}\sigma}$ results in a complementary error function

$$\begin{aligned} S(t) &= A_0 B \int_0^\infty e^{-\lambda x} * e^{-\frac{(t-x)^2}{2\sigma^2}} dx \\ &= A_0 B \cdot e^{-(\frac{\sigma^2}{2}\lambda^2 - \lambda t)} \int_{\frac{-t+\sigma^2\lambda}{\sqrt{2}\sigma}}^\infty e^{-s^2} ds \\ &= A_0 B \cdot e^{(\frac{\sigma^2}{2}\lambda^2 - \lambda t)} \mathrm{erfc}(\frac{-t + \sigma^2\lambda}{\sqrt{2}\sigma}) \qquad (13.6) \\ &= A_0 B \cdot \Lambda_1(t) \end{aligned}$$

The measured signal is consequently:

$$S(t) = \sigma_1 \Lambda_1(t, \lambda_1) \qquad (13.7)$$

where the factor σ_1 incorporates the scaling factors A_0 and B, which represent physical parameters like the ionization efficiency and the detection efficiency. The exponential decay constant λ and the parameter σ are not commonly used when describing decays. More commonly used are the time constant $\tau_1 = \frac{1}{\lambda}$ and the full-width-half-maximum of the laser response $\mathrm{FWHM} = 2\sqrt{2\ln 2}\sigma$. Since Λ_1 incorporates one exponential function, a decay following this model is also referred to as mono-exponential decay.

13.2 Three-state model

A three state model $A \xrightarrow{\tau_1} B \xrightarrow{\tau_2} C$, where both A and B are detectable, gives following two differential

equations:

$$\frac{d[A]}{dt} = -\lambda_1[A] \tag{13.8}$$

$$\frac{d[B]}{dt} = \lambda_1[A] - \lambda_2[B] \tag{13.9}$$

Solving these two differential equations:

$$A(t) = A_0 e^{-\lambda_1 t} \tag{13.10}$$

$$B(t) = \frac{\lambda_1}{\lambda_2 - \lambda_1} A_0 (e^{-\lambda_1 t} - e^{-\lambda_2 t}) \tag{13.11}$$

The total signal will be the sum of A(t) and B(t). For a physical signal the sum of A(t) and B(t) has to be convoluted with the Gaussian temporal profile of the laser. Since both A(t) and B(t) are a monoexponential function and a sum of monoexponential functions respectively, for each exponential a complementary error function analagous to eq. 13.6 is obtained.

$$S(t) = \sigma_1 \Lambda_1(t, \lambda_1) + \sigma_2 \Lambda_2(t, \lambda_1, \lambda_2) \tag{13.12}$$

where σ_1/σ_2 represent different scaling factors. Λ_1 refers to the convolution of A(t) with the Gaussian laser pulse and is composed of only one complementary error function. Λ_2 refers to the convolution of B(t) with the Gaussian laser pulse and is composed of two complementary error functions subtracted from each other. Again in practice the time constant $\tau_2 = \frac{1}{\lambda_2}$ is more commonly used instead of λ_2. Systems following this model are said to exhibit a bi-exponential decay, since for B(t) two exponentials are required.

13.3 Four-state model

A four-state model A $\xrightarrow{\tau_1}$ B $\xrightarrow{\tau_2}$ C $\xrightarrow{\tau_3}$ d, with A, B and C detectable, gives the following three differential equations:

$$\frac{d[A]}{dt} = -\lambda_1[A] \tag{13.13}$$

$$\frac{d[B]}{dt} = \lambda_1[A] - \lambda_2[B] \tag{13.14}$$

$$\frac{d[C]}{dt} = \lambda_2[B] - \lambda_3[C] \tag{13.15}$$

Solving now these three equations:

$$A(t) = A_0 e^{-\lambda_1 t} \tag{13.16}$$

$$B(t) = \frac{\lambda_1}{\lambda_2 - \lambda_1} A_0 (e^{-\lambda_1 t} - e^{-\lambda_2 t}) \tag{13.17}$$

$$\begin{aligned} C(t) = {} & \frac{\lambda_1 \lambda_2}{\lambda_2 - \lambda_1} A_0 \left(\frac{e^{-\lambda_1 t}}{\lambda_3 - \lambda_1} - \frac{e^{-\lambda_2 t}}{\lambda_3 - \lambda_2}\right) \\ & + A_0 \frac{\lambda_2 \lambda_1}{(\lambda_3 - \lambda_1)(\lambda_3 - \lambda_2)} e^{-\lambda_3 t} \end{aligned} \tag{13.18}$$

Just as for the three-state model, the total signal is the sum of A(t), B(t) and C(t) convoluted with the Gaussian laser pulse. All three subfunctions are composed of sums of exponentials, and the total signal is obtained analogous to the three-state model described previously.

$$S(t) = \sigma_1\Lambda_1(t,\lambda_1)+\sigma_2\Lambda_2(t,\lambda_1,\lambda_2)+\sigma_3\Lambda_3(t,\lambda_1,\lambda_2,\lambda_3) \quad (13.19)$$

where $\sigma_1/\sigma_2/\sigma_3$ represent the different scaling factors, and $\Lambda_1/\Lambda_2/\Lambda_3$ the convolution of A(t), B(t) and C(t) with a Gaussian function. Since C(t) involves three exponentials with three different constants, λ_1,λ_2 and λ_3, observed signals following this model are also reffered to as tri-exponential decays.

13.4 State with a long lifetime

An initially excited state A can have a long lifetime compared to the time resolution (ns-lifetimes compared to fs-time resolution), resulting in an offset in the decay trace. But for a correct description the Gaussian laser pulse has to be convoluted as well, this time with the function A(t) = 1.

$$S_{offset}(t) = \int_0^\infty A(x) * y(t-x)dx = \int_0^\infty e^{-\frac{(x-t)^2}{2\sigma^2}}dx \quad (13.20)$$

solving this results again to an error function

$$S_{offset}(t) = \mathrm{erfc}(\frac{-t}{\sqrt{2}\sigma}) \quad (13.21)$$

The total signal is consequently (with σ_{offset} being a scaling factor):

$$S(t) = \sigma_{offset}S_{offset}(t) \quad (13.22)$$

13.5 Final state ionizable

Whether it is a two-, three- or four-state model, the total amount of molecules is constant. So for a

two-state model $A \xrightarrow{\tau_1} B$ the amount of [B] is:

$$B(t) = A_0 - A(t) = A_0(1 - e^{-\lambda t}) \tag{13.23}$$

This has to be convoluted with the Gaussian of the laser pulses, leading to

$$\begin{aligned}\Lambda_{final}(t) &= A_0(\mathrm{erfc}(\frac{-t}{\sqrt{2}\sigma}) - e^{(\frac{\sigma^2}{2}\lambda^2 - \lambda t)}\mathrm{erfc}(\frac{-t+\sigma^2\lambda}{\sqrt{2}\sigma})) \\ &= A_0(S_{offset}(t) - \Lambda_1(t)) \end{aligned} \tag{13.24}$$

The total signal for a two-state model where the final state is ionizable is consequently:

$$S(t) = \sigma_1\Lambda_1(t,\lambda_1) + \sigma_{final}\Lambda_{final}(t,\lambda_1) \tag{13.25}$$

The scaling factor σ_{final} incorporates the fact that the states A and B don't have the same ionization efficiency. Indeed, were they the same, only a constant signal after the laser pulses would be observed.

For a three-and four-state model the reasoning is the similar. For a three-state model the following formulas are obtained for C(t) and S(t):

$$\Lambda_{final}(t) = A_0(S_{offset}(t) - \Lambda_1(t,\lambda_1) - \Lambda_2(t,\lambda_1,\lambda_2)) \tag{13.26}$$

$$S(t) = \sigma_1\Lambda_1(t,\lambda_1) + \sigma_2\Lambda_2(t,\lambda_1,\lambda_2) + \sigma_{final}\Lambda_{final}(t,\lambda_1,\lambda_2) \tag{13.27}$$

and for a four-state model:

$$\Lambda_{final}(t) = A_0(S_{offset}(t) - \Lambda_1(t,\lambda_1) - \Lambda_2(t,\lambda_1,\lambda_2) - \Lambda_3(t,\lambda_1,\lambda_2,\lambda_3)) \tag{13.28}$$

$$S(t) = \sigma_1\Lambda_1(t,\lambda_1) + \sigma_2\Lambda_2(t,\lambda_1,\lambda_2) + \sigma_3\Lambda_3(t,\lambda_1,\lambda_2,\lambda_3) + \sigma_{final}\Lambda_{offset}(t,\lambda_1,\lambda_2,\lambda_3) \tag{13.29}$$

Chapter 14 Developed Software

14.1 Anja's fit decays v3.5

The solved differential equations (see section 13) were implemented in a python gui using pyqt, allowing fast and visually easy fitting of decays. A screenshot of the program is shown in fig. 14.1. Via the button 'Load .evol file' decay data, saved in a xyxy... file (x and y as columns with x in fs) is loaded into the listWidget (white area) as fitfunc0, fitfunc1 etc. If the radiobutton '2 Angles?' is checked, the xy file is considered to have the decays of orthogonal and parallel orientations of pump/probe laser in the format xy_{fitfunc0}(angle 0) xy_{fitfunc0}(angle 1) xy_{fitfunc1}(angle 0).... Loading two angles like this, activates the 'Make the rot. mean' button, which opens a subwidget to calculate the rotational mean.

The selected data is displayed in the center plot. Changing the slider (A—>B—>C—>D) selects either a one-state, two-state, three-state or four-state model. A good fit convergence requires suitable starting values before pushing the button 'fit', which will do a least-square fit based on these starting values. The autocorrelation, the first time-constant τ_1 and the FWHM can be held fixed if the corresponding radiobutton is checked. The user has also the choice of considering an offset, he can choose between three options: 'No Offset', 'y_offset?', and 'y_offset final population'. As their names imply respectively, 'No Offset' considers that the last state is dark (default), 'y_offset?' just adds an offset with no consideration to the mechanism, whereas 'y_offset final population' considers that the final

state is a bright state.

The result of the fit is given with an uncertainty, if the uncertainty reads $\pm$ inf, the fit diverged. This means that either the starting values were not correct or that the assumed model fails. Once fitted, a new entry is added to the listwidget with the fitted parameters. Using the button 'Save selected File', the original data, the total fit and the populations are saved as columns, the fit constants are saved as comments (entries starting with # at the beginning of the file).

It is also possible to treat the loaded data before fitting; to decide how many points should be used for the baseline subtraction (using the button 'subtract'), to invert the decay if it negative (button 'Invert Decay', useful for mass spectra decays) and to normalize a decay (button 'Normalize decay'). Using the last one is obligatory if two data sets are fitted using the same constants - to compare, for example, whether a photoelectron decay and time-of-flight mass decay show the same temporal behavior. Changing the radiobutton selection from 'Fit one decay' to 'Fit two decays' allows to select two data sets; via the radiobutton 'Fit FWHMs separately' the autocorrelation of both can be fitted separately. The offset of both graphs is always considered separate.

Should more functionality or different decays be desired, the python macro 'fit_class.py' can be used, to implement new models based on these preexisting ones.

14.2 Plotting 2D matrices v 0.0

This python macro is designed to help with the analysis of photoelectron spectra as inverted by the

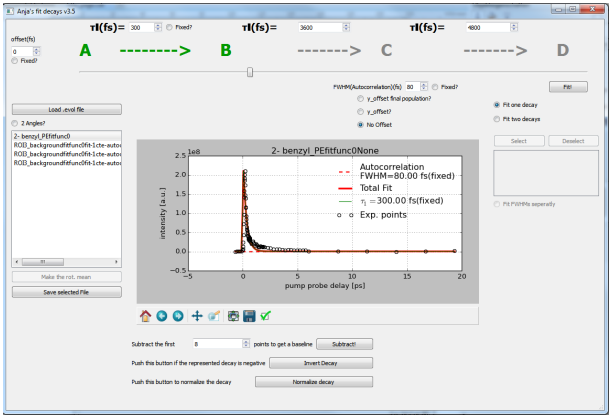

Figure 14.1: *Screenshot of the the program 'Anja's fit decays v3.5'*

Analyse-program. A screenshot of this python macro is shown in fig. 14.2. Via the button 'Load 3D data', it loads xyz-files, saved previously by the python macro 'make_XYZ_severalAngle.py'. Via the button 'load Times', the .html file, characterizing the temporal delay (output by Lionel's measuring program) is loaded. With both the 'Time' and 'Radius' radiobuttons checked, a click on the 'Convert'-button plots the raw xyz-file as the middle graph. The time calibration is directly read from the 'time' file, whereas the energy calibration can be changed using the 'Load Energy Calibration' button and the entries for the repeller and extractor values. If two angles (orthogonal and parallel pump-probe laser polarization, for example) were measured, two entries appear in the 'Data:' listwidget upon 'Convert'-button-click; named angle1 and angle2 respectively. Selecting them will show the respective data in the plot. On the right of the plot the user has several options for data manipulation.

The button 'xX' multiplies the data with the pixel value; the button 'Smooth' smoothes the data. The user can also choose to change the range of the z-values (Z_max and Z_min, a zoom into x and y can be done using the matplotlib buttons under the plot itself). The 'Display-options' button allows changing the title and x/y-axis labels. Switching from the 'Intensity' to the 'Beta' Radiobutton changes Z_max and Z_min. The user has also the possibility to correct for the background, namely for signal from pump only /probe only signals. This can be done either by subtracting the first few (default 6) data points (Method 1), or by choosing xy files containing the signal of pump only/probe only and subtracting them separately from the data. Each time the data is changed, a new entry with the changed data appears in the 'Data:' listwidget.

On the left of the plot the user has more options. The button 'Make PECD' makes a PECD matrix of the two angles (useful if they correspond to left and right circularly polarized light). Via the button 'CorrectBeta' an anisotropy matrix can treated in

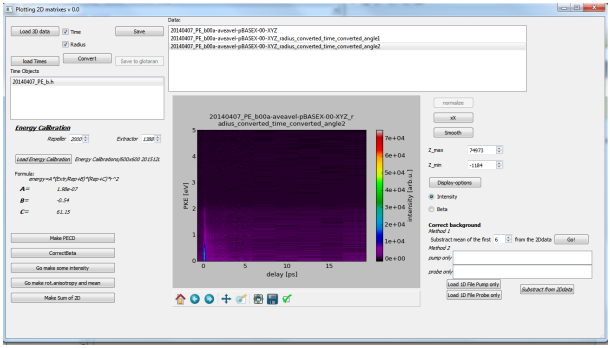

Figure 14.2: *Screenshot of the python program 'Plotting 2D matrices v0.0'*

respect to another matrix (e.g. the total intensity), setting values in the anisotropy matrix to a user-defined value, if the same point in the other matrix is under a certain value. The button 'Go make some intensity' allows the user to add matrices, whereas the button 'Go make rot.anisotropy and mean' allows the user to calculate a rotational anisotropy and a rotational mean matrix. Each matrix can be saved using the 'Save' button on the right of the 'Convert' button.

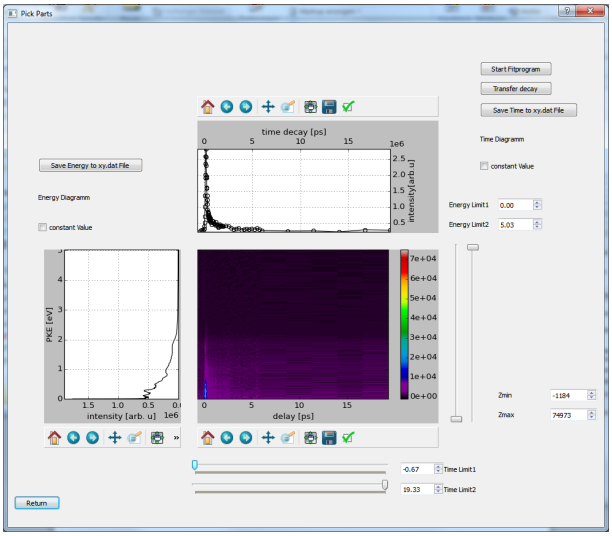

Figure 14.3: *Screenshot of the widget, which opens if the user clicks on the button 'Make Sum of 2D' in the program 'Plotting 2D matrices v0.0'*

A short comment on the button 'Make Sum of 2D': This opens a new widget (see fig. 14.3) which allows the user to sum the xyz matrix either over the delay to display a summed photoelectron spectrum (left plot), or to sum over all energies to display

the total photoelectron decay (upper plot). The energy and time limits can be changed using either the sliders or by entering the numbers in the respective field. Using the buttons 'Save Time to xy.dat File' and 'Save Energy to xy.dat File' the time decay and summed photoelectron spectrum can be saved respectively in a xy-file. Using the button 'Start Fitprogram', a leaner version of the Anja's fit decays is opened, and via the button 'Transfer decay' the user can transfer the decay to the program. It should be noted, however, that this fit program is only useful for preliminary fitting, since several functionalities are amiss, moreover, the fwhm does not correspond to the IRF (factor of 2ln2).

14.3 pBasex** notes on implementation

The complete code (including comments) is available on request. In the following some crucial issues/main points of the program are listed:

- pBasex** was implemented in a python class, called aim, short for anja image. Its methods incorporate all necessary functionality for treatment of an image, namely (excluding submethods):
  - ▷ *set_ center (x, y)*: Sets the center of an image.
  - ▷ *transpose(keep_ center=False)*: Transposes the image and, if keep_ center=False, transposes also the center:
  - ▷ *symmetrize(axis='Y')*: Symmetrizes the image along a given axis, either the 'X' or the 'Y' axis in respect to the chosen center.
  - ▷ *show()*: Plots a graphic of the image data.
  - ▷ *draw_ circle(r, intensity=10)*: Plots a circle of thickness 1 and with the intensity 10 (default)

at a radius r from the center

- ▷ *draw_circle_legendre(r, c, intensity=1)*: Plots a circle of thickness 1 with the intensity 1 (default) at a radius r from the center, the intensity distribution corresponds to a Legendre polynomial c. c is a list specifying the Legendre polynomial, ex: [1,0,0] corresponds to P_0, [0,0,1] to P_2, [0,0,0,0,1] to P_4.
- ▷ *draw_angles(c, r, intensity=4)*: Sets the pixels corresponding to the angle where the intensity of the Legendre polynomial c is zero to the intensity=4 (default).
- ▷ *sort_data_angles_radius(rmax,c,dr=3)*: Sorts the data into the different radii and angles until the radius rmax is reached, depending on the Legendre polynomial c, for $P_0P_2P_4$ c would be [1,0,1,0,1]. dr=3 specifies the distance between the radial data points.
- ▷ *forward_Abel(f)*: ForwardAbel transforms the given data set f. It is based on the algorithm of Hansen and Law [105] as implemented in pyAbel [508].
- ▷ *plot_cylindrical_gaussian(c, k, sigma)*: Plots the a basis function centered on a distance k from the center with sigma corresponding to the square root of the variance of the Gaussian base function.
- ▷ *invert_image(rmax, c, sigma=6, N=0.5, dr=3, basisfunction_file=' ')*: Inverts the image based on the Legendre polynomial c and a distance between the radial data points dr=3 (default). If the basisfunction_file remains on the default value, a new basis set will be calculated. Sigma=6 corresponds to the standart deviation of the Gaussian base function; N=0.5 determines that for every second radial point a

basis function will be calculated.

- The python module numpy.linalg.pinv2 was used for the SVD procedure.
- Setting the center correctly is crucial. For the correct sorting the center should be chosen as the middle of a pixel, e.g. x=300.5, y=300.5, since it calculates the distance towards the next pixels center as well.

List of Publications

Not included in this thesis:

- "Synchrotron-based valence shell photoionization of CH radical", *B. Gans, F. Holzmeier, J. Krüger, C. Falvo, A. Röder, A. Lopes, G. A. Garcia-Macias, C. Fittschen, J.-C. Loison, and C. Alcaraz J.* Chem. Phys. 144, 204307-181101, May 2016

- 'Communication: On the first ionization threshold of the C_2H radical' *B. Gans, G. A. Barcia, F. Holzmeier, J. Kröger, A. Röder, A. Lopes, C. Fittschen, J.-C. Loison and C. Alcaraz*, J. Chem. Phys 146, 011101 (2017)

Included in this thesis:

- 'Femtosecond Dynamics of the 2-Methylallyl Radical: A Computational and Experimental Study' *A. Röder, K. Issler, L. Poisson, A. Humeniuk, M. Wohlgemuth, M. Comte, F. Lepetit, I. Fischer, R. Mitrić, and J. Petersen*, J. Chem. Phys, 147(1), 2017

- 'Femtosecond Time-Resolved Photoelectron Spectroscopy of the Benzyl Radical' *A. Röder, A. Humeniuk, J. Giegerich, I. Fischer, L. Poisson and R. Mitrić*, Phys. Chem. Chem. Phys. (2017)

Bibliography

[1] P. P. Fu, F. A. Beland, S. K. Yang: *Carcinogenis*, 1: 725–727, **1980**

[2] J. L. Durant, W. F. Busby, A. L. Lafleur, B. W. Penman, C. L. Crespi: *Mutation research*, 371: 123–157, **1996**

[3] D. A. Kaden, R. A. Hites, W. G. Thilly: *Cancer Research*, 39: 4152–4159, **1979**

[4] A. W. Wood, W. Levin, R. L. Chang, M.-T. Huang, D. E. Ryan, P. E. Thomas, R. E. Lehr, S. Kumar, M. Koreeda, H. Akagi, Y. Ittah, P. Dansette, H. Yagi, D. M. Jerina, A. H. Conney: *Cancer Research*, 40: 642–649, **1980**

[5] A. L. Lafleur, J. P. Longwell, L. Shirname-More, P. A. Monchamp, W. A. Peters, E. F. Plummer: *Energy & Fuels*, 4: 307–319, **1990**

[6] D. W. Dockery, C. A. P. III, X. Xu, J. D. Spengler, J. H. Ware, M. E. Fay, B. G. Ferris, F. E. Speizer: *The New England Journal of Medicine*, 329(24): 1754–1759, **1993**

[7] H. B. Palmer, C. F. Cullis: *Chemistry and Physics of Carbon*, vol. 1. New York, **1965**

[8] Z. A. Mansurov: *Combustion, Explosion, and Shock Waves*, 41(6): 727–744, **2005**

[9] I. Glassman, R. A. Yetter: *Combustion*. Elsevier, 4th edn., **2008**

[10] H. Richter, J. Howard: *Progress in Energy and Combustion Science*, 26: 565–608, **2000**

[11] A. Indarto: *Theoretical Modelling and Mechanistic Study of the Formation and Atmospheric Transformations of Polycyclic Aromatic Compounds and Carbonaceous Particles.* Ph.D. thesis, **2010**

[12] J. Wang, M. Chaos, B. Yang, T. A. Cool, F. L. Dryer, T. Kasper, N. Hansen, P. Oßwald, K. Kohse-Höinghaus, P. R. Westmoreland: *Physical Chemistry Chemical Physics*, 11: 1328–1339, **2009**

[13] B. F. Magnussen, B. H. Hjertager: *Symposium (international) on Combustion*, 16: 719–729, **1977**

[14] P. Basu: *Chemical Engineering Science*, 54: 5547–5557, **1999**

[15] V. Zimont: *Experimental Thermal and Fluid Science*, 21: 179–186, **2000**

[16] J. Kesselmeier, M. Staudt: *Journal of Atmospheric Chemistry*, 33: 23–88, **1999**

[17] J. H. Seinfeld, S. N. Pandis: *Atmospheric chemistry and Physics, From Air Pollution to Climate Change.* John Wiley & Sohns, **1998**

[18] R. M. Karmens, Z. Guo, J. N. Fulcher, D. A. Bell: *Environmental science & technology*, **1988**

[19] J. Arey, R. Atkinson: *PAHs: An Ecotoxicological Perspective.* **2003**

[20] D. Schiedek, B. Sundelin, J. W. Readman, R. W. Macdonald: *Marine Pollution Bulletin*, 54(12): 1845 – 1856, **2007**. URL `http://www.sciencedirect.com/science/article/pii/S0025326X07003372`

[21] U. Varansi, ed.: *Metabolism of Polycyclic Aromatic Hydrocarbons in the Aquatic Environment.* **1989**

[22] F. S. Rowland: *Angewandte Chemie International Edition in English*, 35: 1786–1798, **1996**

[23] A. R. Mackenzie: *Pollution: Causes, Effects and Control.* 4th edn., **2001**

[24] E. R. DeSombre: *UCLA Journal of Environmental Law & Policy*, 19: 49–81, **2000**

[25] M. J. Molina, F. S. Rowland: *Nature*, 249: 810–812, **1974**

[26] P. Ehrenfreund, S. B. Charnley: *Annual Review of Astronomy and Astrophysics*, 38: 427–483, **2000**

[27] E. A. Bergin, P. F. Goldsmith, R. L. Snell, W. D. Langer: *The Astrophysical Journal*, 482: 285–297, **1997**

[28] URL `http://www.cv.nrao.edu/ awootten/allmols.html`

[29] W. M. Irvine: *Origins of Life and Evolution of the Biosphere*, 28: 365–383, **1998**

[30] J. L. Puget, A. Leger: *Annual Review of Astronomy and Astrophysics*, 27: 161–198, **1989**

[31] J. G. Mangum, A. Wootten: *The Astrophysical Journal Supplement Series*, 89: 123–153, **1993**

[32] A. G. G. M. Tielens: *The Physics and Chemistry of the Interstellar Medium.* Cambridge University Press, **2005**

[33] A. Dalgarno, J. H. Black: *Reports on Progress on Physics*, 39: 573–612, **1976**

[34] F. Salama: NASA Ames Research Center, **206**

[35] S. S. Prasad, S. P. Tarafdar: *The Astrophysical Journal*, 267: 603–609, **1983**

[36] C. Czeslik, H. Seemann, R. Winter: *Basiswissen Physikalischer Chemie*. Teubner Verlag, **2001**

[37] D. A. McQuarrie, J. D. Smith: *Physical chemistry a molecular Approach*. University Science Books, **1997**

[38] G. Herzberg: *Molecular Spectra and Molecular Structure Volume I - Spectra of Diatomic Molecules*. Krieger Publishing Company, **1950**

[39] W. Demtröder: *Laserspektroskopie*. Springer, **2007**

[40] M. A. El-Sayed: *Accounts of Chemical Research*, 1: 8, **1968**

[41] M. A. El-Sayed: *Journal of Chemical Physics*, 38: 2384, **1963**

[42] F. Engelke: *Aufbau der Moleküle Eine Einführung*. Teubner, **1992**

[43] D. E. Levy: *Annu. Rev. Phys. Chem.*, 31: 197–225, **1980**

[44] D. W. Kohn, H. Clauberg, P. Chen: *Review of Scientific Instruments*, 63: 4003 – 4005, **1992**

[45] S. Willitsch, J. M. Dyke, F. Merkt: *Helvetica Chimica Acta*, 86: 1152, **2003**

[46] P. Gorry, R. Grice: *Journal of Physics E: Scientific Instruments*, 12: 587–860, **1979**

[47] P. Engelking: *Review of Scientific Instruments*, 57: 2274 – 2277, **1986**

[48] G. A. Garcia, X. Tang, J.-F. Gil, L. Nahon, M. Ward, S. Batut, C. Fittschen, C. A. Taatjes, D. L. Osborn, J.-C. Loison: *Journal of Chemical Physics*, 142: 164 201, **2015**

[49] K. Hoyermann, J. Nothdurft, M. Olzmann, J. Wehmeyer, T. Zeuch: *The Journal of Physical Chemistry A*, 110(9): 3165–3173, **2005**

[50] P. Chen, S. D. Colson, W. A. Chupka, J. A. Berson: *Journal of Physical Chemistry*, 90: 2319–2321, **1986**

[51] M. R. Cameron, S. H. Kable: *Review of Scientific Instruments*, 67, **1996**

[52] Q. Guan, K. N. Urness, T. K. Ormond, D. E. David, G. B. E. W. Daily: *International Reviews in Physical Chemistry*, 33(4): 447–487, **2014**

[53] A. Laufer, H.Okabe: *Journal of the American Chemical Society*, 93: 4137–7140, **1971**

[54] M. Chase: *NIST-JANAF Thermochemical Tables*. J.Phys.Chem.Ref. Data Monograph 9, **1998**

[55] S. J. Blanksby, G. B. Ellison: *Accounts of Chemical Research*, 36: 255 – 263, **2003**

[56] V. E. Bondybey, A. M. Smith, J. Agreiter: *Chem. Rev.*, 96: 2113–2134, **1996**

[57] J. Küpper, J. M. Merritt: *International Reviews in Physical Chemistry*, 26: 249–287, **2007**

[58] G. Scoles: *Atomic and Molecular Beam Methods*. Oxford University Press, **1988**

[59] J. Giegerich: *Velocity-Map-Imaging Studien an reaktiven Intermediaten: Fulvenallene,* C_3H_2 *Isomere und Alkylradikale*. Ph.D. thesis, Julius-Maximilians-Universität Würzburg, **2015**

[60] A. Röder: *Spectroscopy and Dynamics of* CCl_2 *and CCl*. Ph.D. thesis, **2014**

[61] D. O'Connor, D. Philips: *Time-Correlated Single Photon Counting*. Elsevier, **1984**

[62] H. Mahr, M. D. Hirsch: *Optics Communications*, 13(2): 96–99, **1975**

[63] J. Takeda, K. Nakajima, S. Jurita, S. Tomimote, S. Saito, T. Suemoto: *Journal of Luminescence*, 87-89: 927–929, **2000**

[64] R. Berera, R. van Grondelle, J. T. M. Kennis: *Photosynthetic Research*, 101: 105–118, **2009**

[65] P. C. Engelking: *Chemical Review*, 91: 399–414, **1991**

[66] J. H. Gross: *Mass Spectrometry*. Springer, 2nd edn., **2011**

[67] J. S. Baskin, A. H. Zewail: *Journal of Physical Chemistry A*, 105: 3680–3692, **2001**

[68] A. T. B. Eppink, D. H. Parker: *Review of Scientific Instruments*, 68(9): 3477–3484, **1997**

[69] J. L. Wiza: *Nuclear Instruments and Methods*, 162: 597–601, **1979**

[70] B. R. Dobbie, C. D. Willey, D. E. Mattey, S. A. Brillhart: *Video enhanced night vision goggle*, **2003**

[71] W. B. Colson, J. McPherson, F. T. King: *Review of scientific instruments*, 44: 1694–1696, **1973**

[72] S. Safai, S. Lin, E. Pedroni: *Physics in Medecine and Biology*, 49: 4637–4655, **2004**

[73] J. Moy, A. Koch, M. Nielsen: *Nuclear Instruments and Methods in Physics Research*, A326: 581–586, **1993**

[74] N. Yagi, T. Oka: *Measurement of Phosphor Persistence in Xray Image Intensitifiers*. Tech. rep., Jqpqn Synchrotron Radiation Research Institute, **1998**

[75] M. N. R. Ashfold, N. hendrik Nahler, A. J. Orr-Ewing, O. P. Vieuxmaire, R. L. Toomes, T. N. Kitsopoulos, I. A. Garcia, D. A. Chestakov, S.-M. Wu, D. H. Parker: *Physical Chemistry Chemical Physics*, 8: 15–53, **2006**

[76] D. A. Chestakov, S.-M. Wu, G. Wu, D. H. Parker, A. T. Eppink, T. N. Kitsopoulos: *Journal of Physical Chemistry A*, 108: 8400–8105, **2004**

[77] D. Townsend, M. P. Minitti, A. G. Suits: *Review of scientific instruments*, 74(4): 2530-2539, **2003**

[78] R. A. Marcus: *Journal of Chemical Physics*, 20(3): 359–364, **1952**

[79] M. S. Schuurman, J. Giegerich, K. Pachner, D. Lang, B. Kiendl, R. J. MacDonell, A. Krueger, I. Fischer: *Chemistry - A European Journal*, 21: 14 486–14 495, **2015**

[80] P. L. Houston: *Journal of Physical Chemistry*, 91: 5388–5397, **1987**

[81] G. E. Hall, P. L. Houston: *Annual Reviews of Physical Chemistry*, 40: 375–405, **1989**

[82] J. P. Simons: *Journal of Physical Chemistry*, 91: 5378–5387, **1987**

[83] A. J. Orr-Ewing, R. N. Zare: *Annual Review of Physical Chemistry*, 45: 315–366, **1994**

[84] M. Reid: *Velocity Map Imaging: From Gases to Surfaces*, **2013**

[85] R. Ballard: *Photoelectron Spectroscopy and Molecular Orbital Theory*. Adam Hilger Ltd, Bristol, **1978**

[86] K. L. Reid: *Annual Reviews of Physical Chemistry*, 54: 397–424, **2003**

[87] P. Hockett: *Photoionization Dynamics of Polyatomic Molecules*, **2009**

[88] J. Cooper, R. N. Zare: *Journal of Chemical Physics*, 48: 942–943, **1968**

[89] T. Seidemann: *Annual Reviews of Physical Chemistry*, 53: 41–65, **2002**

[90] G. Wu, P. Hockett, A. Stolow: *Physical Chemistry Chemical Physics*, 13: 18 447–18 467, **2011**

[91] J. Cooper, R. N. Zare: *Journal of Chemical Physics*, 49: 4252, **1968**

[92] S. D. Druger: *The Journal of Chemical Physics*, 64(3): 987–1004, **1976**

[93] C. M. Lee: *Physical Review A*, 10(5): 1558–1604, **1974**

[94] R. N. Compton, J. Stockdale, C. D. Cooper, X.Tang, P.Lambropoulos: *Physical Review A*, 30(4): 1766–1774, **1984**

[95] R. N. Dixon: *The Journal of Chemical Physics*, 122: 194 302, **2005**

[96] S. N. Dixit, V. McKoy: *The Journal of Chemical Physics*, 82: 3546–3553, **1985**

[97] T. Horia, T. Fuji, Y.-I. Suzuki, T. Suzuki: *Journal of the American Chemical Society*, 131: 10 392–10 393, **2009**

[98] C. M. Oana, A. I. Krylov: *Journal of Chemical Physics*, 131: 124 114, **2009**

[99] Z.-G. Yuan: *National Aeronautics and Space Administration*, **2003**

[100] A. D. Poularikas, ed.: *The Transforms and Applications Handbook, Second Edition*. **2000**

[101] B. J. Whitaker, ed.: *Imaging in Molecular Dynamics.* Cambridge University Press, **2005**

[102] L. M. Smith, D. R. Keefer, S. I. Sudharsanan: *journal of quantitative spectroscopy & radiative transfer*, 39: 367–373, **1988**

[103] S. M. Candel: *Computer Physics Communication*, 23: 343–353, **1981**

[104] W. H. Press, B. P. Flannery, S. A. Teukolsky, W. T. Vetterling: *Numerical Recipes in C.* Cambridge University Press, **1988**

[105] E. W.Hansen, P.-L. Law: *Journal of the Optical Society of America*, 2(4): 510–520, **1985**

[106] J. Winterhalter, D. Maier, J. Honerkampf, V. Schyja, H. Helm: *Journal of Chemical Physics*, 110(23): 11 187–11 196, **1999**

[107] C. Bordas, F. Paulig, H. Helm, D. Huestis: *Review of Scientific Instruments*, 67: 2257, **1996**

[108] G. A. Garcia, L. Nahon, I. Powis: *Review of Scientific Instruments*, 75(11): 4990–4996, **2004**

[109] B. Dick: *Physical Chemistry Chemical Physics*, 16: 570–580, **2014**

[110] N. Muller, L. Magaia, B. M. Herbst: *Siam Review*, 46(3): 518–545, **2004**

[111] A. N. Tikhonov: *Doklady Akademii Nauk SSSR*, 151: 501, **1963**

[112] V. Dribinski, A. Ossadtachi, V. A. Mandelshtam, H. Reisler: *Review of Scientific Instruments*, 73(7): 2634–2642, **2002**

[113] L. N. Trefethen, D. Bau: *Numerical linear algebra.* Siam, **1997**

[114] H. Yanai, K. Takeuchi, Y. Takane: *Projection Matrices, Generalized Inverse Matrices, and Singular Value Decomposition.* Springer Science+Business Media, **2011**

[115] M. Briant, L.Poisson, M. Hochlaf, P. de Pujo, M. Gaveau, B. Soep: *Physical Review Letters*, 109: 1943401, **2012**

[116] P. Guyon, T. Baer, L. F. A. Ferreira, I. Nenners, A. Tabche-Fouhaile, R. Botter, T. R. Govers: *Journal of Physics B- Atomic and Molecular Physics*, 11(5): L141–L144, **1978**

[117] P. H. Krupenie: *Journal of Physical and Chemical Reference Data*, 1(2): 423–533, **1972**

[118] J. Giegerich, I. Fischer: *Physical Chemistry Chemical Physics*, 15: 13162, **2013**

[119] J. Giegerich, J. Petersen, R. Mitric, I. Fischer: *Physical Chemistry Chemical Physics*, 16(13): 6294–6302, **2014**

[120] J. Giegerich: *Photofragment-Imaging des Ethylradikals*. Master's thesis, Julius-Maximiliams-Universität Würzburg, **2012**

[121] C. Romanescu, S. Manzhos., D. Boldovsky, J. Clarke, H. Loock: *Journal of Chemical Physics*, 120(2): 767–777, **2004**

[122] D. S. Green, G. A. Bickel, S. C. Wallace: *Journal of Molecular Spectroscopy*, 150: 388–469, **1991**

[123] C. Romanescu: *Velocity imaging of the photodissociation and photoionization dynamics of hydrogen chloride and hydrogen bromide*, **2007**

[124] C. Western: *Journal of Quantitative Spectroscopy and Radiative Transfer*, 186, **2016**

[125] K. Huber, G. Herzberg: *NIST Chemistry WebBook, NIST Standard Reference Database Number 69*, **2017**

[126] J. D. D. Martin, J. W. Hepburn: *Journal of Chemical Physics*, 109(19): 8139–8142, **1998**

[127] A. Kramida, Yu. Ralchenko, J. Reader, and NIST ASD Team: *NIST Atomic Spectra Database (ver. 5.3)*, **2015**. URL `http://physics.nist.gov/asd`

[128] N. Diamantopoulou, A. Kartakoulis, P. Glodic, T. N. Kitsooulos, P. C. Samartzis: *Journal of Chemical Physics*, 134: 194 314, **2011**

[129] L. J. Rogers, M. N. Ashfold, Y. Matsumi, M. Kawaski, B. J. Whitaker: *Chemical Physics Letters*, 258: 159–163, **1996**

[130] P. C. Samartzis, T. N. Kitsopoulos: *Journal of Chemicial Physics*, 133: 014 301, **2010**

[131] C. Schon: *Spektroskopie an substituierten [2.2]Paracyclophanen.* Ph.D. thesis, Julius-Maximiliams-Universität Würzburg, **2011**

[132] A. Lietard: *Dynamique Ultrarapide de Molécules et d'Aggrégats excités électroniquement.* Ph.D. thesis, Université Paris-Sud, **2014**

[133] A. Lietard, L. Poisson, J.-M. Mestdagh, M.-A. Gaveau: *American Institute of Physics Conference Series*, **2016**

[134] MACOR: *Machinable Glass Cermaci for industrial applications, product sheet*

[135] S. G. Ceramics: *Hexology SE Silicon Carbide Technical Data*

[136] G. L. Harris, ed.: *The properties of Silicon Carbide.* INSPEC, Materials Science Research Center of Excellence, Howard University, Washington DC, **1995**

[137] M. Lang, F. Holzmeier, P. Hemberger, I. Fischer: *The Journal of Physical Chemistry A*, 119: 3995–4000, **2015**

[138] E. Barber: *Mischexperimente von Propargyl mit Acetylene bei Pyrolyse(working title)*, **2017**

[139] B. M. Noller: *Excited-State Dynamics of Organic Intermediates.* Ph.D. thesis, Julius-Maximiliams-Universität Würzburg /l'Universite Paris-Sud, **2009**

[140] M. Fink: *VUV-Erzeugung und Photoionisation bei 118 nm*, **2002**

[141] A. Murari, C. Vinante, M. Monari: *Vacuum*, 65(2): 137–145, **2002**

[142] M. C. Steinbauer: *Ionen- und Elektronenimaging reaktiver Moleküle: Ethyl, Propargyl und Fulvenallenyl.* Ph.D. thesis, Julius-Maximiliams-Universität Würzburg, **2012**

[143] S. L. und Plasmatechnik GmbH: *Sirah Pulsed Dye Laser Service Manual Cobra*, **2005**

[144] S. L. und Plasmatechnik GmbH: *Sirah Pulsed Dye Laser Service Manual Precision Scan*, **2002**

[145] M. Schneider: *Elektronische Spektroskopie heterocyclischer Biomoleküle.* Ph.D. thesis, **2009**

[146] J. Giegerich: *Aufbau eines bildgebenden Spektrometers und Programmierung der Auslesesoftware*, **2010**

[147] A. Röder, K. Issler, L. Poisson, A. Humeniuk, M. Wohlgemuth, M. Comte, F. Lepetit, I. Fischer, R. Mitric, J. Petersen: *Journal of Chemical Physics*, **2017**

[148] J. K. Kochi, P. J. Krusic: *The Journal of the American Chemical Society*, 7157–7159, **1968**

[149] T. Takada, M. Dupois: *The Journal of the American Chemical Society*, 105: 1713–1716, **1983**

[150] G. Levin, W. A. G. III: *The Journal of the American Chemical Society*, 1649–1656, **1975**

[151] J. M. Hostettler, L. Castiglioni, A. Bach, P. Chen: *Physical Chemistry Chemical Physics*, 11: 8262–8265, **2009**

[152] J. D. Getty, X. Liu, P. B. Kelly: *Chemical Physics Letters*, 201(1): 236–241, **1993**

[153] J. D. Getty, M. J. Burmeister, S. G. Westre, P. B. Kelly: *The Journal of the American Chemical Society*, 113: 801–805, **1991**

[154] L. Castiglioni, A. Bach, P. Chen: *Physical Chemistry Chemical Physics*, 8: 2591–2598, **2006**

[155] A. Tiesler, H. Zott, H. Heusinger: *Radiation Physics and Chemistry*, 17: 141–144, **1981**

[156] R. W. Fessenden, R. H. Schuler: *The Journal of Chemical Physics*, 39(9): 2147–2195, **1963**

[157] A. B. Callear, H. K. Lee: *Transactions of the Faraday Society*, 64: 308–316, **1968**

[158] T. Zhang, J. Wang, T. Yuan, X. Hong, L. Zhang, F. Qi: *Journal of Physical Chemistry A*, 112: 10 487–10 494, **2008**

[159] Z. Lin, T. Wang, D. Han, X. Han, S. Li, Y. Li, Z. Tian: *Rapid Communications in Mass Spectrometry*, 23: 85–92, **2009**

[160] W. Tsang: *International Journal of Chemical Kinetics*, X: 119–1138, **1978**

[161] A. Webster: *Monthly Notices of the Royal Astronomic Society*, 265: 421–430, **1993**

[162] C. Huang, L. Wei, B. Yang, J. Wang, Y. Li, L. Sheng, Y. Zhang, F. Qi: *Energy & Fuels*, 20: 1505–1513, **2006**

[163] C. K. Westbrook: *Annual Review of Physical Chemistry*, 64: 201–219, **2013**

[164] K. Kohse-Höinghaus, P. Osswald, T. A. Cool, T. Kasper, N. Hansen, F. Qi, C. K. Westbrook, P. R. Westmoreland: *Angewandte Chemie, International Edition*, 49: 3572–3597, **2010**

[165] P. v.R. Schleyer, J. D. Dill, J. A. Pople, W. J. Hehre: *Tetrahedron*, 33: 2497–2501, **1977**

[166] C.-C. Chen, H.-C. Wu, C.-M. Tseng, Y.-H. Yang, Y.-T. Chen: *The Journal of Chemical Physics*, 119: 241–250, **2003**

[167] J. W. Hudgens, C. S. Dulcey: *Journal of Physical Chemistry*, 89: 1505–1509, **1985**

[168] G. Michael, J. A. Frey, J. M. Hostettler, A. Bach: *Journal of Molecular Spectroscopy*, 263: 93–100, **2010**

[169] N. Nakashima, K. Yoshihara: *Laser Chemistry*, 7: 177–196, **1987**

[170] M. Gasser, A. Bach, P. Chen: *Physical Chemistry Chemical Physics*, 10: 1133–1138, **2008**

[171] J. Herterich, T. Gerbich, I. Fischer: *ChemPhysChem*, 14: 3906–3908, **2013**

[172] J. D. Getty, X. Liu, P. B. Kelly: *The Journal of Chemical Physics*, 104: 3176–3180, **1996**

[173] D. H. Tarrant, J. D. Getty, X. Liu, P. B. Kelly: *Journal of Physical Chemistry*, 100: 7772–7777, **1996**

[174] M. Gasser, J. A. Frey, J. M. Hostettler, A. Bach: *Chemical Communications*, 47: 301–303, **2011**

[175] J. C. Schultz, F. Houle, J. Beauchamp: *Journal of the American Chemical Society*, 106: 7336–7347, **1984**

[176] K. Issler: *Nicht-adiabische Dynamik in organischen Radikalen und Simulation der zeitaufgelösten Photoelektron-Imaging-Spektren*, **2016**

[177] M. Lang: *Valence Shell Photoionization of Soot Precursors with Synchrotron Radiation.* Ph.D. thesis, Julius-Maximilians-Universität Würzburg, **2015**

[178] B. Dick: *MEVIR and MEVELER: Program Manual*, **2013**

[179] J. D. Cardoza, F. M. Rudakov, N. Hansen, P. Weber: *Journal of Electron Spectroscopy and Related Phenomena*, 165: 5–10, **2008**

[180] J. L. Gosselin, P. M. Weber: *Journal of Physical Chemistry A*, 109: 4899–4904, **2005**

[181] N. Kuthirummal, P. M. Weber: *Chemical Physics Letters*, 378: 647–653, **2003**

[182] P. Hemberger., J. Kohler, I. Fischer, G. Piani, L. Poisson, J. Mestdagh: *Physical Chemistry Chemical Physics*, 14(18): 6173–6178, **2012**

[183] C. Schick, P. M. Weber: *Journal of Physical Chemistry A*, 105: 3725–3734, **2001**

[184] M. Tsubouchi, T. Suzuki: *Journal of Physical Chemistry A*, 107: 10 897–10 903, **2003**

[185] J. F. Stanton, R. J. Bartlett: *Journal of Chemical Physics*, 98: 7029–7039, **1993**

[186] H. Koch, P. Jorgensen: *Journal of Chemical Physics*, 93: 3333–3344, **1990**

[187] J. Schirmer: *Physical Review A*, 26(5): 2395–2416, **1982**

[188] A. B. Trofimov, J. Schirmer: *Journal of Physics B-Atomic Molecular and Optical Physics*, 28, **1995**

[189] C. Hättig: *Advances in quantum Chemistry*, 50: 37–60, **2005**

[190] R. Bauernschmitt, R. Ahlrichs: *Chemical Physics Letters*, 256: 454–464, **1996**

[191] G. E. S. an dCurtis L. Janssen, H. F. S. III: *Journal of Chemical Physics*, 89: 7382–7387, **1988**

[192] G. D. P. III, R. J. Bertlett: *Journal of Chemical Physics*, 76: 1910–1918, **1982**

[193] *TURBOMOLE V7.0 2015, a development of University of Karlsruhe and Forschungszentrum Karksruhe GmbH, available from http://www.turbomole.com.*

[194] M. J. Frisch, G. W. Trucks, H. B. Schlegel, G. E. Scuseria, M. A. Robb, J. R. Cheeseman, G. Scalmani, V. Barone, B. Mennucci, G. A. Petersson, H. Nakatsuji, M. Caricato, X. Li, H. P. Hratchian, A. F. Izmaylov, J. Bloino, G. Zheng, J. L. Sonnenberg, M. Hada, M. Ehara, K. Toyota, R. Fukuda, J. Hasegawa, M. Ishida, T. Nakajima, Y. Honda, O. Kitao, H. Nakai, T. Vreven, J. A. Montgomery, Jr., J. E. Peralta, F. Ogliaro, M. Bearpark, J. J. Heyd, E. Brothers, K. N. Kudin, V. N. Staroverov, R. Kobayashi, J. Normand, K. Raghavachari, A. Rendell, J. C. Burant, S. S. Iyengar, J. Tomasi, M. Cossi, N. Rega, J. M. Millam, M. Klene, J. E. Knox, J. B. Cross, V. Bakken, C. Adamo, J. Jaramillo, R. Gomperts, R. E. Stratmann, O. Yazyev, A. J. Austin, R. Cammi, C. Pomelli, J. W. Ochterski, R. L. Martin, K. Morokuma, V. G. Zakrzewski, G. A. Voth, P. Salvador, J. J. Dannenberg, S. Dapprich, A. D. Daniels, Ö. Farkas, J. B. Foresman, J. V. Ortiz, J. Cioslowski, D. J. Fox: *Gaussian09 Revision E.01.* Gaussian Inc. Wallingford CT 2009

[195] T. Yanai, D. Tew, N. C. Handy: *Chemical Physics Letters*, **2004**

[196] J.-D. Chai, M. Head-Gordon: *Physical Chemsitry Chemical Physics*, 10: 6115–6620, **2008**

[197] R. Krishnan, J. Binkley, R. Seeger, J. A. Pople: *Journal of Chemical Physics*, 72: 650–654, **1980**

[198] T. Dunning: *Journal of chemical Physics*, 90: 1007–1023, **1989**

[199] R. A. Kendall, T. H. Dunning, R. J. Harrison: *Journal of Chemical Physics*, 96: 6796–6806, **1992**

[200] R. Mitric, J. Petersen, V. Bonacic-Koutecky: *Physical REview A*, 79: 053 416, **2009**

[201] R. Mitric, J. Petersen, M. Wohlgemuth, U. Werner, V. Bonacic-Koutecky, L. Woste, J. Jortner: *Journal of Physical Chemistry A*, 115: 3755–3765, **2011**

[202] R. Mitric, U. Werner, V. Bonacic-Koutecky: *Journal of Chemical Physics*, 129: 164 118, **2008**

[203] U. Werner, R. Mitric, T. Suzuki, V. Bonacic-Koutencky: *Chemical Physics*, 349: 319–324, **2008**

[204] U. Werner, R. Mitric, V. Koutecky: *Journal of Chemical Physics*, 132: 174 301, **2010**

[205] W. C. Swope, H. C. Andersen, P. H. Berens, K. R. Wilson: *Journal of Chemical Physics*, 76: 637–649, **1982**

[206] J. C. Tully: *Journal of Chemical Physics*, 93(2), **1990**

[207] A. Humeniuk, M. Wohlgemuth, T. Suzuki, R. Mitric: *Journal of Chemical Physics*, 139: 134 104, **2013**

[208] A. D. Becke: *Journal of Chemical Physics*, 98: 5648–5652, **1993**

[209] C. Lee, W. Yang, R. G. Parr: *Physical Review B*, 37(2): 785–789, **1988**

[210] S. H. Vosko, L. Wilk, M. Nusair: *Canadian Journal of Physics*, 58: 1200–1211, **1980**

[211] F. J. Devlin, J. W. Finley, P. J. Stephens, M. J. Frisch: *Journal of Physical Chemistry*, 98: 11 623–11 627, **1994**

[212] A. Röder, A. Humeniuk, J. Giegerich, I. Fischer, L. Poisson, R. Mitric: *Physical Chemistry Chemical Physics*, **2017**

[213] Y. Murakami, T. Oguchi, K. Hashimoto, Y. Nosaka: *Journal of Physical Chemistry*, 111: 13 200–13 208, **2007**

[214] R. Sivaramakrishan, J. Michael: *Proceedings of the Combustion Institute*, 33: 225–232, **2011**

[215] R. A. Eng, A. Gebert, elke Goos, H. Hippler, C. Kachiani: *Physical Chemistry Chemical Physics*, 4: 3989–3996, **2002**

[216] B. B. Dangi, D. S. Parker, T. Yang, R. I. Kaiser, A. M. Mebel: *Angewandte Chemie, International Edition*, 53: 4608–4613, **2014**

[217] W. M. Davis, S. M. Heck, H. O. Pritchard: *Journal of Chemical Society Faraday Transactions*, 94: 2725–2728, **1998**

[218] G. de Silva, J. A. Cole, J. W. Bozzelli: *Journal of Physical Chemistry*, 114: 2275–2283, **2010**

[219] M. Derudi, D. Polino, C. Cavallotti: *Physical Chemistry Chemical Physics*, 13: 21 308–21 318, **2011**

[220] H. Fischer: *Zeitschrift fuer Naturforschung, A: Physical Sciences*, 20: 488–489, **1965**

[221] A. Carrington, I. Smith: *Molecular Physics*, 9: 137–147, **1965**

[222] G. B. Ellison, G. E. Davico, V. M. Bierbaum, C. H. Depuy: *International Journal of Mass Spectrometry and Ion Processes*, 156: 109–131, **1996**

[223] W. R. Roth, F. Hunold, M. Neumann, F. Bauer: *Liebigs Annalen*, 1679–1690, **1996**

[224] M. Fukushima, K. Obi: *Chemical Physics Letters*, 242: 443–448, **1995**

[225] K. Uejoh: *Spectrochimica Acta, Part A*, 60: 595–602, **2004**

[226] C. Cossart-Magos, S. Leach: *The Journal of Chemical Physics*, 56: 1534–1545, **1972**

[227] P.G.Carrick, J. Selco: *Journal of Molecular Spectroscopy*, 139: 448–452, **1990**

[228] G. Porter, E. Strachan: *Spectrochimica Acta, Part A*, 12: 299–304, **1958**

[229] N. Ikeda, N. Nakashima, K. Yoshihara: *Journal of Physical Chemistry*, 88: 5803–5806, **1984**

[230] M. A. Hoffbauer, J. W. Hudgens: *Journal of Physical Chemistry*, 89: 5152 – 5154, **1985**

[231] F. Bayrakçeken: *Spectrochimica Acta, Part A*, 68: 143–146, **2007**

[232] G. Porter., M. Savadatti: *Spectrochimica Acta, Part A*, 22: 803–806, **1966**

[233] J. D. Savee, J. Zádor, P. Hemberger, B. Sztáray, A. Bodi, D. L.Osborn: *Molecular Physics*, 113(15-16): 2217–2227, **2015**

[234] A. Nagy, J. Fulara, I. Garkusha, J. P. Maier: *Angewandte Chemie, International Edition*, 50: 3022–3025, **2011**

[235] F. G. Satink, G. Meijer, G. von Helden: *Journal of the American Chemical Society*, 125: 15 714–15 715, **2003**

[236] V. Misic, K. Piech, T. Bally: *Journal of the American Chemical Society*, 135: 8625–8631, **2013**

[237] S. Leach: *Journal de Physique*, 10(32): 155–157, **1971**

[238] J. H. Miller, L. Andrews: *Journal of Molecular Spectroscopy*, 90: 20–26, **1981**

[239] G. C. Eiden, J. C. Weisshaar: *The Journal of Chemical Physics*, 104: 8896–8912, **1996**

[240] C. Cossart-Magos, S. Leach: *The Journal of Chemical Physics*, 64: 4006–4019, **1976**

[241] M. Zierhut, B. Noller, T. Schlutz, I. Fischer: *The Journal of Chemical Physics*, 122: 094 302, **2005**

[242] Y. Song, X. Zheng, M. Lucas, J. Zhang: *Physical Chemistry Chemical Physics*, 13: 8296–8305, **2011**

[243] T. Koenig, W. Snell, J. C. Chang: *Tetrahedron Letters*, 50: 4569–4572, **1976**

[244] F. A. Houle, J. L. Beauchamp: *Journal of the American Chemical Society*, (78): 3290–3294, **1978**

[245] G. C. Eiden, K.-T. Lu, J. Badenhoop, F. Weinhold, J. C. Weisshaar: *The Journal of Chemical Physics*, 104: 8886–8895, **1996**

[246] F. P. Lossing, J. C. Traeger: *Journal of the American Chemical Society*, 97(6): 1579–1580, **1975**

[247] J. P. Perdew, K. Burke, M. Ernzerhof: *Physical Review Letters*, 77: 3865–3868, **1996**

[248] C. Adamo, V. Barone: *Journal of Chemical Physics*, 110: 6158–6170, **1999**

[249] H. Iikura, T. Tsuneda, T. Yanai, K. Hirao: *Journal of Chemical Physics*, 115: 3540–3544, **2001**

[250] K. Kaufmann, W. Baumeister, M. Jungen: *Journal of Physics B-Atomic Molecular and Optical Physics*, 22: 2223–2240, **1989**

[251] H. Werner, P. J. K. and: *Wiley Interdisciplinary Reviews - Computational Molecular Science*, 2: 242–253, **2012**

[252] G. Granucci, M. Persicoa, A. Toniolo: *Journal of Chemical Physics*, 114: 10 608–10 615, **2001**

[253] P. G. Lisinetskaya, R. Mitric: *Physical Review A*, 83: 033 408, **2011**

[254] R. Mitric, U. Werner, M. Wohlgemuth, G. Seifert, V. bonacic Koutecky: *Journal of Physical Chemistry A*, 113: 12 700–12 705, **2009**

[255] K. Tonokura, M. Koshi: *Journal of Physical Chemistry A*, 107(22): 4457–4461, **2003**

[256] F. Negri, G. Orlandi, F. Zerbetto, M. Z. Zgierski: *J. Chem. Phys.*, 93: 600–608, **1990**

[257] B. Ward: *Spectrochimica Acta, Part A-Molecular Spectroscopy*, A 24(7): 813, **1968**

[258] G. Eiden, J. Weisshaar: *Journal of Physical Chemistry*, 95: 6194–6197, **1991**

[259] V. A. Smirnov, V. G. Plotnikov: *Russian Chemical Reviews*, 55: 1633–1666, **1986**

[260] J. Rice, N. Handy, P. Knowles: *Journal of the Chemical Society, Faraday Transactions*, 83: 1643–1649, **1987**

[261] G. Vincow, H. J. Dauben, F. R. Hunter, W. V. Volland: *The Journal of the American Chemical Society*, 91(11): 2823–2827, **1969**

[262] W. G. Fateley, E. R. Lippincott: *The Journal of Chemical Physics*, 26: 1471–1481, **1957**

[263] E. P. F. Lee, T. G. Wright: *Journal of Physical Chemistry*, 102: 4007–4013, **1998**

[264] R. D. J. III: *The Journal of Chemical Physics*, 95: 7108–7113, **1991**

[265] M. Kaufmann, D. Leicht, M. Havenith, B. M. Broderick, G. E. Douberly: *The Journal of Physical Chemistry A*, 120: 6768–6773, **2016**

[266] H. J. Silverstone, D. E. Wood, H. M. McConnel: *The Journal of Chemical Physics*, 41(8): 2311–2323, **1964**

[267] T. Pino, F. Güther, H. Ding., P. Maier: *Journal of Physical Chemistry A*, 106: 10 022–10 026, **2002**

[268] V. L. Stakhursky, I. Sioutis, G. Tarczay, T. A. Miller: *The Journal of Chemical Physics*, 128: 084 310, **2008**

[269] I. Sioutis, V. L. Stakhursky, G. Tarczay, T. A. Miller: *The Journal of Chemical Physics*, 128: 084 311, **2008**

[270] B. Thrush, J. Zwolenik: *Discussions of the Faraday Society*, **1963**

[271] K. H. Fischer, P. Hemberger, A. Bodi, I. Fischer: *Beilstein Journal of Organic Chemistry*, 9: 681–688, **2013**

[272] T. Koenig, C. Chang: *The Journal of the American Chemical Society*, 2240–2242, **1977**

[273] A. G. Harrison, L. R. Honnen, H. J. Dauben, F. Lossing: *The Journal of the American Chemical Society*, 82: 5593–5596, **1960**

[274] F. A. Elder, A. C. Parr: *The Journal of Chemical Physics*, 50: 1027–1028, **1969**

[275] B. J. Smith, N. E. Hall: *Chemical Physics Letters*, 279: 165–171, **1997**

[276] A. Hertwig, H. Hippler, H. Schmid, A.-N. Unterreiner: *Physical Chemistry Chemical Physics*, 1: 5129–5132, **1999**

[277] W. Koban, J. D. Koch, R. K. Hanson, C. Schulz: *Physical Chemistry Chemical Physics*, 6: 2940–2945, **2004**

[278] B. B. Wright, M. S. Platz: *Journal of the American Chemical Society*, 105: 628–630, **1983**

[279] G. de Silva, E. E. Moore, J. W. Bozzelli: *Journal of Physical Chemistry A*, 113: 10 264–10 278, **2009**

[280] J. L. Segura, N. Martin: *Chemical Reviews*, 99: 3199–3246, **1999**

[281] K. L. Tseng, J. Michl: *The Journal of the American Chemical Society*, 4840–4842, **1977**

[282] C. R. Flynn, J. Michl: *The Journal of the American Chemical Society*, 5802–5803, **1973**

[283] C. R. Flynn, J. Michl: *The Journal of the American Chemical Society*, 3280–3288, **1974**

[284] J. J. Mccullough: *Accounts of Chemical Research*, 13: 270–276, **1980**

[285] J. L. Charlton., M. M. Alauddin: *Tetrahedron*, 43(13): 2873–2889, **1987**

[286] N. Martin, C. Seoane, M. Hanack: *Organic Preparations and Procedures International*, 23(2): 237–272, **1991**

[287] L. A. Errede: *The Journal of the Amercian Chemical Society*, 949–954, **1961**

[288] W. R. Roth, M. Biermann, H. Dekker, R. Jochems, C. Mosselman: *Chemische Berichte*, 111: 3892–3903, **1978**

[289] W. S. Trahanovsky, J. R. Macias: *The Journal of the American Chemical Society*, 108: 6820–6821, **1986**

[290] W. R. Roth, B. P. Scholz: *Chemische Berichte*, 114(12): 3714–4010, **1981**

[291] P. Hemberger, A. J. Trevitt, T. Gerber, E. Ross, G. de Silva: *The Journal of Physical Chemistry A*, 118(20): 3593–3604, **2014**

[292] J. Kreile, N. Münzel, R. Schulz, A. Schweig: *Chemical Physics Letters*, 108(6): 609–612, **1984**

[293] E. Migirdicyan, J. Baudet: *The Journal of the American Chemical Society*, 7400–7404, **1975**

[294] R. D. Miller, J. Kolc, J. Michl: *Journal of the American Chemical Society*, 8510–8514, **1976**

[295] C. A. Coulson, D. P. Craig, A. Maccoll, M. A. Pullman: *Journal of the American Chemical Society*, 64: 36–38, **1942**

[296] M. Szwarc: *The Journal of Chemical Physics*, 16: 128, **1948**

[297] W. S. Trahanovsky, S. P. Lorimor: *Journal of Organic Chemistry*, 71: 1784–1794, **2006**

[298] W. F. Gorham: *Journal of polymer science*, 4: 3027–3039, **1966**

[299] S. C. Systems: *SCS Parylene properties*

[300] N. Mitsubayashi, T. Yatsuhashi, N. Nakashima: *Journal of Photochemistry and Photobiology, A: Chemistry*, 219: 273–277, **2011**

[301] P. G. Mahaffy, J. D. Wieser, L. K. Montgomery: *The Journal of the American Chemical Society*, 4514–4515, **1977**

[302] J. M. Pearson, H. A. Six, D. J. Williams, M. Ley: *Journal of the American Chemical Society*, 5034–5036, **1971**

[303] S. K. Pollack, B. C. Raine, W. J. Hehre: *Journal of the American Chemical Society*, 103: 6308–6313, **1981**

[304] M. Bobrowski, P. Skurski, S. Freza: *Chemical Physics*, 382: 20–26, **2011**

[305] T.-K. Ha: *Theoretical Chemistry Accounts*, 66: 111–120, **1984**

[306] T. Koenig, R. Wielesek, W. Snell, T. Balle: *Journal of the American Chemical Society*, 3225–3226, **1975**

[307] T. Koenig, S. Southworth: *Journal of the American Chemical Society*, 2807–2809, **1977**

[308] P. Hemberger, A. J. Trevitt, E. Ross, G. da Silva: *The Journal of Physical Letters*, 4: 2546–2550, **2013**

[309] Y. Hosoi, T. Yatsuhashi, K. Ohtakeyama, S. Shimizu, Y. Sakata, N. Nakashima: *Journal of Physical Chemistry A*, 106: 2014–2019, **2002**

[310] S. Kato, K. Morokuma, D. Feller, E. R. Davidson, W. T. Bordon: *The Journal of the American Chemical Society*, 105: 1791–1795, **1983**

[311] P. G. Wenthold, J. B. Kim, W. C. Lineberger: *The Journal of the American Chemical Society*, 119: 1354–1359, **1997**

[312] V. Blanchet, M. Z. Zgierski, T. Seideman, A. Stolow: *Discerning vibronic molecular dynamics using time-resolved photoelectron spectroscopy*, vol. 401. **1999**

[313] F. Weigend, R. Ahlrichs: *Physical Chemistry Chemical Physics*, 7: 3297–3305, **2005**

[314] F. Weigend: *Physical Chemistry Chemical Physics*, 8: 1057–1065, **2006**

[315] L. A. Curtiss, P. C. Redfern, K. Raghavachari: *The Journal of Chemical Physics*, 126: 084108, **2007**

[316] E. Gloaguen, J. M. Mestdagh, L. Poisson, F. Lepetit, J. Visticot, B. Soep, M. Coroiu, A. Eppink, D. H. Parker: *Journal of the American Chemical Society*, 127(47): 16529–16634, **2005**

[317] H. W. Shin, E. J. Ocola, S. Kim, J. Laane: *The Journal of Chemical Physics*, 140: 034305, **2014**

[318] P. Constantinidis, F. Hirsch, I. Fischer, A. Dey, A. M. Rijs: *J. Phys. Chem. A*, 121: 181–191, **2017**

[319] T. Ellermann: *Chemical Physics Letters*, 189(2): 175–181, **1992**

[320] F. Danis, F. Caralp, B. Veyret, H. Loirat, R. Lesclaux: *International Journal of Chemical Kinetics*, 21: 715–727, **1989**

[321] J. W. Hudgens, R. D. J. III, B. P. Tsai, S. A. Kafafi: *Journal of the American Chemical Society*, 112: 5763–5772, **1990**

[322] E. S. J. Robies, P. Chen: *Journal of Physical Chemistry*, 98: 6919–6923, **1994**

[323] I. A. for Research on Cancer, ed.: *Polychlorinated Dibenzo-para-Dioxins and Polychlorinated Dibenzofurans*. **1997**

[324] E. T. Oppelt: *Environmental Science and Technology*, 20(4): 312–318, **1986**

[325] K. Brudnik, M. Twarda, D. Sarzynski, J. T. Jodkowski: *Journal of Molecular Modeling*, 19: 4181–4193, **2013**

[326] E. J. Hintsa, X. Zhao, W. M. Jackson, W. B. Miller, A. M. Wodtke, Y. T. Lee: *Journal of Physical Chemistry*, 95: 2799–2802, **1991**

[327] D. Smith, M. J. Church: *International Journal of Mass Spectrometry and Ion Physics*, 19: 185–200, **1976**

[328] G. R. D. Maré, G. Huybrechts: *Transactions of the Faraday Society*, 64: 1311–1318, **1968**

[329] S. A. Kostina, A. A. Shestov, V. D. Knyazev: *Journal of Physical Chemistry A*, 107: 10 292–10 295, **2003**

[330] K. Oum, K. Luther, J. Troe: *Journal of Physical Chemistry A*, 108: 2690–2699, **2004**

[331] V. D. Knyazev, I. R. Slagle, M. G. Bryukov: *Journal of Physical Chemistry A*, 107: 6558–6564, **2003**

[332] J. M. anf D. Caralp, A. Jemi-Alade, P. Lightfoot, R. L. L. Rayez: *Journal of Physical Chemistry*, 97: 3237–3244, **1993**

[333] I. Matheson, H. W. Sidebottom, J. M. Tedder: *International Journal of Chemical Kinetics*, VI: 493–506, **1974**

[334] M. Pesa, M. J. Pilling, S. H. Robertson, D. M. Wardlaw: *Journal of Physical Chemistry A*, 102: 8526–8536, **1998**

[335] J. Burkholder, S. P. Sander, J. Abbatt, J. R. Barker, R. E. Huie, C. E. Kolb, M. J. Kurylo, V. L. Orkin, D. M. Wilmouth, P. H. Wine: *Chemical Kinetics and Photochemical Data for Use in Atmospheric Studies Evaluation Number 18.* Tech. rep., National Aeronautics and Space Administration, **2015**

[336] J. E. Bennet, S. C. Graham, B. Mile: *Spectrochimica Acta, Part A*, 29A: 375–383, **1973**

[337] C. Hesse, N. Leray, J. Roncin: *Molecular Physics*, 22(1): 137–145, **1971**

[338] B.-S. Cheong, H.-G. Cho: *Journal of Physical Chemistry A*, 101: 7901–7906, **1997**

[339] F.-W. F.-W. Breitbarth, H.-J. Tiller, R. Reinhardt: *Plasma Chemistry and Plasma Processing*, 5(4): 293–316, **1985**

[340] F.-W. Breitbarth, D. Berg: *Chemical Physics Letters*, 149(3): 334–338, **1988**

[341] T. Ibuki, N. Takahashi, A. Hiraya, K. Shobatake: *The Journal of Chemical Physics*, 85: 5717–5722, **1986**

[342] B. Lesigne, L. Gilles, R. J. Woods: *Canadian Journal of Chemistry*, 52: 1135–1139, **1974**

[343] F. Lossing: *Bulletin des Societes Chimiques Belges*, 81: 125–134, **1972**

[344] Y.-L. He, L. Wang: *Structural Chemistry*, 20: 461–479, **2009**

[345] M. Horn, P. Boschwina: *Chemical Physics Letters*, 228: 259–267, **1994**

[346] D. Lide, ed.: *Handbook of Chemistry and Physics; Ionization potential of atoms and atomic Ions*, vol. 10. **1992**

[347] J. L. Tech: *Journal of Research*, 67A: 505–555, **1963**

[348] W. H. Brune, J. G. Anderson, D. W. Toohey, D. W. Fahey, S. R. Kawa, R. L. Jones, D. S. McKenna, L. Poole: *Science*, 252: 1260–1266, **1991**

[349] J. G. Anderson, D. W. Toohey, W. H. Brune: *Science*, 251: 39–46, **1991**

[350] M. B. McElroy, R. J. Salawitch: *Science*, 243: 763–770, **1989**

[351] R. Toumi, R. L. Jones, J. A. Pyle: *Nature*, 365: 37–39, **1993**

[352] P. Fogg, J. M. Sangster, eds.: *Chemicals in the Atmosphere - Solubility, Sources and Reactivity.* Wiley, **2003**

[353] Y. L. Yung, J. P. Pinto, R. T. Watson, S. P. Sander: *American Meteorological Society*, 339–353, **1980**

[354] J. J. Orlando, G. S. Tyndall, T. J. Wallington, M. Dill: *International Journal of Chemical Kinetics*, 28: 433–442, **1996**

[355] S. Penkett, J. Butler, R. Cicerone, A. Golombek, M. Kurylo, J. Lcvine, M. Molina, R. Prinn, C. Reeves, J. Rodriguez, H. Singh, D. Toohey, R. Weiss: *Scientific Assessment of Ozone Depletion.* UNEP, WMO, **1994**

[356] K. D. Bayes, R. R. Friedl, S. P. Sander: *Journal of Physical Chemistry A*, 109: 3045–3051, **2005**

[357] T. D. Tzima, K. D. Papavasileiou, D. K. Papayannis, V. S. Melissas: *Chemical Physics*, 324: 491–599, **2006**

[358] E. Villenave, R. Lesclaux: *Chemical Physics Letters*, 236: 376–384, **1995**

[359] D. W. Smith, L. Andrews: *The Journal of Chemical Physics*, 55(11): 5295–5303, **1971**

[360] S. P. Mishra, G. W. Neilson, M. C. R. Symons: *Journal of the Chemical Society Faraday Transactions 2*, 70: 1165–1174, **1974**

[361] S. Bailleux, P. Dréan, M. Godon, Z. Zelinger, C. Duan: *Physical Chemistry Chemical Physics*, 6: 3049–3051, **2004**

[362] S. Bailleux, P. Dréan, Z. Zelinger, S. Civis, H. Ozeki, S. Saito: *The Journal of Chemical Physics*, 122: 134 302, **2005**

[363] H. Ozeki, T. Okabayashi, M. Tanimoto, iS. Saito, S. Bailleux: *The Journal of Chemical Physics*, 127: 224 301, **2007**

[364] P. B. Davies, Y. Liu, Z. Liu: *Chemcial Physics Letters*, 214(3,4): 305–309, **1993**

[365] R. Ma, M. Chen, M. Zhou: *The Journal of Physical Chemistry A*, 113: 12 926–12 931, **2009**

[366] Z.-X. Ma, C.-L-Liao, C. Ng, N. L. Ma, W.-K. Li: *The Journal of Chemical Physics*, 99(9): 6470–6473, **1993**

[367] R. I. Reed, W. Snedden: *Transactions of the Faraday Society*, 876–879, **1958**

[368] C. K. Chong, X. Zheng, D. L. Phillips: *Chemical Physics Letters*, 328: 113–118, **2000**

[369] J. Moc, J. Panek: *Chemical Physics Letters*, 345: 497–504, **2001**

[370] J. Moc: *Chemical Physics*, 247: 365–373, **1999**

[371] L. Andrews, J. M. Dyke, N. Jonathan, J. Keddar, A. Morris: *The Journal of Physical Chemistry A*, 88: 1950–1954, **1984**

[372] M. Steinbauer, P. Hemberger, I. Fischer, M. Johnson, A. Bodi: *Chemical Physics Letters*, 500: 232–236, **2010**

[373] O. J. Nielsen, J. Munk, G. Locke, T. J. Wallington: *Journal of Physical Chemistry*, 95: 8714–8719, **1991**

[374] Y. Li, J. S. Francisco: *The Journal of Chemical Physics*, 114(7): 2879–2882, **2001**

[375] R. A. Vogt, T. G. Gray, C. E. Crespo-Hernandez: *Journal of American Chemical Society*, **2012**

[376] D. Xu, J. S. Francisco, J. Huang, W. M. Jackson: *Journal of Chemical Physics*, 117(6): 2578–2585, **2002**

[377] C. Wentrup: *Australian Journal of Chemistry*, 63: 979–986, **2010**

[378] R. Brückner: *Reaktionsmechanismen: Organische Reaktionen, Stereochimie, Modern Synthesemethoden (Sav Chemie)*. Elsevier, **2004**

[379] H. H. Wenk, M. Winkler, W. Sander: *Angewandte Chemie*, 115(5): 518–546, **2003**

[380] H. Pellissier, M. Santelli: *Tetrahedron*, 59: 701–730, **2003**

[381] F. Zhang, D. Parker, Y. S. Kim, R. I. Kaiser, A. M. Mebel: *The Astrophysical Journal*, 728(141), **2011**

[382] F. Carelli, F. Sebastianelli, I. Baccarelli, F. A. Gianturco: *The Astrophysical Journal*, 712: 445–452, **2010**

[383] S. L. W. Weaver, A. J. Reöijan, R. J. McMahon, B. J. McCall: *The Astrophysical Journal*, 671: L153–L156, **2007**

[384] H. Wang, A. Laskin, N. W. Moriarty, M. Frenklach: *Proceedings of the Combustion Institute*, 28: 1545–1555, **2000**

[385] Y. Song, M. Lucas, M. Alcaraz, J. Zhang, C. Brazier: *The Journal of Chemical Physics*, 136: 044 308, **2012**

[386] A. Matsugi, A. Miyoshi: *Physical Chemistry Chemical Physics*, 14: 9722–9728, **2012**

[387] R. Warmuth: *Angewandte Chemie*, 109(12): 4106–1409, **1997**

[388] P. G. Wenthold: *Australian Journal of Chemistry*, 63: 1091–1098, **2010**

[389] P. G. Wenthold, J. A. Paulino, R. R. Squires: *Journal of the American Chemical Society*, 113: 7415–7417, **1991**

[390] A. Schweig, N. Münzel, H. Meyer, A. Heidenreich: *Structural Chemistry*, 1: 89–100, **1989**

[391] C. W. B. Jr, A. Ricca: *Chemical Physics Letters*, 566: 1–3, **2013**

[392] H. Li, S.-Y. Yu, M.-B. Huang, Z.-X. Wang: *Chemical Physics Letters*, 450: 12–18, **2007**

[393] H. Jiao, P. von Rague Schleyer, B. R. Beno, ken N. Houk, R. Warmuth: *Angewandte Chemie*, 109(24): 2929–2933, **1997**

[394] G. Ghigo, A. maranzana, G. Tonachini: *Physical Chemistry Chemical Physics*, 16: 23 944–23 951, **2014**

[395] T. Helgaker, O. B. Lutnaes, M. Jusyunski: *Journal of Chemical Theory and Computation*, 3: 86–94, **2007**

[396] H. Li, M.-B. Huang: *Physical Chemistry Chemical Physics*, 10: 5381–5387, **2008**

[397] S. Keller, K. Bouguslawski, T. Janowski, M. Reiher, P. Pulay: *The Journal of Chemical Physics*, 142: 224 104, **2015**

[398] T.-C. Jagau, J. Gauss: *The Journal of Chemical Physics*, 137: 044 116, **2012**

[399] H. U. Suter, T.-K. Ha: *Chemical Physics Letters*, 198(3,4): 259–265, **1992**

[400] E. Kraka, D. Cremer: *Chemical Physics Letters*, 216(3,4,5,6): 333–340, **1993**

[401] S. G. Kukolich, C. Tanjaroon, M. McCarthy, P. Thaddeus: *The Journal of Chemical Physics*, 119: 4353–4359, **2003**

[402] S. G. Kukolich, M. C. McCarthy, P. Thaddeus: *Journal of Physical Chemistry A*, 108: 2645–2651, **2004**

[403] P. Groner, S. G. Kukolich: *Journal of Molecular Structure*, 780-781: 178–181, **2006**

[404] P. D. Godfrey: *Australian Journal of Chemistry*, 63: 1061–1065, **2010**

[405] E. G. Robertson, P. D. Godfrey, D. McNaughton: *Journal of Molecular Spectroscopy*, 217: 123–126, **2003**

[406] R. Brown, P. D. Godfrey, M. Rodler: *Journal of the American Chemical Society*, 108: 1296–1297, **1986**

[407] O. Chapman, K. Mattes, C. L. McIntosh, J. Pacansky, G. Calder: *Journal of the American Chemical Society*, 95: 6134–6135, **1973**

[408] J. G. Radziewzeski, B. A. Hess, R. Zahradnik: *Journal of the American Chemical Society*, 114: 52–57, **1992**

[409] N. Münzel, A. Schweig: *Chemical Physics Letters*, 147(2,3), **1988**

[410] A. Chrostowska, G. Pfister-Guillouzo, F. Gracian, C. Wentrup: *Australian Journal of Chemistry*, 63: 1084–1090, **2010**

[411] M. S. Dewar, T.-P. Tien: *Journal of the Chemical Society, Chemical Communications*, 1243–1244, **1985**

[412] I. H. Hillier, M. A. Vincent, M. F. Guest, W. von Niessen: *Chemical Physics Letters*, 134(5): 403–406, **1987**

[413] J. G. G. Simon, H. Specht, A. Schweig: *Chemical Physics Letters*, 200(5): 459–464, **1992**

[414] X. Zhang, P. Chen: *Journal of the American Chemical Society*, 114: 3147–3148, **1992**

[415] E. Reusch: *Photoionisation von ortho-Benzin*. Master's thesis, Julius-Maximiliams-Universität Würzburg, **2016**

[416] O. Christiansen, H. Koch, P. Jorgensen: *Chemical Physics Letters*, 243: 409–418, **1995**

[417] K. Andersson, P. A. Malqvist, B. Roos, A. J. Sadlej: *Journal of Physical Chemistry*, 94: 5483–5488, **1990**

[418] K. Andersson, P. Malmqvist, B. Roos: *The Journal of Chemical Physics*, 96: 1218–1226, **1992**

[419] G. Karlström, R. Lindh, P. Malmqvist, B. O. Roos, U. Ryde, V. Veryazov, P. Widmark, M. Cossi, B. Schimmelpfennig, P. Neograd y, L. Seijo: *Computational Materials Science*, 28: 222–239, **2003**

[420] I. Hahndorf, Y. Lee, R. Kaiser, L. Vereecken, J. Peeters, H. F. Bettlinger, P. Schreiner, P. Schleyer, W. Allen, H. S. III: *The Journal of Chemical Physics*, 116(8): 3248–3262, **2002**

[421] V. Detilleux, J. Vandooren: *The Journal of Physical Chemistry A*, 113: 10 913–10 922, **2009**

[422] Y. Li, L. Zhang, Z. Tian, T. Yuan, J. Wang, B. Yang, F. Qi: *Energy & Fuels*, 23: 1473–1485, **2009**

[423] R. Sivaramakrishnan, R. S. Tranter, K. Brenzinsky: *The Journal of Physical Chemistry A*, 110: 9388–9399, **2006**

[424] P. Dagaut, G. Pengloan, A. Ristori: *Physical Chemistry Chemical Physics*, 4: 1846–1854, **2002**

[425] A. S. AlRamadan, S. M. Sarathy, M. Khurshid, J. Badra: *Fuel*, 180: 175–186, **2016**

[426] K. Kohse-Höinghaus, B. Atakan, A. Lamprecht, G. G. Alatorre, M. Kamphus, T. Kasper, N.-N. Liu: *Physical Chemistry Chemical Physics*, 4: 2056–2062, **2002**

[427] D. Trogolo, A. Maranzana, G. Ghigo, G. Tonachini: *The Journal of Physical Chemistry A*, 118: 427–440, **2014**

[428] H. N, T. Kasper, S. J. Klippenstein, P. Westmoreland, M. Law, C. Taatjes, K. Kohse-Höinghaus, J. Wang, T. Cool: *The Journal of Physical Chemistry A*, 111: 4081–4092, **2007**

[429] G. de Silva, J. A. Cole, J. W. Bozzelli: *The Journal of Physical Chemistry A*, 113: 6111–6120, **2009**

[430] S. Matzinger, T. Bally: *The Journal of Physical Chemistry A*, 104: 3544–3552, **2000**

[431] C. Müller, A. Schweig, W. Thiel, W. Grahn, R. G. Bergman, K. C. Vollhardt: *The Journal of the American Chemical Society*, 5579–5581, **1979**

[432] M. Steinbauer, P. Hemberger, I. Fischer, A. Bodi: *ChemPhysChem*, 12: 1795–1797, **2011**

[433] D. Polino, C. Cavallotti: *The Journal of Physical Chemistry A*, 115: 10281–10289, **2011**

[434] D. Polino, A. Famulari, C. Cavallotti: *The Journal of Physical Chemistry A*, 115: 7928–7936, **2011**

[435] S. Matzinger, T. Bally, E. V. Patterson, R. J. McMahon: *The Journal of the American Chemical Society*, 118: 1535–1542, **1996**

[436] M. W. Wong, C. Wentrup: *Journal of Organic Chemistry*, 61: 7022–7029, **1996**

[437] G. de Silva, A. J. Trevitt, M. Steinbauer, P. Hemberger: *Chemical Physics Letters*, 517: 144–148, **2011**

[438] E. V. Patterson, R. J. McMahon: *Journal of Organic Chemistry*, 62: 4398–4405, **1997**

[439] J. Jones, G. B. Bacskay, J. C. Mackie: *The Journal of Physical Chemistry A*, 101: 7105–7113, **1997**

[440] C. Cavallotti, M. Derudi, R. Rota: *Proceedings of the Combustion Institute*, 32: 115–121, **2009**

[441] H. Wang, M. Frenklach: *Combustion and Flame*, 110: 173–221, **1997**

[442] C.-W. Zhou, V. V. Kislov, A. M. Mebel: *The Journal of Physical Chemistry A*, 116: 1571–1585, **2012**

[443] S. Iglesias-Groth, A. Manchado, D. A. Garcia-Hernandez, J. I. G. Hernandez, D. L. Lambert: *The Astrophysical Journal*, 685: 55–58, **2008**

[444] F. Pauzat, D. Talbi, Y. Ellinger: *Astronomy and astrophysics*, 293: 263–277, **1995**

[445] P. Du, F. Salama, G. H. Loew: *chemical Physics*, 173: 321–437, **1993**

[446] D. L. Kokkin, T. W. Schmidt: *Journal of Physical Chemistry A*, 110: 6173–6177, **2006**

[447] K. M. Erwin, T. M. Ramond, G. E. Davico, R. L. Schwartz, S. M. Casey, W. C. Lineberger: *Journal of Physical Chemistry A*, 105: 10 822–10 831, **2001**

[448] M. L. Weichmann, J. B. Kim, J. A. DeVine, D. S. Levine, D. M. Neumark: *Journal of the American Chemical Society*, 137: 1420–1423, **2015**

[449] B. N. Papas, S. Wang, N. J. DeYonker, H. L. Woodcok, H. F. S. III: *Journal of Physical Chemistry A*, 107: 6311–3616, **2003**

[450] A. K. Dutta, P. U. Manohar, N. Vaval, S. Pal: *The Journal of Chemical Physics*, 140: 114 312, **2014**

[451] S. Rayne, K. Forest: *Computational and Theoretical Chemistry*, 983: 69–75, **2012**

[452] H. A. Galue, J. Oomens: *Angewandte Chemie International Edition*, 50: 7004–7007, **2011**

[453] E. Reusch, D. Schleier, I. Fischer, P. Hemberger: **2017**

[454] A. B. Fialkov, K.-H. Homann: *Combustion and Flame*, 127: 2076–2090, **2001**

[455] N. M. Marinov, W. J. Pitz, C. K. Westbrook, A. M. V. andMarco J. Castaldi, S. M. Senkan, C. F. Melius: *Combustion and Flame*, 114: 192–213, **1998**

[456] P. Lindstedt, L. Maurice, M. Meyer: *Faraday Discussions*, 119: 401–432, **2001**

[457] M. Frenklach: *Physical Chemistry Chemical Physics*, 4: 2028–2037, **2002**

[458] R. I. Kaiser, O. Asvany, Y. T. Lee: *Planetary and Space Sciences*, 48: 483–492, **2000**

[459] R. Kaiser., O. Asvany, Y. Lee, H. F. Bettinger, P. v. R. Schleyer, H. S. III: *Journal of Chemical Physics*, 112(11): 4994–5001, **2000**

[460] T. Wallington, H. Egsgaard, O. Nielsen, J. Platz, J. Sehested, T. Stein: *Chemical Physics Letters*, 290: 363–370, **1998**

[461] K. Tonokura, Y. Norikane, M. Koshi, Y. Nakano, S. Nakamichi, M. Goto, S. Hashimoto, M. Kawasaki, M. P. S. Andersen, M. D. Hurley, T. J. Wallington: *Journal of Physical Chemistry A*, 106: 5908–5917, **2002**

[462] J. Park, J. Nam, I. V. Tokmakov, M. C. Lin: *Journal of Physical Chemistry A*, 110: 8729–8735, **2006**

[463] R. J. McMahon, C. McCarthy, C. A. Gottlieb, J. B. Dudek, J. F. Stanton, P. Thaddeus: *The Astrophysical Journal*, 590: L61–L64, **2003**

[464] O. Martinez, K. N. Crabtree, C. A. Gottlieb, J. F. Stanton, M. C. McCarthy: *Angewandte Chemie, International Edition*, 54: 1808–1811, **2015**

[465] J. E. Benent, J. Mile, A. Thomas: *Chemical Communications*, (12): 265, **1965**

[466] P. H. Kasai, E. Hedaya, E. B. whippie: *Journal of the American Chemical Society*, 91: 4364–4368, **1969**

[467] E. N. Sharp, M. A. Roberts, D. J. Nesbitt: *Physical Chemistry Chemical Physics*, 10: 6592–6596, **2008**

[468] C.-H. Chang, D. J. Nesbitt: *The Journal of Chemical Physics*, 145: 0044 304, **2016**

[469] J. G. Radiziszewski, M. R. Nimlos, P. R. Winter, G. B. Ellison: *The Journal of the American Chemical Society*, 118: 7400–7401, **1996**

[470] A. V. Friederichsen, J. G. Radiziszewski, M. R. Nimlos, P. R. Winter, D. C. Dayton, D. E. David, G. B. Ellison: *The Journal of the American Chemical Society*, 123: 1977–1988, **2001**

[471] A. Lapinski, J. Spanget-Larsen, M. Langgard, J. Waluk, J. G. Radzisezwski: *Journal of Physical Chemistry A*, 105: 10 520–10 524, **2001**

[472] B. Cerek, M. Kongshaug: *The Journal of Physical Chemistry*, 74(25): 4319–4322, **1970**

[473] N. Ikeda, N. Nakashima, K. Yoshihara: *The Journal of the American Chemical Society*, 107: 3381–3382, **1985**

[474] J. G. Radzisezwski: *Chemcial Physics Letters*, 301: 565–570, **1999**

[475] J. M. Engert, B. Dick: *Applied Physics B: Lasers and Optics*, 63: 531–535, **1996**

[476] S. M. Mattar: *Journal of Physical Chemistry A*, 111: 251–260, **2007**

[477] M. Krauss, S. Roszak: *Journal of Molecular Structure (Theochem)*, 310: 155–160, **1994**

[478] G.-S. Kim, A. M. Mebel, S. H. Lin: *Chemical Physics Letters*, 361: 421–431, **2002**

[479] I. P. Fisher, T. F. Palmer, F. P. Lossing: *Journal of the American Chemical Society*, 86: 2741–2742, **1964**

[480] V. Butcher, M. Costa, J. Dyke, A. R. Ellis, A. Morris: *Chemical Physics*, 115: 261–267, **1987**

[481] K. Freel, J. Park, M. Lin, M. C. Heaven: *Chemical Physics Letters*, 507: 216–220, **2011**

[482] M. Biczysko, J. Bloino, V. Barone: *Chemcial Physics Letters*, 471: 143–147, **2009**

[483] B. Negru, S. J. Groncher, A. L. Brunsvold, G. M. P. Just, D. Park, D. M. Neumark: *The Journal of Chemical Physics*, 133: 074 302, **2010**

[484] A. M. Mebel, A. Landera: *The Journal of Chemical Physics*, 136: 234 305, **2012**

[485] N. C. Cole-Filipiak, M. Shapero, B. Negru, D. M. Neumark: *The Journal of Chemical Physics*, 141: 1040 307, **2014**

[486] P. Constantinidis, H.-C. Schmitt, I. Fischer, B. Yan, A. M. Rijs: *Physical Chemistry Chemical Physics*, 17: 29 064–29 071, **2015**

[487] D. S. N. Parker, R. I. Kaiser, T. P. Troy, O. Kostko, M. Ahmed, A. Mebel: *The Journal of Physical Chemistry*, 119: 7145–7154, **2015**

[488] *Amtsblatt der Europäischen Union*, L 171, **2007**

[489] O. of Air Quality Planning, Standards: *National Service Center for environmental Publications*, **1998**

[490] A. Terentis, A. Doughty, J. C. Mackie: *The Journal of Physical Chemistry A*, 96(25): 10 334–10 339, **1992**

[491] A. Doughty, J. C. Mackie: *The Journal of Physical Chemistry A*, 96: 10 339–10 348, **1992**

[492] E. Ikeda, J. C. Mackie: *Journal of Analytical and Applied Pyrolysis*, 34: 47–63, **1995**

[493] J. Jones, G. B. Bacskay, J. C. Mackie: *Israel Journal of Chemistry*, 36: 239–248, **1996**

[494] J. A. Bray, E. R. Bernstein: *The Journal of Physical Chemistry A*, 103: 2208–2213, **1999**

[495] F. Holzmeier: *Photoionization of Nitrogen-Containing Reactive Molecules with Synchrotron Radiation.* Ph.D. thesis, Julius-Maximiliams-Universität Würzburg, **2015**

[496] E. Reusch, F. Holzmeier, P. Constantinidis, P. Hemberger, I. Fischer: *Angewandte Chemie International Edition*

[497] J. M. Vrtilek, C. A. Gottlieb, P. Thaddeus: *The Astrophysical Journal*, 314: 716–725, **1987**

[498] H. Liszt, P. Sonnentrucker, M. Cordiner, M. Gerin: *The Astrophysical Journal Letters*, 753, **2012**

[499] P. Thaddeus, C. A. Gottlieb, R. Mollaaghababa, J. M. Vrtilek: *Journal of the Chemical Society, Faraday Transactions*, 89(13): 2125–2129, **1993**

[500] J. Takahashi, K. Yamashita: *Journal of Chemical Physics*, 104(17): 6613–6627, **1996**

[501] C. Ochsenfeld, R. I. Kaiser, Y. T. Lee, A. G. Suits, M. Head-Gordon: *Journal of Cheimcal Physics*, 106(10): 4141–4151, **1997**

[502] D. J. DeFrees: *The Astrophysical Journal*, 308: L31–L35, **1986**

[503] R. A. Seburg, E. V. Pattersson, R. J. McMahon: *Journal of the American Chemical Society*, 131: 9442–9455, **2009**

[504] M. Steinbauer, M. Lang, I. F. ad Barbara K. Cunha de Miranda, C. Romanzin, C. Alcaraz: *Physical Chemistry Chemical Physics*, 13: 17956–17959, **2011**

[505] C. A. Taatjes, S. J. Klippenstein, N. Hansen, J. A. Miller, T. A. Cool, J. Wang, M. E. Law, P. R. Westmoreland: *Physical Chemistry Chemical Physics*, 7: 806–813, **2005**

[506] E. Reusch: *Photodissoziation des Propargylens*, **2013**

[507] W. von E. Doering, L. Knox: *The Journal of the American Chemical Society*, 79(2): 352–356, **1957**

[508] D. D. Hickstein, R. Yurchak, D. Das, C.-Y. Shih, S. T. Gibson: *PyAbel (v0.7): A Python Package for Abel Transforms*, **2016**. URL `http://doi.org/10.5281/zenodo.47423`

université PARIS-SACLAY
ÉCOLE DOCTORALE
Sciences chimiques : molécules, matériaux, instrumentation et biosystèmes

Titre : Dynamique des états excités dans des molécules à couche ouverte

Mots clés : Dynamique des états éxcités, Spectroscopie de masse, Spectroscopie photoélectron

Résumé : Dans cette thèse, la dynamique des états excités des radicaux et biradicaux a été examinée en utilisant la spectroscopie pompe-sonde résolue en temps à l'échelle femto-seconde. Les molécules à couche ouverte jouent un rôle primordial comme intermédiaires dans les processus de combustion, dans la formation de la suie et des hydrocarbures aromatiques polycycliques, dans la chimie atmosphérique ou dans la formation des molécules organiques complexes du milieu interstellaire et des nuages galactiques. Dans tous ces processus les molécules sont souvent excitées, soit par échauffement thermique, soit par irradiation. En conséquence la réactivité et la dynamique de ces états excités sont particulièrement intéressantes afin d'obtenir une compréhension globale de ces processus. Dans ce travail les radicaux et biradicaux ont été produits par pyrolyse à partir de molécules précurseur adaptées et ont été examinés dans un jet moléculaire en absence de collisions. Les radicaux sont ensuite portés dans un état excité bien défini, et ionisés avec un deuxième laser. La spectrométrie de masse à temps de vol permet une première identification de la molécule. Via des spectres de photoélectrons la molécule est caractérisée, pourvu que le spectre de masse ne montre majoritairement qu'une seule masse. Les spectres de photoélectrons ont été obtenus par l'imagerie de vitesse, permettant d'obtenir des informations sur l'état électronique du radical au moment de l'ionisation. L'imagerie de vitesse des ions permet de distinguer les ions issus d'une ionisation directe et ceux issus d'une ionisation dissociative. Pendant cette thèse un algorithme modifié de pBasex a été développé et implémenté en langage *python* : cet algorithme inverse des images sans interpolation des points expérimentaux. Pour des images bruitées, cet algorithme montre une meilleure performance.

Title : Excited-state dynamics of open-shell molecules

Keywords : Excited-state dynamics, mass spectroscopy, photoelectron spectroscopy

Abstract : In this thesis the excited-state dynamics of radicals and biradicals were characterized with femtosecond pump-probe spectroscopy. These open-shell molecules play important roles as combustion intermediates, in the formation of soot and polycyclic aromatic hydrocarbons, in atmospheric chemistry and in the formation of complex molecules in the interstellar medium and galactic clouds. In these processes molecules frequently occur in some excited state, excited either by thermal energy or radiation. Knowledge of the reactivity and dynamics of these excited states completes our understanding of these complex processes. These highly reactive molecules were produced via pyrolysis from suitable precursors and examined in a molecular beam under collision-free conditions. A first laser now excites the molecule, and a second laser ionizes it. Time-of-flight mass spectrometry allowed a first identification of the molecule, photoelectron spectroscopy a complete characterization of the molecule - under the condition that the mass spectrum was dominated by only one mass. The photoelectron spectrum was obtained via velocity-map imaging, providing an insight in the electronic states involved. Ion velocity map imaging allowed separation of signal from direct ionization of the radical in the molecular beam and dissociative photoionization of the precursor. During this thesis a modified pBasex algorithm was developed and implemented in *python*, providing an image inversion tool without interpolation of data points. Especially for noisy photoelectron images this new algorithm delivers better results.

Université Paris-Saclay
Espace Technologique / Immeuble Discovery
Route de l'Orme aux Merisiers RD 128 / 91190 Saint-Aubin, France